MESO-π-EXTENDED BODIPY DERIVATIVES: SELF-ASSEMBLY, OPTICAL PROPERTIES AND APPLICATIONS

Thesis Submitted to AcSIR for the Award of the Degree of
DOCTOR OF PHILOSOPHY
in Chemical Sciences

By

SANDEEP C.

Registration No: 10CC11J39002

Under the guidance of

Dr. A. AJAYAGHOSH

CSIR-NATIONAL INSTITUTE FOR INTERDISCIPLINARY
SCIENCE AND TECHNOLOGY (CSIR-NIIST)
THIRUVANANTHAPURAM-695 019, KERALA, INDIA

August, 2017

DEDICATED TO
MY MOTHER

DECLARATION

I hereby declare that the matter embodied in the thesis entitled: "***Meso*-π-Extended Bodipy Derivatives: Self-Assembly, Optical Properties and Applications**" is the result of the investigations carried out by me at the Photosciences and Photonics Section, Chemical Sciences and Technology Division, CSIR-National Institute for Interdisciplinary Science and Technology (CSIR-NIIST), Thiruvananthapuram, under the supervision of Prof. A. Ajayaghosh and the same has not been submitted elsewhere for any other degree.

In keeping with the general practice of reporting scientific observations, due acknowledgement has been made wherever the work described is based on the findings of other investigators.

Sandeep C.

Thiruvananthapuram
04-08-2017

75 Years of
CSIR Touching Lives

राष्ट्रीय अंतर्विषयी विज्ञान तथा प्रौद्योगिकी संस्थान
वैज्ञानिक तथा औद्योगिक अनुसंधान परिषद्
इंडस्ट्रियल इस्टेट पी.ओ., पाप्पनंकोड, तिरुवनंतपुरम, भारत-695 019
CSIR-NATIONAL INSTITUTE FOR INTERDISCIPLINARY SCIENCE & TECHNOLOGY (CSIR-NIIST)
Council of Scientific & Industrial Research
Industrial Estate P.O., Pappanamcode, Thiruvananthapuram, India-695 019

डॉ. ए. अजयघोष एफएनए, एफटीडब्ल्यूएस
निदेशक

Dr. A. Ajayaghosh FNA, FTWAS
Director

04-08-2017

CERTIFICATE

This is to certify that the work embodied in this Ph. D. thesis entitled “***Meso*-π-Extended Bodipy Derivatives: Self-Assembly, Optical Properties and Applications**” submitted by **Mr. Sandeep C.** to Academy of Scientific and Innovative Research (AcSIR), in partial fulfilment of the requirements for the award of the **Degree of Doctor of Philosophy in Chemical Sciences**, has been carried out under my supervision and guidance at the Photosciences and Photonics Section, Chemical Sciences and Technology Division of the CSIR-National Institute for Interdisciplinary Science and Technology (CSIR-NIIST), Thiruvananthapuram. I further certify that this work has not been submitted to any other University or Institution in part or full for the award of any degree or diploma.

A. Ajayaghosh
(Thesis Supervisor)

ACKNOWLEDGEMENTS

It is with great pleasure that I extend my deep sense of gratitude to Prof. A. Ajayaghosh, my thesis supervisor, for suggesting the research problem, for his valuable guidance, support, encouragement and scientific freedom of thought and action, leading to the successful completion of this work.

I would like to express my gratitude to Prof. M. V. George for being a huge inspirational figure for budding chemists like me at CSIR-NIIST.

I thank Dr. Suresh Das, former Director of CSIR- NIIST, Trivandrum, for providing me the necessary facilities for carrying out this work.

I express my deep sense of gratitude to our collaborator Dr. G. V. Pavan Kumar and Mr. Ravi P. N. Tripathi from IISER-Pune for waveguiding studies and valuable discussions. My sincere thanks are also due to:

- *Dr. K. R. Gopidas, Dr. D. Ramaiah, Dr. Joshy Joseph, Dr. Narayanan Unni, Dr. K. Yoosaf, Dr. C. Vijayakumar, Dr. B. Deb and Dr. V. Karunakaran, present and former scientists of the Photosciences and Photonics, Chemical Sciences and Technology Division, for their help and support.*
- *Dr. Mangalam S. Nair and Dr. R. Luxmi Varma, former and present AcSIR co-ordinators.*
- *Dr. K. V. Radhakrishnan, Dr. Rajeev Kumar Sukumaran, Dr. K. Yoosaf my DAC members.*
- *Mr. Adarsh, Mr. Alex, Ms. Shine K. Albert from IISER-Trivandrum for the NMR, Single crystal and AFM analyses.*
- *Dr. V. K. Praveen, Dr. Sunil Varughese for the effective fruitful discussions.*
- *Dr. J. D. Sudha for supporting and helping me in every possible way during my stay at CSIR-NIIST.*
- *Mr. C. K. Chandrakanth and Mr. M. R. Chandran, Ms. Soumya for SEM analysis and Mr. Kiran M. for TEM analysis.*

- *Dr. R. K. Mishra, Dr. Manas Panda, Dr. Manoj, Dr. Rahul Mukhopadhyay and Mr. R. Thirumalai for discussions.*
- *Ms. Vidya for helping me in experiments.*
- *All present and former members of 'The AG Group' and other members of Photosciences and Photonics Section, for their help and cooperation.*
- *Special thanks to Mr. Samrat Ghosh, Dr. Divya Susan Philips for their timely help.*
- *Mr. Robert Philip and Mr. J. S. Kiran for their general help and support.*
- *Mrs. M. Saumini, Mr. Adarsh, Mr. P. Preethanuj, Mr. T. Arun, Mr. P. Saran and Mr. R. Gokul for NMR and Mrs. S. Viji, Ms. Athira for mass spectral analyses.*
- *All my beloved teachers in every stages of my academic career.*
- *All my friends at NIIST.*
- *University Grants Commission (UGC) & CSIR network project for the financial assistance.*

I deeply acknowledge my parents and sister for their constant source of love, confidence and support.

Sandeep C.

CONTENTS

CHAPTER 2: An Unprecedented Amplification of Near-Infrared Emission in a Bodipy Derived π-System by Stress or Gelation 49-98

List of Abbreviations

A	Absorbance
ACQ	Aggregation caused quenching
AFM	Atomic force microscopy
AIE	Aggregation induced emission
ATR	Attenuated total reflection
a.u.	Arbitrary unit
BCP	Block copolymer
$BF_3.OEt_2$	Boron trifluoride diethyletherate
Bodipy	4,4-Difluoro-4-bora-3a,4a-diaza-*s*-indacene
BOP	((Benzotriazol-1-yloxy)tris(dimethylamino)phosphonium hexafluorophosphate
c	Concentration
COSY	Correlation spectroscopy
cm	Centimeter
CCDC	Cambridge crystallographic data centre
$CDCl_3$	Deuterated chloroform
CGC	Critical gelation concentration
$CHCl_3$	Chloroform
CuI	Copper iodide
d	Doublet
DCM	Dichloromethane
DLS	Dynamic light scattering
DMF	Dimethyl formamide
DMSO	Dimethyl Sulfoxide
DMSO-d_6	Deuterated dimethyl sulfoxide
DSC	Differential Scanning Calorimetry
EDA	Ethylenediamine
ESI	Electrospray ionization

et al.	*Et alii/aliae*
etc.	*et cetera*
Et_3N	Triethylamine
EtOH	Ethanol
FAB	Fast atom bombardment
FE-SEM	Field emission scanning electron microscopy
FT-IR	Fourier transform infrared
g	gram
GPa	Giga pascal
h	Hour
H-bonding	Hydrogen bonding
HCl	Hydrochloric acid
HOMO	Highest occupied molecular orbital
HRMS	High resolution mass spectrometry
Hz	Hertz
I_{em}	Intensity of emission
IR	Infrared
J	Coupling constant
K	Kelvin
KBr	Potassium bromide
K_2CO_3	Potassium carbonate
KF	Potassium fluoride
kJ	kilojoule
KOH	Potassium hydroxide
LUMO	Lowest unoccupied molecular orbital
M	Molar
m	Multiplet
M^+	Molecular ion
MALDI TOF-MS	Matrix assisted laser desorption ionisation time-of-flight mass spectrometer
MHz	Megahertz

Mp	Melting point
max	Maximum
mg	Milligram
min	Minutes
mmol	Millimolar
mL	Milliliter
MW	Molecular weight
n	Normal
ns	Nanosecond
NaOH	Sodium hydroxide
NIR	Near-infrared
nm	Nanometer
NMR	Nuclear magnetic resonance
OPE	Oligo(*p*-phenyleneethynylene)
p	para
PC	Photonic crystal
$PdCl_2(PPh_3)_2$	Bis(triphenylphosphine)palladium (II) dichloride
PDP	Pentadecylphenol
PEG	Polyethylene glycol
POM	Polarising optical microscope
ppm	Parts per million
PS	polystyrene
P4VP(MSA)	Poly(4-vinylpyridiniummethanesulphonate)
PXRD	Powder X-ray diffraction
ROESY	Rotating frame nuclear overhauser effect spectroscopy
rt	Room temperature
s	Singlet
SEM	Scanning electron microscopy
SAXS	Small angle X-ray scattering
T	Temperature

t	Triplet
TEA	Triethylamine
TEM	Transmission electron microscopy
TGA	Thermogravimetric analysis
THF	Tetrahydrofuran
TMS	Tetramethylsilane
UV	Ultraviolet
Vis	Visible
vs	versus
WAXS	Wide angle x-ray scattering
XRD	X-ray diffraction
α	Alpha
α_{Agg}	Fraction of aggregates
°C	Degree Celsius
ϕ_{f}	Fluorescence quantum yield
λ	Wavelength
λ_{ex}	Excitation wavelength
λ_{em}	Emission wavelength
θ	Theta
ε	Molar extinction coefficient
µm	Micrometer
1D	One-dimensional
2D	Two-dimensional
3D	Three-dimensional

PREFACE

Self-assembly is a powerful tool to create not only aesthetically appealing structures, but also opens up new vistas of developing fluorescent materials for stimuli responsive and photonic waveguiding applications. Most of these systems do have a π-conjugated backbone, hydrogen bonding units and a hydrophobic alkyl chains in addition to the chromophoric units present. It is possible to tune the material properties of these materials by using the noncovalent interactions such as π-π stacking, hydrogen bonding and van der Waals forces. Bodipy dyes continue to lure scientists around the world for decades because of their demand in developing high-end photonic materials. In fact, self-assembled bodipy based materials in the condensed states are least explored from the view point of application. The first Chapter of the thesis describes the general way of synthesis of Bodipy, basic photophysical properties and some of the recent literature report on Bodipy based self-assembled systems. In addition, specific objectives of the present thesis are briefly described at the end of this chapter.

NIR emitting small organic molecules are relatively rare when compared to UV-Vis light emitting molecules, however are important in the fields of materials and biology. NIR emission is generally achieved by decreasing the HOMO-LUMO gap by strong donor-acceptor interactions, by extension of π-conjugation or through metal complexation. Chapter 2 of the thesis deals with an unprecedented strategy to generate and amplify near-infrared (NIR) emission in an organic chromophore by mechanical stress or gelation pathways. There are a few reports of generation of NIR emission by mechanical force which are explained based on the molecular packing. A greenish-yellow emitting film of a π-extended Bodipy-1, obtained from *n*-decane, turned into orange-red upon mechanical shearing, with a 15-fold enhancement in NIR emission at

738 nm. Alternatively, a DMSO gel of the Bodipy-1 exhibited a 7-fold increment in NIR emission at 748 nm with a change in the emission color from yellow to orange-red upon drying. The reason for the amplified NIR emission in both cases is established from the difference in the chromophore packing, by single crystal analysis of a model compound (Bodipy-2), which also exhibited a near identical emission spectrum with red to NIR emission (742 nm). Comparison of the emission features, WAXS and FT-IR data of the sheared *n*-decane film and the DMSO xerogel with the single crystal data are in support of a head-to-tail slipped arrangement driven by the N–H···F–B bonding in the sheared or xerogel states, which facilitate strong exciton coupling and the resultant NIR emission.

In the third chapter of the thesis, we describe the photonic structure formed by annealing the self-assembly of Bodipy-3 which gives different color with different angles, exhibiting distinct irreversible fluorescence response from yellow to red. Photonic property of Bodipy-3 is proved by different microscopic analyses and spectroscopic methods. SAXS analysis revealed the structural transition from cubic to lamellar phase upon annealing the film. Reversible luminescence of the annealed photonic materials is achieved by making stimuli responsive ink using PEG as binder, ethanol as dispersant. An in-situ polymerised polystyrene gel when made into film also exhibited photonic property and demonstrated in security application to check the authenticity of the document. Finally, the optical waveguiding property of the photonic material is demonstrated in 2D planar microcrystals of Bodipy-3 using 532 and 633 nm laser excitation sources.

The fourth chapter of the thesis describes the synthesis, self-assembly and toroid formation of Bodipy-4. As far as the applications are concerned, toroidal architectures are very important in natural as well as synthetic world. For mimicking these structures, chemists have adopted several strategies, leading to nanotoroids formation. However, microtoroids formations by organic molecular assemblies are not reported. Bodipy-4 has two amide bonds connected through a flexible linker which allow both inter and intramolecular H-bonding. At lower concentrations, disk shaped particles are formed whereas at higher concentrations 1D supramolecular tapes are formed. A xerogel obtained from DMSO exhibited the presence of micrometer sized toroids.

In summary, the present thesis is a detailed study on the self-assembly properties of a few Bodipy derivatives exhibiting different hierarchical structures and luminescence properties. The important conclusion of the present study is the significant modulation in the photophysical and morphological features even with subtle change in the molecular structures of Bodipy derivatives. The findings of this study will help the design of new stimuli responsive fluorescent materials for security and waveguiding applications.

References

1. An Unprecedented Amplification of Near-Infrared Emission in a Bodipy Derived π-System by Stress or Gelation. **S. Cherumukkil**, S. Ghosh, V. K. Praveen, A. Ajayaghosh, *Chem. Sci.* **2017**, DOI: 10.1039/c7sc01696d.
2. A Bodipy Derived Photonic Material for Security and Waveguiding Applications. **S. Cherumukkil**, R. P. N. Tripathi, S. Ghosh, G. V. Pavan Kumar, A. Ajayaghosh (Manuscript under preparation).
3. A Bodipy Derived Liquid Crystalline π-Gelator that Forms Micron Sized Toroidal Structures. **S. Cherumukkil**, A. Ajayaghosh (Manuscript under preparation).

Chapter 1

Self-Assembled Bodipy Dyes and Their Applications: An Overview

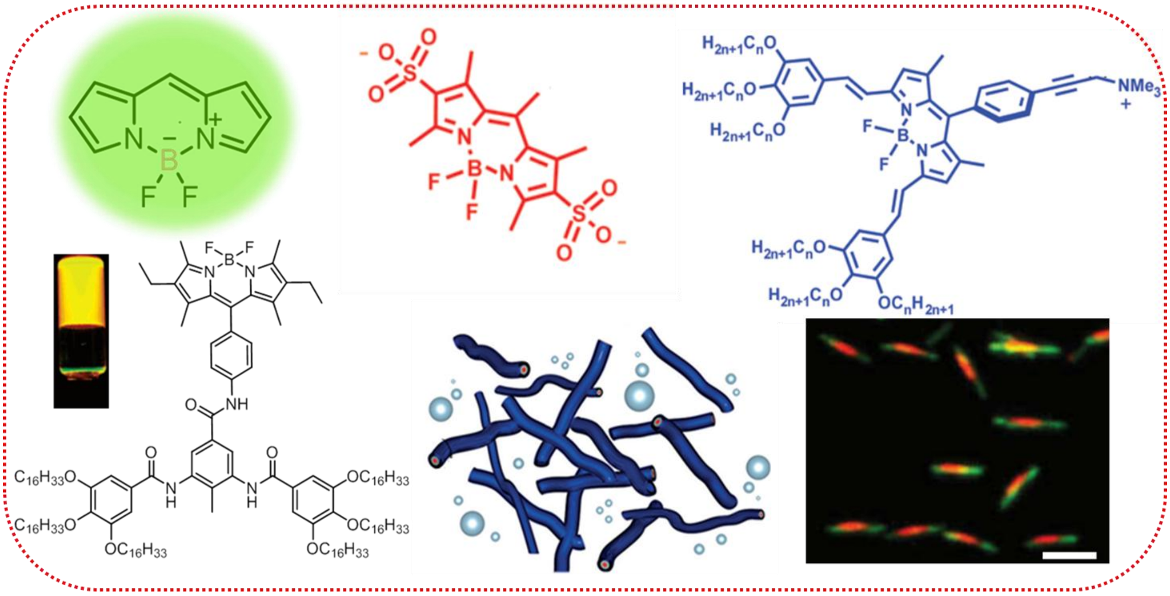

1.1. Abstract

Self-assembly is a powerful tool not only to create aesthetically appealing well organized assemblies but also for the development of functional materials for various applications. Out of the umpteen numbers of chromophores available in the synthetic world, Bodipy finds a special role because of the high fluorescent quantum yield, good solubility, excellent photostability and the synthetic easiness associated with them. Recently, research on Bodipy dyes has been getting momentum because of its diverse range of potential applications. The present

chapter gives an overview of the structure, general synthesis, photophysics and the self-assembly properties of a few bodipy derivatives. A few lines on the importance of linear π*-conjugated systems in self-assembly have been mentioned in the final part in order to arrive at the objective of the thesis. In the last part of the chapter, scope and objective of the thesis is presented.*

1.2. Introduction

Supramolecular chemistry is a broad interdisciplinary area, rapidly expanding and always concerned with exploiting various noncovalent interactions available with molecules.[1a-c] Noncovalent interactions such as hydrogen bonding, π-π stacking, dipole-diople, ion-dipole and van der Waals interactions *etc.* do often act synergistically in a supramolecular system leading to stable supramolecular assemblies with superior optoelectronic properties.[1d-h] Even though these forces are fairly weak in nature when considered individually, the combined effect of all these forces shapes the bulk properties of the molecule. Any subtle changes in their magnitude can often give an opportunity to make a dramatic change in the material properties. Molecular self-assembly is an all pervading phenomenon which involves the spontaneous association of molecules through noncovalent interactions into structurally well-defined entities. Self-assembly of molecules has created great opportunities for chemists to design functional assemblies similar to that of several biological assemblies from a simple conjugated molecular system. So far, the growth of an assembly is considered as one-dimensional, for instance, the growth of self-assembled cylinders is considered only from their ends. But recent trends in self-assembly demonstrated the growth in two-dimensions by making platelet-like structures with controlled size and composition through crystallization-driven self-assembly (CDSA) approach.[33] Supramolecular gels are particular classes of self-assembled materials where the chromophores are precisely organized in the gel matrix, used to make smart materials because of their unusual optoelectronic properties and stimuli responsive nature.[1d-f] These particular classes of materials are still holding the position as an intense research area in self-assembly because of their applications in the area of sensing, molecular electronics, catalysis, paints, inks, cosmetics *etc*. Self-assembly of functional dyes are widely explored in materials as well as biological applications. Merocyanine, naphthalimide, perylene bisimide, Bodipy, phthalocyanine, porphyrin, squaraine *etc.* are some of the examples of functional dyes which have a tendency to aggregate and exhibit interesting optoelectronic properties. Emission properties of the self-assembly of these functional dyes have been extensively used for sensing of various analytes.[1e,3a-f] In addition, these fluorescent molecular assemblies have also been utilised for imaging and security applications.[3g-k] Therefore, synthesis of new functional dyes and their self-assembly are of great importance.

1.3. Noncovalent Interactions

Major interactions that governs the self-assembly of molecular systems are hydrogen bonding, π-π stacking and van der Waals interactions.[2] Manipulation of these forces often leads to molecular assemblies with exciting properties. Hydrogen bonds are attractive interaction between a hydrogen atom attached to an electronegative atom (Donor) and an electronegative element having lone pair electrons (Acceptor). Hydrogen bonding acts as the most important secondary interaction by imparting selectivity, tunable strength and directionality for the supramolecular architectures.[2a] Hydrogen bonding directionality can be best introduced by incorporating amide or urea based gelators. The π-π stacking interaction can be seen in aromatic systems due to the presence of π-surface. Hunter and Sanders have come up with a model to explain the phenomenon of π-π interaction.[2b,c] In the electrostatic interaction model, three point charges are assigned to the atoms in the aromatic molecule (one at the positively charged carbon atom and the other two as above and below the plane of the π-system (-1/2 charge)). In the extended linear π-conjugated systems, the adjacent chromophores will have varying π-π stacking interaction which affects their functional properties when it undergoes self-assembly.

Table 1.1. Average calculated energies of various noncovalent interactions.[2a]

Entry	Type of interaction	Strength (~ kJ/mol)
1	Covalent	100-400
2	Coulomb	250
3	Hydrogen bond	10-65
4	Ion-dipole	50-200
5	Dipole-dipole	5-50
6	Cation-π	5-80
7	π-π	0-50
8	van der Waals forces	< 5
9	Hydrophobic effects	Difficult to assess
10	Metal-ligand	0-400

The van der Waals interaction arises due to the hydrophobic alkyl chains and their inter-digitation in the supramolecular systems leading to ordered lamellar structures. Among all the forces mentioned here, the weakest one is the van der Waals interaction; however, has significant impact in altering molecular level properties. An ordinary covalent bond has a strength ranging from 100-400 kJ/mol and is considerably greater than most of the prominent noncovalent interactions such as hydrogen bonding (~50 kJ/mol), van der Waals forces (~5 kJ/mol) and the coulombic interactions (~250 kJ/mol).[2a]

1.4. 4,4-Difluoro-4-bora-3a-4a-diaza-*s*-indacenes (Bodipy Dyes)

Fluorescent dyes continue to lure scientists because of their rampant use in personal diagnostics, organic light emitting devices (OLED), and smart functional materials. Out of countless varieties, the difluro-boraindacene family (4,4-difluoro-4-borata-3a-azonia-4a-aza-*s*-indacene, abbreviated as F-Bodipy) has gained popularity over the past two decades not only due to high molar absorption coefficients (40,000 to 110,000 M^{-1} cm^{-1}), large fluorescent quantum yields (60-90%) and relatively long excited lifetimes (1 to 10 ns), but also possess excellent chemical and photochemical stability in solution and in the solid state with superior charge-transfer properties.[4] In addition, Bodipy dyes find superior among other dyes such as perylene bisimide (PBI) and porphyrins since the optical properties of Bodipy dyes can be tuned by modifying the central *meso* position, pyrrole core and the boron atom. Similar to porphyrins and pthalocyanines, Bodipy can be used for vacuum deposition in organic electronic devices.[9] The first report on Bodipy synthesis came from Treibs and Kreuzer in 1968 and much attention was given only after 1980s.[5] Since, the Bodipy core consists of an extended delocalized π-system, two equivalent delocalized structures (A and B) can be drawn as shown below (**Figure 1.2**).[7]

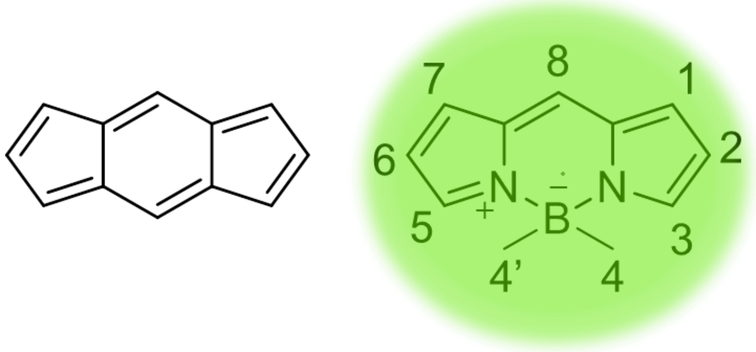

s-Indacene

4-Bora-3a,4a-diaza-*s*-indacene

Figure 1.1. Structure and the numbering of Bodipy system derived from indacene.

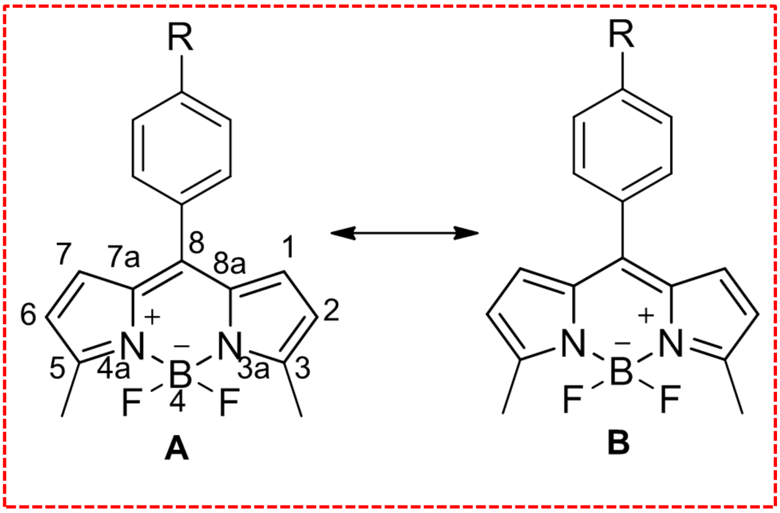

Figure 1.2. Equivalent resonance structures of Bodipy core.

While considering the Bodipy core, a strong π-electron delocalization is observed within central six membered ring and the adjacent two pyrrole rings. This π-electron delocalization is disrupted between both B-N bonds. In Bodipy, all the ring atoms assume a position within a plane. Although Bodipy resembles to that of monomethine dyes, a closer inspection reveals that the chromophore consists of 12 π-electrons distributed over 11 atoms, making it isoelectronic with heptamethine cyanines.

The rigidified dipyrromethene-boron difluoride structure can generally accessed by the complexation between dipyrromethene unit with a boron trifluoride salt and this rigidity is attributed to the high quantum yield of the dye. The name boradiazaindacene is analogous to that of all-carbon tricyclic ring (**Figure 1.2**) and similar to the porphyrinic systems, the 8-position is referred to as '*meso*'. The general way of preparation of Bodipy is by the condensation between highly electrophilic carbonyl compounds such as acyl chloride, acid anhydride and an aldehyde with two pyrrole units in presence of a base (**Figure 1.3**). The pyrrole is often substituted with methyl groups to prevent it from polymerization or porphyrin formation. Further complexation with $BF_3.OEt_2$ in presence of a base like triethylamine leads to the formation of F-Bodipy dyes.[4] One of the easiest ways of functionalization on Bodipy dye is the *meso* substitution at the 8-position which will not dilute the electronic properties of the dye. In addition, substitution on the pyrrole group can preserve the orthogonal geometry by restricting the rotation of the aromatic groups at the *meso* position of the dye which causes a minimal interaction between the *meso* substituent and the dye. The active methyl groups at the 3,5-positions of the F-Bodipy can be easily protonated under mild conditions resulting in an intermediate which attack nucleophilically at the carbonyl carbon of the aldehyde, resulting in styryl derivatives. These derivatives do have bathochromic absorption and emission properties. Coupling reactions such as Sonogashira, Heck, Suzuki or Stille are used to introduce ethyne, ethane and aryl groups on F-Bodipy if it is suitably substituted with a halogen atom.[4]

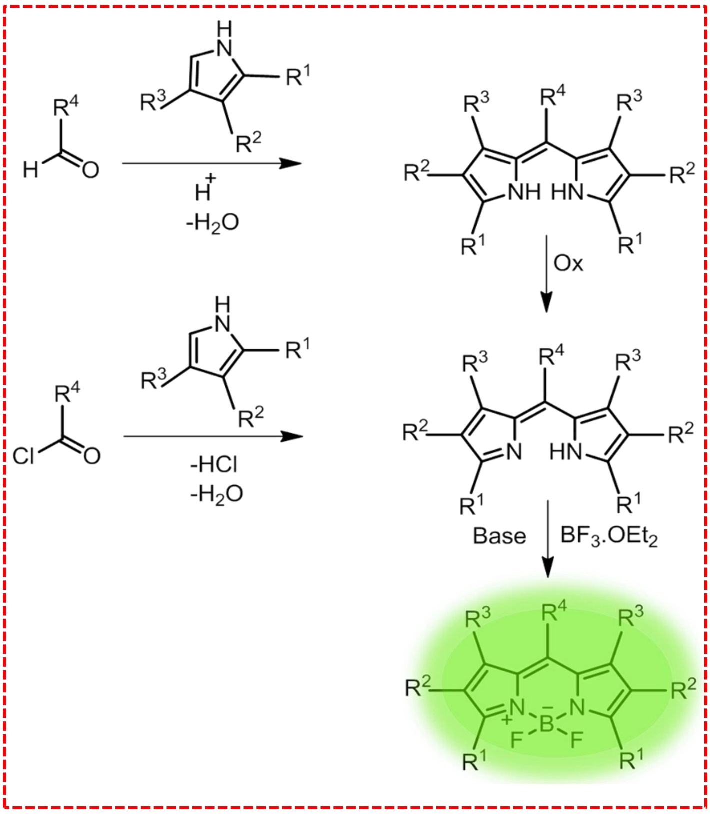

Figure 1.3. Schematic representation of synthesis of symmetric F-Bodipy dyes.

1.5. Photophysical Properties of Bodipy Dyes

Bodipy dyes absorb strongly in the UV-vis region and show sharp fluorescence band with excellent quantum yields. Since relatively insensitive to polarity and pH, they exhibit reasonably good stability under physiological conditions. Upon small modification on its structure, the fluorescence can be tuned enabling them to use in DNA and protein labeling studies. Alkyl or aryl substitution at the *meso* position of the Bodipy core does not bring much change on the absorption and emission maxima (comparing **1** with **4** and **2** with **5**).[10] Nevertheless, the quantum yield of the Bodipy **4** is considerably less than the Bodipy **5**. This is attributed to the restricted rotation associated with the more substituted (1,7) derivative **5** where the non-radiative decay pathway is blocked to a greater extend. Similar logic can be applied for the introduction of *ortho* substituents on the phenyl ring where the quantum yield is found to be more. Sometimes the change in emission maxima cannot be rationalized based on the aliphatic substituents attached to the pyrrole ring. For instance, even though the Bodipy dyes **6** and **3** have three substituents on the pyrrole ring, the former has a shorter emission wavelength than the latter. Although the molecule **7** has only two attachments on the pyrrole ring, it shows the longest wavelength fluorescence maximum (560 nm) (**Figure 1.4**).

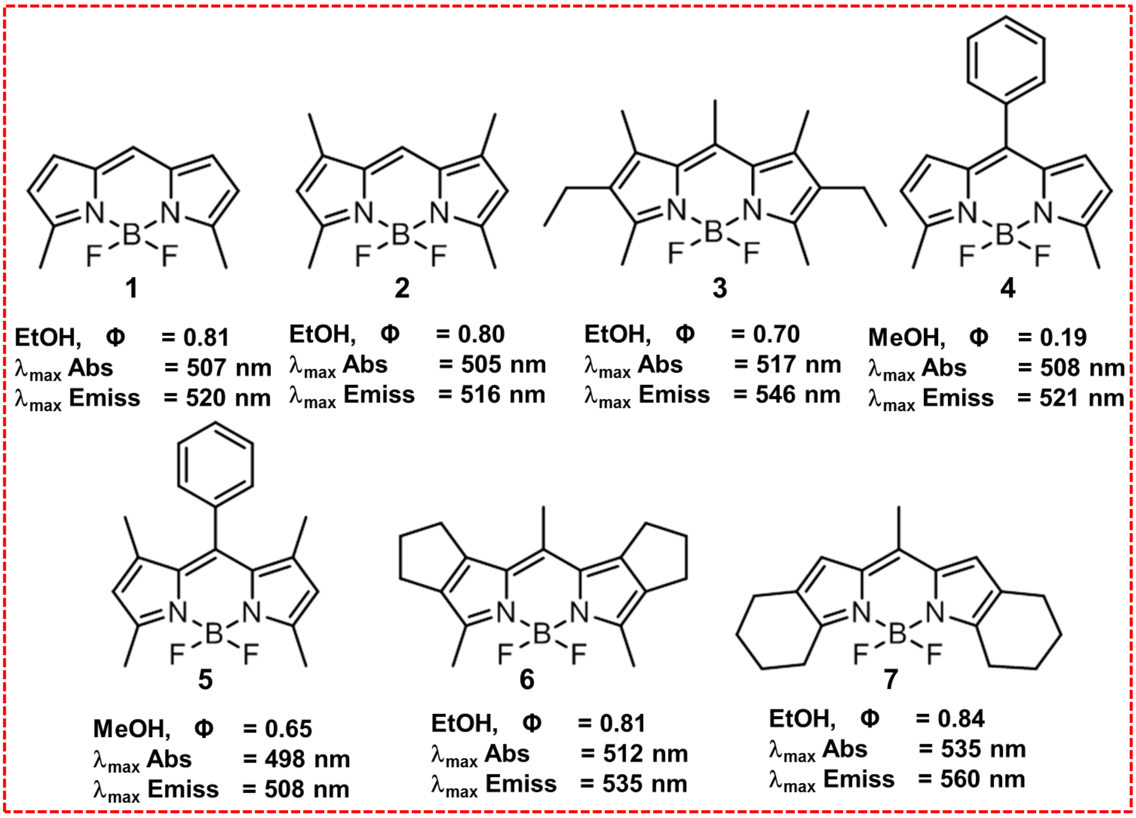

Figure 1.4. Simple Bodipy derivatives and their variation in photophysical parameters.

The absorption spectrum of the simple Bodipy derivative **8** shows a strong narrow absorption maximum at 510 nm (S_0-S_1, 0-0 vibrational transition) and a shoulder at the short wavelength side with a maximum of around 480 nm (0-1, vibrational transition) in relatively non-polar cyclohexane (**Figure 1.5b**).[7] As the polarity of the solvent is increased from toluene to acetonitrile, a slight blue shift from 512 to 505 nm has been observed in the absorption spectrum of the molecule **8 (Figure 1.5c)**. A blue shift from 524 to 517 nm also observed in its emission spectra under similar circumstances which is consistent with the general photophysical behavior of Bodipy chromophores. Additionally, a very weak band at 375 nm (S_0-S_2 transition) is also observed in the absorption spectrum of the molecule **8** which is barely affected by solvent polarity. Slightly Stokes-shifted mirror image shaped (with respect to absorption) emission spectrum is observed at 510 nm in cyclohexane. Not only the fluorescence bands are hypsochromically shifted (524 to 517 nm) but also their fluorescence quantum yield got decreased (0.52 to 0.21) while increasing the solvent polarity from toluene to acetonitrile. The decrease in quantum yield is attributed to the increase of the non-radiative rate constants in polar solvents. The perfect mirror symmetry between absorption and emission spectra indicates that the main band in the absorption spectrum corresponds to S_0-S_1 transition. Generally, with increasing the strength of the electron withdrawing group in the *meso* position, a slight bathochromic shift is appeared in the absorption and emission spectra. For instance, in molecule **9** the absorption (513 nm in toluene and 507 nm in acetonitrile) and emission maxima red shift by 3-4 nm, whereas the carbo-methoxy group in molecule **10** (λ_{abs} =

517/511 nm (toluene/acetonitrile) and λ_{em} = 538/531 nm (toluene/acetonitrile)) showed a larger red shift of 5 and 15 nm in the absorption and emission spectra, respectively when compared with the spectral properties of the molecule **8**.

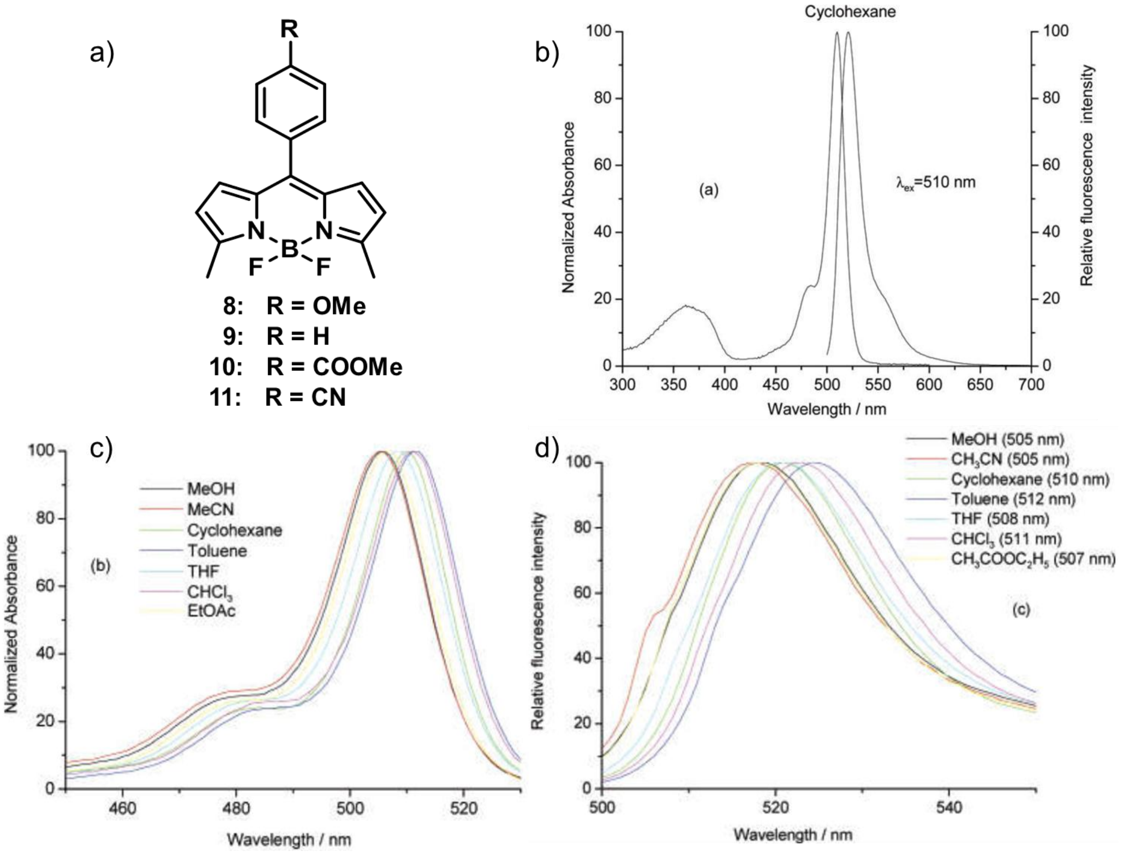

Figure 1.5. (a) Molecular structures, (b) normalised absorption and emission of **8** in cyclohexane and (c, d) absorption and emission spectra (excitation wavelength given in parentheses) of **8** in different solvents.

Similarly, in the case of the cyano derivative **11**, the corresponding spectral shifts of 7 and 20 nm were observed for their absorption and emission maxima, respectively. The reason for the observed red shift with respect to the increase in the electron withdrawing group attached at *para* position can be attributed to the greater stabilization of the LUMO without affecting the HOMO level. As a result, an electron withdrawing group at 8-position will decrease the HOMO-LUMO energy difference. Generally, most of the Bodipy dyes do not show fluorescence in the solid state. The primary reason is attributed to their small Stokes shift (5-20 nm) which increases the energy transfer between dyes and the trapping of excitation energy by aggregates. Secondly, their planarity favors π-π stacking which leads to the loss of emission efficiency.[11] Kasha's molecular exciton theory has been used by chemists to explain the intermolecular coupling in the condensed phase.[12] A schematic illustration for the dimer aggregate is represented over here (**Figure 1.6**). This quantum mechanical theory basically depends on the dipole-dipole interaction between the dye monomers in the aggregates, which predicts the splitting of the excited state of the monomers from the initial degenerated E* into excited states of energies E (+) and E (-).[13]

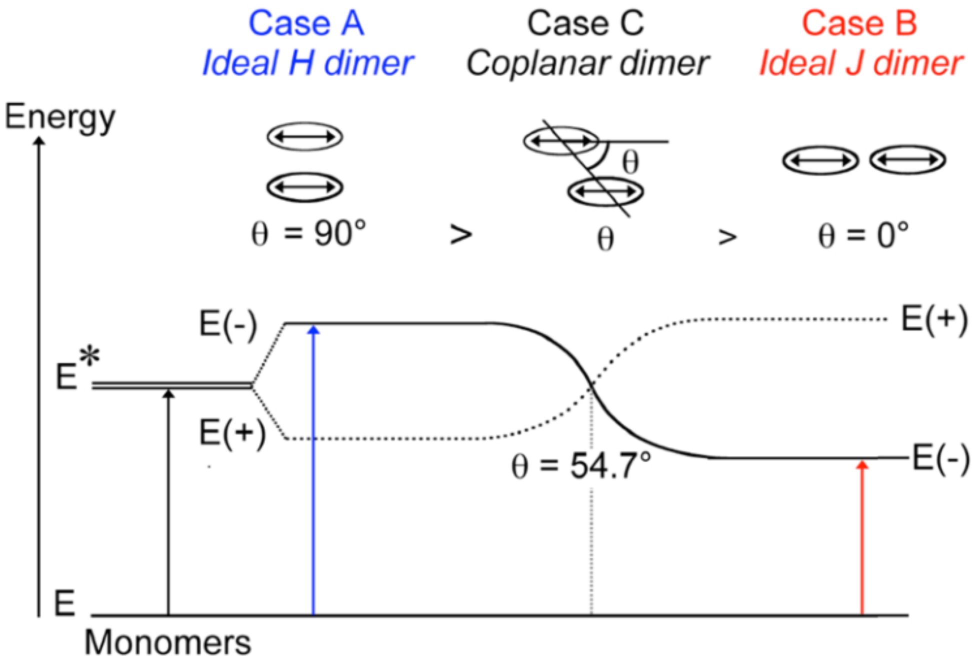

Figure 1.6. Exciton splitting of the electronically excited states for different geometric dispositions of the monomer units in a dimer. Full line, allowed electronic transition/state; dotted line, forbidden electronic transition/state; oval shaped object, monomer unit; double arrow, transition moment.[13]

In H-aggregates, where the molecular units are aligned parallel (sandwich-like structure) or coplanar with an angle of $\theta > 54.7°$, where only the transition to the highest level is allowed in the absorption process and the deactivation happens through a non-radiative pathway from the lowest excited state to the ground state. As a result, H-dimers are characterised by the blue shift in the absorption maximum when compared to the monomeric band and a very weak fluorescence observed owing to the increased non-radiative pathway of the de-excitation mechanism.[14] On the other hand, monomeric units in J-aggregates are placed in a head-to-tail manner (Case B in **Figure 1.6**) or coplanar displacements with $\theta <$ 54.7° where only the transition to the lowest excited state is allowed. Consequently, J-aggregates can be distinguished by the bathochromic shift in the observed absorption maximum when compared to that of the monomeric absorption band and a nearly resonant fluorescence (very small Stokes shift) with narrow band.

1.6. Self-Assembly of Bodipy Dyes with Ionic Groups

Synthesis, characterization and photophysical properties of a variety of Bodipy dyes have been reported. For example, Ziessel *et al.* have reported the self-assembly of a number of Bodipy derivatives having ionic groups which are (**Figure 1.7**) efficient energy transfer systems useful as a potential light-harvesting array for solar cell applications.[15] The self-assembly between sodium salt of dianionic sulfo Bodipy dye **13** (which acts as a donor) with planar cationic distyryl Bodipy core **12** (which acts as acceptor) in a ratio of 1:2 formed a complex **13*12**. The absorption spectrum of complex **13*12** is a combination of

13 (λ_{max} = 513 nm, ε_{max} = 75 000 M^{-1} cm^{-1}) and **12** (λ_{max} = 646 nm, ε_{max} = 240 000 M^{-1} cm^{-1}).

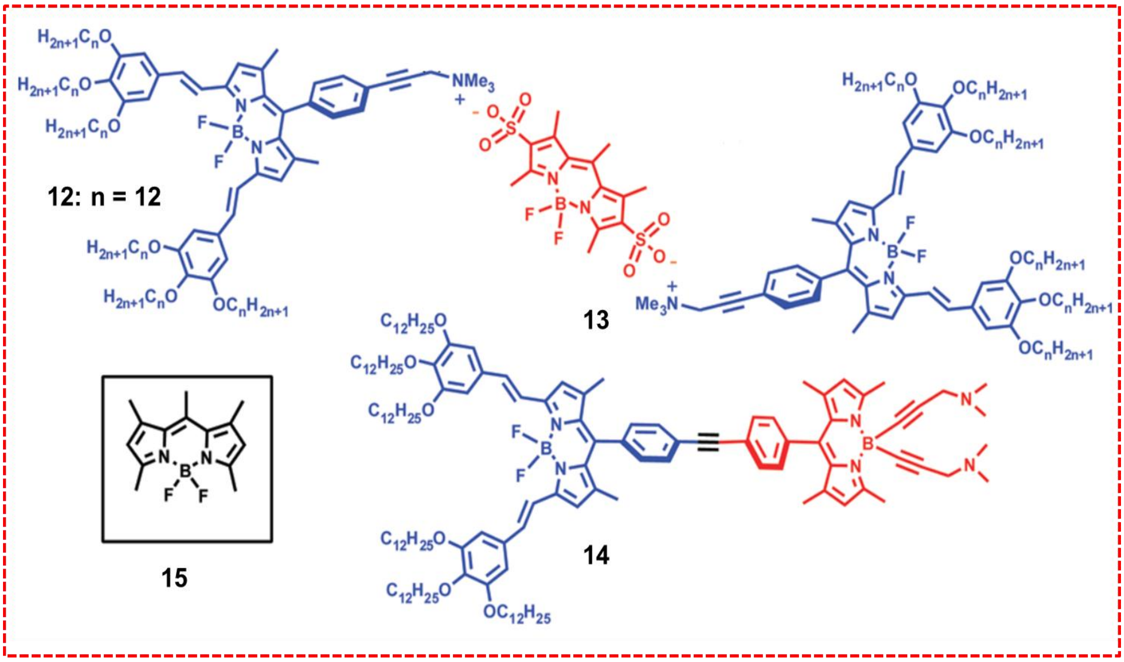

Figure 1.7. Charged Bodipy derivatives for the ionic self-assembly.

The molecule **13** is known to absorb at 495 and emit at 520 nm (when excited at 500 nm) in isolated solutions. For complex **13*12**, the main absorption spectrum of the molecule **13** is shifted from 495 nm to 513 nm in the complex, maintaining the absorption maximum of **12** (646 nm) as the same (**Figure 1.8a**). Also, a strong fluorescence centered at 670 nm was obtained along with quenching of the emission band at 520 nm for the complex **13*12** when excited at 500 nm (**Figure 1.8a**). This observation implies that approximately > 98% energy transfer is happening in the complex **13*12** from the dianionic sulfo Bodipy dye **13** to the acceptor distyryl Bodipy core **12**. This is further confirmed by the observed matching between the excitation and the emission spectra of the complex **13*12** over the entire spectral window. On the other hand, when the molecule **12** is mixed with the neutral molecule **15** in a ratio of 2:1 in THF, the absorption spectrum resembles that of the complex **13*12**. However, excitation at 480 nm results strong emission at 511 nm together with a very weak band characteristic of **12** at 670 nm (**Figure 1.8b**). The latter emission is attributed to direct excitation of **12** where the dye shows slight absorption at 480 nm. The absence of electronic energy transfer in the mixture **12:15** is further confirmed by the mismatch observed between the absorption and excitation spectra of the mixture. The excitation spectrum of the mixture by monitoring the emission at 680 nm has shown only contribution from the molecule **12**. This is a clear manifestation of the importance of electrostatic interaction for efficient electronic energy transfer in a donor-acceptor mixture. In addition, only electrostatic complex forms hexagonal columnar mesophases under heating when analyzed through polarizing optical microscope (POM) and differential scanning calorimeter (DSC). This particular situation is not observed in the covalently bonded donor-acceptor molecule **14** where the molecule crystallizes without going through the mesomorphic state, again highlighting the importance of ionic self-assembly for optoelectronic properties. The complex formed by the ionic self-assembly (**13*12**) which exist in the columnar mesophase has also shown an intense, broad emission profile in the NIR region when dispersed on a glass slide (**Figure 1.8c**).[15] More red-shifted emission is seen in the film state than in the solution state which indicates the propensity of the molecule to form higher ordered aggregates in the film state.

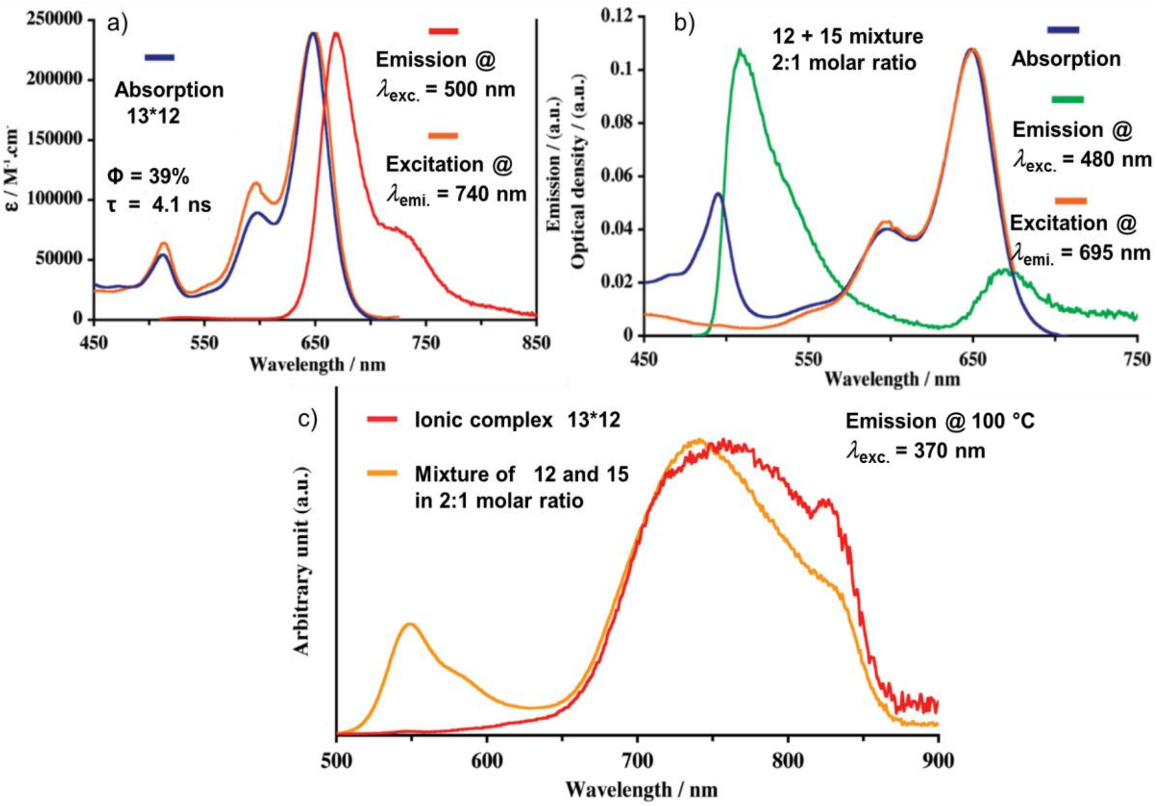

Figure 1.8. a and b) Absorption, fluorescence and excitation spectra in THF, at RT, 1 x 10^{-6} M: (a) complex **13*12** (λ_{ex} = 500 nm, λ_{em} = 740 nm), (b) 2/1 mixture of **12** and dye **15** (λ_{ex} = 480 nm, λ_{em} = 695 nm), and c) Fluorescence spectra (λ_{ex} = 370 nm) of complex **13*12** in the columnar mesophase at 100 °C (red trace) and complex **12** mixed with dye **15** in 2 to 1 mol stoichiometry in the solid state at 100 °C (orange trace).

Similar instance of ionic self-assembly of 2,6-disulfonate dye of Bodipy (**13**) derivative (**13*16)** with trialkoxy benzyl-functionalised imidazolium cations (**Figure 1.9**) lead to the formation of hexagonal columnar mesophase which is confirmed by polarising optical microscope (POM) observing a characteristic birefringent pseudo-fan shaped texture upon cooling from the hot isotropic melt of the complex. On the other hand, when the terminal group of trialkoxy phenyl part is substituted with a polymerisable double bond (**17**), polymerization was possible under mild conditions using radical photoinitiator which were used to write information on the film. Within the film, the dye remains in the aggregated state and exhibited red shifted luminescence in the solid state (**Figure 1.10b**).[16]

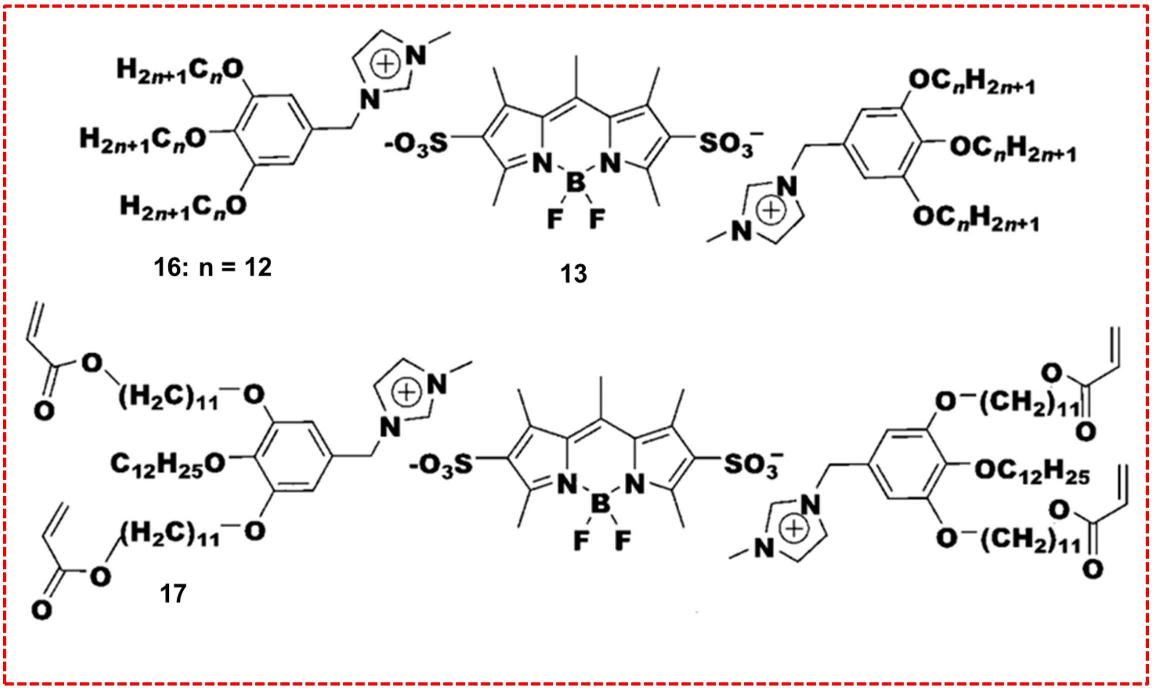

Figure 1.9. Structures of the complex **13*16** and **13*17**.

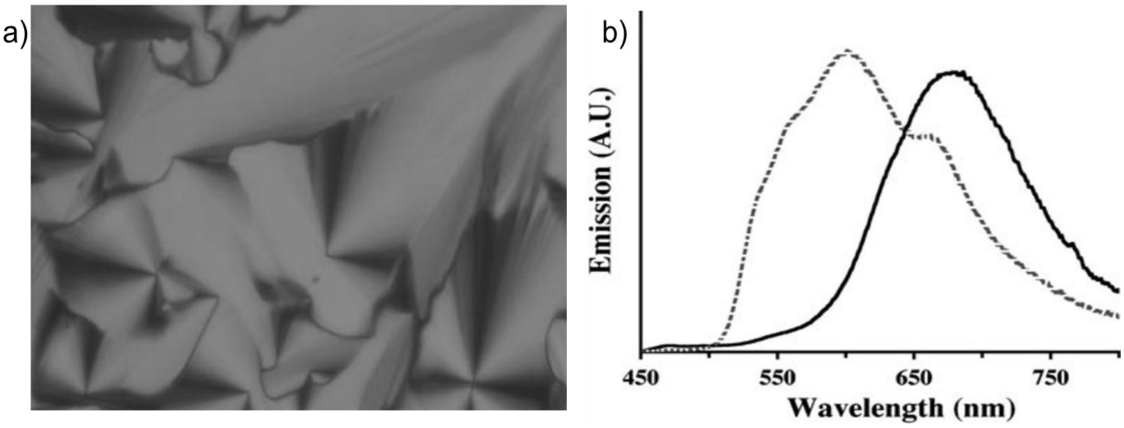

Figure 1.10. a) Pseudo fan shaped columnar textures observed under POM at 100 °C for **13*16.** b) Solid state emission spectra (λ_{ex} = 390 nm) of **13*16** (solid line) and **13*17** (dashed line).

1.7. Bodipy Derived Gelators

Supramolecular gels are important class of soft materials having multiple applications. A new class of Bodipy based gelators were developed by Ziessel *et* *al.* by making use of diacylamidotoluene platform functionalized with two lateral aromatic rings appended with aliphatic long chains (**Figure 1.11a**).[17] In this case, the Bodipy not only forms gel but also exhibited fluorescence from the texture of a thermotropic liquid crystalline mesophase. Heating of **18** in nonane solvent gave a homogeneous solution which upon cooling lead to a yellow emitting gel (**Figure 1.11b**) with a fluorescent band at 592 nm. The unique molecular design in which the methyl substituent at the central ring of the diacylamido platform makes the adjacent amide units to tilt at an angle thereby facilitating intermolecular hydrogen bonding. In addition, the *meso* substitution mitigates the inhibition for the π-stacking tendency in the solid state.

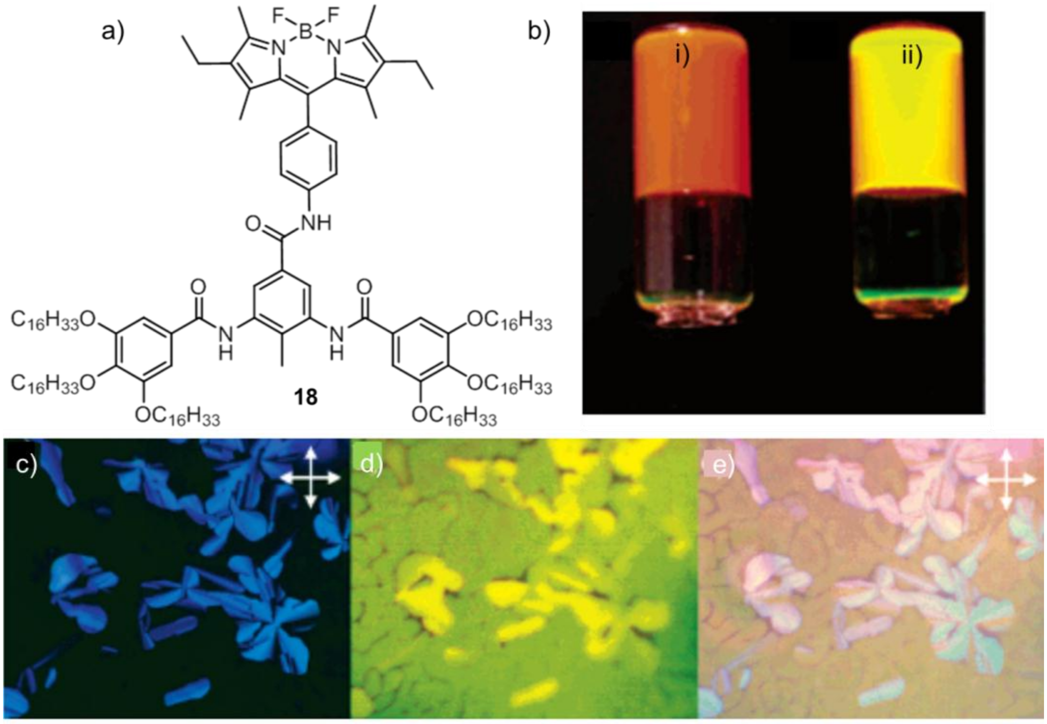

Figure 1.11. a) Molecular structure, b) gel photograph under normal light (i) and UV light (ii), (c) POM image at 212 °C with white light transmitted between crossed polarizers, d) corresponding fluorescent microscopic image without polarizer and e) superposition of c and d.

Aggregation of the indacene core is the main driving force for the gelation. The morphology of the gel in nonane (CGC 16 g/L) was investigated with TEM and freeze fracture electron microscopic studies, which revealed the presence of fibrils of upto the dimension of 500 nm length and 20 nm wide. Yellow-green luminescence was observed in the isotropic state. While cooling back to 212 °C, brightly luminescent pseudo-fan shaped textures were observed without any polarizer (**Figure 1.11d**). Fluorescence color is again changed from yellow-green to orange-red during the transition from mesophase to the crystalline state at 28°C.

The Bodipy based pol**y**(*p*-phenyleneethynylenes) derivative (**Figure 1.12**) shows excellent luminescent properties, and its self-assembly leads to interesting morphological features such as particles, fibres and intertwined network structures (gel) owing to the rod-coil type structure of the polymer.[18]

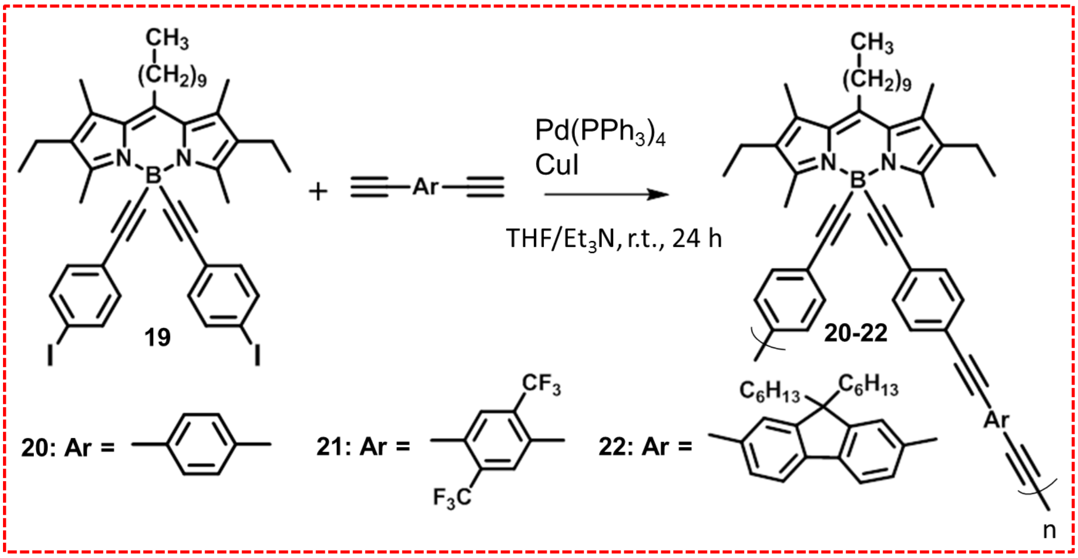

Figure 1.12. Polymerisation of Bodipy based monomer **19** with diyne monomers.

SEM analysis of the molecule **19** revealed the formation of particles ranging from nanometer to micrometer dimensions (**Figure 1.13**). On the other hand, polymer **20** self-assembles to form particles; however these particles further aggregates to form fibre-like structures in THF solution. Interestingly, at a concentration of 2 x 10^{-2} M, the polymer **20** forms gel in chloroform. The quantum yield of the gel was found to be less when compared to that in the non-gelated form owing to greater π-π stacking, leading to the collisional quenching of the excited state. The absorption maximum corresponding to $\pi \rightarrow \pi^*$ transition in polymers **20**, **21** and **22** are 348, 370, 372 nm which are bathochromically shifted from that of the band (265 nm) observed for **19** (**Figure 1.14a**). The above observed bathochromic shift in the absorption maximum is a clear indication of the extension of π-conjugation along the polymer chain when it was analysed in chloroform having a concentration of 1 x 10^{-5} M.

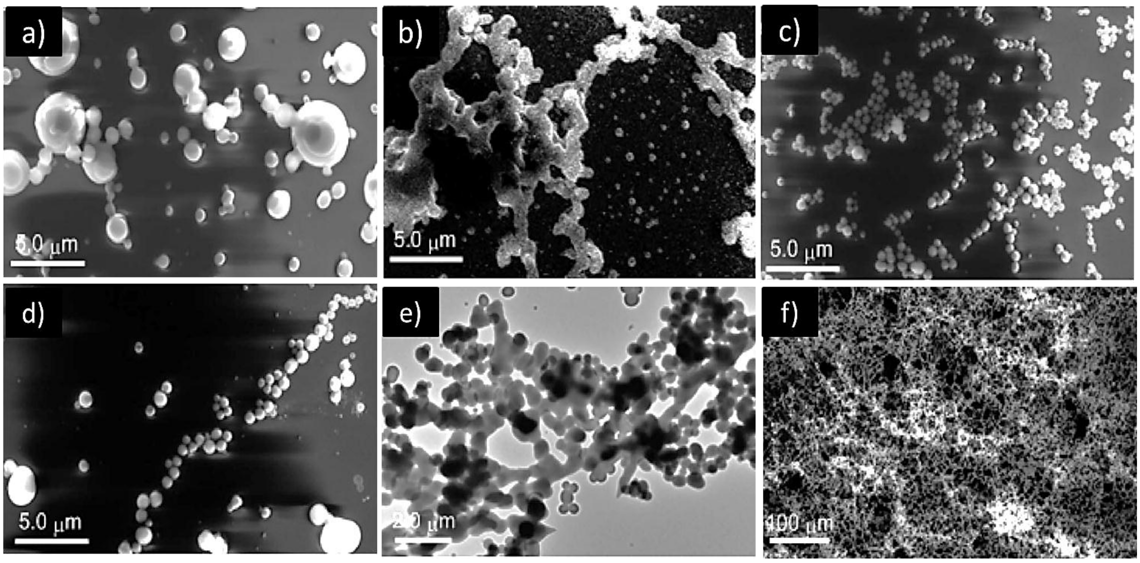

Figure 1.13. SEM micrographs of a) **19**, b) **20**, c) **21** and d) **22** dried at ambient temperature for 3.0 h on a glass plate. TEM micrograph of e) **20** dried at ambient temperature for 5.0 h on a carbon-coated copper grid, and f) SEM micrograph of chloroform (2 x 10^{-2} M) dried gel of **20**. Concentration of all samples corresponding to figures a-e is 1.0 g/L in THF.

Compounds **19-22** (1 x 10^{-5} M, $CHCl_3$) exhibited the same emission maximum (532 nm) when excited both in the absorption maximum 519 nm of Bodipy ligand and the π→π* bands of individual compounds, indicating that their emissive sources consist of Bodipy moiety. The absolute fluorescence quantum yield for the molecule **19** (Φ_F = 92%) when excited directly at the absorption maximum (519 nm) is slightly larger than that of the polymers **20** (Φ_F = 80%), **21** (Φ_F = 71%) and **22** (Φ_F = 85%), when excited at their respective π→π* bands. The observed difference in quantum yields of these polymers is probably attributed to the difference in the energy transfer efficiency (from π-conjugated linkers to Bodipy) of each co-monomer. The film state emission undergoes a red shift when compared to their solution state especially in the case of **20** which is attributed to the higher degree of ordering in the polymer originating from the regulated fibre and network formation (**Figure 1.14b**).

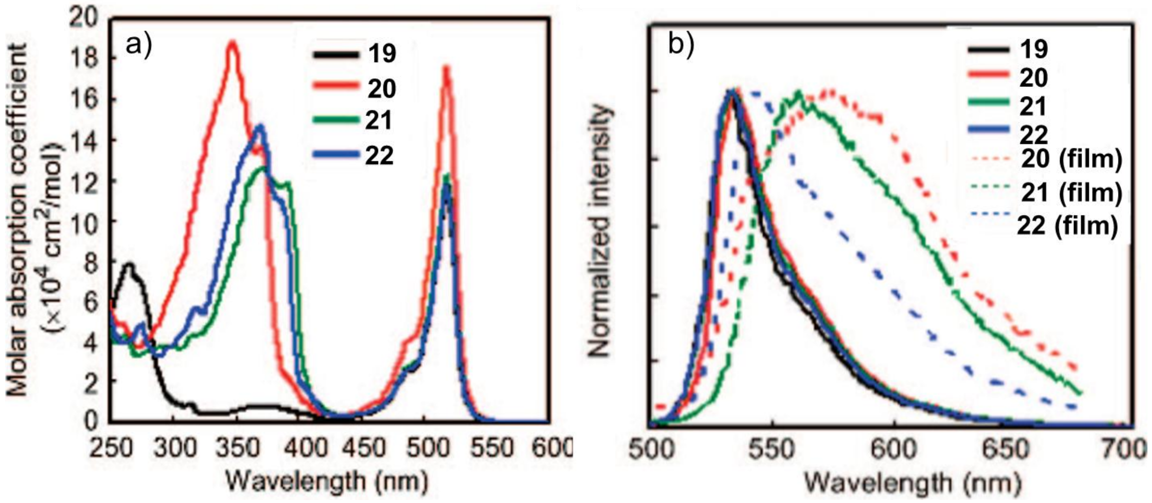

Figure 1.14. a) Absorption and b) emission spectra of **19, 20, 21, 22** in $CHCl_3$ (1 x 10^{-5} M).

Fluorescent Bodipy based rotaxane gel (**23**) which responds to multiple stimuli such as temperature, solvent polarity and acid/base vapors was reported by Jiang *et al*.[19] Authors have used 1,4-diethoxypillar[5]arene as wheel over a long alkyl axle with Bodipy as stopper at its one end (**Figure 1.15**). The shuttling nature triggered by the external stimuli was confirmed through ^{1}H-NMR spectral analyses.

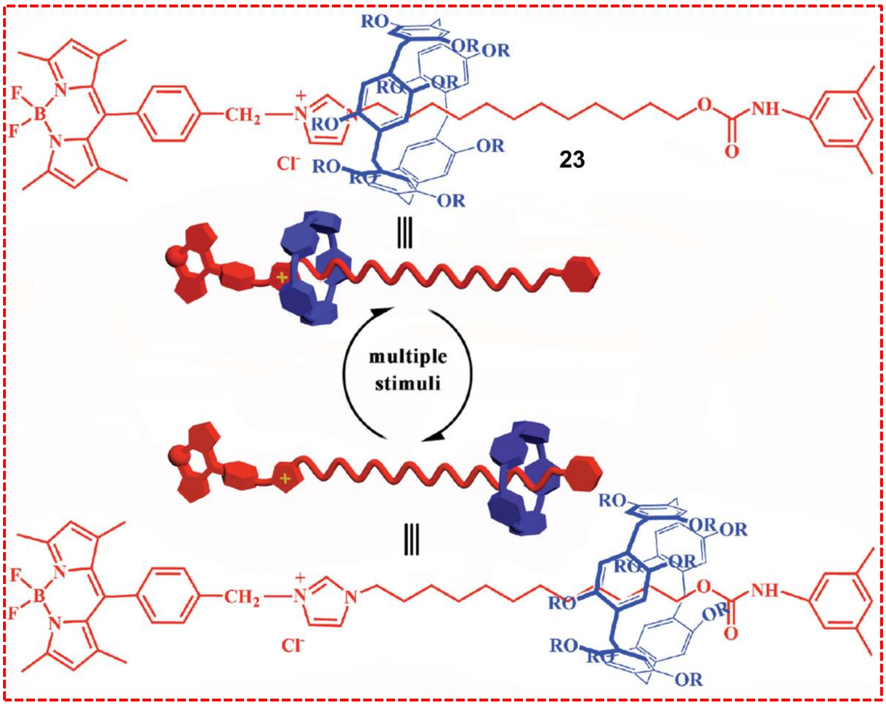

Figure 1.15. Molecular structures and the schematic representation of **23** under multiple stimuli.

A supramolecular reversible gel of **23** in DMSO (CGC 11.2 wt%) formed a 3D network structure comprised of nanofibres which resulted in a porous structure as evident from the SEM analysis (**Figure 1.16b**). The xerogel film prepared from the above gel showed weak emission with a red shifted broadened band at 534 nm. When exposed to HCl gas, the luminescence intensity considerably reduced followed by a fluorescence color change from yellow to purple-red under UV light (**Figure 1.16a, c**). In contrast, when exposed to NH_3 gas, the luminescence intensity increased to 100%. These results confirm the potential use of this supramolecular gel as an acid/base gas sensor.

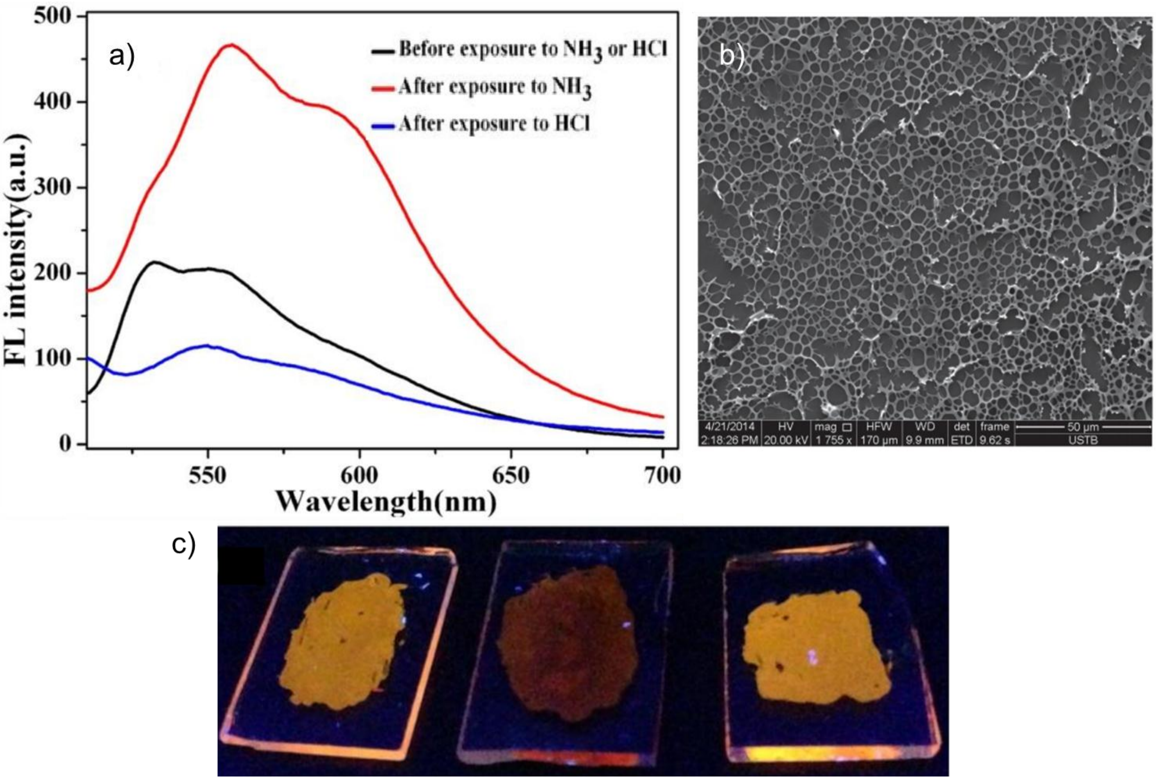

Figure 1.16. a) Fluorescence spectral response of xerogel film before and after exposure to NH_3/HCl. b) SEM image showing the porous network structure of **23** DMSO gel. c) Photograph of the xerogel under UV light (λ_{ex} = 365 nm) before (left) and after exposure to HCl (middle) and NH_3 (right).

1.8. NIR Emitting Bodipy Self-Assemblies

Near-infrared emitting Bodipy based fluorescent organic nanoparticles based on the self-assembly of lipidic Bodipy dyes were reported by Ziessel and coworkers.[20] The π-extended Bodipy derivative **26** contains two styryl moieties having long alkyl chains and a cationic moiety at the *meso* position (**Figure 1.17**). The absorption spectrum of the blue distyryl-based Bodipy dye **26** has got an $S_0 \rightarrow S_1$ transition at 646 nm and a second peak at 370 nm possessing a fluorescence maximum at 669 nm in the monomeric state (THF, 5 x 10^{-6} M). However, upon gradual addition of water to the monomeric THF solution, there occurred a red-shift of the absorption maximum which is more predominant for the 65% water content where the molecule forms J-type aggregates with absorption maximum in the NIR region at 737 nm (**Figure 1.18b**).

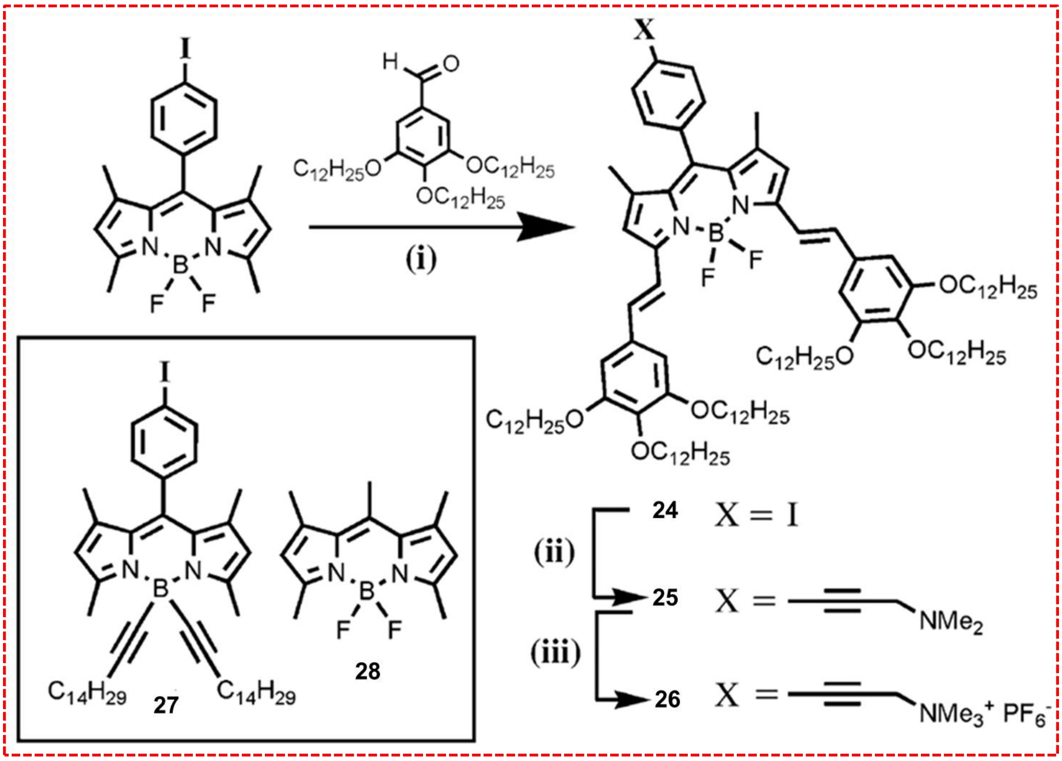

Figure 1.17. Synthetic outline for molecules **24, 25, 26** and structures of dyes **27** and **28**.

Transmission electron microscopy (TEM) and dynamic light scattering (DLS) analyses revealed that the aggregates are composed of spherical nanoparticles with a narrow size distribution of 1.4 to 1.6 nm. The nanoparticles possess an unusual stability of more than one month, as confirmed by the DLS data. The addition of the yellow dye **27** (20 mol%) into the aggregated nanoparticle **26** resulted in the intercalation of the dye into the nanoparticle system. The intercalated dye acts as an efficient donor for electronic energy transfer to the blue aggregate of molecule **26**. This in turn is confirmed from the excitation spectrum

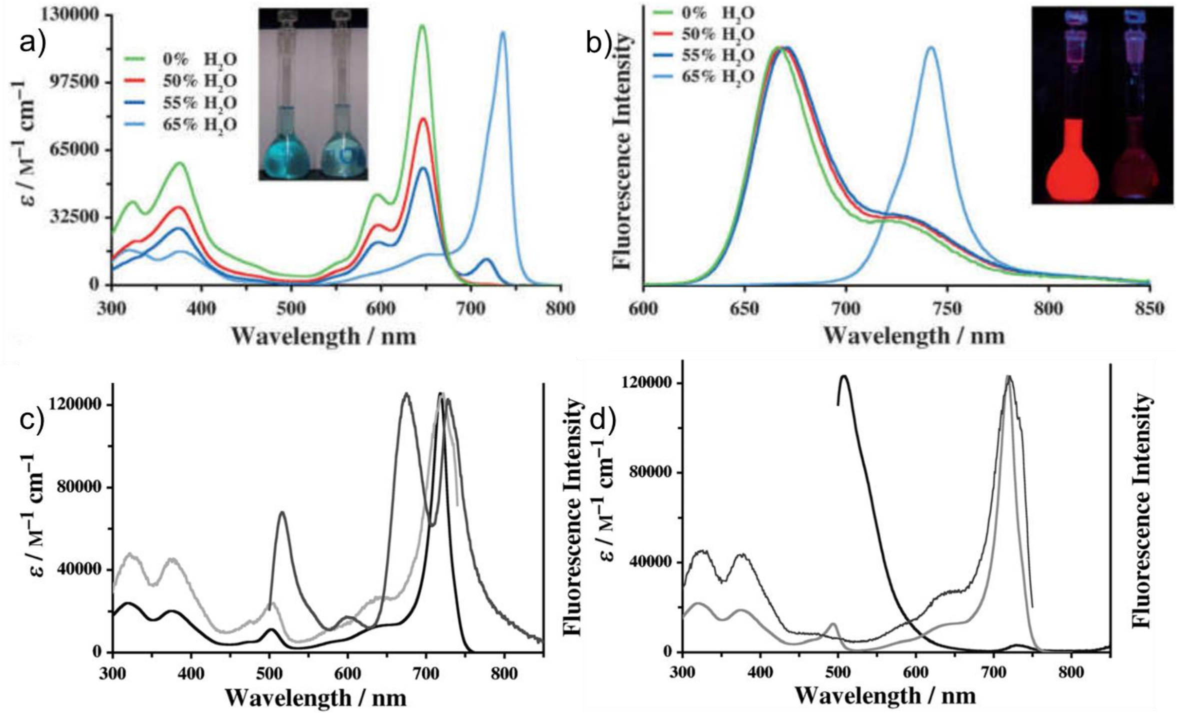

Figure 1.18. (a) Absorption spectra of **26** with respect to water addition and inset show the photographs of before and after addition of water (65%) under day light. (b) The corresponding fluorescence changes by the addition of water and the photograph showing before and after addition of water (65%) under UV light. c) Absorption spectrum of aggregated solution of **26** (5.5 x 10^{-6} M) in THF/water (65%) containing dye **27** (20%; —) and emission (λ_{ex} = 490 nm) spectrum (—). Excitation (λ_{em} = 760 nm) spectrum (—) d) Corresponding spectral changes after addition of dye **28**.

of the aggregates of **26** in presence of **27** and also from the fluorescent band intensities at 500 and 737 nm indicating nearly 100% energy transfer efficiency from guest molecule to the host (**Figure 1.18c**). Such a kind of energy transfer did not take place when dye **28** was added into the nanoparticle system which implies the clear role of the paraffinic chains in funneling energy to the acceptor part. In this particular case, upon dye addition, a strong emission at 520 nm and a weak one at 743 nm were observed confirming the absence of energy transfer (**Figure 1.18d**).

1.9. AIE in Bodipy Self-Assemblies

Fluorescent organic molecules exhibit emission quenching in the solution as well as in the solid state due to the inevitable phenomenon called aggregation caused quenching (ACQ). Tang *et al.* coined the term aggregation-induced emission (AIE), which is a phenomenon shown by certain chromophores such as tetraphenyl ethene (TPE), cyanostilbenes, hexaphenylsilol (HPS) *etc.*[21] which exhibit enhanced emission in the aggregated solution as well as in the solid states. AIE phenonmenon arises due to restricted intramolecular rotation caused by the geometric constraints (propeller shape) of chromophores which blocks the non-radiative pathway and opens up the radiative channel in them. Several Bodipy derivatives connected with TPE moieties have been reported and their structure-property relationship by considering the modulation of fluorescence, solvatochromism and AIE effects have been studied (**Figure 1.19**).[22] The molecule **29** exhibited a sharp locally excited (LE) state emission at 528 nm in toluene. A broad TICT (Twisted Intramolecular Charge Transfer) state emission at 643 nm appeared in chloroform (**Figure 1.20a)**. However, both the emission (red and green) got weakened with increasing the solvent polarity indicating the role of TICT state in the luminescent properties of **29**. Similarly, **30** also shows a locally excited (LE) emission peak at 533 nm in toluene. When the solvent was changed to 1,4-dioxane, a peak at 608 nm appears due to the TICT phenomenon and it shifts to 646 nm in chloroform followed by a large decrease in the LE peak intensity (**Figure 1.20b**). The luminescence behavior of the Bodipy derivative **31** is similar to that of **29** (**Figure 1.20c)**. Interesting photophysical properties were

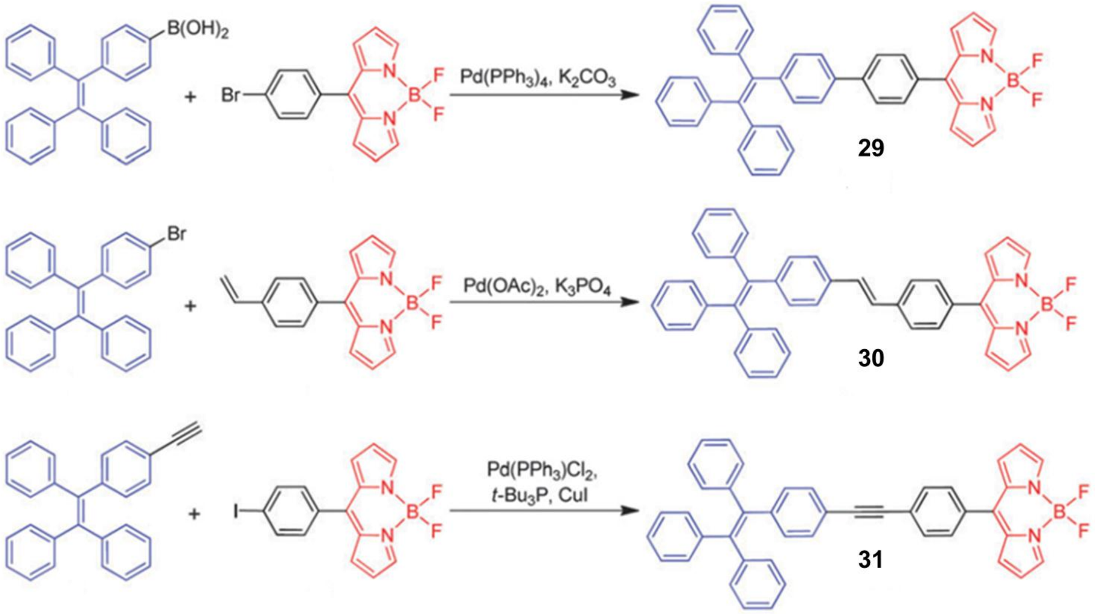

Figure 1.19. Schematic representation for the synthesis of **29, 30, 31**.

also observed when the aggregation studies were conducted in THF-water mixture. Aggregates of the molecule **29** are non-emissive although they show LE emission at 524 and TICT emission at 650 nm (**Figure 1.20a)**. On the other hand, the molecule **30** was found to be an AIE-active luminogen as indicated from its photophysical studies conducted in THF-water mixture. The molecule **30** showed a TICT emission at 640 nm in THF solution, and when water was added upto 75%, luminescent intensity increased by 3-fold. The maximum intensity was observed when the molecule forms aggregates in 90% water-10% THF mixture **(Figure 1.21b)**. A culmination of the above two properties exist in the case of **31** which has got an LE emission at 529 nm in THF solvent and when the water content is more than 65%, the LE emission intensity quenches and a peak due to the TICT phenomenon began to dominate at 600 nm (**Figure 1.21c**). This means that the TICT state of **31** is AIE-active and LE state is ACQ (Aggregation Caused Quenching)-active.

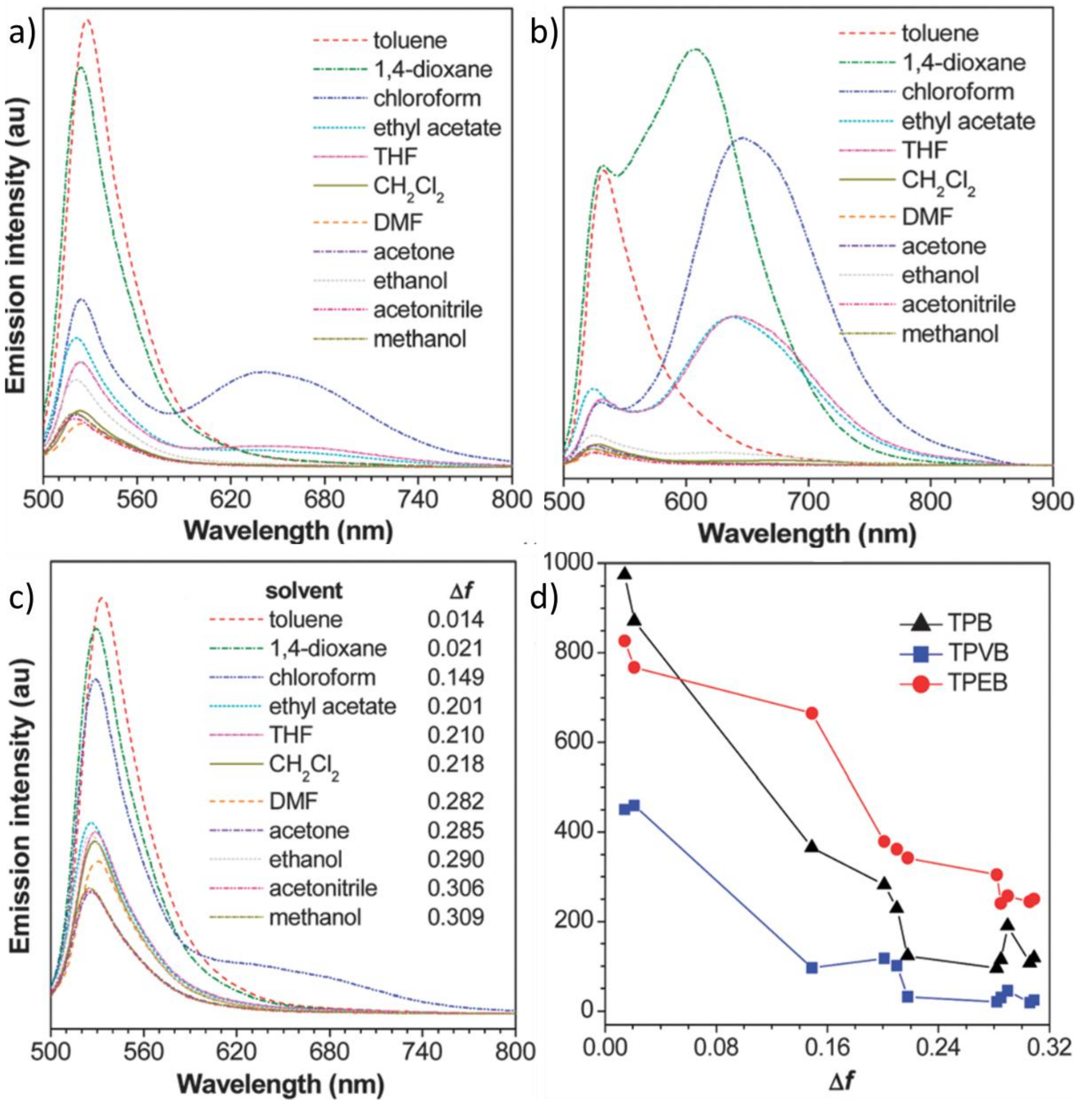

Figure 1.20. Photoluminiscence spectra of (a) **29**, (b) **30** and (c) **31** in solvents (10 μM) with different polarities. (d) Plots of LE emission intensity of **29**, **30** and **31** against solvent polarity parameter (Δf). Excitation wavelength (nm): absorption maximum (~500 nm).

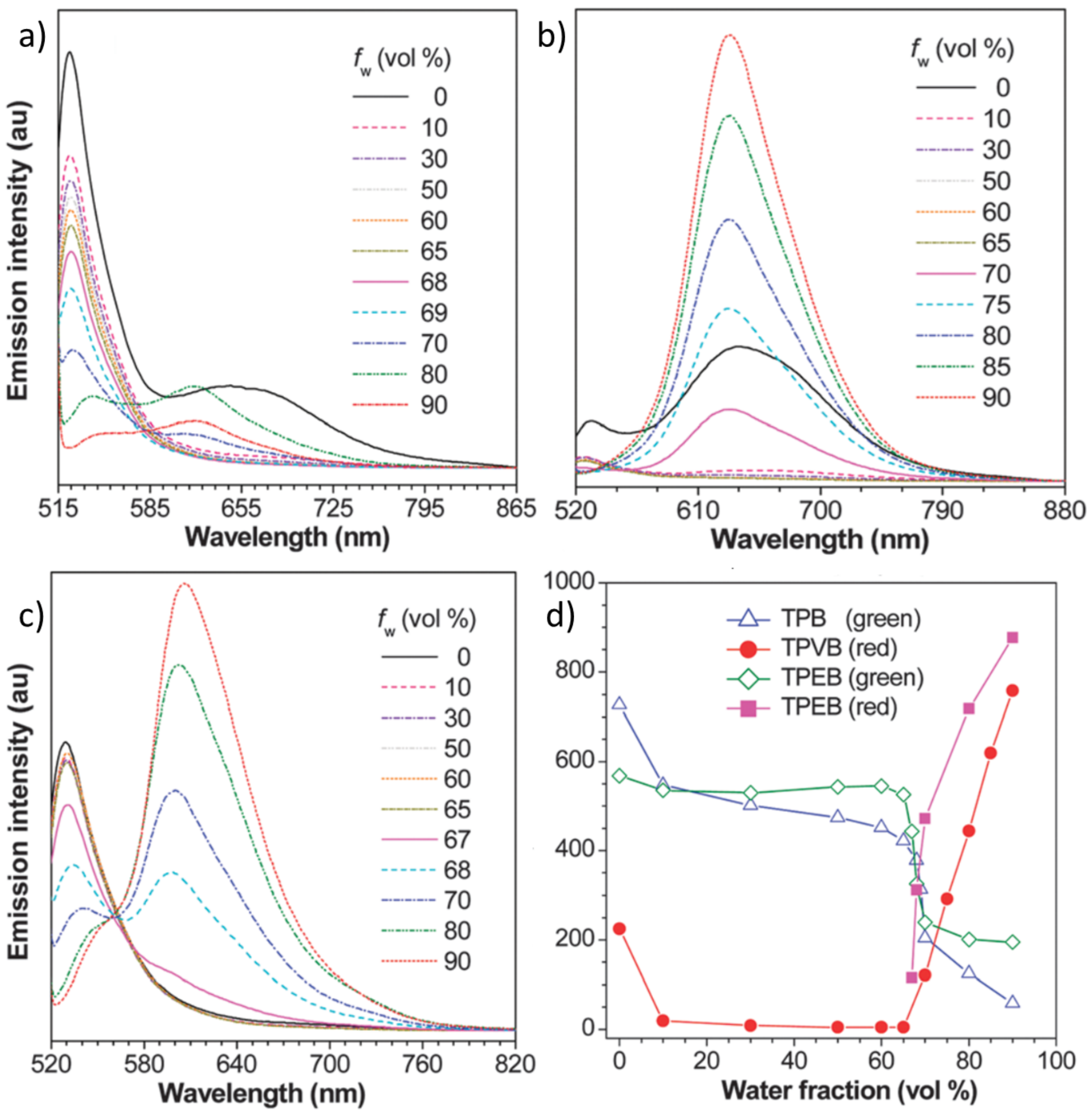

Figure 1.21. PL spectra of (a) **29**, (b) **30**, (c) **31** in THF-water mixtures (10 μM). (d) Emission intensity max. vs percentage water content. Excitation wavelength (nm): 501 (**29**), 502 (**30**), 504 (**31**).

1.10. Self-Assembly of π-Extended Bodipy Dyes

Recently, a few reports have appeared describing the modification of Bodipy core with π-extended moieties. For example, Gustavo *et al.* have reported the synthesis and properties of an oligo(*p*-phenyleneethynylene) (OPE) linked Bodipy system.[23] The symmetrical molecule **34** (**Figure 1.22**) was synthesized by the Sonogashira reaction between 2,6-diiodo-Bodipy (**32**) and ethynylphenyl based derivative **33**.

The photophysical studies of the molecule **34** revealed greater π-π interaction in the OPE part by observing a broadening at 340 nm in cyclohexane solvent which corresponds to π-π* transition of the OPE part (1 x 10^{-2} M).

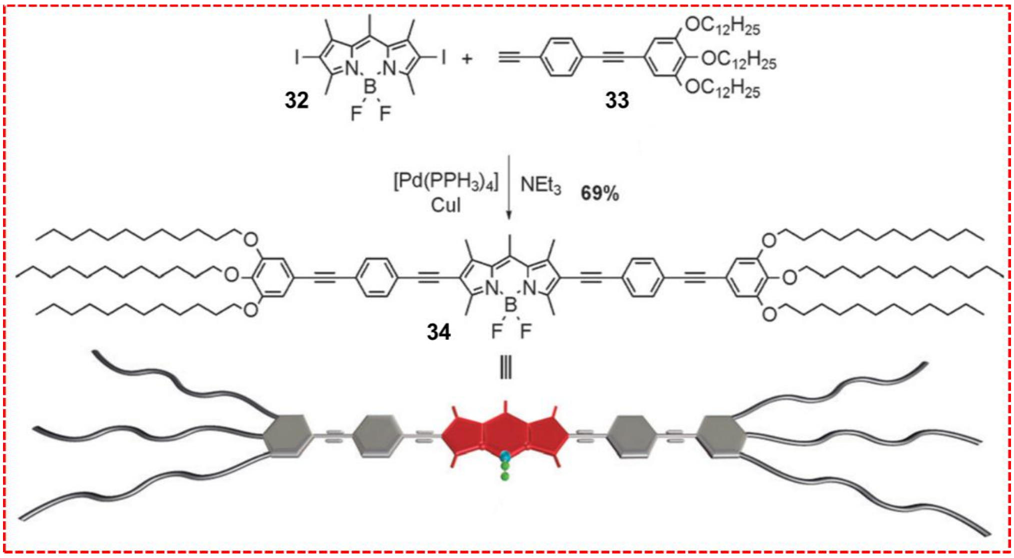

Figure 1.22. Synthesis, chemical structure and the cartoon representation of the molecule **34**.

The $S_0 \rightarrow S_1$ transition of the Bodipy part which appeared as an intense band at 577 nm in the absorption spectrum (cyclohexane, 1 x 10^{-2} M) followed by a blue-shifted weak shoulder band at 554 nm suggest a weak excitonic coupling between Bodipy chromophores. The small band at 400 nm is attributed to the $S_0 \rightarrow S_2$ transition of the Bodipy chromophore. The progressive broadening of the transitions at λ = 340 and 577 nm with respect to the increase in concentration from 5 x 10^{-4} M to 1 x 10^{-2} M for molecule **34** is an indication of the aggregate formation which is supported by the reduced emission intensity in nonpolar cyclohexane (1 x 10^{-2} M). The absence of any precise blue-shifted or red-shifted transitions rules out the possible H or J-type excitonic coupling in the supramolecular assemblies.

Gustavo *et al.* investigated the aqueous self-assembly behavior of the bolaamphiphile OPE-Bodipy derivative **35** (**Figure 1.23**) into flexible fibre-like H-aggregates. Subsequently, their reversible transformation upon guest encapsulation (tetracene and anthracene) into rigid fibres and spherical nanoparticles where the encapsulation mechanism changes from isodesmic to cooperative depending on the type of guest molecule were studied.[24]

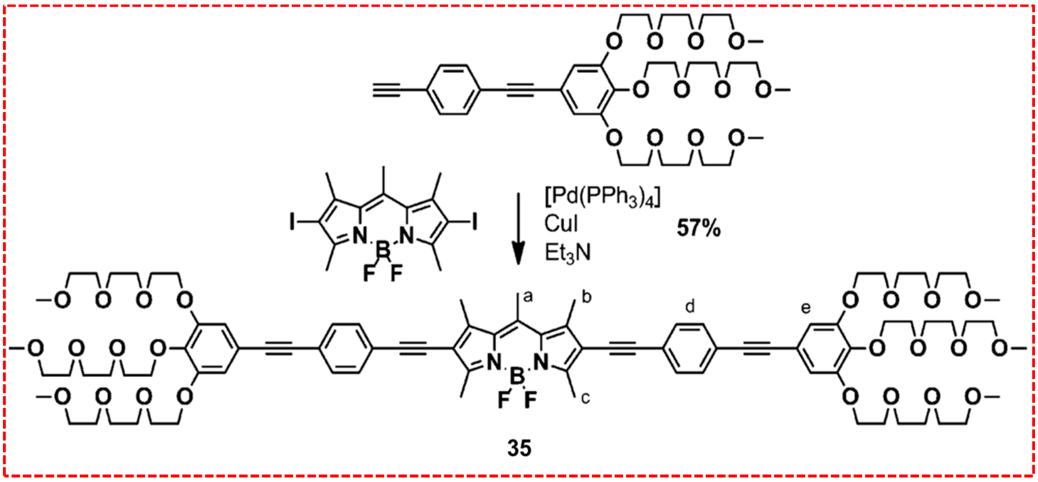

Figure 1.23. Synthesis scheme of molecule **35**.

The hypsochromic shift observed in the absorption maximum with a shoulder band at 590 nm in water is an indication of H-type stacking with a slight twist in the conformation of the dye molecules within the stack. The sharper bands corresponding to the OPE absorption in water and acetonitrile are attributed to the planarization of the alkyne-aryl groups. In acetonitrile and water, the emission spectra of **35** are red-shifted and quenched when compared with that of DCM/MeOH, which is attributed to the H-type excitonic coupling between Bodipy chromophores.

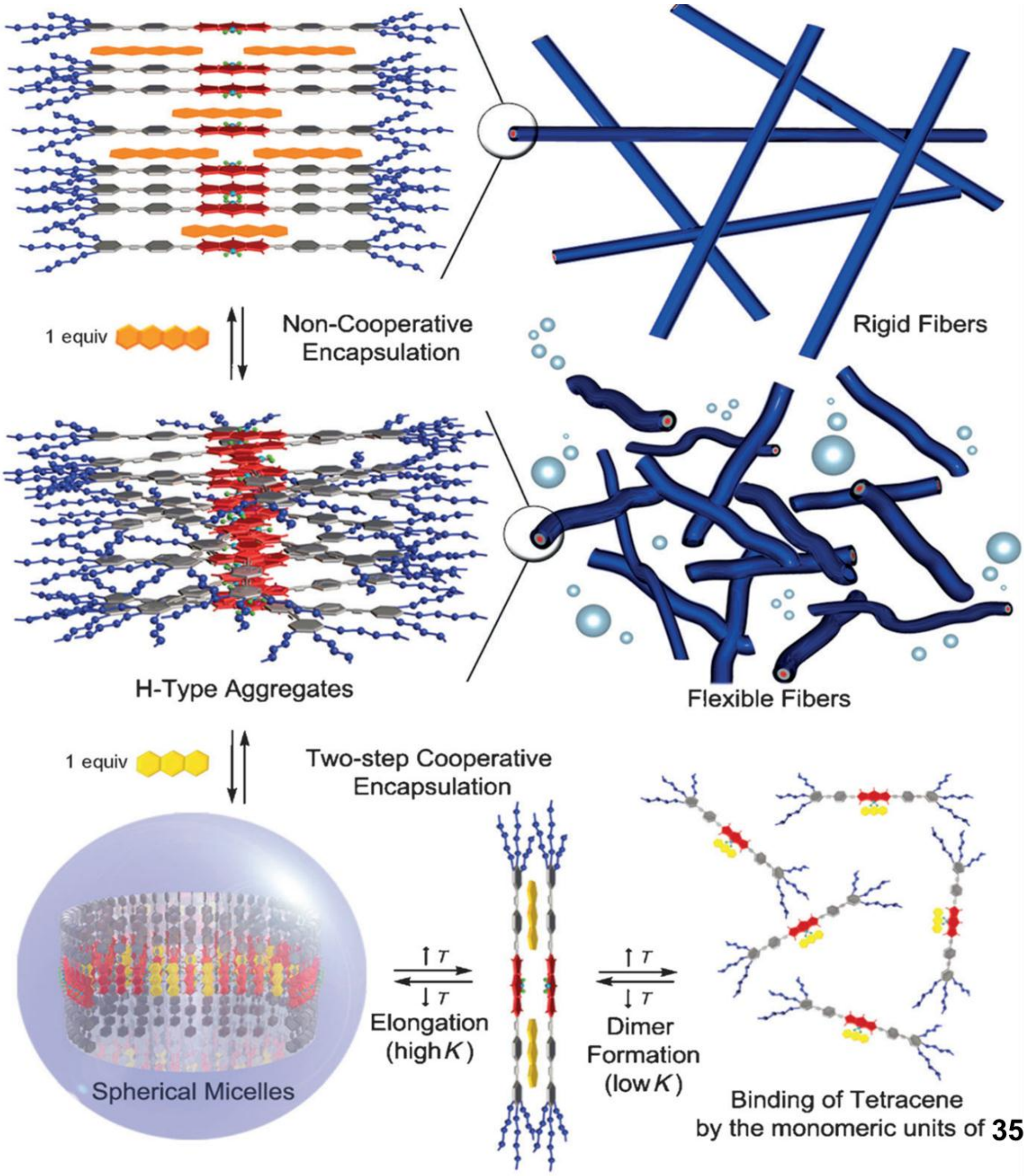

Figure 1.24. Schematic representation of the self-assembly of **35** into H-type aggregates and its reversible guest-dependent encapsulation processes.

When one or two equivalents of tetracene are added to the aggregated solution of **35** in 3 × 10^{-5} M water, the immediate encapsulation of the dye takes places because of the effective uptake of the guest molecule by the fibrilar assemblies. The photophysical studies indicated that tetracene forms a coassembly with the molecule **35** in THF-water mixtures and the former was in the aggregated state upon encapsulation. The mechanistic studies confirmed the assembly process between the molecule **35** and the guest tetracene as a reversible isodesmic co-assembly process. The tetracene interaction leads to more rigid fibres when compared to that of the flexible fibres produced by the pristine **35**. On the other hand, the encapsulation of anthracene, does take the cooperative pathway of self-assembly process, significantly different from the sigmoidal pathway observed for the tetracene case in the aggregated solution of THF-water mixture (**Figure 1.24**). A high degree of cooperativity was seen in the co-assembly of anthracene with molecule **35** when the cooling curve for the aggregated co-assembled solution was fitted with the nucleation-elongation model developed by ten Eikelder, Markvoort and Meijer.

1.11. Coordination-Driven Bodipy Self-Assembly

Coordination-driven self-assembly deals with the spontaneous formation of metal-ligand bonds in solution, thereby forming 2D metallacycles and 3D metallacages with tunable cavities and fluorescence properties, widely used for biomedical and biochemical applications.[25]

The coordination-driven self-assembly preserves the photophysical properties of the parent Bodipy unit in a design of rhomboid cavitand shown by Pistolis *et al.*[26] In their design, they replaced the tetrahedral fluorine atoms present in the Bodipy with ethynyl pyridine donor linker so that the fluorophore subunit is vertically aligned to the plane formed by the ethynyl pyridine donor units. The above tecton when connect with a 90° organoplatinum acceptor unit resulted in the formation of brightly fluorescent rhomboid cavitand in solution.

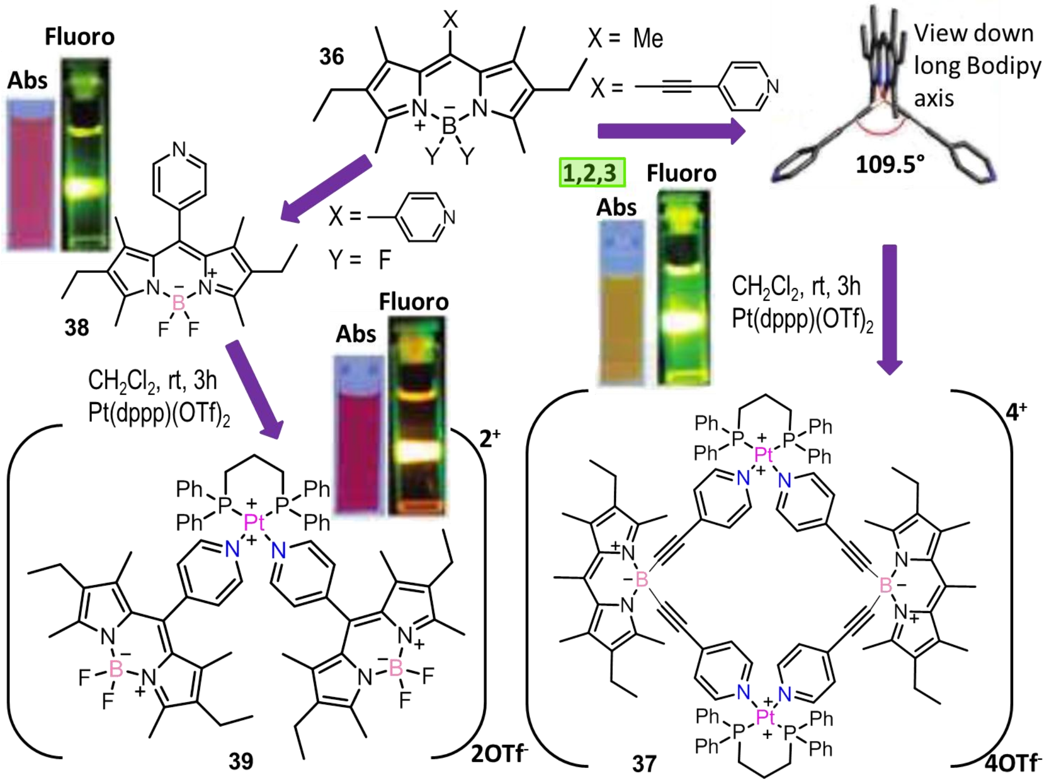

Figure 1.25. Schematic illustration of supramolecular synthesis via coordination-driven self-assembly of properly designed Bodipy donors and platinum triflate acceptor in specific stoichiometric ratios.

The replacement of the fluorine atoms of **36** with ethynyl pyridine and the subsequent coordination with platinum acceptor units to form rhomboid cavitant **37** doesn't make any perturbation for the photophysical properties of the Bodipy chromophores. The high fluorescence quantum yield ($\Phi_f = 0.86$), lifetime ($\tau = 6.9$ ns) and the high anisotropy (r = 0.37) still maintained in molecule **37**. On the other hand, when the pyridine is attached to the *meso* position of the Bodipy where it is further connected to the acceptor platinum unit to form **39,** does not preserve the photophysical properties of the parent Bodipy molecule **36**. Quantum yield of the molecule **38** ($\Phi_f = 0.47$) is higher than that of quantum yield of the metal complex **39** ($\Phi_f = 0.06$, **Figure 1.25)**.

1.12. Crystallisation-Driven Bodipy Self-Assembly

Crystallisation-driven self-assembly (CDSA) has emerged as a new technique for making complex 2D nano-architectures from block copolymers.[27-32] Manners *et al.* adopted CDSA method using polyferrocenyldimethylsilane (PFS) as a core to

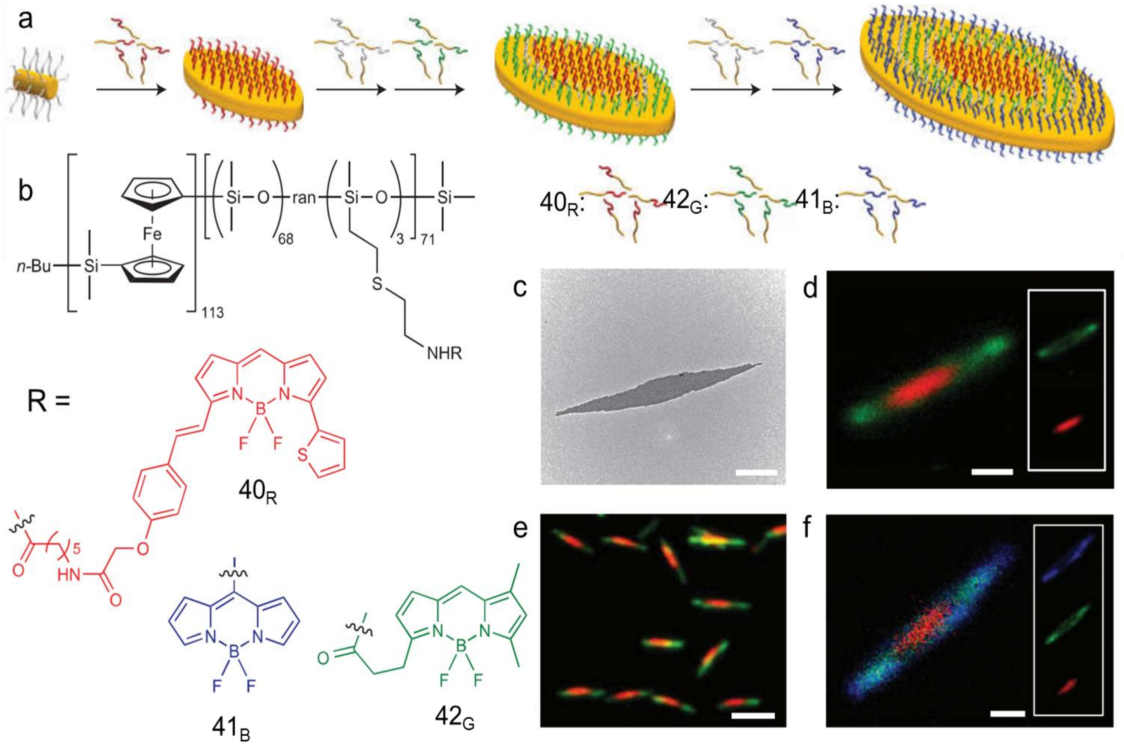

Figure 1.26. Growth of concentric lenticular block co-micelles in 2D. (**a**) Schematic diagram showing the formation of concentric lenticular block co-micelles in 2D from a cylindrical crystallite seed. (**b**) Chemical structures of functional polymers **40_R, 42_G and 41_B**. (**c**) TEM micrograph of a lenticular platelet micelle formed from the sequential addition of **40_R**, **1** and **42_G** to a pre-sonicated crystallite seeds in ethyl-acetate (A_n = 6, 25, 900 nm^2, A_w = 6, 32, 800 nm^2, A_n/A_w = 1.01, σ/A_n = 0.10). (**d,e**) LSCM images of these block co-micelles showing their concentric structure. **d)**, Inset: Green and red channels illuminated individually. (**f**) Pentablock concentric micelle formed from the sequential addition of **1** and **41_B** to the micelle solution in **d** (A_n = 718,000 nm^2, A_w = 740, 000 nm^2, A_n /A_w = 1.03, σ /A_n = 0.17), inset: Blue, green and red channels illuminated individually. Scale bars, 500 nm (**c, d, f**) and 2,000 nm (**e**).

make uniform platelet nanostructures from different kinds of block copolymers (**Figure 1.26b**).[33] The living nature of the self-assembly process has open the door for making 2D block co-micelles with nanoseggregated defined regions of luminescent properties. Initially, authors have synthesized a polymer (PFS_{113}- b-($PDMS_{68}$ -*r* -$PMVS_3$) (where PDMS = poly(dimethylsiloxane) and PMVS = poly(methylvinylsiloxane)) with PDMS corona containing low concentration of vinyl groups which on photoinitiated hydrothiolation in presence of cystamine hydrochloride resulted in the formation of a block copolymer (BCP) with 5% amino group available in the corona (**Figure 1.26**). These amino groups were then functionalized with varieties of Bodipy derivatives which lead to the formation of platelet forming BCPs as fluorescent red (**40_R**), green (**42_G**) and blue (**41_B**).

CDSA method is also used for the preparation of nanoscale cylinders with tunable length and emission colors.[34] Block copolymer of the form PFS_{62}-b-($PDMS_{605}$-*r*- $PMVS_{21}$) was prepared initially where the PFS is the crystallizable block, vinyl group acts as the reactive site for the introduction of more functionality. Finally, fluorescent block copolymers (**43-45**) of red, green and blue were prepared by functionalization with Bodipy dyes. When the solutions of these block copolymers in THF are added into ethyl acetate, they readily self-assemble to form color tunable fluorescent micelles. The length of the cylinders is controlled by adding pre-formed crystallite seed as initiators to serve as a nucleation site for self-assembly. In short, the combined use of CDSA method and fluorescent BCPs gives an opportunity to create nanoscale pixels of fully tunable emission colors.

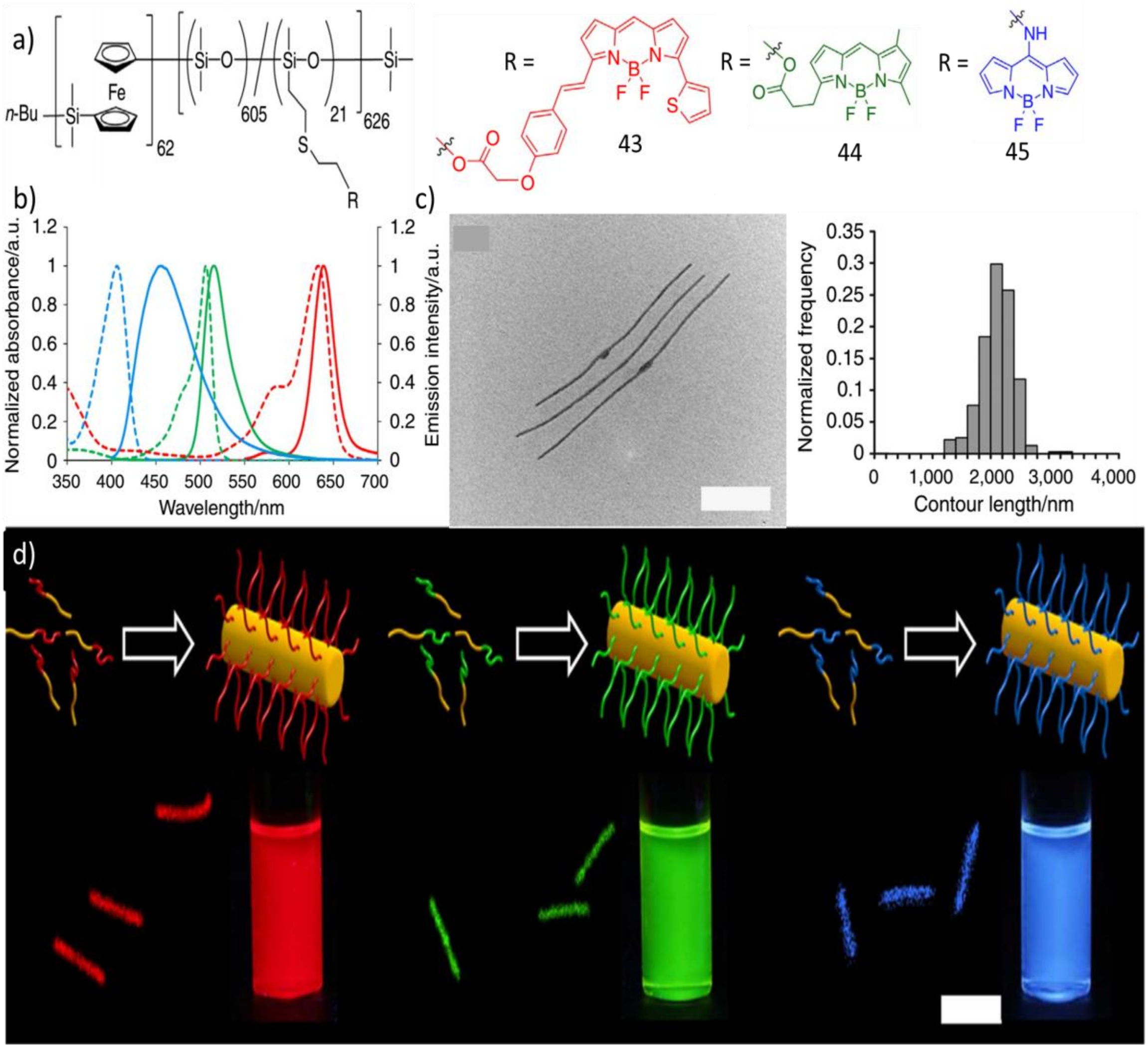

Figure 1.27. a) Structures of fluorescent BCPs **43-45**. b) Normalized absorption (dashed) and emission (solid) spectra of unimers of **43-45** (c = 1 x 10^{-5} M in THF). c) TEM image and corresponding contour length distribution of cylindrical micelles made from **43-45**. Scale bar, 500 nm. d) Graphical representation of self-assembly of **43-45** forming micelles with corresponding confocal fluorescence images and photographs of micellar solutions under UV light (λ_{ex} = 365 nm). Scale bar, 3 μm.

1.13. The Scope and Objective of the Thesis

From the above literature reports it is understood that Bodipy dyes can be synthesized easily, their photophysical properties can be tuned by proper substitution and their self-assembly lead to interesting material properties. Since Bodipy has an intrinsic capability to form aggregates because of the rigid aromatic backbone, a subtle structural modification inevitably brings interesting multi-luminescence properties which can be tuned from UV-Vis to NIR region. Moreover, the self-assembly of Bodipy dyes in the solution state has brought the attention to the scientific community about its potential use as energy transfer cassettes, liquid crystalline materials, and for bio-imaging and labeling studies. The condensed state properties of this particular class of dyes are not much reported. However, most of the practical application can be achieved by utilizing the condensed state properties. Therefore, it is of paramount importance to have deeper understanding of the solid state properties of Bodipy derivatives for their use in various applications.

Bodipy dyes most of the time hardly fluoresce in the solid state. Two obvious reasons are their very small Stokes shift (5-20 nm) which facilitates the energy transfer thereby potentially trapping the excitation energy by aggregates and the strong π-π stacking favored by the planarity leading to the loss of emission efficiency.[12b] As a result, the film state properties of the Bodipy based assemblies are yet to be known deeply. By utilizing the self-assembly design principles, it is possible to control the chromophore-chromophore distances to an optimum level so that the luminescence quenching can be suppressed while maintaining the intermolecular interaction.

In order to facilitate the self-assembly and impart specific material properties to Bodipy, it has to be connected with appropriate π-conjugated systems. Linear π-conjugated systems are the most extensively studied class of compounds for integrating with functional dyes.[1e,35] Earlier we have reported the self-assembly of linear π-conjugated systems such as OPVs, OTVs and OPEs.[1e,36] Phenyleneethynylene conjugated backbone adopts both planar and twisted forms, which can often lead to interesting stimuli responsive luminescent properties. Additionally, it is possible to alter the molecular packing in amide hydrogen bonded supramolecular systems using various external stimuli.[37-41] It is also known that based on the substitution or the extent of aggregation of Bodipy, its luminescence properties can be varied from vis to NIR region.[42-47] Based on the above arguments, we have set our objectives to investigate in details the self-assembly and the optical properties of *meso* phenyleneethynylene derived amide hydrogen bonded Bodipy derivatives in solution as well as in the solid states. Gelation is another property which we wanted to investigate. As far as the literature reports are concerned, there are a few reports available for Bodipy based gels. To meet this objective we planned to design Bodipy based gelators by appropriate functionalization. Detailed study on the morphology and optical properties of these gelators were planned. The influence of hydrogen bonding units and the alkyl chain effect on the self-assembly properties of Bodipy chromophore were investigated. Detailed investigations were planned to have insight in the morphological features of the self-assembly, deeper understanding on the NIR emission, photonic behavior and the waveguiding properties of the synthesized Bodipy dyes and their self-assembly.

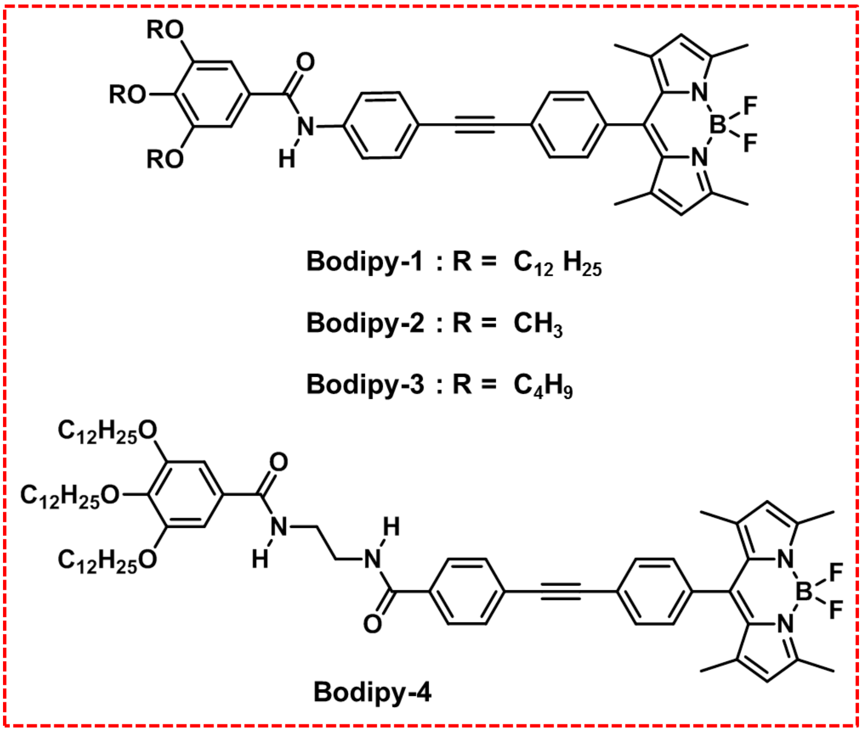

Scheme 1.1. Proposed molecular structures.

In summary, the present thesis describes the results of detailed study of the above objectives by investigating the self-assembly and photophysical properties of a few Bodipy dyes, the structures of which are shown in **Scheme 1.1**. These studies may help researchers to design more of bodipy derivatives with intriguing optical and morphological properties.

1.14. References

1. a) J.-M. Lehn, *Supramolecular Chemistry*; VCH: Winheim, Germany, **1995**; b) H.- J. Schneider, A. Yatsimirsky, *Principles and Methods in Supramolecular Chemistry*; Wiley: Chichester, **2000**; c) J. W. Steed, J. L. Atwood, *Supramolecular Chemistry*; Wiley: Chichester, **2000**; d) M. George, R. G. Weiss, *Acc. Chem. Res.* **2006**, *39*, 489-497; e) S. S. Babu, V. K. Praveen, A. Ajayaghosh, *Chem. Rev.* **2014**, *114*, 1973-2129; f) S. Ghosh,

V. K Praveen, A. Ajayaghosh, *Annu. Rev. Mater. Res.* **2016**, *46*, 235-262; g) E. Krieg, M. M. C. Bastings, P. Besenius, B. Rybtchinski, *Chem. Rev.* **2016**, *116*, 2414-2477; h) L. Albertazzi, D. van der Zwaag, C. M. A. Leenders, R. Fitzner, R. W. van der Hofstad, E. W. Meijer, *Science* **2014**, *344*, 491-495.

2. a) F. J. M. Hoeben, P. Jonkheijm, E. W. Meijer, A. P. H. J. Schenning, *Chem. Rev.* **2005**, *105*, 1491-1546; b) C. A. Hunter, J. K. M. Sanders, *J. Am. Chem. Soc.* **1990**, *112*, 5525-5534; c) C. A. Hunter, J. Perkins, C. J. Urch, *J. Chem. Soc., Perkin Trans. 2* **2001**, 651-669; d) J. Cao, C. H. Lu, J. Zhuang, M. X. Liu, X. X. Zhang, Y. M. Yu, Q. C. Tao, *Angew. Chem. Int. Ed.* **2017**, *56*, 8795-8800; e) K. Sato, W. Ji, L. C. Palmer, B. Weber, M. Barz, S. I. Stupp, *J. Am. Chem. Soc.* **2017**, *139*, 8995-9000; f) S. Vela, J. A. Berrocal, C. Atienza, E. W. Meijer, N. Martin, *Chem. Commun.* **2017**, *53*, 4084-4087.
3. a) P. Anees, S. Sreejith, A. Ajayaghosh, *J. Am. Chem. Soc.* **2014**, *136*, 13233-13239; b) H. Kobayashi, M. Ogawa, R. Alford, P. L. Choyke, Y. Urano, *Chem. Rev.* **2010**, *110*, 2620-2640; c) S. Pramanik, V. Bhalla, M. Kumar, *New J. Chem.* **2017**, *41*, 4806-4813; d) H. Shigemitsu, I. Hamachi, *Acc. Chem. Res.* **2017**, *50*, 740-750; e) Z. Z. Zhang, L. Wang, G. P. Li, B. X. Ye, *Analyst* **2017**, *142*, 1821-1826; f) Q. Lin, T. T. Lu, X. Zhu, T. B. Wei, H. Li, Y. M. Zhang, *Chem. Sci.* **2016**, *7*, 5341-5346; g) K. K. Kartha, S. S. Babu, S. Srinivasan, A. Ajayaghosh, *J. Am. Chem. Soc.* **2012**, *134*, 4834-4841; h) T. Naddo, Y. Che, W. Zhang, K. Balakrishnan, X. Yang, M.

Yen, J. Zhao, J. S. Moore, L. Zhang, *J. Am. Chem. Soc.* **2007**, *129,* 6978-6979; i) J. H. Zhang, Y. M. Huang, D. S. Wang, A. C. Pollard, Z. Chen, E. Egap, *J. Mater. Chem.* C **2017**, *5*, 5685-5692; j) E. Kim, Y. Lee, S. Lee, S. B. Park, *Acc. Chem. Res.* **2015**, *48*, 538-547; k) S. Shanmugaraju, P. S. Mukherjee, *Chem. Eur. J.* **2015**, *21*, 6656-6666.

4. a) G. Ulrich, R. Ziessel, A. Harriman, *Angew. Chem. Int. Ed.* **2008**, *47*, 1184-1201; b) N. Zhao, S. T. Xuan, F. R. Fronczek, K. M. Smith, M. G. H. Vicente, *J. Org. Chem.* **2017**, *82*, 3880-3885; c) S. T. Xuan, N. Zhao, X. Y. Ke, Z. H. Zhou, F. R. Fronczek, K. M. Kadish, K. M. Smith, M. G. H. Vicente, *J. Org. Chem.* **2017**, *82*, 2545-2557; d) P. Stachelek, A. Harriman, J *Phys. Chem. A* **2016**, *120*, 8104-8113; e) X. F. Zhang, Y. Xiao, J. Qi, J. L. Qu, B. Kim, X. L. Yue, K. D. Belfield, *J. Org. Chem.* **2013**, *78,* 9153-9160.
5. a) A. Treibs, F.-H. Kreuzer, *Justus Liebigs Ann. Chem.* **1968**, *718*, 208-223; b) H. Falk, O. Hofer, H. Lehner, *Monatsh. Chem.* **1974**, *105*, 169-178; c) E. VosdeWael, J. A. Pardoen, J. A. Vankoeveringe, J. Lugtenburg, *Recl. Trav. Chim. Pays-Bas* **1977**, *96*, 306-309; d) H. J. Wories, J. H. Koek, G. Lodder, J. Lugtenburg, R. Fokkens, O. Driessen, G. R. Mohn, *Recl. Trav. Chim. Pays-Bas* **1985**, *104*, 288-291.
6. Source: CAS SciFinder.
7. W. Qin, M. Baruah, M. Van der Auweraer, F. C. De Schryver, N. Boens *J. Phys. Chem. A* **2005**, *109*, 7371-7384.
8. a) M. Shah, K. Thangraj, M. L. Soong, L. Wolford, J. H. Boyer, I. R. Politzer, T. G. Pavlopoulos, *Heteroat. Chem.* **1990**, *1*, 389-399; b) A.

Burghart, H. Kim, M. B. Welch, L. H. Thorensen, J. Reibenspies, K. Burgess, *J. Org. Chem.* **1999**, *64*, 7813– 7819.

9. a) A. Costela, I. G.-Moreno, C. Gomez, R. Sastre, F. A.-Guerri, M. Liras, F. L. Arbeloa, J. B. Prieto, I. L. Arbeloa, *J. Phys. Chem. A* **2002**, *106*, 7736-7742; b) M. Kollmannsberger, K. Rurack, U. R.-Genger, J. Daub, *J. Phys. Chem. A* **1998**, *102*, 10211-10220; c) J. B. Prieto, F. L. Arbeloa, V. M. Martínez, T. A. Lopez, F. A.-Guerri, M. Liras, I. L. Arbeloa, *Chem. Phys. Lett.* **2004**, *385*, 29-35.

10. A. Loudet, K. Burgess, *Chem. Rev.* **2007**, *107*, 4891-4932.

11. a) J. B. Birks, *Photophysics of aromatic molecules*, Wiley: London, **1970**; b) H. Auweter, H. Haberkorn, W. Heckmann, D. Horn, E. Luddeecke, J. Rieger, H. Weiss, *Angew. Chem. Int. Ed.* **1999**, *38*, 2188-2191.

12. a) E. G. McRae, M. Kasha, *Physical process in Radiation Biology*, Academy Press: Newyork, **1964**; b) T. Ozdemir, S. Atilgan, I. Kutuk, L. T. Yildirim, A. Tulek, M. Bayindir, E. U. Akkaya, *Org. Lett.* **2009**, *11*, 2105-2107; c) M. Kasha, H. R. Rawls, M. A. El-Bayoumi, *Pure Appl. Chem.* **1965**, *11*, 371-392.

13. a) V. M. Martínez, F. L. Arbeloa, J. B. Prieto, T. A. López, I. L. Arbeloa, *J. Phys. Chem. B* **2004**, *108*, 20030-20037; b) T. T. Vu, M. Dvorko, E. Y. Schmidt, J.-F. Audibert, P. Retailleau, B. A. Trofimov, R. B. Pansu, G. Clavier, R. M.-Renault, *J. Phys. Chem. C* **2013**, *117*, 5373-5385.

14. a) F. Würthner, T. E. Kaiser, C. R. S.-Möller, *Angew. Chem. Int. Ed.* **2011**, *50*, 3376-3410; b) P. Verma, H. Pal, *J. Phys. Chem. A* **2012**, *116*, 4473-4484; c) J. Bujdak, N. Iyi, R. Sasai, *J. Phys. Chem.* B **2004**, *108*, 4470-4477; d) D. Tleugabulova, Z. Zhang, J. D. Brennan, *J. Phy. Chem. B* **2002**, *106*, 13133-13138.

15. J.-H. Olivier, J. Barbera, E. Bahaidarah, A. Harriman, R. Ziessel, *J. Am. Chem. Soc.* **2012**, *134*, 6100–6103.

16. J.-H. Olivier, F. Camerel, G. Ulrich, J. Barbera, R. Ziessel, *Chem. Eur. J.* **2010,** *16*, 7134-7142.

17. F. Camerel, L. Bonardi, M. Schmutz, R. Ziessel, *J. Am. Chem. Soc.* **2006**, *128*, 4548-4549.

18. A. Nagai, J. Miyake, K. Kokado, Y. Nagata, Y. Chujo, *J. Am. Chem. Soc.* **2008**, *130*, 15276-15278.

19. N. Sun, X. Xiao, W. Li, J. Jiang, *Adv. Sci.* **2015**, *2*, 1500082.

20. J.-H. Olivier, J. Widmaier, R. Ziessel, *Chem. Eur. J.* **2011**, *17*, 11709-11714.

21. a) Y. Hong, J. W. Y. Lam, B. Z. Tang, *Chem. Soc. Rev.* **2011**, *40*, 5361-5388; b) Y. Hong, J. W. Y. Lam, B. Z. Tang, Chem. Commun. 2009, 4332-4353; c) R. Hu, E. Lager, A. A.-Aguilar, J. Liu, J. W. Y. Lam, H. H. Y. Sung, I. D. Williams, Y. Zhong, K. S. Wong, E. P.-Cabrera, B. Z. Tang, J. *Phys. Chem. C* **2009**, *113*, 15845-15853; d) F. Ito, J.-I. Fujimori, N. Oka,

M. Sliwa, C. Ruckebusch, S. Ito, H. Miyasaka, *Faraday Discuss.* **2017**, *196*, 231-243.

22. R. Hu, C. F. A. G.-Duran, J. W. Y. Lam, J. L. B.-Vázquez, C. Deng, S. Chen, R. Ye, E. P.-Cabrera, Y. Zhong, K. S. Wong, B. Z. Tang, *Chem. Commun.* **2012**, *48*, 10099-10101.

23. A. Florian, M. J. Mayoral, V. Stepanenko, G. Fernandez, *Chem. Eur. J.* **2012**, *18*, 14957-14961.

24. N. K. Allampally, A. Florian, M. J. Mayoral, C. Rest, V. Stepanenko, G. Fernández, *Chem. Eur. J.* **2014**, *20*, 10669-10678.

25. a) T. R. Cook, V. Vajpayee, M. H. Lee, P. J. Stang, K. W. Chi, *Acc. Chem. Res.* **2013**, *46*, 2464-2474; b) V. S. P. K. Neti, M. L. Saha, X. Z. Yan, Z. X. Zhou, P. J. Stang, *Organometallics* **2015**, *34*, 4813-4815; c) B. H. Northrop, Y. R. Zheng, K. W. Chi, P. J. Stang, *Acc. Chem. Res.* **2009**, *42*, 1554-1563; d) S. Shanmugaraju, V. Vajpayee, S. Lee, K. W. Chi, P. J. Stang, P. S. Mukherjee, *Inorg. Chem.* **2012**, *51*, 4817-4823; e) K. Campbell, C. J. Kuehl, M. J. Ferguson, P. J. Stang, R. R. Tykwinski, *J. Am. Chem. Soc.* **2002**, *124*, 7266-7267.

26. A. K.-Chantzea, N. Karakostas, C. P. Raptopoulou, V. Psycharis, E. Saridakis, J. Griebel, R. Hermann, G. Pistolis, *J. Am. Chem. Soc.* **2010**, *132*, 16327-16329.

27. X. Wang, G. Guerin, H. Wang, Y. Wang, I. Manners, M. A. Winnik, *Science* **2007**, *317*, 644-647.

28. J. B. Gilroy, T. Gädt, G. R. Whittell, L. Chabanne, J. M. Mitchels, R. M. Richardson, M. A. Winnik, I. Manners, *Nat. Chem.* **2010**, *2*, 566-570.

29. N. Petzetakis, A. P. Dove, R. K. O'Reilly, *Chem. Sci.* **2011**, *2*, 955-960.

30. S. K. Patra, R. Ahmed, G. R. Whittell, D. J. Lunn, E. L. Dunphy, M. A. Winnik, I. Manners, *J. Am. Chem. Soc.* **2011**, *133*, 8842-8845.

31. J. Schmelz, A. E. Schedl, C. Steinlein, I. Manners, H. Schmalz, *J. Am. Chem. Soc.* **2012**, *134*, 14217-14225.

32. T. Gädt, N. S. Ieong, G. Cambridge, M. A. Winnik, I. Manners, *Nat. Mater.* **2009**, *8*, 144-150.

33. Z. M. Hudson, C. E. Boott, M. E. Robinson, P. A. Rupar, M. A. Winnik, I. Manners, *Nat. Chem.* **2014**, *6*, 893-898.

34. Z. M. Hudson, D. J. Lunn, M. A. Winnik, I. Manners, *Nat. Commun.* **2014**, *5*, 3372.

35. a) L. Maggini, D. Bonifazi, *Chem. Soc. Rev.* **2012**, *41*, 211-241; c) A. P. H. J. Schenning, E. W. Meijer, *Chem. Commun.* **2005**, 3245-3258; d) P. F. H. Schwab, J. R. Smith, J. Michl, *Chem. Rev.* **2005**, *105*, 1197-1280.

36. a) A. Ajayaghosh, R. Varghese, V. K. Praveen, S. Mahesh, *Angew. Chem. Int. Ed.* **2006**, *45*, 3261-3264; b) A. Ajayaghosh, R. Varghese, S. Mahesh,

V. K. Praveen, *Angew. Chem. Int. Ed.* **2006**, *45*, 7729-7732; c) S. S. Babu, S. Prasanthkumar, A. Ajayaghosh, *Angew. Chem. Int. Ed.* **2012**, *5*, 1766-1776.

37. Y. Sagara, T. Kato, *Angew. Chem. Int. Ed.* **2011**, *50*, 1-6.

38. Y. Sagara, Y, T. Mutai, I. Yoshikawa, K. Araki, *J. Am. Chem. Soc.* **2007**, *129*, 1520-1521.

39. M. Sase, S. Yamaguchi, Y. Sagara, I. Yoshikawa, T. Muthai, K. Araki, *J. Mater. Chem.* **2011**, *21*, 8347-8354.

40. Y. Sagara, T. Kato, *Angew. Chem. Int. Ed.* **2011**, *47*, 5175-5178.

41. Y. Sagara, S. Yamane, T. Mutai, K. Araki, T. Kato, *Adv. Funct. Mater.* **2009**, *19*, 1869-1875.

42. H. Lu, J. Mack, Y. Yang, Z. Shen, *Chem. Soc. Rev.* **2014**, *43*, 4778-4823.

43. J. H. Ryu, Y. K. Eom, J. C. G. Bunzli, H. K. Kim, *New J. Chem.* **2012**, *36*, 723-731.

44. M. Nakamura, H. Tahara, K. Takahashi, T. Nagata, H. Uoyama, D. Kuzuhara, S. Mori, T. Okujima, H. Yamada, H. Uno, *Org. Biomol. Chem.* **2012**, *10*, 6840-6849.

45. X. D. Jiang, R. N. Gao, Y. Yue, G. T. Sun, W. L. Zhao, *Org. Biomol. Chem.* **2012**, *10*, 6861-6865.

46. O. Galangau, C. Dumas-Verdes, R. Meallet-Renault, G. Clavier, *Org. Biomol. Chem.* **2010**, *8*, 4546-4553.

47. J. Bartelmess, M. Baldrighi, V. Nardone, E. Parisini, D. Buck, L. Echegoyen, S. Giordani, *Chem. Eur. J.* **2015**, *21*, 9727-9732.

Chapter 2

An Unprecedented Amplification of Near-Infrared Emission in a Bodipy Derived π-System by Stress or Gelation

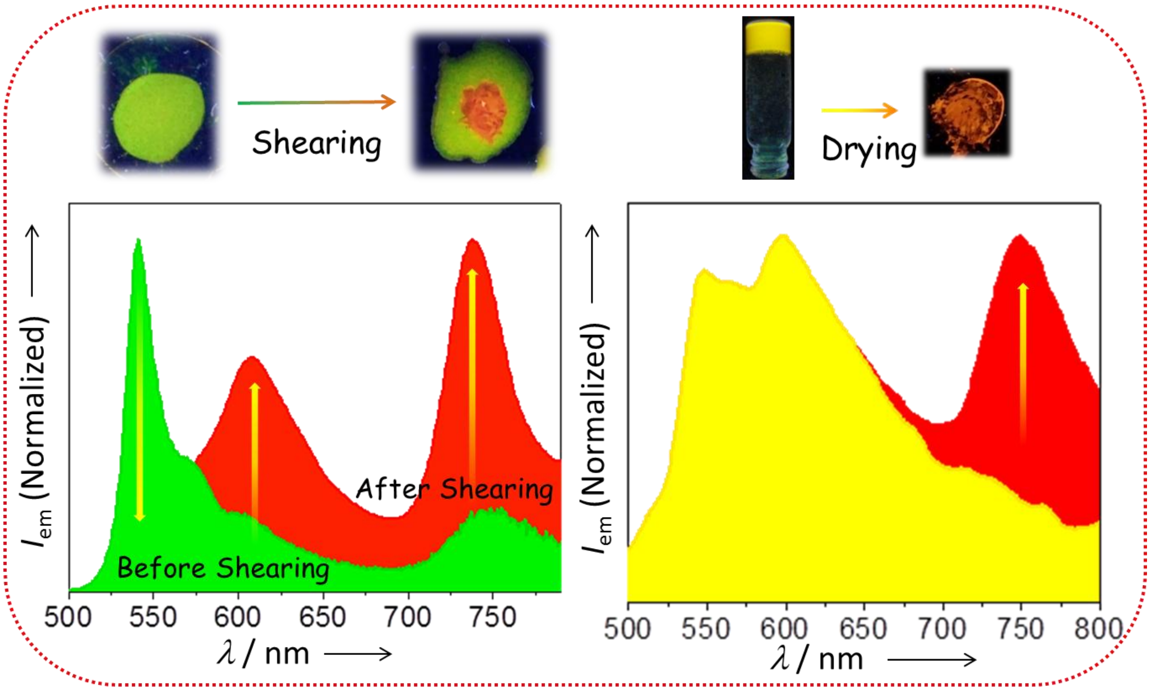

2.1. Abstract

In this chapter, we describe the synthesis, self-assembly and mechano responsive properties of amide functionalised meso phenyleneethynylene derived Bodipy dyes ***Bodipy-1*** *and* ***Bodipy-2****.* ***Bodipy-1*** *showed interesting morphological and optical properties in nonpolar and polar solvents. A film of the π-extended* ***Bodipy-1*** *obtained from n-decane changed the emission color (green to orange)*

upon mechanical shearing with a 15-fold enhancement in NIR emission at 738 nm. Alternatively, a DMSO gel of the ***Bodipy-1*** *exhibited a 7-fold increment in NIR emission at 748 nm with a change in the emission color from yellow to orange-red upon removal of the solvent. The reason for the amplified NIR emission is established by the single crystal analysis of a model compound (****Bodipy-2****), which exhibited a near identical emission spectrum with intense red emission having an NIR band at 730 nm. The emission features of the sheared n-decane film, DMSO xerogel and the single crystals indicated identical molecular packing in the sheared* ***Bodipy-1*** *and the crystalline* ***Bodipy-2*** *which involves a head-to-tail slipped arrangement of the molecules driven by the N–H···F–B H-bonding. Shearing assisted breakage of the amide H-bond in the initially formed supramolecular polymer and the formation of N–H···F–B H-bonds lead to the amplification in NIR emission due to the strong intermolecular exciton coupling.*

2.2. Introduction

The luminescence tuning of supramolecular functional materials in the solid state with various external stimuli has drawn significant attention from the scientific community for more than a decade. Molecular self-assembly as well as gelation of chromophores are alternate approaches for the modulation of emission towards longer wavelength.[13-16] Mechanochromism is the change in optical properties of molecular assemblies by the application of mechanical force (shear, stress, pressure *etc.*), however in most of the cases, the modulation occurs in the UV-visible range.[17-21] In this context, there is a report pertaining to mechanochromic change of NIR (Near-infrared) emission to blue emission and another on mechanically induced phosphorescence in organometallic systems.[22,23] However, there is only one report on mechanical force induced amplification of NIR emission in organic molecular assemblies. NIR emission is usually achieved by decreasing the HOMO-LUMO gap by strong donor-acceptor interaction or by extension of π-conjugation or through metal complexation.[1-12] NIR emitting small organic molecules are relatively rare when compared to UV-vis light emitting molecules. However, NIR emitting molecules are important in the fields of materials and biology.[1-6] For example, NIR emitting chromophores are required for telecommunications, security application, displays, bio-imaging etc.[1-12] However, the quantum yield of NIR emission and the stability of NIR emitting organic molecules are relatively weak.[1,2]

4,4-Difluoro-4-bora-3a-4a-diaza-*s*-indacene (Bodipy) is one of the well-studied functional dyes due to their intriguing emission properties.[24-26] The strong and sensitive fluorescence of Bodipy derivatives have been exploited for chemosensing, energy transfer and related optoelectronic applications.[27-31] In addition, self-assembled Bodipy has generated considerable interests due to the possible design of soft materials with tunable optical properties and liquid crystalline behavior.[27,28] In this context, a few examples for Bodipy based gelators have already been known.[33-36] Reversible interconversion between different assemblies is supposed to be one of the reasons for inducing mechanochromism in self-assembled organic dyes.

There is no hard and fast rule to synthesise mechanochromic materials since most of the incidence happen to be serendipitous. However, Araki *et al.* came up with a design principle which involved pyrene which is a rigid aromatic π-conjugated backbone, connected to hexyl amide groups at the *para* position of the phenyl units (**Figure 2.1**).[49] Authors have studied the mechanochromic response of different amide and ester derivatives and emphasised the role of amide and alkyl chains for a repeatable mechanochromism. Addition of methanol to the chloroform solution of **1** gave a white powder (here called 'B-form') which shows blue emission under UV irradiation. Upon pressing with a spatula, the 'B-form' is converted into an yellow solid 'G-form' which exhibits green emission and the process is reversed by heating below melting temperature. Hydrogen bond directed ordered H-type columnar packing is

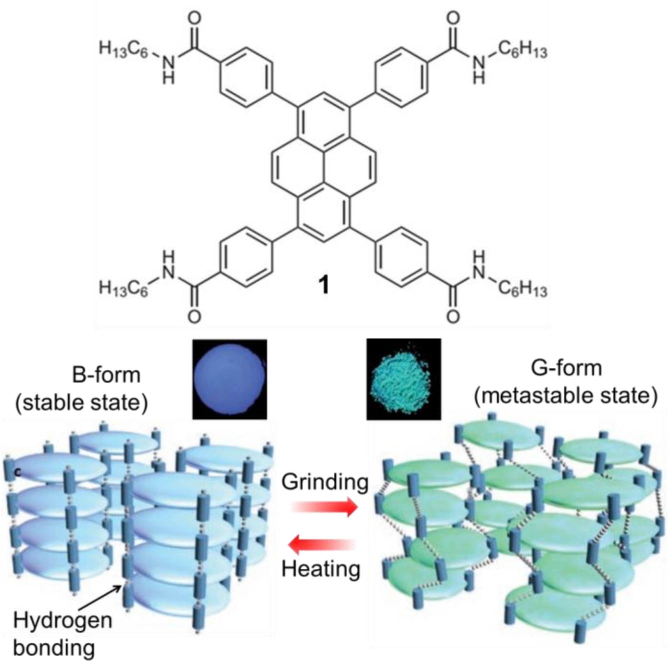

Figure 2.1. Molecular structure, luminescence and schematic representation of molecular assembly changes upon grinding.

disturbed by the application of pressure, resulting in a change in the twist angle between the pyrene and the phenyl groups leading to a disordered metastable G-form (**Figure 2.1**).

Generally, application of mechanical force leads to structural transition from ordered crystalline to disordered amorphous states. However, there are some instances where the application of mechanical force involves the changes from one liquid crystalline state to another with distinct fluorescent response. In one of such reports, Kato *et al.* have studied the mechanochromic fluorescence behaviour of liquid crystalline phases.[50] In this case, authors have designed a molecular system involving two dendritic moieties having long alkyl chains which is attached to a luminescent core such as pyrene or anthracene through amide groups (**Figure 2.2a**). This bulky compound initially forms a meta-stable cubic phase by hydrogen bonding and π-π stacking. The pyrene groups are arranged in a π-stacked structure, which is enough to form excimers and leads to the emission of yellow color. These segmented columnar structures are disordered structures since the distance between amide hydrogen bonds is around 5 Å whereas the distance between the aromatic rings forming stable π-stacked structures is approximately 3.5 Å (**Figure 2.3a**). Mechanical shearing (at 160 °C) induces a change in molecular packing for the pyrene assembly from ‘segmented columnar’ (cubic phase, yellow excimer emission) to ‘non-segmented columnar’ (columnar, blue-green) which is driven by a more ordered linear hydrogen bonded structure where the excimer formation is prevented (**Figure 2.3a & b**). The optical properties of **1** in the cubic (160 °C), shear- induced columnar (160 °C), and isotropic (200 °C) phases were examined by absorption and emission spectroscopy.

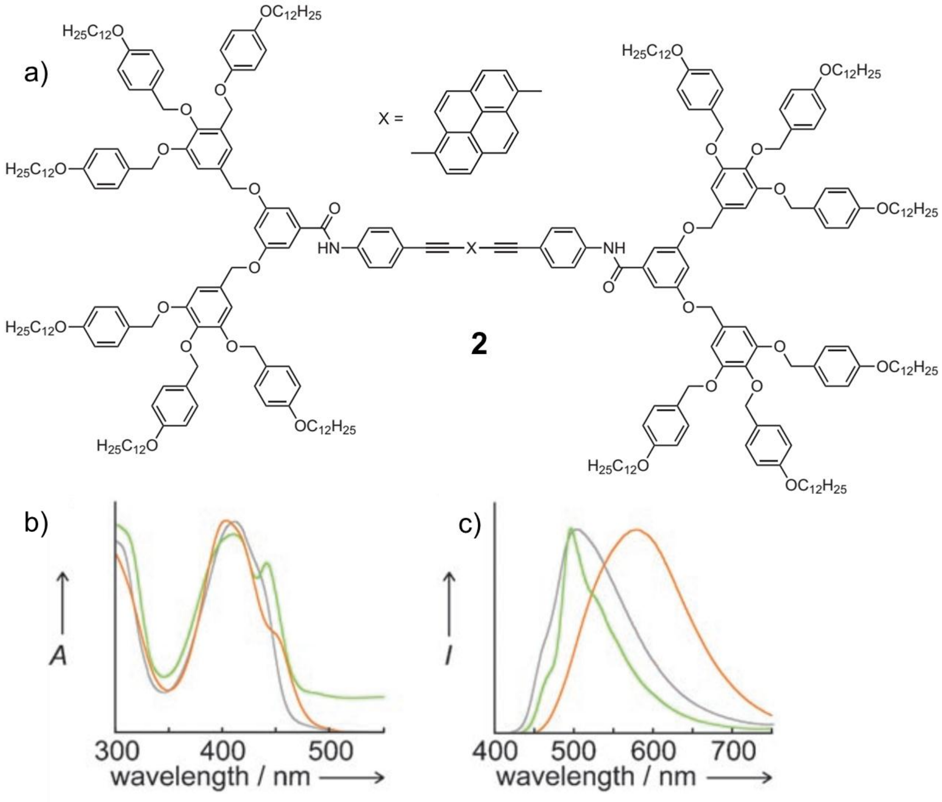

Figure 2.2. a) Molecular structure of **2**. b and c) Absorption and emission spectra in the cubic (160 °C, orange line), shear induced columnar (160 °C, green) and isotropic phases (200 °C, grey).

The C=O stretching band observed for **2** in the cubic phase shifts from 1655 to 1645 cm^{-1} upon shear-induced cubic–columnar phase transition. This shift indicates that the weaker H-bonded state in the cubic phase changes to a stronger H-bonded state in the shear-induced columnar phase. In addition, peaks corresponding to the C=O and N-H stretches observed in the shear-induced columnar phase become sharper than those observed in the cubic phase (**Figure 2.3c-e**). These observations also suggest that mechanical shearing induces a change in the self-assembled structures of **2** at a molecular level.

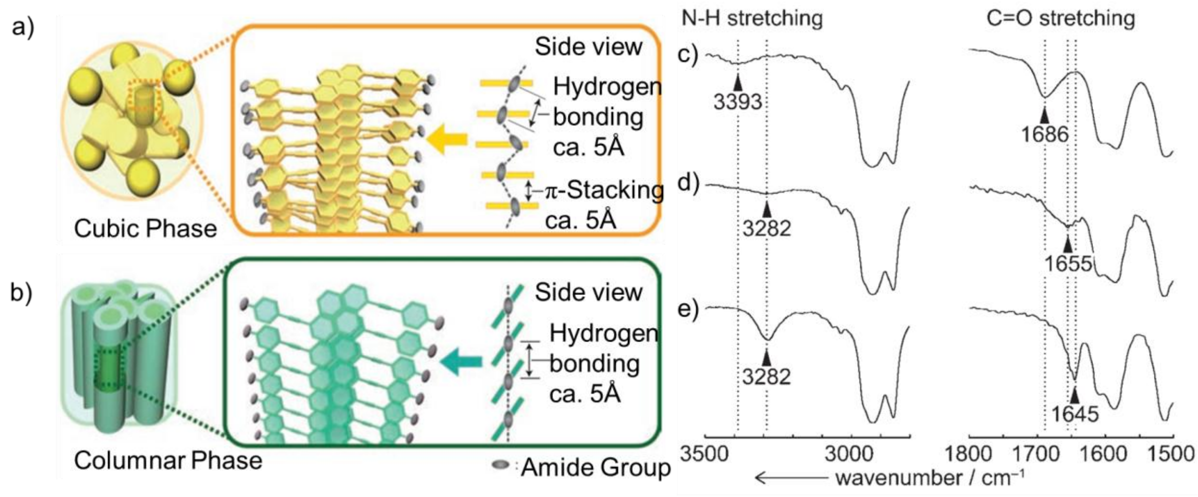

Figure 2.3. Schematic representation of assemblies of **2** in a) cubic b) columnar phases. c-e) IR spectra in isotropic (200 °C), cubic (160 °C) and shear induced columnar (160 °C) phases, respectively.

Boron containing organic crystals has attracted much attention in recent times because of its interesting stimuli responsive luminescence properties. Fraser *et al.* have reported morphology dependent polymorphic and reversible mechanochromic luminescence of difluoroboron avobenzone (**3**).[51] Slow evaporation from dichloromethane resulted in the formation of green and cyan emitting needle like crystals (**Figure 2.4b** and **c**). A third dendritic solid form with blue emission is also obtained via dichloromethane evaporation from a cotton swab (**Figure 2.4d**). Single crystal XRD analysis of **3** revealed the reason for multiple emission based on the molecular conformation and different intermolecular interactions in the aggregates. In green state, boron diketone and phenyl rings are coplanar and also the *tert*-butyl aromatic ring in the cyan crystal is twisted at an angle of ~8° with respect to BF_2 diketone arene plane. Moreover, these two crystals have different symmetries. For example, in green crystals, molecules are antiparallel (*tert*-buyl opposite) and in cyan, the *tert*-butyl groups are clustered on the same side of the dimer (**Figure 2.4e, f**). The blue shifted emission of cyan crystal is explained based on shorter conjugation length in the twisted structures and weaker π-π stacking.

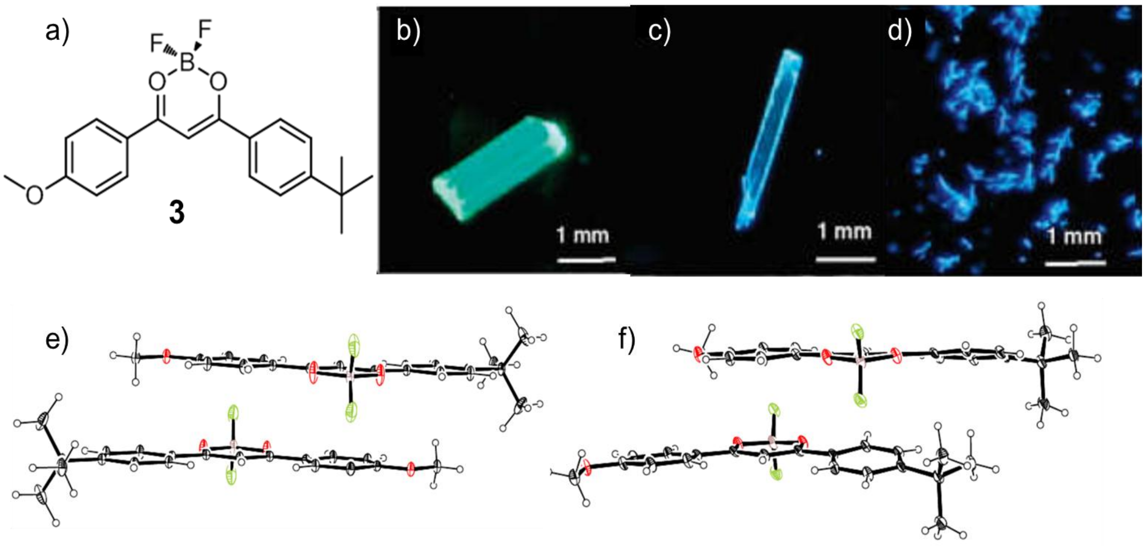

Figure 2.4. Chemical structure of **3**. b-d) Photographs under UV light corresponding to green (b) and cyan (c) crystals, and blue solid (d). e) Molecular conformation and relative arrangement of molecules in green and f) in cyan crystals.

An additional molecular level interaction is provided from Hirshfeld surface calculations. The molecular surfaces and the fingerprint plots suggest closer C(methyl)–H···O and C(methyl)–H···F contacts (including possible C–H···F hydrogen bonds) in the cyan form than in the green form (**Figure 2.5**). Grinding of the blue emitting dendritic solid of **3** resulted in a change in luminescence to yellow which progressively changes its luminescence to greenish-blue emission (**Figure 2.6**). Upon pressing the thermally activated film of **3**, the luminescence is shifted from green-blue to yellow and the recovery to the initial luminescent state is achieved gradually at room temperature (**Figure 2.6**).

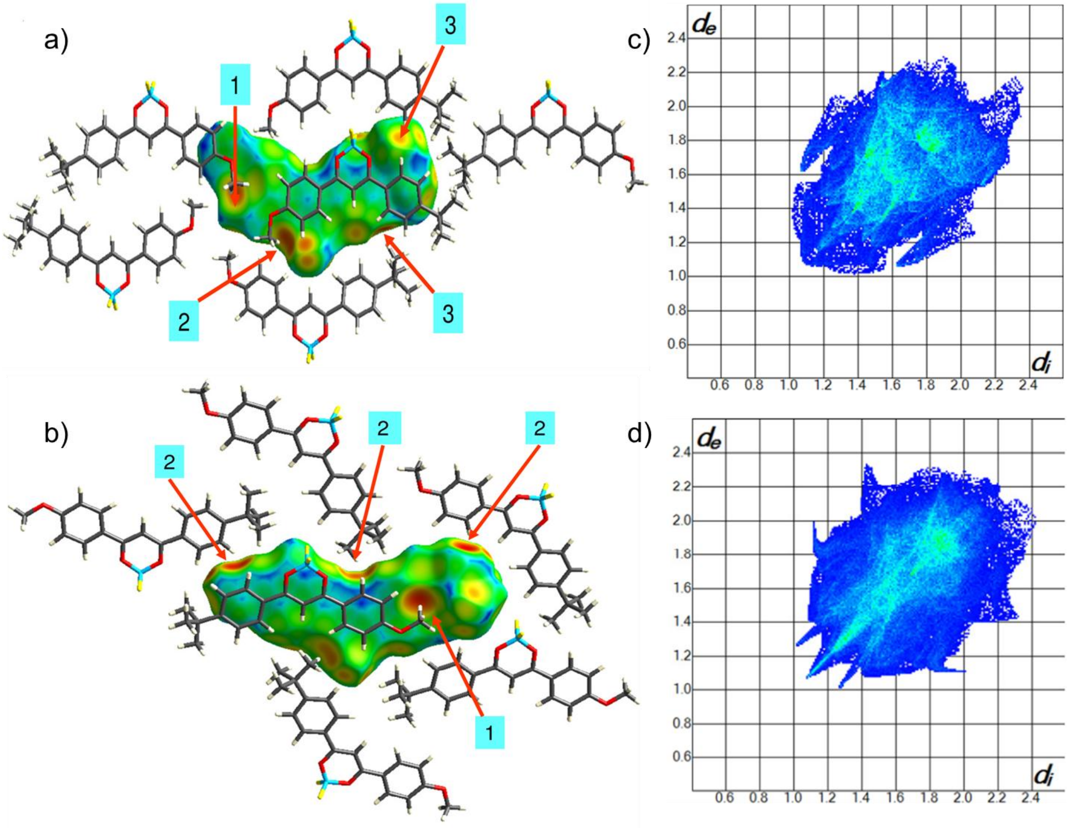

Figure 2.5. a & b) d_e-mapped Hirshfeld surfaces of green and cyan crystals, respectively. c, d) Fingerprint plots. Intermolecular interactions: C–H···π (A1), C–H···F hydrogen bond (A2) and short H···H contacts (A3). C–H···π (B1) and short H···H contacts (B2).

It is not clear on the specific interactions responsible for the molecular organization after smearing. The strong, dipolar nature of BF_2dbm (dibenzoylmethane), offset arene stacking, hydrogen bonding between the fluorine, the arene hydrogen atoms, and other interactions could be the reasons involved. The yellow emission may be attributed to the excimer formation since the mechanical perturbation resulted in greater rotational degrees of freedom favoring excimer formation.

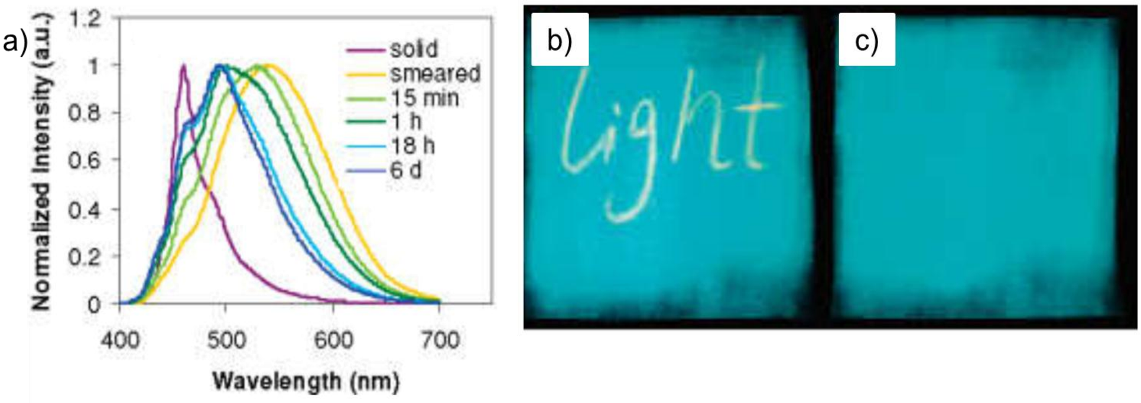

Figure 2.6. a) Fluorescence emission spectra of **3** blue solid and the smeared solid film monitored for long time. b) Mechanochromic fluorescence of "light" written with cotton swab c) Background emission restored by heating for ~3-5 seconds.

Mechanical stimuli in the form of compression, grinding and smashing lead to interesting luminescent properties in the case of certain boron diketonate complexes. The luminescent properties of boron diketonate crystals with respect to different mechanical stimuli has been studied by Wang *et al.*[52] Diffusion of molecule **4** from CH_2Cl_2 to hexane produced orange emitting **4OC** (λ_{em} = 585 (main) and 610 nm (shoulder)) and, red emitting **4RC** (605 nm) rod-like crystals which are less stable due to the trapping of CH_2Cl_2 in the crystalline lattice (**Figure 2.7a-c**). These polymorphs form a dimer structure which are stabilized by strong face-to-face π-π and dipole-dipole interactions with slightly different intermolecular distances (**4OC** 3.5Å, **4RC** = 3.6Å).

Smashing the orange crystals (**4OC**) leads to blue shift of the emission from 585 to 565 nm (**Figure 2.7d**) with the formation of fragmented crystals. Also, upon grinding the fragmented crystals (565 nm), orange red emitting powders (585 nm) are formed with an emission profile similar to that of the initial **4OC** orange crystals. Different molecular arrangements such as π-stacked dimers have been formed after grinding, which caused the red shifted luminescence. Molecular packing and structural transformation have been understood from powder X-ray diffraction (PXRD) of the sample before and after smashing.

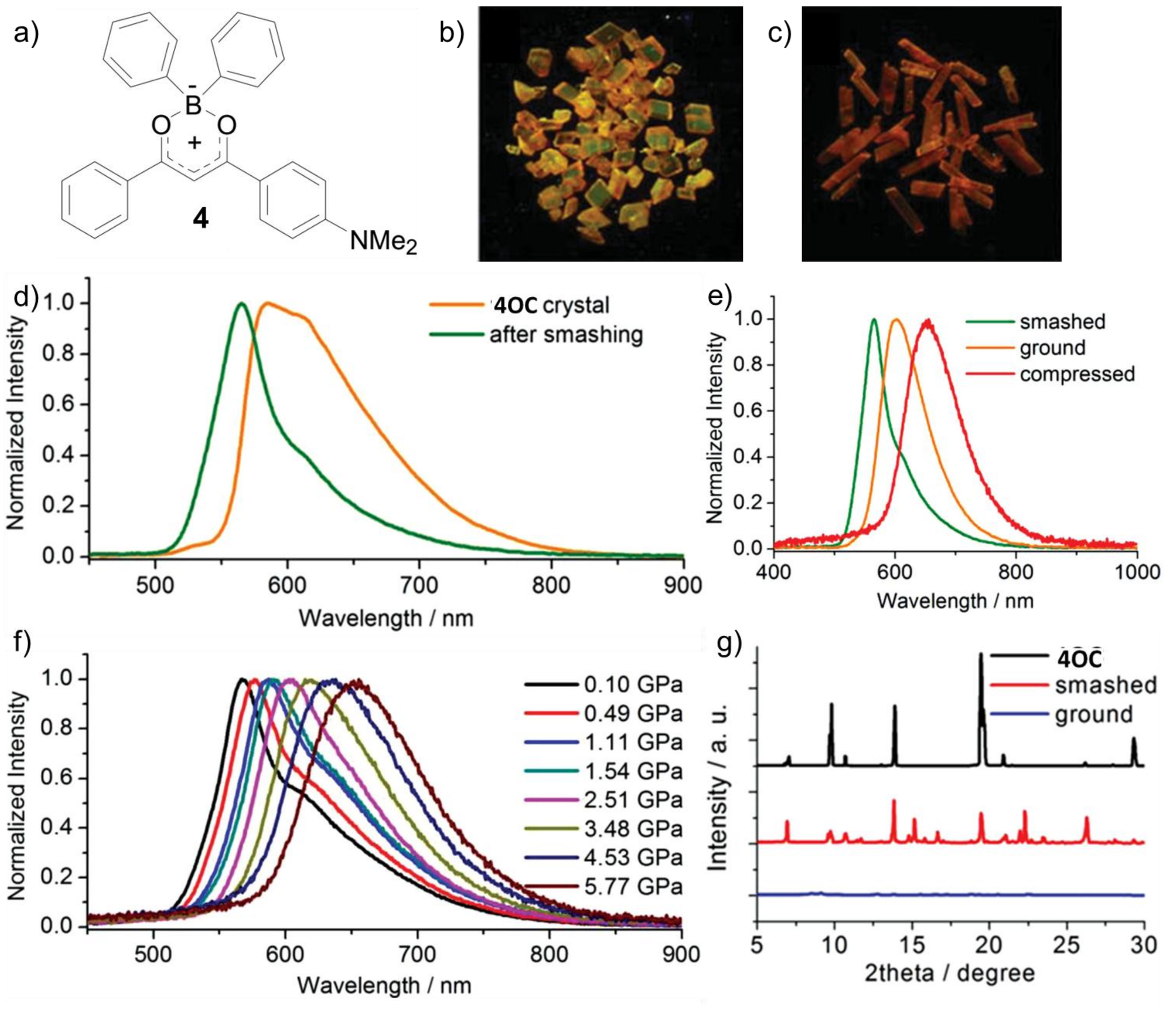

Figure 2.7. a) Molecular structure of **4.** b, c) Orange crystal **4OC** and red crystal **4RC**, respectively**.** d) Fluorescence spectra of **4OC** crystal and after smashing. e) Comparative luminescence features of smashed ground and compressed samples of **4OC.** f) Luminescence shift of **4OC** crystals on different hydrostatic pressures. g) PXRD patterns of **4OC** in different states.

PXRD patterns of the ground sample revealed weakened and broadened peaks when compared with **4OC** crystals, indicating that the crystals have almost converted into amorphous solids (**Figure 2.7g**). On the other hand, tensile forces weaken the molecular interactions and loose molecular aggregates, but isotopic compression leads to more close packing of the molecules in the crystal. The luminescence of **4OC** crystals gradually shifts from 580 to 660 nm when increasing the hydrostatic pressure to 5.77 GPa in a silicon oil media. Compression may shorten the distance between π-planes in a dimer and hence leads to red-shifted luminescence.

Mechanochromic organic molecules that exhibit a large difference of fluorescence wavelength between two states have potential applications. Enomoto *et al.* have reported switchable mechanochromic molecule **5** (***cis*** **ABPX01**) which shows a luminescence shift from NIR to blue region by the application of mechanical force (**Figure 2.8a-c**).[22] From the spectroscopic and single crystal data analysis, it is evident that the NIR fluorescence is attributed to slip-stacked dimeric structures in crystals while the blue fluorescence is due to the formation of monomers. The powder X-ray diffraction (XRD) pattern of ground $\mathbf{5}_{\boldsymbol{cis}}$ did not show noticeable reflection peaks when compared with the XRD pattern of $\mathbf{5}_{\boldsymbol{cis}}$ (**Figure 2.8d**). The switching between the two states is achieved by dynamic structural inter-conversion between the two molecular packing arrangements in response to mechanical grinding and solvent vapor fuming.

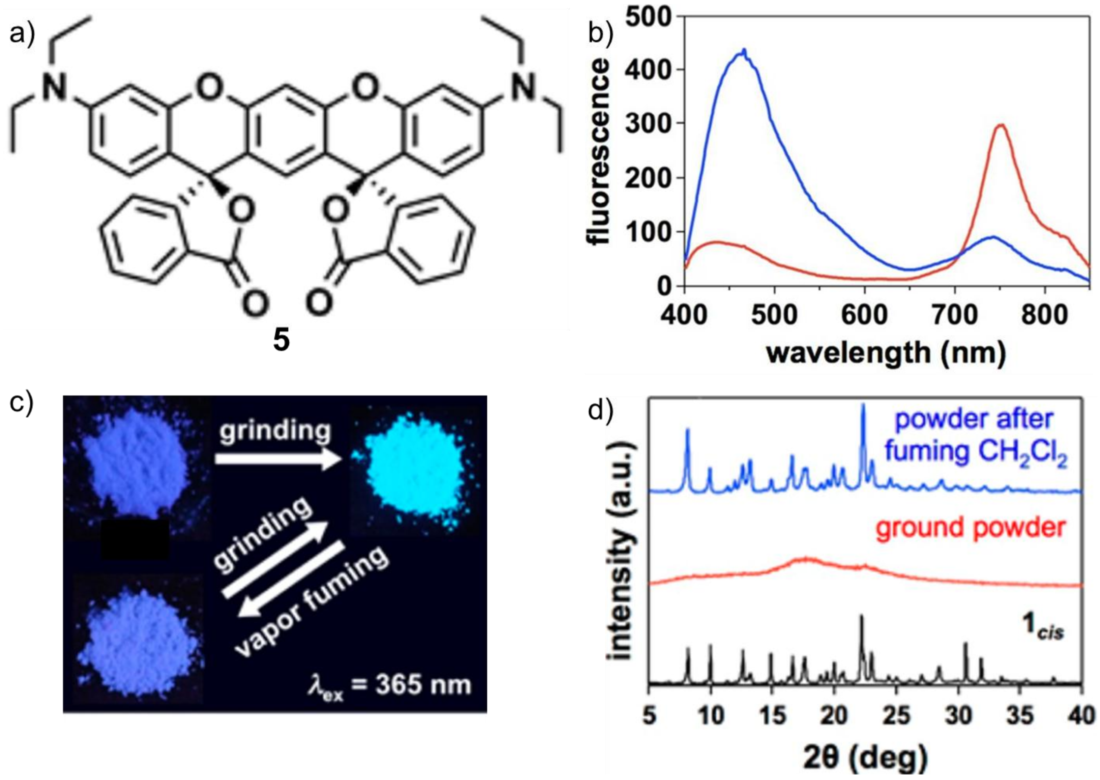

Figure 2.8. a) Molecular structure of **5**. b) Emission spectra of non-grind $\mathbf{5}_{cis}$ derivative (red) and after grinding (blue). c) Photograph under uv light of $\mathbf{5}_{cis}$ derivative upon grinding and fuming d) PXRD of $\mathbf{5}_{cis}$ derivative under different conditions.

From the literature reports it is understood that mechanochromic luminescence shifts are a well-known phenomenon and have been studied widely. Most of these systems show only small variation in their luminescence shift. These luminescence shifts may be either a blue shift or a red shift depending on the formation of monomers or excimers. Generally, depending on the initial state of the assembly, mechanical forces disturb either from more ordered state into less ordered state or vice versa. Sometimes the luminescence shift is attributed to a change in one liquid crystalline phase into the other possessing distinct luminescent properties. The majority of the luminescence shift associated with mechanochromic systems are in the UV-visible luminescence region although there is a report on luminescence shift from NIR to blue fluorescence.[22] However, NIR luminescence amplification for a simple organogelator has not been reported in the literature so far. In the present study, we report on a Bodipy based mechanochromic system which shows amplification of NIR emission by the application of mechanical force on a film processed from *n*-decane solution. The NIR emission amplification is also achieved by the preparation of a xerogel of the **Bodipy-1** gel from DMSO. A detailed photophysical, X-ray diffraction and single crystal study has been done to arrive at a conclusive packing.

2.3. Results and Discussion

2.3.1. Syntheses of Bodipy-1 and Bodipy-2

Bodipy-1 is synthesized by the Sonogashira coupling between 3,4,5-tributoxy-*N*-(4-ethynylphenyl)benzamide (**11**) and (4-iodophenyl)-1,3,5,7-tetramethyl-4,4-difluoro-4-bora-3a,4a-diaza-*s*-indacene (**14**) in presence of bis(triphenylphosphine) palladium (II) dichloride (10 mol%), and copper (I) iodide (10 mol%) using degassed triethylamine and THF as solvents in 30% yield (**Scheme 2.2**). The precursor molecule **11** was synthesized from compound **6** with a yield of 33% as shown in the **Scheme 2.1** and **2.2**. All intermediates and final product are characterised by ^{1}H NMR, ^{13}C NMR, HRMS/MALDI and FT-IR spectroscopic techniques.

The total steps involved in the synthesis of **Bodipy-1** are depicted in **Scheme 2.1-2.3**.

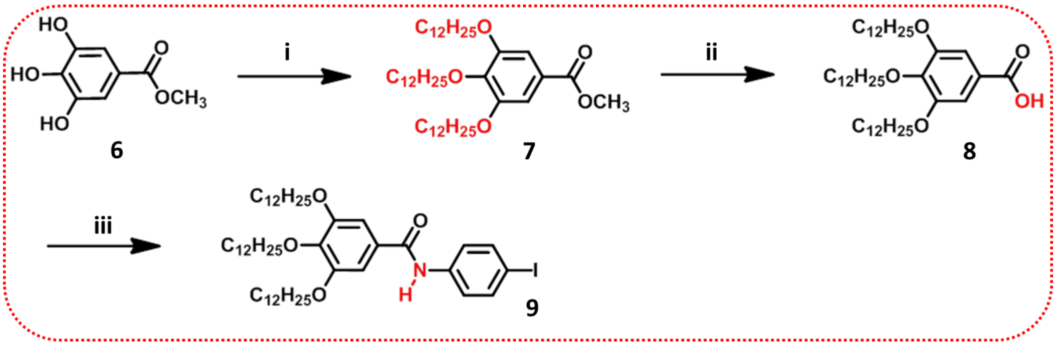

Scheme 2.1. Reagents and conditions: i) 1-Bromododecane, K_2CO_3, DMF, 100 °C, 24 h, 78%; ii) KOH, ethanol, reflux, 12 h, 80%; iii) a) $SOCl_2$, dry dichloromethane, rt., 5 h; b) 4-Iodoaniline, dry toluene, rt., 12 h, 50%.[32,44]

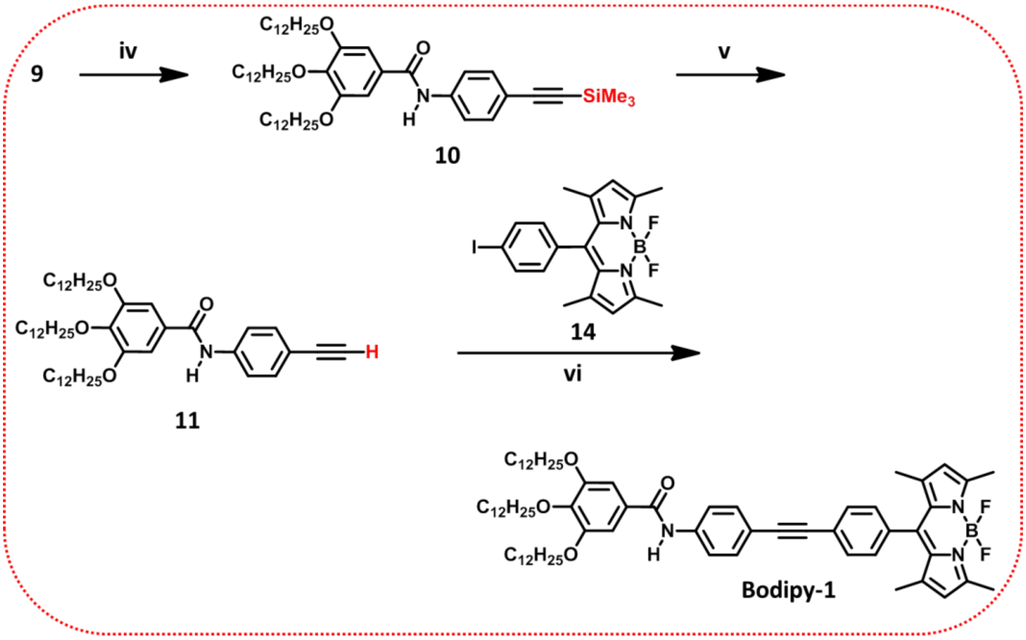

Scheme 2.2. Reagents and conditions: v) Trimethylsilyl acetylene, CuI, $PdCl_2(PPh_3)_2$, dry Et_3N, dry THF (oxygen free), rt., 12 h, 80%; v) KF, dichloromethane/methanol (1:5), rt, 12 h, 76% vi) CuI, $PdCl_2(PPh_3)_2$, dry Et_3N, dry THF (oxygen free), 60 °C, 24 h, 30%.[32,44]

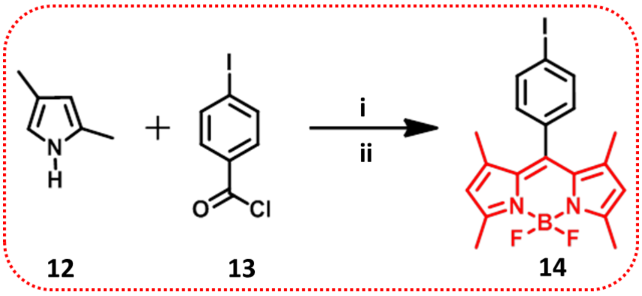

Scheme 2.3. Reagents and conditions: i) a) Dry dichloroethane, reflux, 3 h; ii) Et_3N, BF_3•OEt_2, 25 °C then reflux, for 30 min, 36%.

The model compound **Bodipy-2** having methoxy groups is synthesized as shown in **Scheme 2.4**. The structure of **Bodipy-2** is characterised by ^{1}H NMR, ^{13}C NMR, HRMS, FT-IR and single crystal analyses.

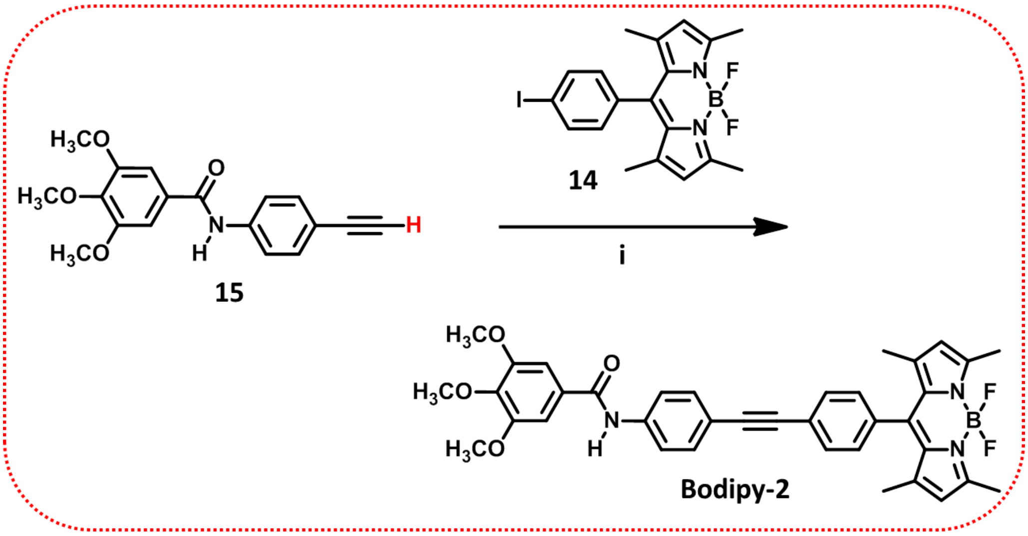

Scheme 2.4. Reagents and conditions: i) CuI, $PdCl_2(PPh_3)_2$, dry Et_3N, dry THF (oxygen free), 60 °C, 24 h, 40%.

2.3.2. Photophysical Properties

2.3.2.1. Absorption and Emission Spectral Properties

In chloroform, (1×10^{-4} M), **Bodipy-1** exists in the monomeric state with absorption maxima at 315 and 504 nm with a shoulder band at 474 nm (**Figure 2.9a**). The absorption maximum at 315 nm corresponds to the phenyleneethynylene part, whereas the narrow absorption maximum at 504 nm ($\varepsilon = 88{,}400$ M^{-1} cm^{-1}) corresponds to the strong S_0-S_1 electronic transition involving ($0 \rightarrow 0$) vibrational states of the Bodipy.[26-33] The broad absorption feature observed around 380 nm can be assigned to the S_0-S_2 transition of the Bodipy unit.[26-33] The high fluorescent quantum yield ($\Phi_f = 0.53$, $\lambda_{ex} = 475$ nm, fluorescein in 0.1 NaOH as standard, $\Phi_f = 0.91$) and the small Stokes shift (608 cm^{-1}) observed are the indications of the singlet emitting excited state (**Figure 2.9a**). The near identical quantum yields of 0.52 and 0.53 at two different excitation wavelengths of 315 nm corresponding to the phenyleneethynylene and 474 nm corresponding to the Bodipy indicate a good electronic communication between the two moieties.

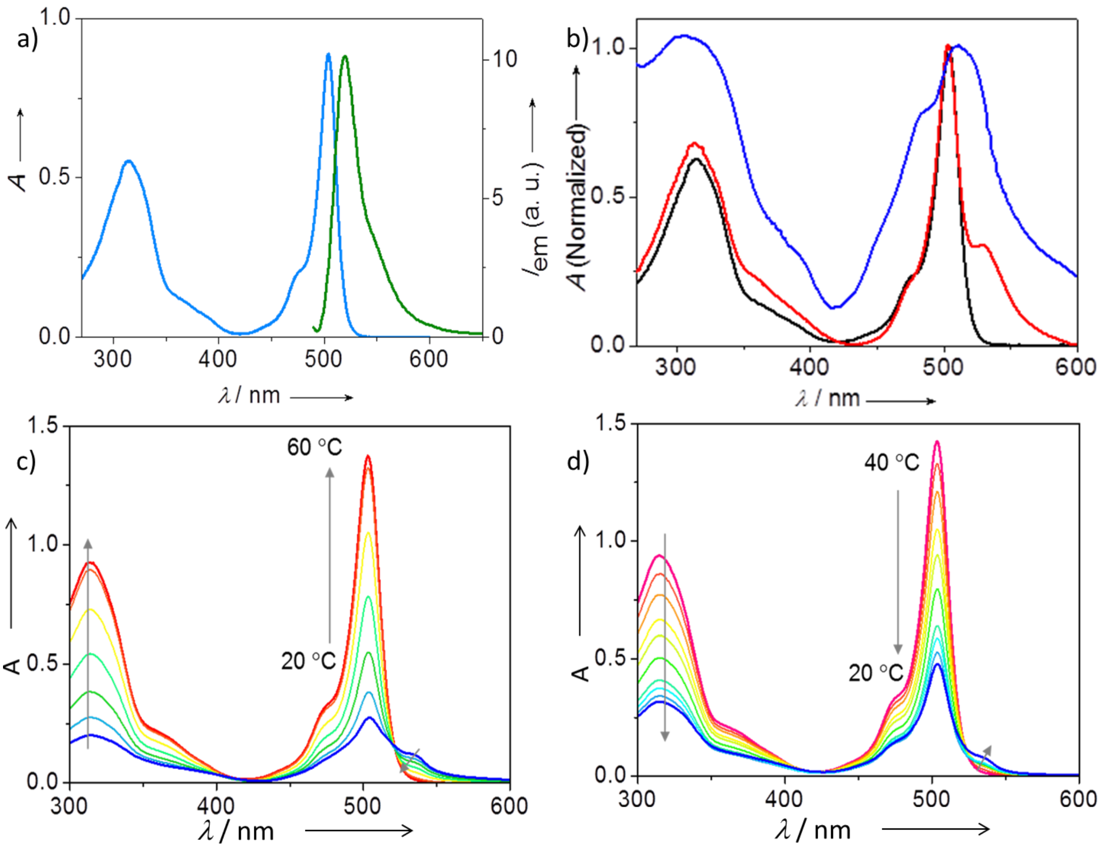

Figure 2.9. a) Absorption (blue) and emission spectra (green) in chloroform (1 x 10^{-4} M) λ_{ex} = 475 nm. b) Normalized absorption spectra (c = 1 x 10^{-4} M) of **Bodipy-1** in $CHCl_3$ (black), *n*-decane (red) and DMSO (blue). Temperature-dependent absorption spectra of **Bodipy-1** aggregates in *n*-decane (c = 1 x 10^{-4} M) for c) heating from 20 – 60 °C, d) cooling from 40 – 20 °C. Arrows indicate the spectral changes for the heating and cooling processes.

Comparison of the absorption spectra of **Bodipy-1** in a variety of solvents (1 x 10^{-4} M, **Figure 2.9b** and **2.10d**) reveals an additional red-shifted band at 530 nm in *n*-decane, probably due to J-type aggregation. Variable temperature absorption spectral changes in *n*-decane for the heating process indicates a decrease in the intensity of the shoulder band at 530 nm (**Figure 2.9c**). The shoulder band at 530 nm is reformed upon cooling the decane solution gradually from 40 – 20 °C (**Figure 2.9d**), which indicates the reversible nature of decane aggregates. In DMSO (1 × 10^{-4} M), the molecule exhibited a broad absorption spectrum with maxima at 310 and 511 nm (**Figure 2.9b**). The effect of solvent on photoluminescence shift indicates the absence of intramolecular charge-transfers in the excited state energy levels.[18]

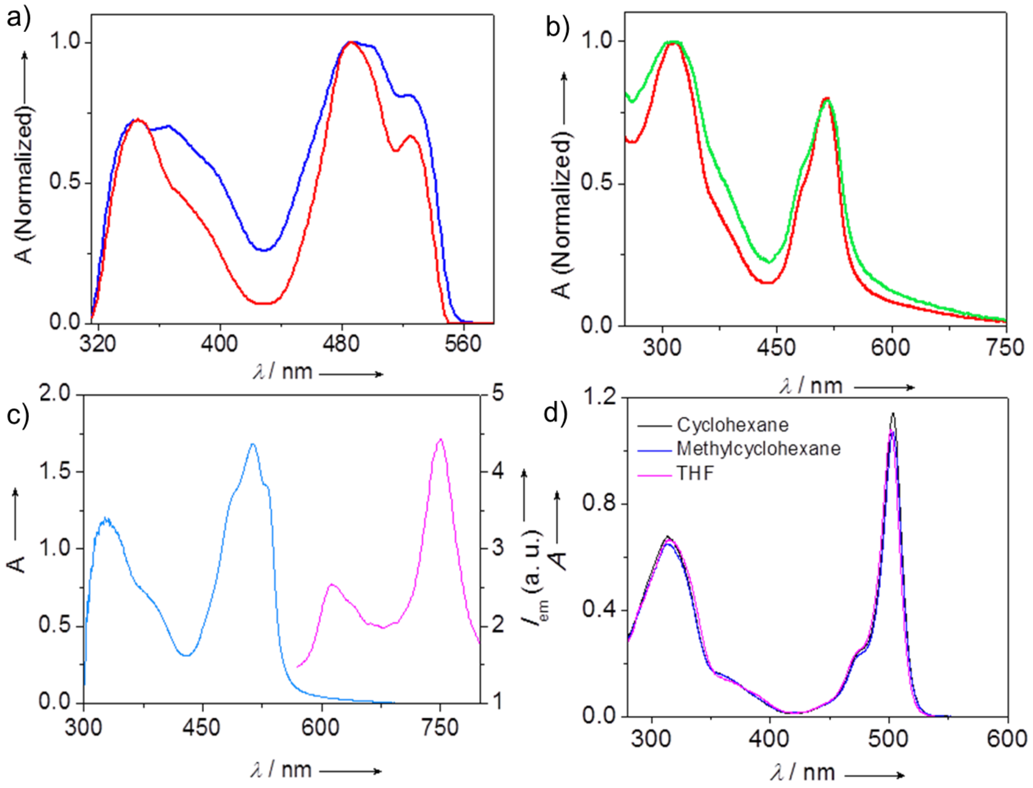

Figure 2.10. a) Absorption spectra of **Bodipy-1** and *n*-decane film before (red) and after shearing (blue). b) Absorption spectra before (red) and after (green) shearing of **Bodipy-2** single crystal. c) Absorption and emission spectra (λ_{ex} = 550 nm) of **Bodipy-1** DMSO xerogel. d) Absorption spectra of **Bodipy-1** in cyclohexane, methylcyclohexane and THF (*c* = 1 x 10^{-4} M).

2.3.2.2. Mechanochromic Amplification of NIR Emission

The emission of **Bodipy-1** in *n*-decane solution occurred at 516 nm with a shoulder band at around 542 nm (**Figure 2.11a**). A film prepared from the *n*-decane solution exhibited a greenish-yellow emission with a maximum at 541 nm, and two shoulder bands at 574 and 604 nm (**Figure 2.11a**). Surprisingly, a weak NIR band is observed at 738 nm, which was absent in the *n*-decane solution. The absolute quantum yield (Φ_f) of the film measured by a calibrated integrated sphere attached to the spectrofluorimeter is 0.076 (± 0.008). When the film was mechanically sheared, intensity of the initial emission band at 541 nm was decreased with increase in the emission intensities at 608 and 738 nm (15-fold, **Figure 2.11a**) without much change in the absorption spectrum (**Figure 2.10a**). The emission color of the sheared portion of the film changed into orange-red from the initial greenish-yellow (**Figure 2.11a**, inset) with a fluorescence quantum yield (Φ_f) of 0.079 (± 0.008). The reversibility of the mechanochromic emission change is possible by re-aggregating the sheared sample in *n*-decane.

Interestingly, in DMSO at a concentration of 1×10^{-2} M, a gel was formed which exhibited a yellow emission (**Figure 2.11b**). The emission spectrum of the DMSO gel showed a broad band between 500 - 800 nm with two maxima at 548 and 598 nm with a weak shoulder between 700 - 800 nm. Surprisingly, when the gel was transferred on a glass plate, followed by evaporation of the solvent, an orange-red emission was observed (**Figure 2.11b**, inset). In this process, the intensities of the initial emission peaks at 548 and 598 nm were significantly

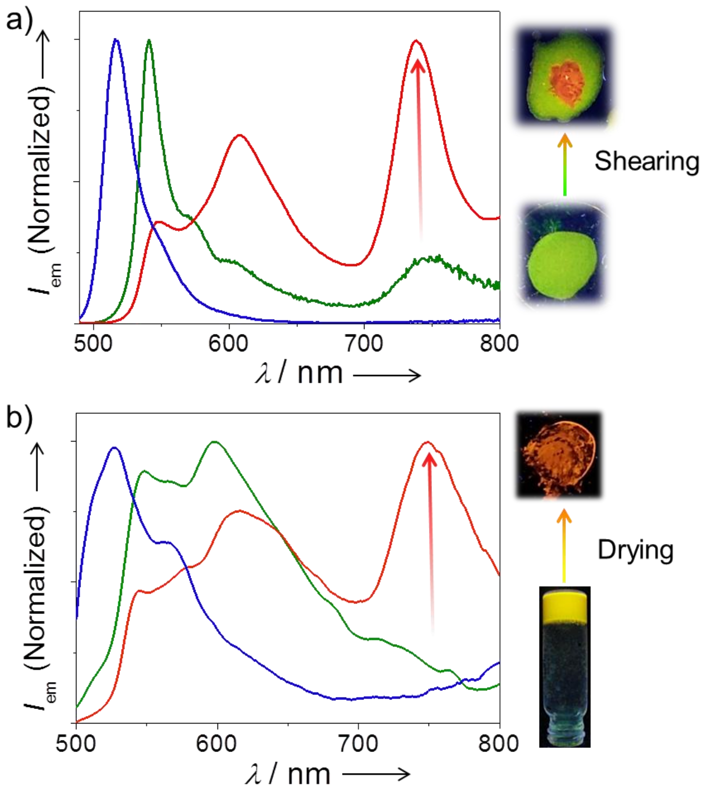

Figure 2.11. a) Emission profiles of **Bodipy-1** self-assembly in *n*-decane (1 x 10^{-4} M, blue), film processed from *n*-decane self-assembly (green) and after shearing the film (red), λ_{ex} = 475 nm. b) Emission profiles of **Bodipy-1** self-assembly in DMSO solution (1 x 10^{-4} M, blue), DMSO gel (green) and xerogel (red), λ_{ex} = 475 nm. The corresponding fluorescence color changes under UV light illumination are also shown.

decreased and a strong NIR emission band at 748 nm appeared with 7-fold enhancement. The emission spectrum of the DMSO xerogel of the **Bodipy-1** is nearly identical to that of the mechanically sheared *n*-decane film (**Figure 2.11b**), indicating the possibility that in the sheared film and in the xerogel states the molecular packing may be identical.

2.3.2.3. Fluorescence Lifetime Studies

The preliminary lifetime data of **Bodipy-1** in chloroform (1 x 10^{-4} M) monomer has shown a single exponential decay profile with a lifetime value of 2.66 ns whereas the aggregated decane solution (1 x 10^{-4} M) has exhibited a biexponential decay profile with a decrease in lifetime (2.11 ns) for the major component (**Figure 2.12a, b**). This hypothesis was further supported by comparing the fluorescence decay profiles of the sheared *n*-decane film with that of the DMSO xerogel. For this experiment, both films were excited with 375 nm light and the emission was collected at 606 and 740 nm (**Figure 2.13** and **Table 2.2**). The sheared *n*-decane film exhibited a triexponential decay (λ_{em} = 740 nm) with lifetimes of 0.31 (45.37%), 1.43 (34.93%) and 2.16 ns (19.7%). Interestingly, the xerogel also exhibited a triexponential decay (λ_{em} = 740 nm) with near identical lifetimes of 0.39 (48.6%), 1.0 (41.2%) and 2.74 ns (10.2%) confirming the presence of alike molecular aggregates. This observation was further confirmed

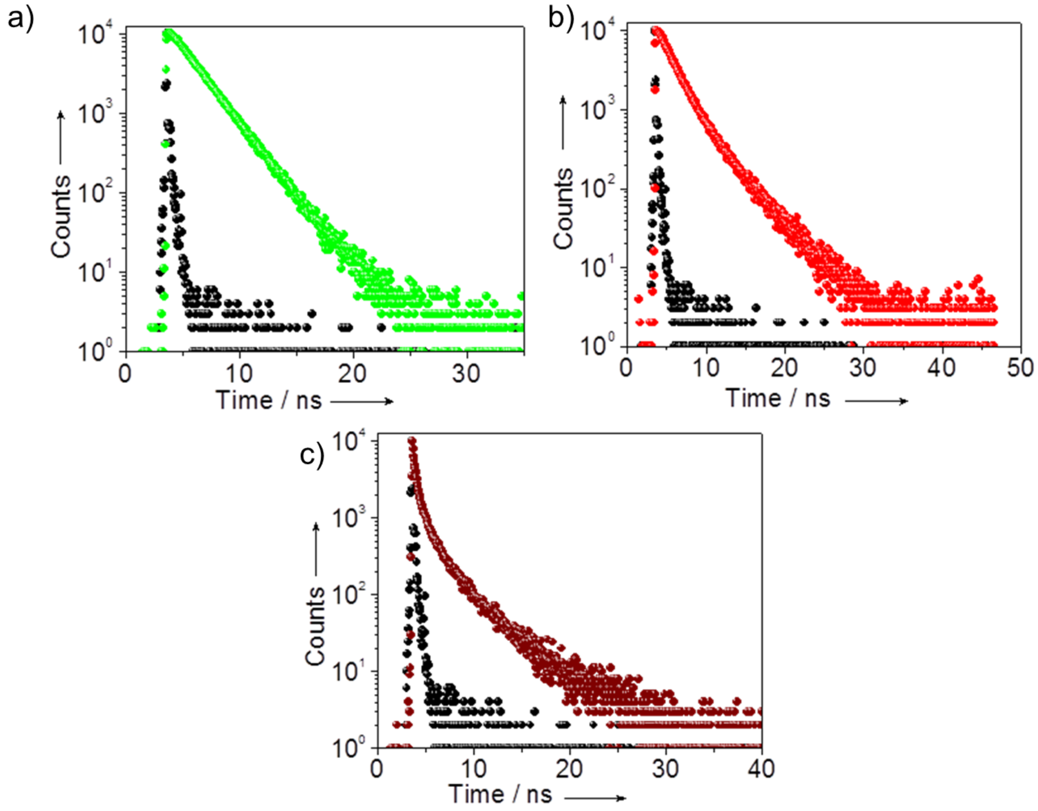

Figure 2.12. Lifetime decay profiles of **Bodipy-1** in a) $CHCl_3$ (1 x 10^{-4} M), b) *n*-decane (1 x 10^{-4} M) and c) film processed from *n*-decane. Emission was monitored 520 nm for a) and b). In all cases black profile corresponds to prompt and 375 nm LED used for excitation.

by monitoring the emission decay at 606 nm. Furthermore, absence of long lifetime components when the emission is monitored at 740 nm rules out the possibility of any excimer formation. These observations indicate that the sharp NIR emission originates from a slipped molecular organization, in analogy to previous reports on the spectral properties of Bodipy systems.

Table 2.1. Fluorescence lifetime data of **Bodipy-1** (λ_{ex} = 375 nm) in monomer and aggregated states along with the respective quantum yield values.

Sample Type	Absorption Max. (nm)	Emission Max. (nm)	Quantum Yield	Lifetime (ns)
Bodipy-1 $CHCl_3$ 1 x 10^{-4} M	315, 504	520	0.52 (Relative)	2.66
Bodipy-1 Decane 1 x 10^{-4} M	313, 504	518	0.28 (Relative)	2.11 (72.48%) 4.74 (27.52%)
Bodipy-1 *n*-Decane film	346, 486, 526	542 (strong), 575 (shoulder) 605 (shoulder), 740 (weak)	0.076 (Absolute)	1.19 (17.31%) 4.42 (8.23%) 0.26 (74.46%)

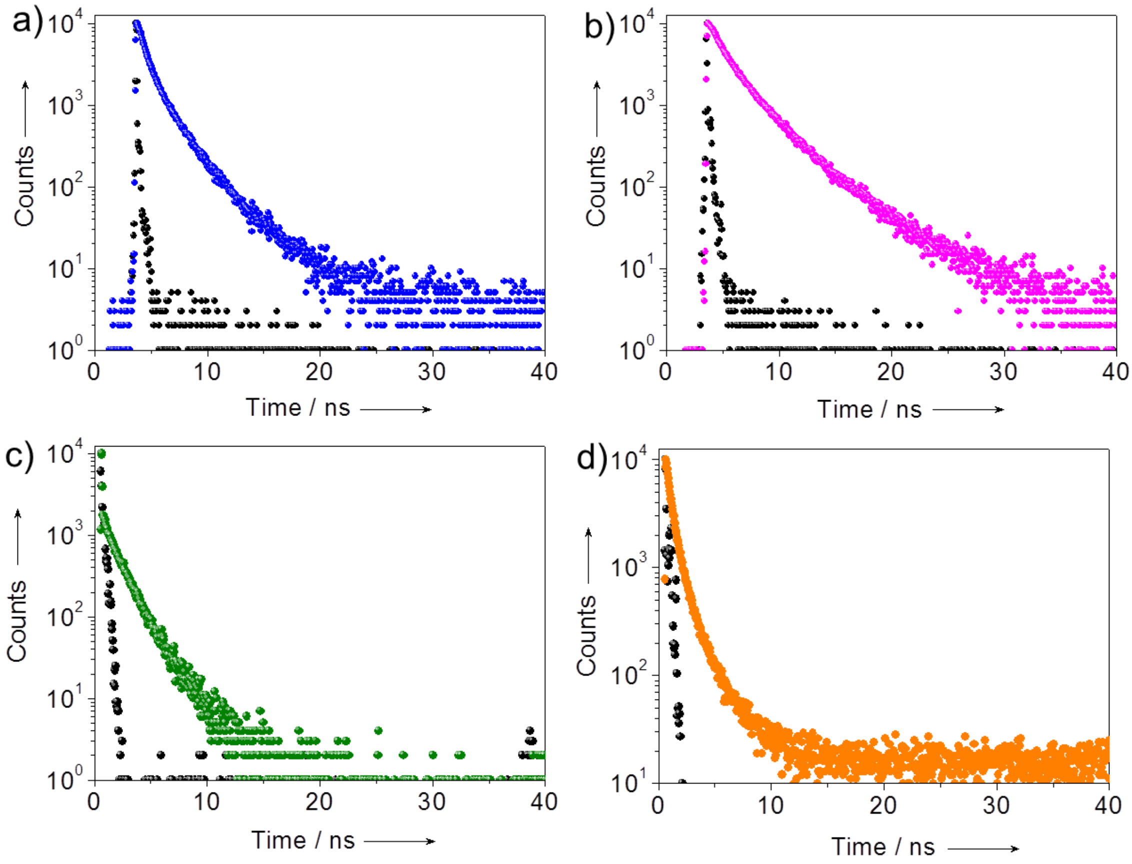

Figure 2.13. Lifetime decay profiles of **Bodipy-1** when the emission was monitored at 606 nm. a) Sheared *n*-decane film (blue) and b) DMSO xerogel (pink). Lifetime decay profiles of **Bodipy-1** c) sheared *n*-decane film (green) and d) DMSO xerogel (orange) (emission monitored at 740 nm). In all cases black profile corresponds to prompt. λ_{ex} = 375 nm.

Table 2.2. Fluorescence lifetime data of **Bodipy-1** sheared *n*-decane film and DMSO xerogel (λ_{ex} = 375 nm).

Bodipy-1	Sheared *n*-Decane Film	DMSO Xerogel
λ_{em} = **606 nm**	0.70 (39.26%), 2.13 (52.12%) and 6.1 ns (8.62%)	0.80 (20.3%), 2.48 (58.92%) and 5.70 ns (20.78%)
λ_{em} = **740 nm**	0.31 (45.37%), 1.43 (34.93%) and 2.16 ns (19.7%).	0.39 (48.6%), 1.0 (41.2%) and 2.74 ns (10.2%)

2.3.3. Morphological Studies

Before going into the details of the exact molecular packing of **Bodipy-1** self-assembly, we attempted to understand the morphological features. Fluorescent microscopic images of the assembly in *n*-decane revealed the formation of greenish-yellow emitting rods of micrometer length (**Figure 2.14a**). On the other hand the DMSO xerogel showed micrometer sized spherical particles with orange red emission (**Figure 2.14b**). Upon applying a stress on DMSO xerogel the fluorescence color is slightly changed to red as shown in **Figure 2.14c**. The fluorescence change observed in the case of decane film upon shearing is from greenish-yellow to orange red as shown in **Figure 2.14d**.

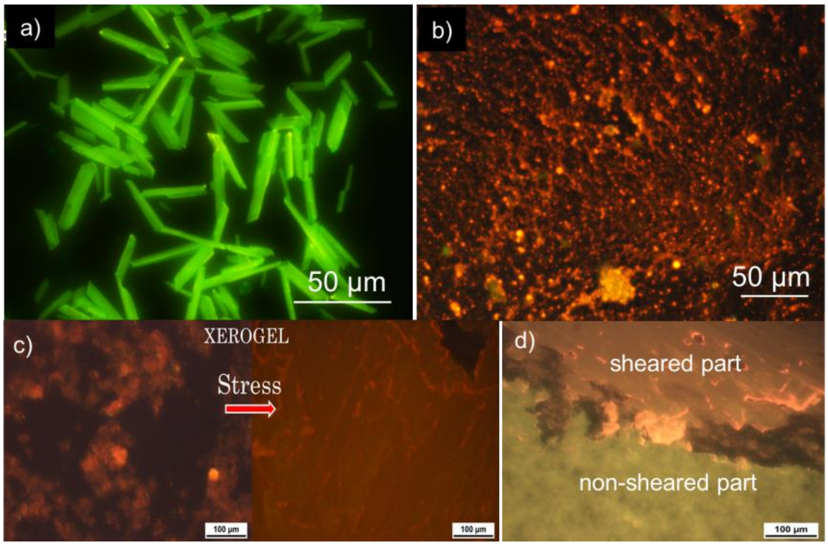

Figure 2.14. Fluorescent microscopic images of **Bodipy-1** aggregates in a) *n*-decane ($c = 1 \times 10^{-4}$ M) and b) DMSO gel ($c = 1 \times 10^{-2}$ M). Fluorescent microscopic images of the sheared and non-sheared parts of c) xerogel and d) decane film.

The scanning electron microscopy (SEM) images of the **Bodipy-1** self-assembly at different concentration are shown in **Figure 2.15**. At a higher concentration of 1×10^{-2} M in decane, dense microfibers of length 50-60 μm are formed. Formations of these microfibers are more clear in the case of the SEM image obtained at a lower concentration of 1 x 10^{-4} M (**Figure 2.15c**). Interestingly, micrometer sized spherical particles were observed under SEM for the DMSO xerogel (**Figure 2.15b**). This morphology is an exception to the usually found fibrous morphology of organogels.[14]

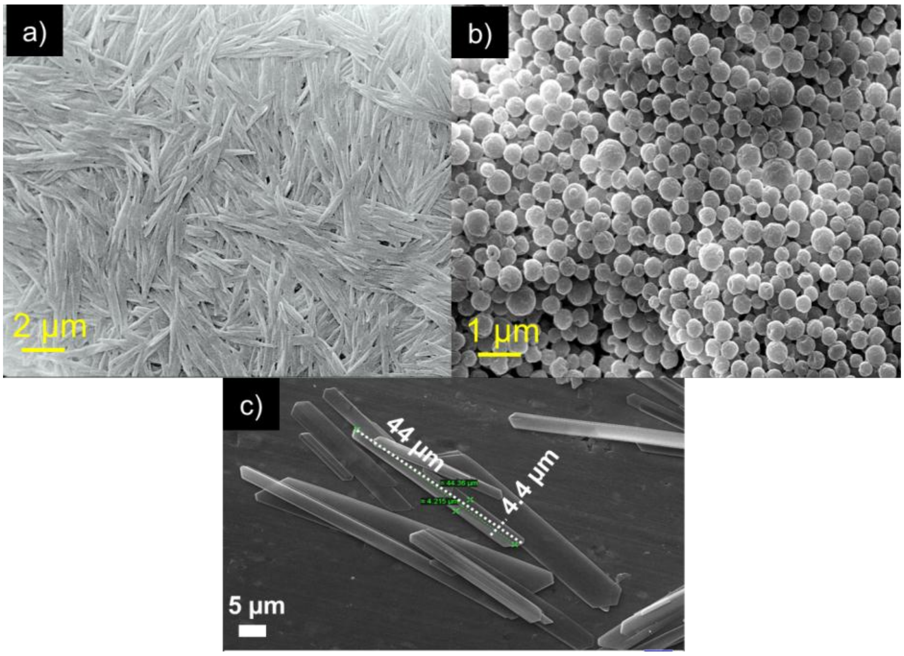

Figure 2.15. SEM images of a, c) decane aggregates of **Bodipy-1** at *c* = 1 x 10^{-2} and 1 x 10^{-4} M, respectively. b) SEM image of **Bodipy-1** DMSO gel, *c* = 1 x 10^{-2} M.

2.3.4. WAXS Analysis

For an in-depth understanding of the molecular interactions and packing of **Bodipy-1** in the *n*-decane film before and after shearing and also in the DMSO xerogel, WAXS experiments were performed. WAXS revealed the formation of a

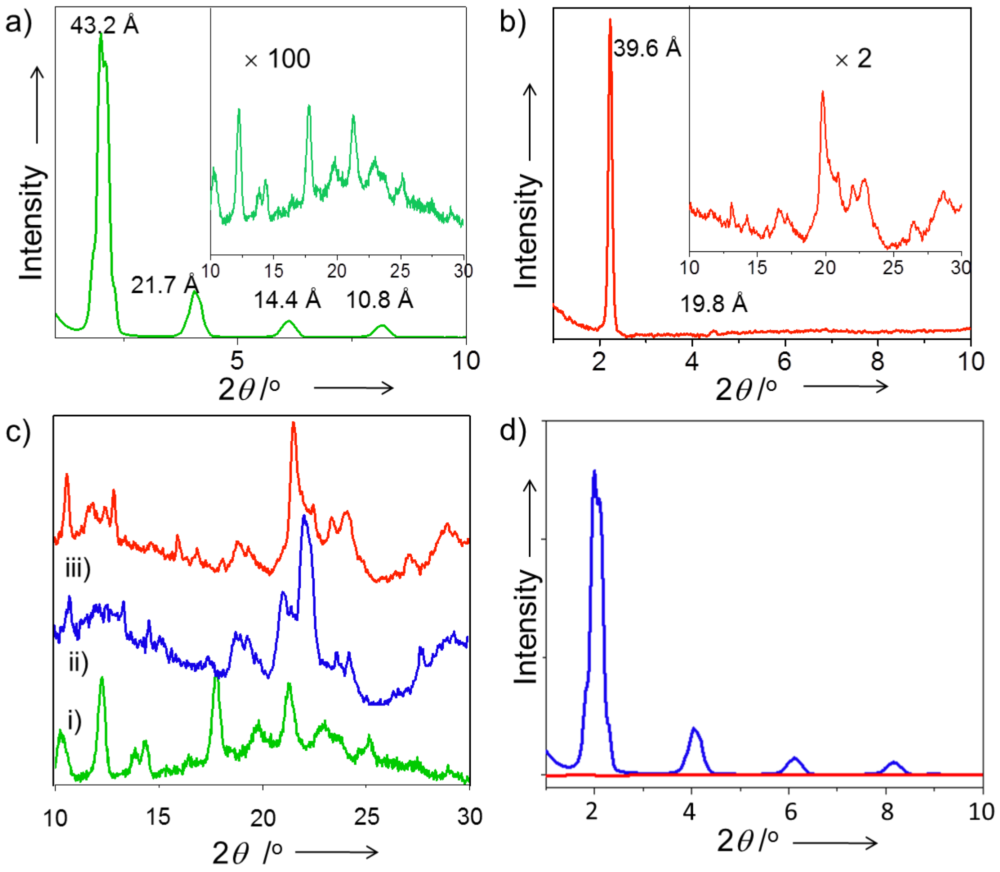

Figure 2.16. WAXS of **Bodipy-1** a) film processed from *n*-decane. b) Xerogel. c) Comparison of WAXS (2*θ* = 10-30°). d) WAXS of **Bodipy-1** film processed from *n*-decane (blue) and the same film after shearing (red).

sharp crystalline lamellar assembly in *n*-decane with *d*-spacing of 43.2 Å having reciprocal spacing ratio of 1:2:3:4 (**Figure 2.16a**).[18] In addition, several weak signals were seen in the range of 2*θ* angle of 10-30° indicating the lesser extent of π-stacking (**Figure 2.16a** inset). On the other hand, long range ordering was disturbed upon shearing, as revealed from the disappearance of the sharp peaks at the lower 2*θ* (**Figure 2.16d**). Also, the WAXS pattern of the sheared film indicates reorganization in the short range ordering with respect to the pristine film (**Figure 2.16c**). The DMSO xerogel exhibited a lamellar organization (**Figure 2.16b**) with sharp peak at 2*θ* = 2.25 (d-spacing = 39.6 Å).[18,43,44] A comparison of the diffraction peaks of the xerogel with the *n*-decane film before and after shearing at the wide-angle region of 10-30° is shown in **Figure 2.16c**. These data revealed considerable similarity in the molecular packing of the xerogel and the sheared *n*-decane film.

2.3.5. Single Crystal Analysis

In order to get more insight on the molecular organization in the assembly before and after shearing and also in the xerogel, we carried out the single crystal x-ray analysis of a model derivative of **Bodipy-1**. For this purpose, **Bodipy-2** was synthesized and single crystals were grown from chloroform/n-hexane solvent mixture by vapor diffusion method. Crystal system formed is triclinic with a space group P-1. The **Bodipy-2** crystals exhibited a red emission with an NIR band at 742 nm, which did not show any further change upon grinding, indicating a stable molecular packing (**Figure 2.17** and **2.18**). The emission profile of **Bodipy-2** single crystal (**Figure 2.17a**) was similar to that of the **Bodipy-1** xerogel (**Figure 2.11b**) except for the slight variation in the intensities of the peaks, indicating identical molecular packing in both cases. **Bodipy-2** (P1-space group) has a slipped-stack packing as evident from the crystal structure analysis (**Figure 2.17c** and **2.18**). Molecules form extended chains through distinct centric $C–H\cdots O_{(\text{-OMe})}$ and $C–H\cdots F_{(\text{Bodipy})}$ interactions. The layers stack to yield a centrosymmetric head-to-tail arrangement.

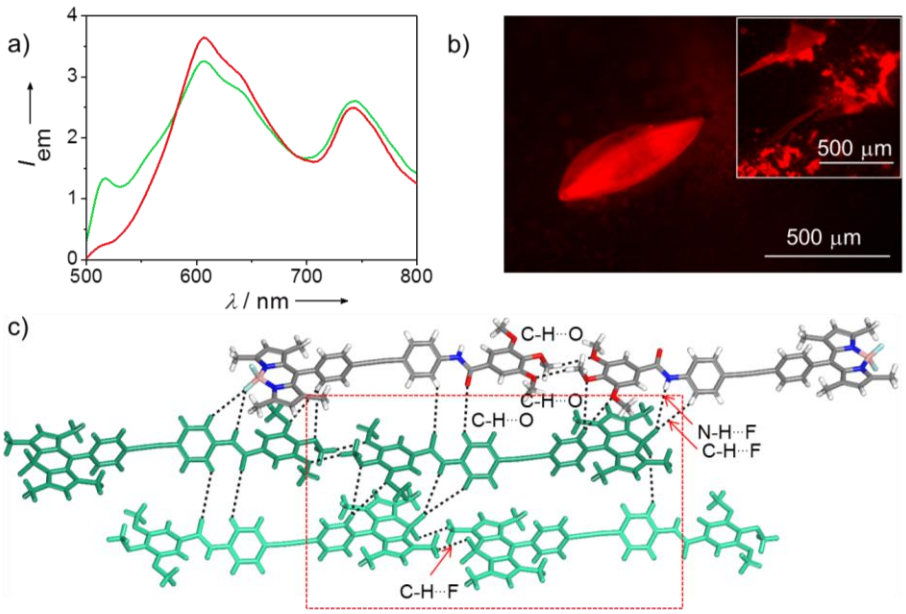

Figure 2.17. a) Emission spectra before (red) and after (green) shearing, b) fluorescent microscopic image and c) crystal packing with different interactions of **Bodipy-2** single crystal. Inset (of b) shows the emission of the sheared crystal.

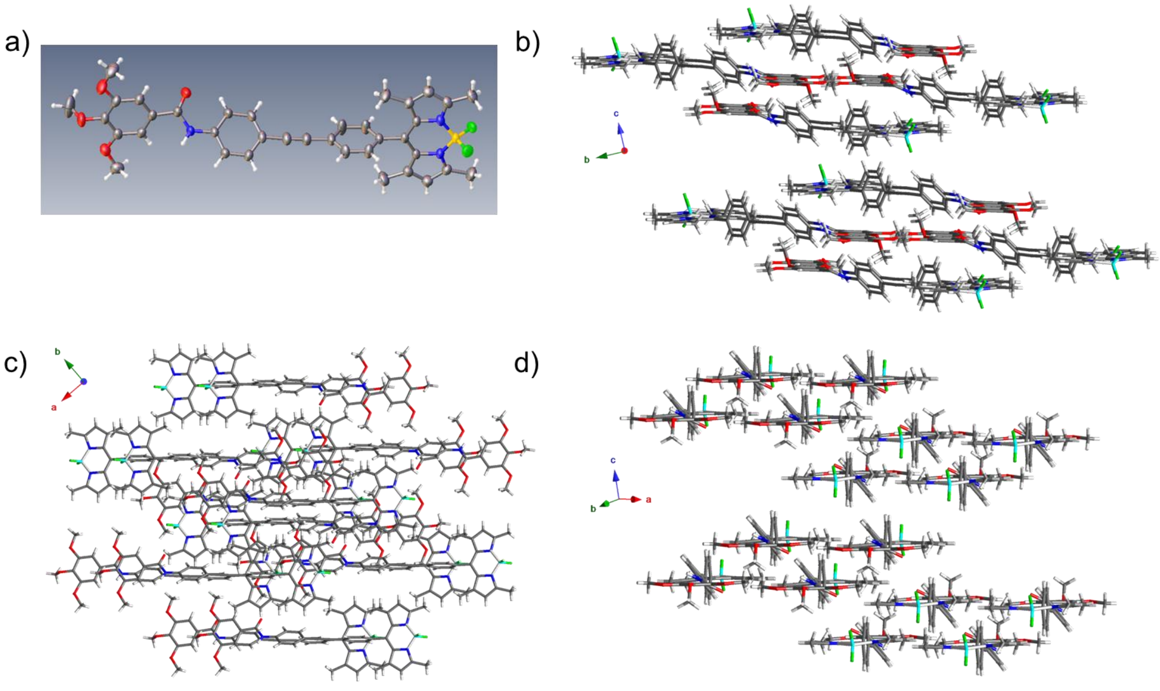

Figure 2.18. Bodipy-2 single crystal a) structure and b-d) packing viewed from different axes.

In a typical head-to-tail arrangement, the observed N–H···F bonds[45] are augmented by a range of weak interactions such as C–H···O, C–H···F and C–H···π.

Further, the terminal Bodipy moieties of a unique dimer make π-π interactions with the 3,4,5-trisalkoxy benzamide of the two adjacent dimers. An average stacking distance of 3.64 Å qualifies for an optimized stacking interaction.

2.3.6. Hirshfeld Surface and 2D-Fingerprint Analyses

The interactions are quantified by Hirshfeld surface and two dimensional fingerprint analyses of the crystal structure.[46-47] The definition of the Hirshfeld surface has been described by Spackman *et al*.[46] For every point on the surface, the distances to the nearest atoms outside (intermolecular), d_e, and inside (intramolecular), d_i, are estimated and used for color coded mapping of the surface. The deep red spots indicate closest contacts with neighboring molecules; the deep blue color means very little or no interaction with the surrounding

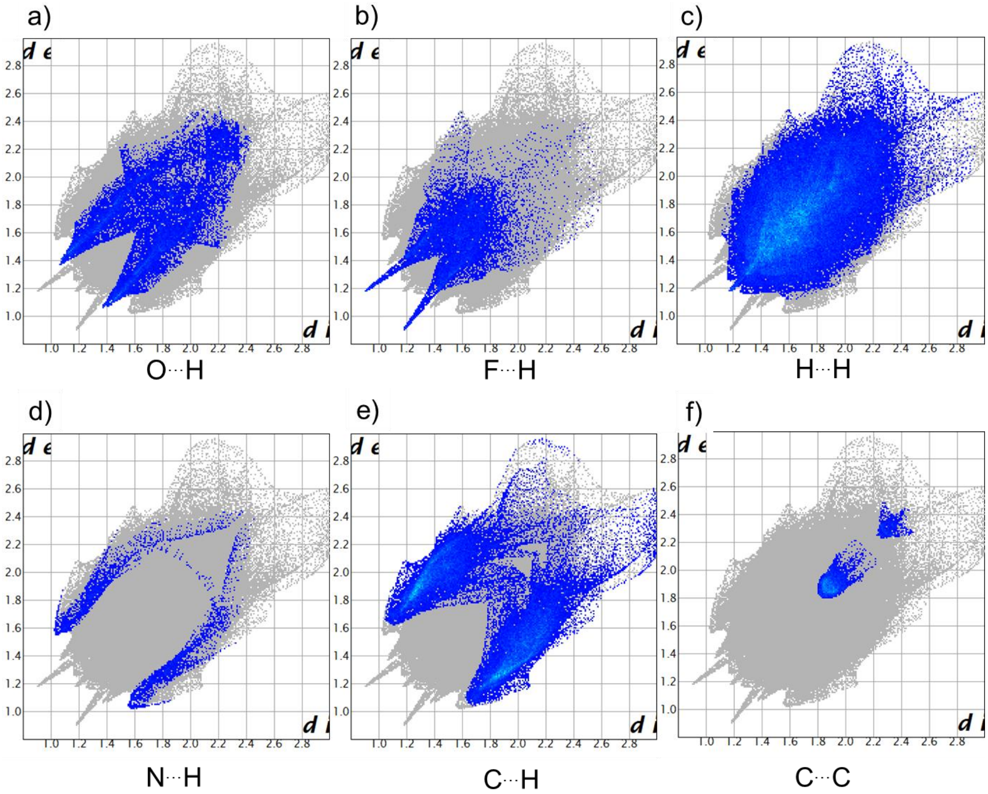

Figure 2.19. Hirshfeld 2D-fingerprint plots depicting various interactions in the **Bodipy-2** crystal.[47] Sharp spikes for F···H, O···H and pair of wings observed for C···H and N···H interactions.

molecules. In the absence of any classic hydrogen bonds, the structure is dominated by a wide variety of weak interactions such as C–H···π (23.4%), C–H···O (11.1%), N–H···F (7.9%) and other noncovalent interactions (**Figure 2.19** and **2.20**).

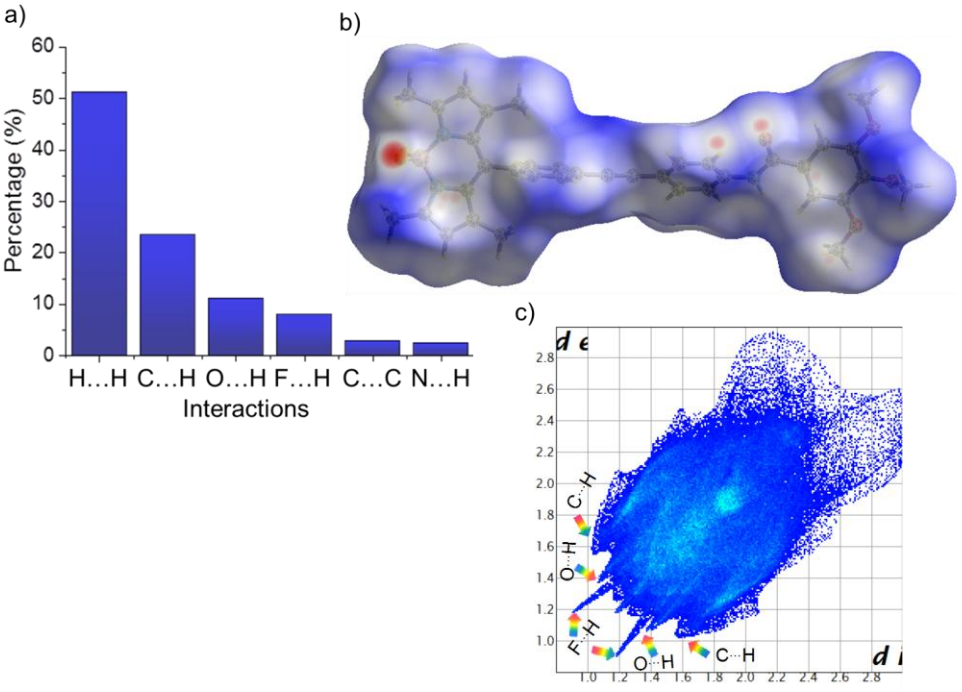

Figure 2.20. a) Histogram representing various intermolecular interactions in **Bodipy-2**. b) Hirshfeld surface (d_{norm}) analysis of **Bodipy-2.** c) Hirshfeld 2D-fingerprint plot showing prominent interactions.[47]

In order to confirm that the molecular packing in the sheared *n*-decane film as well as DMSO xerogel of **Bodipy-1** is comparable to that of the single crystal of **Bodipy-2**, the WAXS pattern of the former is compared with the simulated powder X-ray diffraction peaks of the latter (**Figure 2.21**). These data indicate more or less identical structural organization in both cases.

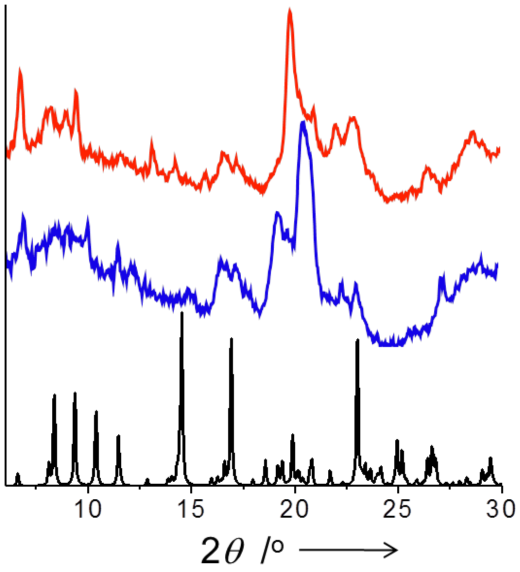

Figure 2.21. Simulated WAXS pattern corresponding to **Bodipy-2** (black), the measured WAXS pattern of **Bodipy-1** *n*-decane sheared film (blue) and DMSO xerogel (red).

2.3.7. FT-IR Spectral Studies

FT-IR (ATR) spectral data of **Bodipy-1** (**Figure 2.22b**) indicates the presence of intermolecular H-bonds either with the carbonyl oxygen (C=O) or with the fluorine attached to the boron (B-F).[45] FT-IR spectrum of the *n*-decane film before shearing revealed H-bonded N-H stretching frequency at 3320 (major) and 3421 cm^{-1} (**Figure 2.22a**), indicating 1D supramolecular polymer formation through the amide H-bonding. Shearing resulted in the rupture of the amide H-bonding which is clear from the appearance of 3421 cm^{-1} band. To have a deeper insight, we monitored the carbonyl stretching vibrations around 1650 cm^{-1} (Amide I) and N-H bending vibrations around 1530 cm^{-1} (Amide II).

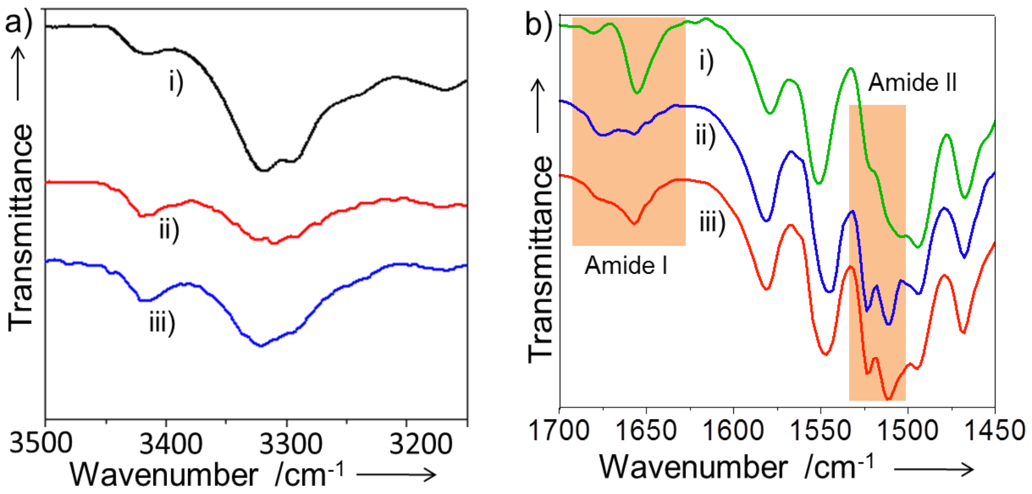

Figure 2.22. a, b) FT-IR (ATR) spectra of **Bodipy-1,** i) *n*-decane film ii) *n*-decane film after shearing and iii) DMSO xerogel.

The sharp amide I band at 1656 cm^{-1} gets broadened with an equally intense band at 1676 cm^{-1} upon shearing (**Figure 2.22b**). This result indicates that shearing leads to the partial breakage of the H-bond between N-H and C=O groups. Consequently, the N-H moiety must be H-bonded with the B-F moiety upon shearing, which is supported by the presence of a sharp band at 1523 cm^{-1}. The FT-IR spectrum of the DMSO xerogel resembles very much to that of the sheared *n*-decane film (**Figure 2.22b**).

2.3.8. Thermal Analysis of Bodipy-1

The thermal property of the solid **Bodipy-1** was studied by differential scanning calorimetry (DSC). Detectable phase transitions were observed for the sheared and non-sheared film processed from *n*-decane below the melting transition temperature of 156 °C (**Figure 2.23**). The DSC trace of the first heating of the pristine *n*-decane film has shown an endothermic transition at 77 °C indicating the crystalline nature of the green state. Shearing results in an initial amorphous phase formation as indicated by the exothermic transition at the same transition temperature.

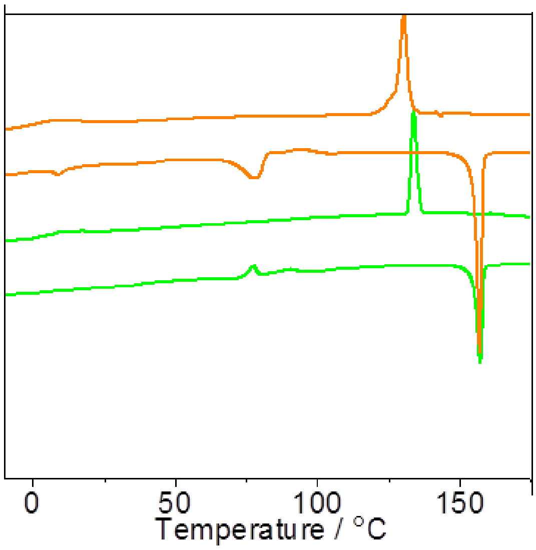

Figure 2.23. DSC of the sheared (green) and non-sheared (orange) *n*-decane film.

2.3.9. Proposed Molecular Packing

Based on the already discussed experimental data, it is reasonable to propose an extended molecular organization in the *n*-decane film, which upon shearing changes into a more organized assembly as shown in **Figure 2.24**. Initially, the decane film of **Bodipy-1** forms a 1D supramolecular assembly driven by N-H···O=C H-bonding, which is a less organized state as a result of weak intermolecular interactions such as π–π stacking (as evident from XRD) and Bodipy-Bodipy interactions. In the adjacent dimers, Bodipy units are far apart which restricts its interaction. Upon shearing, due to the partial breaking of N-H···O=C hydrogen bonding, a reorganization of the adjacent dimers takes place. The reorganization of the molecular assembly is driven by N-H···F-B hydrogen bonding between adjacent molecules on the top and bottom layer, together with

C-H···O interactions between Bodipy ring and O-alkyl groups. Also, after shearing the decane film, more Bodipy-Bodipy interaction is expected in the same parallel layer through favorable C-H···F interaction as observed in **Bodipy-2** crystal structure. Multiple noncovalent interactions in such chromophoric assemblies will generate aggregates of varying excited state energy levels which are responsible for the low energy emission ranging from red to NIR region. Thus, the crystal structure, WAXS, FT-IR and the available photophysical data suggest that the NIR emission originates from the extended ground state slipped dimer formation between Bodipy.[37-42]

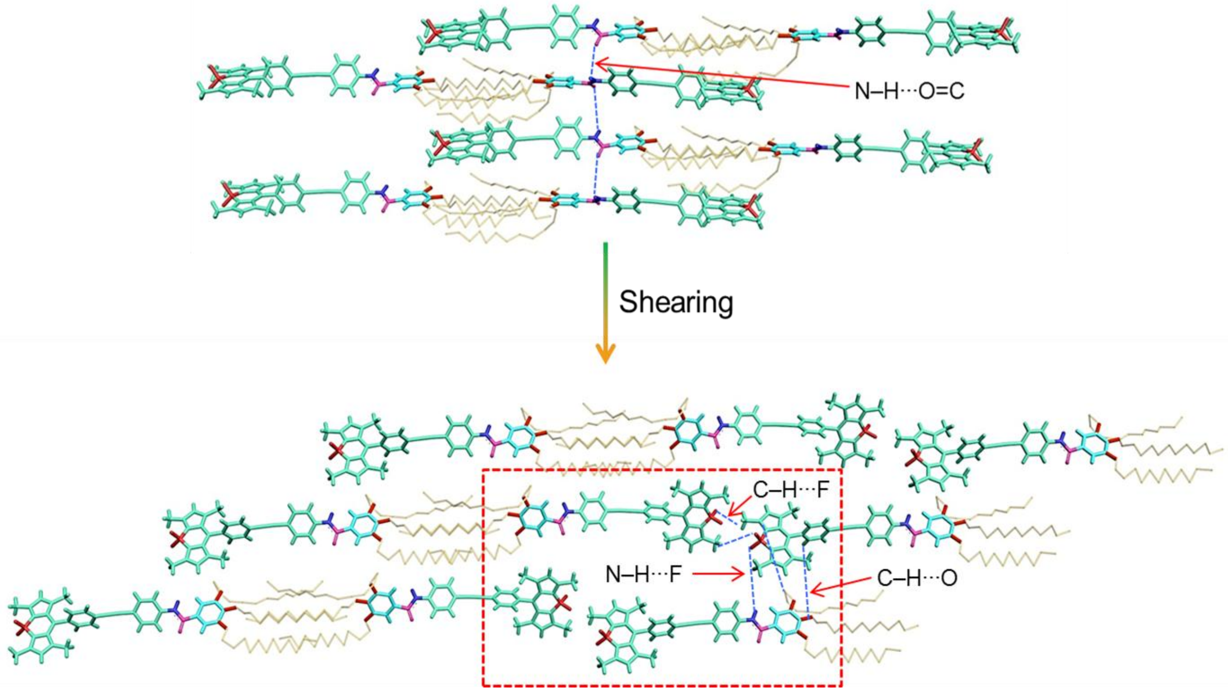

Figure 2.24. Schematic representation showing the plausible molecular organization of **Bodipy-1** before and after shearing of the film processed from *n*-decane.

2.4. Conclusion

In conclusion, presented herein is a unique and novel method to generate NIR emission in an organic chromophore. Even though mechanical stress and gelation have been previously shown to modulate the emission of organic chromophores, this is the first demonstration of stimuli induced amplified generation of NIR emission. Moreover, **Bodipy-1** is the first π-gelator, which exhibits NIR emission through a gelation pathway. The *meso*-π-extended molecular structure of **Bodipy-1**, the weak π-stacking between chromophores and the labile supramolecular amide linkage facilitate mechanical stress induced formation of weak N–H···F–B bonds, resulting in a head-to-tail extended slipped molecular packing which may allow strong electronic coupling between the chromophores. This method allows an alternate strategy to NIR emitting Bodipy derivatives for specific applications and hence has great opportunity for further investigation.

2.5. Experimental Section

2.5.1. Synthesis – General Procedures

Unless otherwise stated, all starting materials and reagents were purchased from commercial suppliers and used without further purification. The solvents used for the reactions were purified and dried by using the standard laboratory methods. The reactions were monitored using thin layer chromatography on silica gel 60 F254 (0.2 mm; Merck) or Al_2O_3 (0.2 mm; Merck) and visualization was accomplished using a hand held UV-lamp (365 nm). Column chromatography was used to purify the reaction products in a glass column packed with silica gel of size, 100-200 microns.

2.5.1.1. Syntheses of Bodipy-1 and Bodipy-2

Compound **14** (0.21 g, 0.47 mmol), bis(triphenylphosphine)palladium (II) dichloride (33 mg, 10 mol%), and copper (I) iodide (9 mg, 10 mol%) were added to an oven-dried two-neck round bottom flask equipped with a magnetic stirring bar. The round bottom flask was then sealed with a rubber septum, evacuated and backfilled with argon three times. Degassed triethylamine (30 mL) was added followed by degassed THF (50 mL). After stirring for 5 minutes at room temperature, compound **11** (0.43 g, 0.56 mmol) dissolved in 10 mL (1:1) mixture of degassed triethylamine and THF was added followed by stirring at 60 °C for 24 h. The reaction mixture was extracted using chloroform and washed with dilute hydrochloric acid. The organic layer was washed with brine and dried over anhydrous sodium sulphate and then evaporated under reduced pressure. The crude product was then purified by column chromatography using silica gel as adsorbent. The pure compound (**Bodipy-1**) was eluted with 40% dichloromethane-*n*-hexane solvent mixture (Mp, 156 °C). Yield: 30%, FT-IR (KBr): ν_{max} = 3420, 3325, 3293, 2924, 2852, 2211, 1909, 1657, 1583, 1550, 1522, 1509, 1495, 1468, 1427, 1403, 1390, 1373, 1362, 1334, 1309, 1260, 1237, 1194, 1155, 1117, 1089, 1049, 1020, 984, 899, 871, 832, 816, 764, 719, 707 cm^{-1}; ^1H NMR (500 MHz, $CDCl_3$): δ = 7.79 (*s*, 1H; -N*H*), 7.67 (*d*, *J* = 8 Hz, 4H; Phenyl-*H*), 7.57 (*d*, *J* = 8 Hz, 2H; Phenyl-*H*), 7.3 (*d*, *J* = 8 Hz, 2H; Phenyl-*H*), 7.05 (*s*, 2H; Phenyl-*H*), 6.0 (*s*, 2H; =C*H*-), 4.05-4.01 (*m*, 6H; $-OCH_2-$), 2.56 (*s*, 6H; pyrrole-CH_3), 1.84-1.76 (*m*, 6H; $-CH_2-$), 1.50-1.47 (*m*, 6H; $-CH_2-$), 1.44 (*s*, 6H; pyrrole-CH_3), 1.36-1.27 (*m*, 48H; $-CH_2-$) 0.88 (*t*, *J* = 6.5 Hz, 9H; $-CH_3$) ppm; ^{13}C NMR (125 MHz, $CDCl_3$): δ = 165.62, 155.75, 153.31, 143.04, 141.77, 140.86, 138.37, 134.85, 133.59, 132.56, 132.25, 131.23, 129.57, 128.23, 124.19, 121.37, 119.80, 118.51, 105.86, 100.00, 90.59, 88.45, 73.61, 69.52, 31.93, 30.33, 29.74, 29.71, 29.67, 29.65, 29.59, 29.41, 29.37, 26.08, 22.70, 14.61, 14.12 ppm. HRMS (ESI): m/z calculated for $C_{70}H_{100}BF_2N_3O_4$ $[M+H]^+$: 1096.78544, found: 1096.78459.

Compound **14** (0.175 g, 0.39 mmol), bis(triphenylphosphine)palladium (II) dichloride (27 mg, 10 mol%), and copper (I) iodide (7.4 mg, 10 mol%) were added to an oven-dried two-neck round bottom flask equipped with a magnetic stirring bar. The round bottom flask was then sealed with a rubber septum, evacuated and backfilled with argon three times. Degassed triethylamine (30 mL) was added followed by degassed THF (50 mL). After stirring for 5 minutes at room temperature, compound **15** (0.145 g, 0.47 mmol) dissolved in 10 mL (1:1) mixture of degassed triethylamine and THF was added and the reaction mixture was stirred at 60 °C for 24 h. The reaction mixture was extracted using chloroform and washed with dilute hydrochloric acid. The organic layer was washed with brine and dried over anhydrous sodium sulphate and then evaporated under reduced pressure. The crude product was then purified by column chromatography using silica gel as adsorbent. The pure compound (**Bodipy-2**) was eluted with 50% dichloromethane-*n*-hexane solvent mixture (Mp, 266 °C). Yield: 40%, FT-IR (KBr): ν_{max} = 3387, 3000, 2955, 2924, 2853, 2213, 1738, 1676, 1585, 1545, 1514, 1499, 1468, 1412, 1406, 1368,1335, 1308, 1288, 1261, 1240, 1196, 1160, 1128, 1084, 1055, 1001, 986, 972, 870, 851, 837, 831, 816, 766, 737, 704 cm^{-1}; ^1H NMR (500 MHz, $CDCl_3$): δ = 7.81 (*s*, 1H; -N*H*), 7.68 (*d*, *J* = 8 Hz, 4H; Phenyl-*H*), 7.58 (*d*, *J* = 8 Hz, 2H; Phenyl-*H*), 7.3 (*d*, *J* = 8 Hz, 2H; Phenyl-*H*), 7.09 (*s*, 2H, Phenyl-*H*), 6.0 (*s*, 2H; =C*H*-), 3.94 (*s*, 9H; $-OCH_3$), 2.56

(*s*, 6H; pyrrole-CH_3), 1.44 (*s*, 6H; pyrrole-CH_3) ppm; ^{13}C NMR (125 MHz, $CDCl_3$): δ = 165.56, 155.94, 153.64, 143.69, 141.97, 140.93, 138.40, 135.48, 135.11, 132.75, 132.41, 130.26, 128.42, 124.34, 121.53, 120.04, 118.94, 118.25, 104.81, 100.16, 92.82, 91.01, 88.70, 86.93, 61.14, 56.65, 29.51, 14.74, ppm. HRMS (ESI): m/z calculated for $C_{37}H_{34}BF_2N_3O_4$ $[M+Na]^+$: 656.25081, found: 656.25214.

2.5.1.2. Synthesis of Methyl 3,4,5- tris(dodecyloxy)benzoate (7)

Methyl 3,4,5- trihydroxy benzoate **6** (3 g, 16.3 mmol) and potassium carbonate (11.24 g, 81.5 mmol) were stirred in a 250 mL round bottom flask containing 60 mL dry DMF. The reaction mixture was stirred for 20 minutes under room temperature and 1-bromododecane (13.6 mL, 57 mmol) was added dropwise. It was then heated to 90 °C for 24 h. After cooling to room temperature, the reaction mixture was poured into water and extracted the organic part with chloroform repeatedly. Washed the organic layer with enough water and brine solution and dried over anhydrous sodium sulphate. Removed the solvent under reduced pressure and then subjected to purification by column chromatography (silica gel, 1% ethylacetate/*n*-hexane) to afford compound (**5**) as a white solid (Mp, 50 °C). Yield: 78%, ^{1}H NMR (500 MHz, $CDCl_3$): δ = 7.25 (*s*, 2H, Ar-*H*), 4.03-4.00 (*m*, 6H; -OCH_2-), 3.89 (*s*, 3H; -OCH_3-), 1.84-1.71(*m*, 20H; -CH_2-), 1.49-1.26 (*m*, 40H; -CH_2-), 0.89-0.88 (*m*, 9H; -CH_3) ppm. MALDI TOF-MS (matrix: α-cyano-4-hydroxycinnamic acid): calculated for $C_{44}H_{80}O_5$ $[M]^+$: *m/z* = 688.6, found: 689.6.

2.5.1.3. Synthesis of 3,4,5-tris(dodecyloxy)benzoic acid (8)

Compound **7** (5 g, 7.26 mmol) was refluxed in ethanol (60 mL) with KOH (2 g, 36.3 mmol) in a 250 mL round bottom flask for 12 h. The reaction mixture was cooled to normal temperature, acidified with dilute HCl, again cooled in ice-cold water and the precipitate was filtered. The obtained solid was washed with water and dried under vacuum to get the pure product **8** (Mp, 65 °C). Yield: 80%, ^{1}H NMR (500 MHz, $CDCl_3$): δ = 7.25 (*s*, 2H; Ar-*H*), 4.08-4.03 (*m*, 6H; -OCH_2-), 1.84-1.71 (*m*, 20H; -CH_2-), 1.49-1.26 (*m*, 40H; -CH_2-), 0.89-0.88 (*m*, 9H; -CH_3) ppm. MALDI TOF-MS (matrix: α-cyano-4-hydroxycinnamic acid): calculated for $C_{43}H_{78}O_5$ $[M]^+$: *m/z* = 675.6, found: 674.6.

2.5.1.4. Synthesis of 3,4,5-tris(dodecyloxy)-*N*-(4-iodophenyl) benzamide (9)

The acid **8** (3 g, 4.4 mmol) was dissolved in dry dichloroethane (20 mL) and taken in a 250 mL round bottom flask under argon atmosphere. Thionyl chloride (1 mL, 13. 3 mmol) was added dropwise to the reaction chamber and continued stirring for 5 h. Excess solvent and thionyl chloride were purged out by argon gas and dried completely in vacuum. It was then re-dissolved in 20 mL dry toluene and added to another reaction chamber containing 4-iodoaniline (1.17 g, 5.3 mmol) dissolved in toluene (20 mL) and 2 mL of dry triethyl amine. Stirring was continued for another 12 h under argon atmosphere. After completion of the reaction, the solvent was evaporated and the residue was extracted using chloroform. The organic layer was washed with water and brine solution and dried over anhydrous sodium sulphate. The crude product was purified on a silica column by eluting the compound with 1% ethylacetate/*n*-hexane solvent system to get the pure product **9** as a white powder (Mp, 106 °C). Yield: 50%, ^{1}H NMR (500 MHz, $CDCl_3$): δ = 7.71 (*s*, 1H; -*NH*-), 7.68 (*d*, *J* = 7Hz, 2H, Phenyl-*H*), 7.43 (*d*, *J* = 9Hz, 2H; Phenyl-*H*), 7.03 (*s*, 2H; Ar-*H*), 4.05-4.01 (*m*, 6H; OCH_2-) 1.84-1.71(*m*, 20H; -CH_2-), 1.49-1.26 (*m*, 40H; -CH_2-), 0.89-0.88 (*m*, 9H; -CH_3) ppm. MALDI TOF-MS (matrix: α-cyano-4-hydroxycinnamic acid): calculated for $C_{49}H_{82}INO_4$ $[M]^+$: *m/z* = 875.53, found: 876.53.

2.5.1.5. Synthesis of 3,4,5-tris(dodecyloxy)-*N*-(4-((trimethyl silyl)ethynyl)phenyl)benzamide (10)

Compound **9** (2.6 g, 3.0 mmol), bis(triphenylphosphine)palladium (II) dichloride (208 mg, 10 mol%), and copper (I) iodide (56 mg, 10 mol%) were added to an oven-dried two-neck round bottom flask equipped with a magnetic stirring bar. The round bottom flask was then sealed with a rubber septum, evacuated and backfilled with argon three times. Degassed triethylamine (10 mL) was added followed by degassed THF (20 mL). After stirring for 5 minutes at room temperature, trimethylsilyl acetylene (0.65 mL, 4.45 mmol) was added dropwise into the reaction mixture and continued stirring for 12 h. The reaction mixture was extracted using chloroform and washed with dilute hydrochloric acid. The organic layer was washed with brine and dried over anhydrous sodium sulphate and then evaporated under reduced pressure. The residue thus obtained was purified by silica gel column chromatography using 2% ethylacetate/*n*-hexane as an eluent (Mp, 101 °C). Yield: 80%, ^{1}H NMR (300 MHz, $CDCl_3$): δ = 7.79 (*s*, 1H; -N*H*), 7.59 (*d*, *J* = 9 Hz, 2H; Phenyl-*H*), 7.47 (*d*, *J* = 8.7 Hz, 2H; Phenyl-*H*), 7.02 (*s*, 2H, Phenyl-*H*), 4.01 (*t*, *J* = 6 Hz, 6H; -OCH_2-), 1.84-1.75 (*m*, 6H; -CH_2-), 1.5-1.26 (*m*, 54H; -CH_2-), 0.88 (*t*, *J* = 6 Hz, 9H; -CH_3), 0.05 (*s*, 9H; -SiMe_3) ppm. MALDI-TOF-MS (matrix: α-cyano-4-hydroxycinnamic acid): m/z calculated for $C_{54}H_{91}NO_4Si$ $[M+H]^+$: 846.72, found: 847.0.

2.5.1.6. Synthesis of 3,4,5-tris(dodecyloxy)-*N*-(4-ethynyl phenyl)benzamide (11)

To a solution of **10** (1.9 g, 2.25 mmol) in 10 mL dichloromethane, KF (2.6 g, 44.9 mmol) in 50 mL methanol was added and allowed to stir at room temperature for 12 h. After completion of the reaction, the content was extracted using chloroform, washed with water, brine and then dried over anhydrous sodium sulphate. Solvent was evaporated under reduced pressure. The residue thus obtained was purified by silica gel column chromatography using 5% ethylacetate/*n*-hexane as an eluent to afford the compound **9** as a white solid (Mp, 70 °C). Yield: 76%, ^{1}H NMR (300 MHz, $CDCl_3$): δ = 7.79 (*s*, ^{1}H; -N*H*), 7.61 (*d*, *J* = 8.5 Hz, 2H; Phenyl-*H*), 7.50 (*d*, J = 8.4 Hz, 2H; Phenyl-*H*), 7.02 (*s*, 2H; Phenyl-*H*), 4.02 (*t*, *J* = 6 Hz, 6H; -OCH_2-), 3.07 (*s*, 1H; Acetylenic-*H*), 1.84-1.75 (*m*, 6H; -CH_2-), 1.5-1.26 (*m*, 54H; -CH_2-), 0.87 (*t*, *J* = 6 Hz, 9H; -CH_3) ppm. MALDI-TOF-MS (matrix: α-cyano-4-hydroxycinnamic acid): m/z calculated for $C_{51}H_{83}NO_4$ $[M+H]^+$: 774.61, found: 774.6.

2.5.1.7. Synthesis of (4-iodophenyl)-1,3,5,7- tetramethyl-4,4-difluoro-4-bora-3a,4a-diaza-*s*-indacene (14)

4-Iodo benzoyl chloride (**13**) (0.45 g, 1.69 mmol) and 2,4 dimethyl pyrrole (**12**) (0.38 mL, 3.71 mmol) were taken in an oven-dried two-neck round bottom flask equipped with magnetic stirrer. Dry dichloroethane (40 mL) was added and refluxed for 3 h. The reaction mixture was cooled back to room temperature, added triethylamine (3.53 mL, 25.4 mmol), $BF_3.OEt_2$ (3.7 mL, 33.8 mmol) and again refluxed for 30 minutes. The reaction mixture was cooled, washed with water, extracted the organic part in chloroform, dried over anhydrous sodium sulphate and purified the compound by silica column chromatography. The pure compound was eluted in 15% dichloromethane/*n*-hexane solvent system (Mp, 110 °C). Yield: 76%, ^{1}H NMR (300 MHz, $CDCl_3$): δ = 7.86 (*d*, 2H, *J* = 8 Hz; Phenyl-*H*), 7.06 (*d*, 2H, *J* = 8 Hz; Phenyl-*H*), 6.00 (*s*, 2H; =C*H*), 2.56 (*s*, 6H; -CH_3), 1.430 (*s*, 6H; -CH_3) ppm. HRMS (FAB): calculated for $C_{19}H_{18}BF_2IN_2$ $[M]^+$: *m/z* = 450.06, found: 451.15. ^{13}C NMR (125 MHz, $CDCl_3$): δ = 155.88, 142.92, 140.07, 138.36, 134.54, 131.13, 129.95, 121.46, 94.76, 14.66 ppm.

2.5.2. Characterization Techniques

NMR spectra were measured on a 300 or 500 MHz Bruker Avance DPX spectrometer. Chemical shifts are reported in parts per million (ppm) using tetramethylsilane (TMS) (δ H = 0 ppm) as an internal reference. The resonance multiplicity is described as *s* (singlet), *d* (doublet), *t* (triplet) and *m* (multiplet). FT-IR spectra were recorded on a Shimadzu IR Prestige-21 Fourier Transform Infrared Spectrophotometer (FT-IR) using KBr pellet method. Electrospray ionization (ESI) high-resolution mass spectra were recorded on using Thermo Scientific Exactive mass spectrometer. Matrix-assisted laser desorption ionization time-of-flight (MALDI-TOF) mass spectra were obtained on a Shimadzu

AXIMA-CFR PLUS spectrometer using α-cyano-4-hydroxycinnamic acid as the matrix.

2.5.3. Measurements

The electronic absorption spectra were recorded on a Shimadzu spectrophotometer UV-2100. The fluorescence spectra were recorded on a SPEX-Fluorolog-3 FL3-221 spectrofluorimeter. Solid-state emission spectra were recorded using a front face sample holder. Optical studies in solution-state were carried out in a 1 cm quartz cuvette. Relative quantum yield measurements were carried out at two different excitation wavelengths (315 and 475 nm) for the monomeric state using fluorescein in 0.1 N NaOH as the standard which has a reported quantum yield of $\Phi_f = 0.91$. Absolute fluorescence quantum yields in the film state were measured by using a calibrated integrating sphere attached to SPEX Fluorolog spectrofluorimeter and the quantum yield value was estimated based on the de Mello method.

Lifetime measurements were carried out using IBH (model 5000 DPS) time-correlated single photon counting (TCSPC) system. Experiments were carried out with 375 nm LED excitation source (pulse width < 100 ps, repetition rate 1 MHz). Film state FT-IR spectra were recorded on a Shimadzu IR Prestige-21 FT-IR spectrophotometer using attenuated total reflection (ATR)-8200HA accessory. SEM images were taken on a Zeiss EVO 18 cryo SEM Special Edn with variable pressure detector working at 20-30 kV after sputtering with gold. Samples were prepared by drop casting the aggregates of **Bodipy-1** in *n*-decane and DMSO gel over a smooth aluminium foil. The drop cast samples were allowed to dry under normal condition for one day and subsequently dried under vacuum for 12 h. Fluorescence microscopy images were taken by using Leica DFC 290 microscope. The WAXS analysis was carried out using XEUSS SAXS/WAXS system by Xenocs operated at 50 kV and 0.6 mA. The data were collected in the transmission mode geometry using Cu-K_α radiation of wavelength 1.54 Å. DSC measurements were carried out using PerkinElmer Pyris 6 DSC where sample is heated to 175 °C at a heating and cooling rate of 5 °C min^{-1}.

2.5.3.1. Crystal Data of Bodipy-2

The single crystal analysis of **Bodipy-2** was carried out on a Bruker SMART APEX CCD diffractometer with graphite-monochromatized Mo-*K*, λ = 0.71073 Å radiation. The data can be obtained free of charge from the Cambridge Crystallographic Data Centre www.ccdc.cam.ac.uk/data_request/cif for the **CCDC 1523313.** $C_{37}H_{34}BF_2N_3O_4$, M = 633.48, yellowish orange crystals with crystal size 0.25 x 0.15 x 0.10 mm, triclinic, space group P-1, a = 11.1514(3), b = 11.5496(3), c = 14.0875(4) Å ; α = 75.2910(10), β = 76.2440(10), γ = 74.6950(10)°. Volume, V = 1664.09(8) Å^3, Z = 2, T = 296(2) K, Reflections collected / unique 31516 / 6535 [R(int) = 0.0242], θ range for data collection 1.52 to 26.00°, Absorption correction Semi-empirical from equivalents, Max. and min. transmission 0.9911 and 0.9780, Refinement method, Full-matrix least-squares on F^2, Data / restraints / parameters 6535 / 0 / 431, Goodness-of-fit on F^2 1.079, Final R indices [I >2sigma(I)] R1 = 0.0443, wR2 = 0.1260, R indices (all data) R1 = 0.0666, wR2 = 0.1528, $\rho_{calcd.}$ = 1.264 Mg/m^3.

2.6. References

1. a) T. Weil, T. Vosch, J. Hofkens, K. Peneva, K. Müllen, *Angew. Chem. Int. Ed.* **2010**, *49*, 9068–9093; b) J.-C. G. Bünzli, S. V. Eliseeva, *J. Rare Earths* **2010**, *28*, 824–842; c) C. Jiao, J. Wu, *Synlett* **2012**, 171–184; d) Z. Y. Wang, *Near-Infrared Organic Materials and Emerging Applications. CRC Press, Florida*, **2013**; e) A. Barbieri, E. Bandini, F. Monti, V. K. Praveen, N. Armaroli, *Top. Curr. Chem.* **2016**, *374*, 47.

2 a) K. Kiyose, H. Kojima, T. Nagano, *Chem. Asian J.* **2008**, *3*, 506–515; b) S. A. Hilderbrand, R. Weissleder, *Curr. Opin. Chem. Biol.* **2010**, *14*, 71–79; c) V. J. Pansare, S. Hejazi, W. J. Faenza, R. K. Prud’homme, *Chem. Mater.* **2012**, *24*, 812–827; d) S. Luo, E. Zhang, Y. Su, T. Cheng, C. Shi, *Biomaterials* **2011**, *32*, 7127–7138; e) L. Yuan, W. Lin, K. Zheng, L. He, W. Huang, *Chem. Soc. Rev.* **2013**, *42*, 622–661; f) C. Wu, D. T. Chiu, *Angew. Chem. Int. Ed.* **2013**, *52*, 3086–3109; g) E. A. Owens, S. Lee, J. Choi, M. Henary, H. S. Choi, Wiley *Interdiscip. Rev.: Nanomed. Nanobiotechnol.* **2015**, *7*, 828–838.

4 A. B. Descalzo, H.-J. Xu, Z. Shen, K. Rurack, *Ann. N. Y. Acad. Sci.* **2008**, *1130*, 164–171.

5. H. Lu, J. Mack, Y. Yang, Z. Shen, *Chem. Soc. Rev.* **2014**, *43*, 4778-4823.

6. Y. Ni, J. Wu, *Org. Biomol. Chem.* **2014**, *12*, 3774–3791.

7 K. Umezawa, Y. Nakamura, H. Makino, D. Citterio, K. Suzuki, *J. Am. Chem. Soc.* **2008**, *130*, 1550–1551.

8. G. Qian, Z. Zhong, M. Luo, D. Yu, Z. Zhang, Z. Y. Wang, D. Ma, *Adv. Mater.* **2009**, *21*, 111–116.

9. J. R. Sommer, A. H. Shelton, A. Parthasarathy, I. Ghiviriga, J. R. Reynolds, K. S. Schanze, *Chem. Mater.* **2011**, *23*, 5296–5304.

10. U. Mayerhöffer, B. Fimmel, F. Würthner, *Angew. Chem. Int. Ed.* **2012**, *51,* 164–167.

11. U. Mayerhöffer, M. Gsänger, M. Stolte, B. Fimmel, F. Würthner, *Chem. Eur. J.* **2013**, *19*, 218–232.

12. X. Cheng, K. Wang, S. Huang, H. Zhang, H. Zhang, Y. Wang, *Angew. Chem. Int. Ed.* **2015**, *54*, 8369–8373.

13 L. Maggini, D. Bonifazi, *Chem. Soc. Rev.* **2012**, *41*, 211–241.

14 S. S. Babu, V. K. Praveen, A. Ajayaghosh, *Chem. Rev.* **2014**, *114*, 1973–2129.

15 K. Tanaka, Y. Chujo, *NPG Asia Mater.* **2015**, *7*, 223–15.

16 S. Ghosh, V. K. Praveen, A. Ajayaghosh, *Annu. Rev. Mater. Res.* **2016**, *46*, 235–262.

17 Z. Chi, X. Zhang, B. Xu, X. Zhou, C. Ma, Y. Zhang, S. Liu, J. Xu, Chem. Soc. Rev. 2012, 41, 3878–3896.

18. S. Yagai, S. Okamura, Y. Nakano, M. Yamauchi, K. Kishikawa, T. Karatsu, A. Kitamura, A. Ueno, D. Kuzuhara, H. Yamada, *Nat. Commun.* **2014**, *5*, 4013-4022.

19. L. Wang, K. Wang, B. Zou, K. Ye, H. Zhang, Y. Wang, *Adv. Mater.* **2015**, *27*, 2918–2922.

20. S. Mukherjee, P. Thilagar, *J. Mater. Chem. C* **2016**, *4*, 2647–2662.

21. Y. Sagara, S. Yamane, M. Mitani, C. Weder, T. Kato, *Adv. Mater.* **2016**, *28*, 1073–1095.

22. For NIR to blue mechanofluorochromism, see: M. Tanioka, S. Kamino, A. Muranaka, Y. Ooyama, H. Ota, Y. Shirasaki, J. Horigome, M. Ueda, M. Uchiyama, D. Sawada, S. Enomoto, *J. Am. Chem. Soc.* **2015**, *137*, 6436−6439.

23. For mechanically triggered fluorescence (Vis)/phosphorescence (NIR) switching via intermolecular metal-metal distance variation of a Copper(I) complex, see: Q. Xiao, J. Zheng, M. Li, S.-Z. Zhan, J.-H. Wang, D. Li, *Inorg. Chem.* **2014**, *53*, 11604–11615.

24. A. Loudet, K. Burgess, *Chem. Rev.* **2007**, *107*, 4891–4932.

25. G. Ulrich, R. Ziessel, A. Harriman, *Angew. Chem. Int. Ed.* **2008**, *47*, 1184–1201.

26. a) J. Banuelos, *Chem. Rec.* **2016**, *16*, 335–348; b) G.-G. Luo, J.-X. Xia, K. Fang, Q.-H. Zhao, J.-H. Wu, J.-C. Dai, *Dalton Trans.* **2013**, *42*, 16268-16271.

27. a) M. D. Yilmaz, O. A. Bozdemir, E. U. Akkaya, *Org. Lett.* **2006**, *13*, 2871–2873; b) A. Harriman, L. J. Mallon, K. J. Elliot, A. Haefele, G. Ulrich, R. Ziessel, *J. Am. Chem. Soc.* **2009**, *131*, 13375–13386.

28. J.-H. Olivier, J. Barbera, E. Bahaidarah, A. Harriman, R. Ziessel, *J. Am. Chem. Soc.* **2012**, *134*, 6100–6103.

29. L. Bonardi, H. Kanaan, F. Camerel, P. Jolinat, P. Retailleau, R. Ziessel, *Adv. Funct. Mater.* **2008**, *18*, 401–413.

30. A. Florian, M. J. Mayoral, V. Stepanenko, G. Fernandez, *Chem. Eur. J.* **2012**, *18*, 14957–14961.

31. N. K. Allampally, A. Florian, M. J. Mayoral, C. Rest, V. Stepanenko, G. Fernández, *Chem. Eur. J.* **2014**, *20*, 10669–10678.

32. A. Rödle, B. Ritschel, C. Mück-Lichtenfeld, V. Stepanenko, G. Fernández, *Chem. Eur. J.* **2016**, *22*, 15772–15777.

33 F. Camerel, L. Bonardi, M. Schmutz, R. Ziessel, *J. Am. Chem. Soc.* **2006**, *128*, 4548–4549.

34. F. Camerel, L. Bonardi, G. Ulrich, L. Charbonniere, B. Donnio, C. Bourgogne, D. Guillon, P. Retailleau, R. Ziessel, *Chem. Mater.* **2006**, *18*, 5009–5021.

35. A. Nagai, J. Miyake, K. Kokado, Y. Nagata, Y. Chujo, *J. Am. Chem. Soc.* **2008**, *130*, 15276–15278.

36. N. Sun, X. Xiao, W. Li, J. Jiang, *Adv. Sci.* **2015**, *2*, 1500082.

37. T. Ozdemir, F. Sozmen, *RSC Adv.* **2016**, *6*, 10601–10605.

38. T. Ozdemir, S. Atilgan, I. Kutuk, L. T. Yildirim, A. Tulek, M. Bayindir, E. U. Akkaya, *Org. Lett.* **2009**, *11*, 2105–2107.

39. J.-H. Olivier, J. Widmaier, R. Ziessel, *Chem. Eur. J.* **2011**, *17*, 11709–11714.

40. C.-L. Liu, Y. Chen, D. P. Shelar, C. Li, G. Cheng, W.-F. Fu, *J. Mater. Chem. C*, **2014**, *2*, 5471–5478.

41. H.-T. Feng, J.-B. Xiong, Y.-S. Zheng, B. Pan, C. Zhang, L. Wang, Y. Xie *Chem. Mater.* **2015**, *27*, 7812−7819.

42. D. Okada, T. Nakamura, D. Braam, T. D. Dao, S. Ishii, T. Nagao, A. Lorke, T. Nabeshima, Y. Yamamoto, *ACS Nano* **2016**, *10*, 7058–7063.

43 J. M. Malicka, A. Sandeep, F. Monti, E. Bandini, M. Gazzano, C. Ranjith, V. K. Praveen, A. Ajayaghosh, N. Armaroli, *Chem. Eur. J.* **2013**, *19*, 12991–13001.

44. R. Thirumalai, R. D. Mukhopadhyay, V. K. Praveen, A. Ajayaghosh, *Sci. Rep.* **2015**, *5*, 09842.

45. S. Mathieu, G. Trinquier, *J. Phys. Chem. B* **2012**, *116*, 8863–8872.

46. M. A. Spackman, D. Jayatilaka, *CrystEngComm.* **2009**, *11*, 19–32.

47. S. K. Wolff, D. J. Grimwood, J. J. Mckinnon, M. J. Turner, D. Jayatilaka, M. A. Spackman, CrystalExplorer 3.1 (2013), University of Western Australia, Crawley, Western Australia, 2005-2013, http://hirshfeldsurface.net/CrystalExplorer.

48. **CCDC 1523313** contains the supplementary crystallographic data for this paper. This data are provided free of charge by The Cambridge Crystallographic Data Centre.

49. a) Sagara, T. Mutai, I. Yoshikawa, K. Araki, *J. Am. Chem. Soc.* **2007**, *129*, 1520-1521; b) M. Sase, S. Yamaguchi, Y. Sagara, I. Yoshikawa, T. Mutai, K. Araki, *J. Mater. Chem.* **2011**, *21*, 8347-8354.

50. a) Y. Sagara, T. Kato, *Nat. Chem.* **2009**, *1*, 605-610; b) Y. Sagara, S. Yamane, T. Mutai, K. Araki, T. Kato, *Adv. Funct. Mater.* **2009**, *19*, 1869-1875; c) Y. Sagara, T. Kato, *Angew. Chem. Int. Ed.* **2008**, *47*, 5175-5178.

51. G. Zhang, J. Lu, M. Sabat, C. L. Fraser, *J. Am. Chem. Soc.* **2010**, *132*, 2160-2162.

52. L. Wang, K. Wang, B. Zou, K. Ye, H. Zhang, Y. Wang, *Adv. Mater.* **2015**, *27*, 2918-2922.

Chapter 3

A Bodipy Derived Material for Photonic and Waveguiding Applications

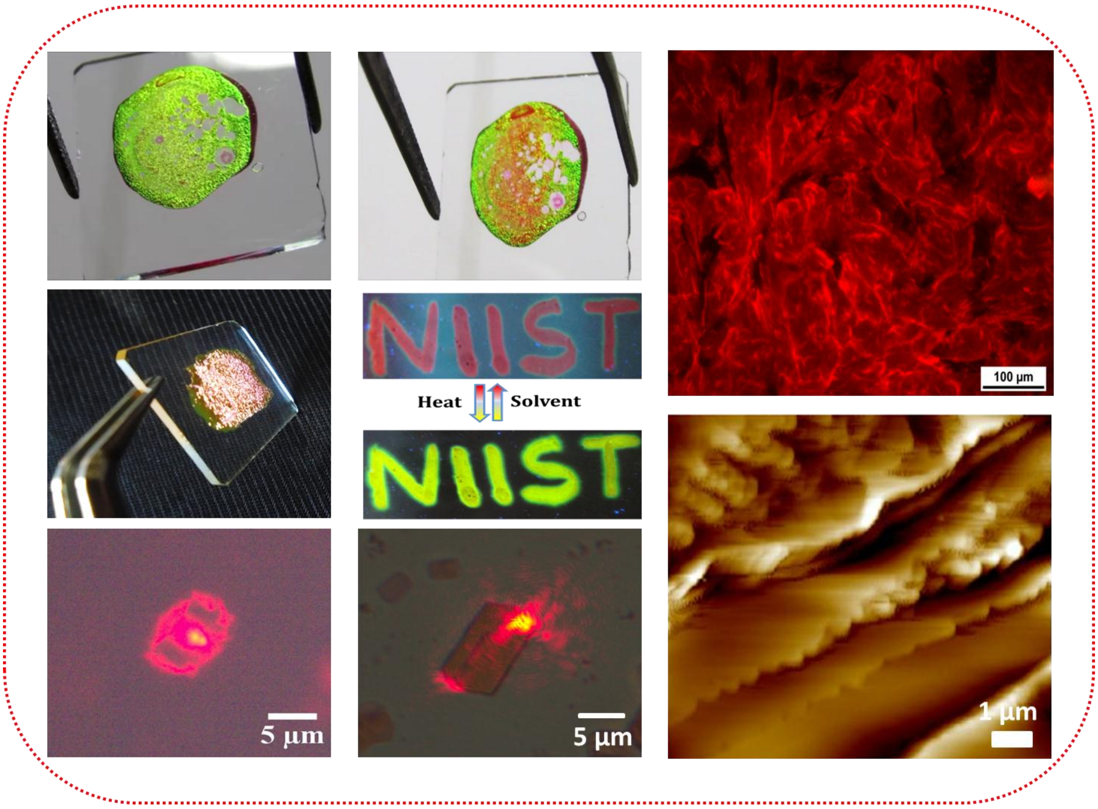

3.1. Abstract

*The present chapter describes the synthesis, self-assembly, thermochromic, photonic structures and waveguiding properties of an amide functionalised meso phenyleneethynylene derived Bodipy (***Bodipy-3***).* ***Bodipy-3*** *self-assembles in nonpolar cyclohexane and also forms microcrystals of 2D blocks in toluene. These blocks exhibit both active and passive waveguiding properties when excited*

with 532 and 633 nm laser sources. Anisotropic waveguiding properties are especially observed upon excitation with 633 nm indicates the high crystalline and photonic nature of the material. Single crystal analysis of ***Bodipy-3*** *has shown existence of CH···π, CH···O and NH···F-B hydrogen bonding interactions. These intermolecular interactions lead to supramolecular ordering which is suitable for waveguiding properties. Thermal annealing of the film or powder of* ***Bodipy-3*** *to its melting point has shown an irreversible thermochromic luminescence shift from yellow to red with a slight change in quantum yield from 0.09 to 0.1. Interestingly, more ordered photonic structures are formed upon annealing the film exhibiting angle dependent color changes. AFM cross-sectional analysis has shown the micro and nano periodicity associated with the structure. Annealing resulted the phase change from cubic to highly ordered lamellar as evident from SAXS analysis. Additionally, annealed powder was utilized for stimuli responsive ink observing a reversible emission shift from red to yellow upon heating and solvent exposure in polymer medium (PEG). An in situ polymer (polystyrene) gel of annealed powder leads to formation of macroscopic waveguiding fibres and photonic structures.*

3.2. Introduction

Nature has the mastery to create a variety of exotic and functional materials such as the wings of butterflies and the feathers of peacock exhibiting different colors. These colors can be achieved by different methods such as pigments, dyes and structure. Pigments and dyes owe their color by absorption of light where as the structural color arises by the manipulation light through reflection or diffraction processes of the periodically arranged nanostructures.[1] These materials exhibit distinct optical properties comprising angle dependent reflection and light propagation. The special properties of such materials originate out of the nanoscopic and microscopic ordering of the molecular components. Over the years, scientists have been trying to understand the science behind such creations with the object of mimicking these properties with artificial materials. These come under the class of photonic molecular materials because of their exceptional properties of molecular flexibility, broadband spectral tunability, diffraction limited light manipulation, refractive index tunability and high localized electric field.[2-8] Since photonic structures have periodic modulation of refractive indices for different layers, optical interference takes place resulting multiple reflection of specific wavelengths and hence gives the appearance of structural color. The periodic modulation of refractive indices in polymeric layered photonic structures can be achieved by either a bottom-up self-assembly method or by thermochromic processes. Organic molecular materials have been identified for photonics, opto-electronic, sensors, light emission devices, optical nanoantenna and optical communications based applications.[9-14]

The field of thermochromism has gained much attention and progress since last decade and is considered as one of the simplest ways of making periodically ordered structures.[15] Thermochromic composites or pigments from leuco dyes or cholestic liquid crystals and their incorporation in polymers have become todays' the state of the art technology.[16,17] From the application view point, the introduction of thermochromism into commercial paints, lacquers, inks, thermoplastics, and thermosetting plastics is of special interest. Microencapsulated leuco dye−developer−solvent systems are the most common thermochromic pigments. Thermochromism lead to changes in the optical properties such as reflection, absorption and emission. Reflection change occurs if there is a change of the optical pathlength in periodic structured materials upon heating. Normally reflected light has a wavelength in the visible range and thus structural color occurs. On the other hand absorption and emission changes occur when there are some structural changes of chromophoric moieties up on heating.

In a one-dimensional photonic crystal, Bragg mirror or Bragg stacks reflects different wavelength of light. According to the Bragg's law which can be mathematically expressed as $\mathbf{m\lambda = 2\,(\Sigma_i\, n_i d_i)}$**…….. (1)**, where 'm' is the order of diffraction, 'λ' is the wavelength, n_i and d_i are the refractive index and thickness of the particular layer 'i'. Based on the above equation it is clear that the changes in the *d*-spacing or the refractive index of at least one layer by temperature can bring the properties associated with one-dimensional photonic crystal.[15] According to equation (**1**), thermo responsive 1D photonic crystal is obtained if at least one of the layer spacing alters or changes the refractive index with temperature. It is already reported that a thermochromic effect can bring significant alteration of the refractive index of the material.

Ikkala *et al*. demonstrated a thermo responsive reversible switching of photonic bandgap in the solid state based on the self-assembly of a block copolymer where the reversibility of hydrogen bonding and the polymer additive phase behavior allow temperature response.[18] No solvent contact is necessary for the thermochromic effect. The photonic crystal consists of a block copolymer and a low molecular weight additive leading to the formation of a self-assembled polymeric solid film. A complex of polystyrene-block-poly(4-vinylpyridinium methanesulphonate) and 3-*n*-pentadecylphenol leads to the supramolecular comb-shaped architecture with a particularly long lamellar period. The sample exhibit

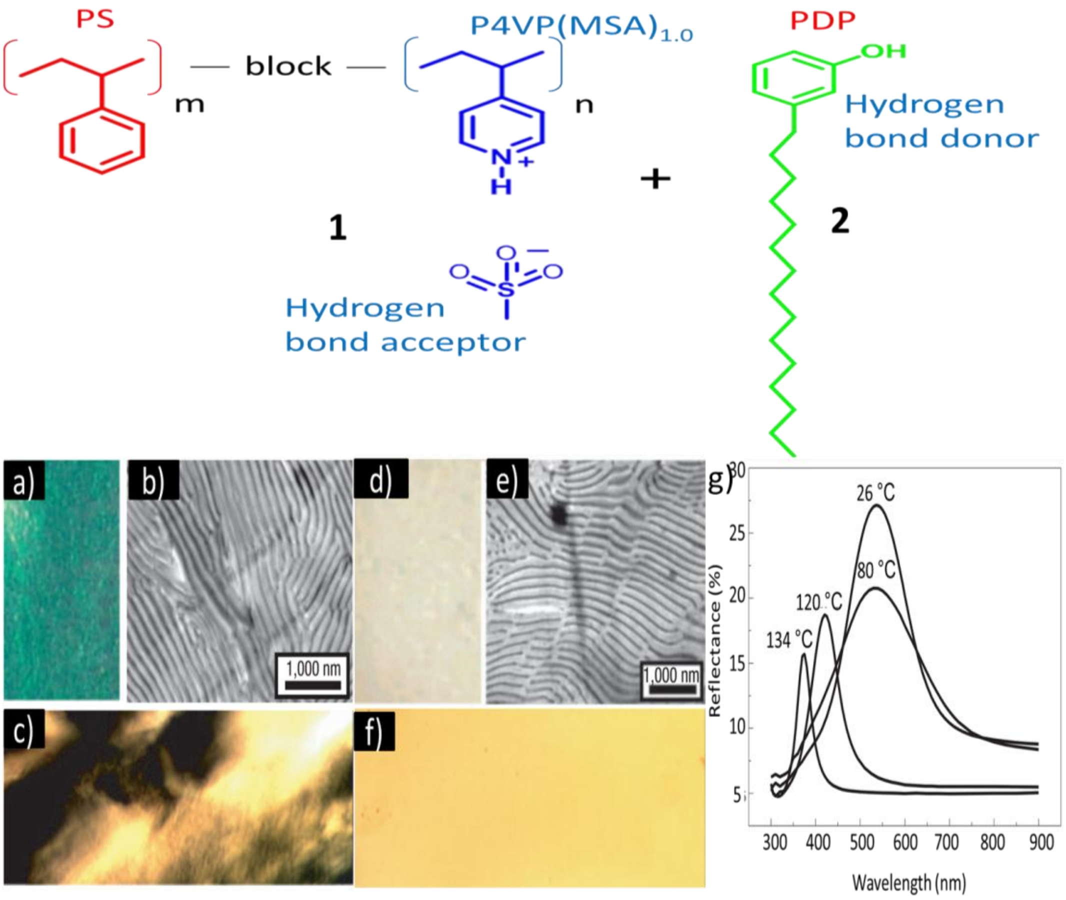

Figure 3.1. PS-block-P4VP(MSA)$_{1.0}$(PDP)$_{1.5}$ at room temperature and at T > ~ 125 °C a) at room temperature (green), b) TEM image showing lamellar structure c) Optically anisotropic birefringent texture observed below ~125 °C with crossed polarizers suggesting an internal self-assembly within P4VP(MSA)$_{1.0}$(PDP)$_{1.5}$ domains. d) at $T \gtrsim 125$ °C, colorless e) TEM showing rapidly quenched sample from 170 °C shows lamellar structure f) above 125 °C, the sample becomes non-birefringent in agreement with an internal phase transition to a disordered phase within the P4VP(MSA)$_{1.0}$ domains g) Reflectance measurements for different temperatures.

green color at room temperature, as an incomplete photonic bandgap due to the formation of a dielectric reflector. On heating, hydrogen bonds are broken and 3-*n*-pentadecylphenol additionally becomes soluble in polystyrene, leading to a sharp and reversible transition at ~125 °C to colorless material due to collapse of the long period. The temperature responsive nature is based on the fact that the alkyl chains involved in the molecular packing are bonded by weak interactions such as hydrogen bonding. The TEM image (**Figure 3.1b**) shows lamellar structure with the long period of ~160 nm due to stretching of the alkyl chains and appeared as green in reflection (**Figure 3.1a**). Rapidly quenched sample from 170 °C (**Figure 3.1e**) shows the reversibility of the lamellar structure upon cooling. Increasing the temperature shifts the reflectance peak position (**Figure 3.1g**).

Grubbs *et al.* have shown that blends between brush BCPs (block copolymers) of different MW form highly uniform, stacked lamellar morphologies.[19] The resulting domains of the 1D PC architectures scale linearly with the weight-percent incorporation of the two polymers. A film prepared from the controlled evaporation of a solution of polymer **5** and **6** in a weight-percent ratio of 50:50 in dichloromethane exhibited a single reflection peak with $\lambda_{\max}$ = 541 nm. By varying the weight-percent ratio of the two brush BCPs (**5** and **6**) from 100 % of polymer **5** to 100 % **6**, at 10% intervals, a total of 11 different films were prepared and the each composition involved distinct spectral shifts (**Figure 3.2e**).

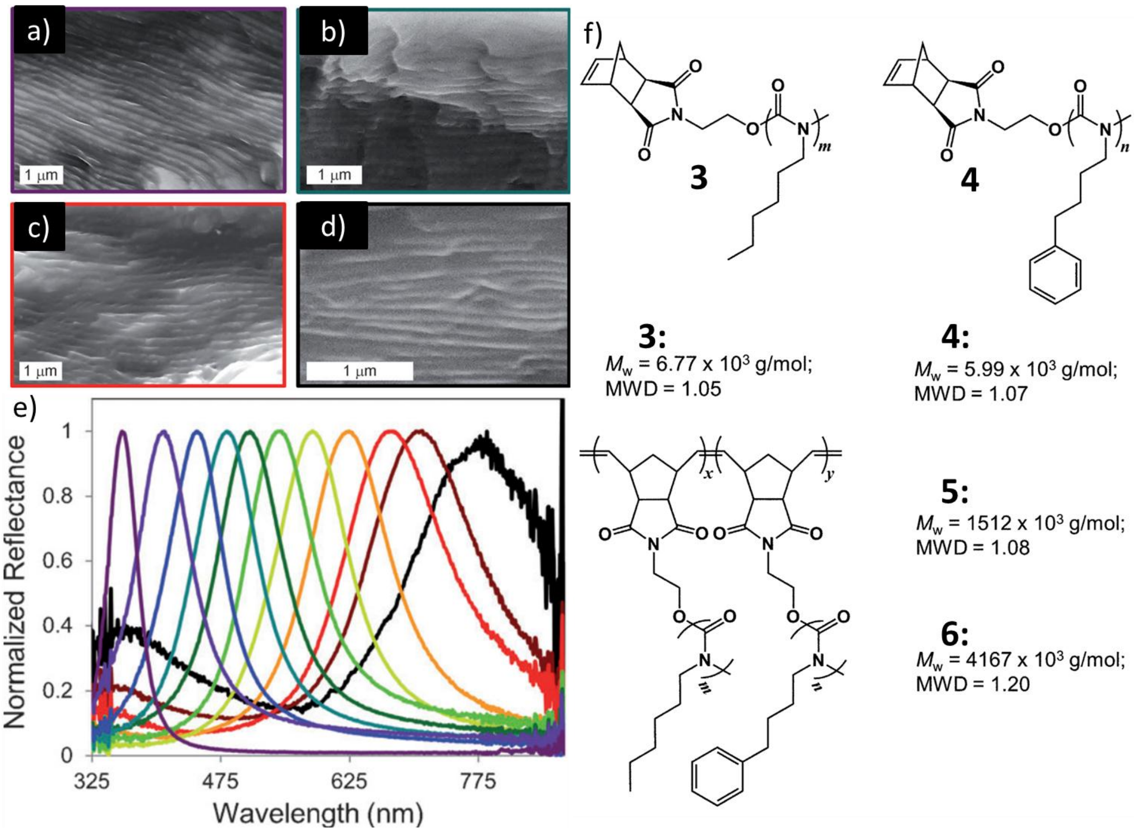

Figure 3.2. SEM images of cross-sections of brush block copolymer (BCPs) blends with a) 0%, b) 30% c) 80% and d) 100% of polymer **6.** e) Plots of reflectance against wavelength of the different brush block copolymer blends f) Structures and molecular-weight properties of macromonomers and brush block copolymers.

Optical waveguides are one of the important components of miniaturized photonics devices.[20] Based on the type of light propagation, organic optical waveguides are classified into active and passive waveguides.[21-23] For active waveguides, the molecular building block of the organic solid is electronically excited and the coupled exciton–polariton propagates to the output end as luminescence. Although this area is relatively young, a few excellent examples have been reported for this type of exciton–polariton based active waveguide. On the other hand, passive organic waveguides function almost similar to commercial optical fibers and other dielectric-based guided wave structures, i.e., here the input light directly propagates along the organic medium to the output end.

Chandrasekhar *et al.* prepared organic rhombus shaped 2D sheets by the self-assembly of 1,4-bis(1,2′:6′,1″-bis(3-butyl-1*H*-3,4,5-triazolyl)pyridin-4′-yl)benzene (**Figure 3.3d**) in CH_3CN.[24] Examination of the X-ray structure that was obtained from the sheet like single crystals of **7** (monoclinic; $P\ 2_1/c$) showed unique structural features for hierarchical supramolecular self-assembly. Compound **7** has a nearly planar, rod-shaped arrangement of three aromatic rings as the central segment ($N_{py}\cdots N_{py}$ distance = 1.13 nm) and four triazole rings with butyl chains attached to the four corners of the rigid segment. Furthermore, the triazole ring nitrogen atom (N2) participates in two C-H···N intermolecular hydrogen-bonding interactions with the phenyl ring protons [N2···H4 = 2.737 Å; N2···H5 = 2.635 Å] that play a vital role in the supramolecular ordering and self-assembly. Because of these intermolecular forces, molecules of **7** aggregates to form sheet-like structure with a thickness of 1.76 nm in the crystallographic *b*,*c* plane (**Figure 3.3b**). Molecular-level layers of **7** are tightly packed along the crystallographic *a* axis with interpenetrating alkyl chains, which then stack and form sheet-like supramolecular aggregates (**Figure 3.3a, c**). For the waveguiding experiments, the output of the Ar laser beam (488 nm) was directly focused on the sample. Since **7** does not have any absorption in the 488 nm region, no molecular excitation (hence, no absorption and fluorescence) as a result of the laser energy was expected. When the laser beam was focused orthogonally at the center of the

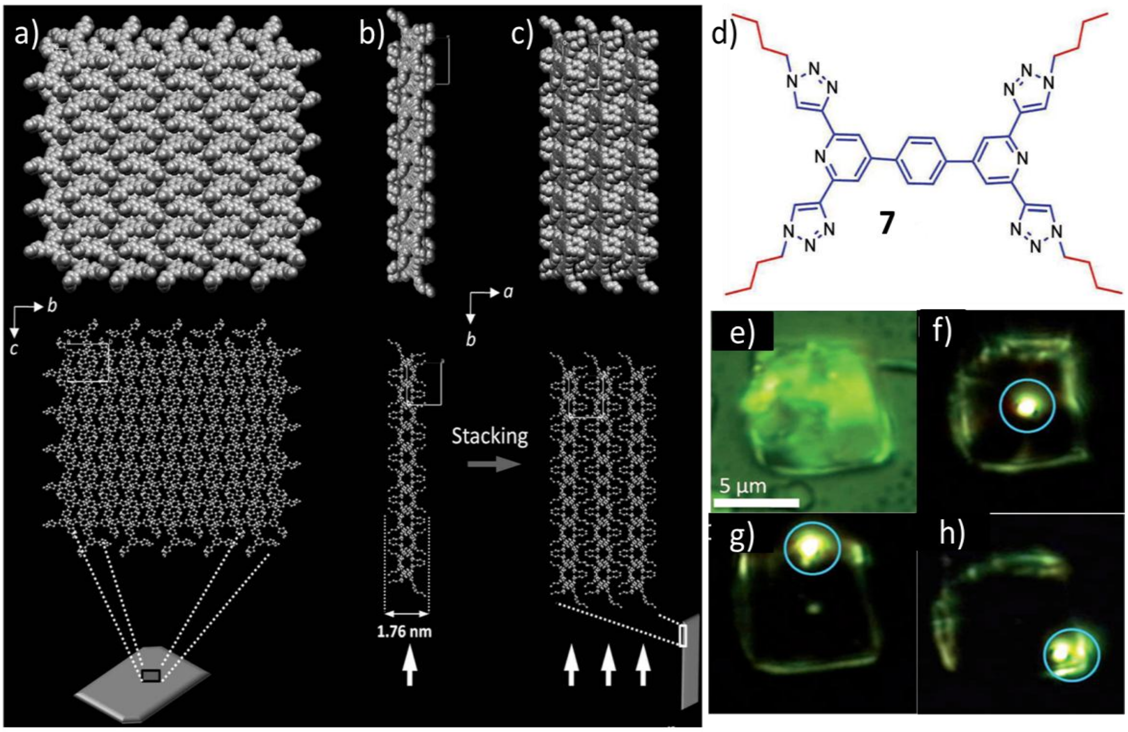

Figure 3.3. Possible formation mechanism of 2-D sheet like aggregates from molecular sheets and waveguiding properties. a) Top view of the single-crystal X-ray packing diagram of 1 along the crystallographic *a* axis b) Side view of a 1.76 nm molecular-level sheet along the crystallographic *c* axis. c) Side view of layer-by-layer aggregation of molecular-level sheets along the crystallographic *a* axis. d) Molecular structure.e-h) confocal laser microscopy images collected through a 488 nm long-pass edge filter.

plane of a 2D sheet, propagation of laser light in all the four directions of the sheet was observed (**Figure 3.3f**). Focusing the laser beam at one of the edges showed that the sheet guided the light mostly towards the opposite edge (**Figure 3.3g**). Interestingly, illumination at the corner of the sheet with the laser beam resulted in light propagation to the two diagonal edges (**Figure 3.3h**). These results confirmed that the nanosheets acted as a waveguide in two-dimensions, and that the direction of propagation of the light is dependent on the path of the light input.

Yamamoto *et al*. demonstrated a simple Bodipy doped polystyrene microspheres' cavity mediated long range energy transfer from energy-donating sphere to energy-accepting sphere, exposing its potential applications in compact optical integrated devices.[25]

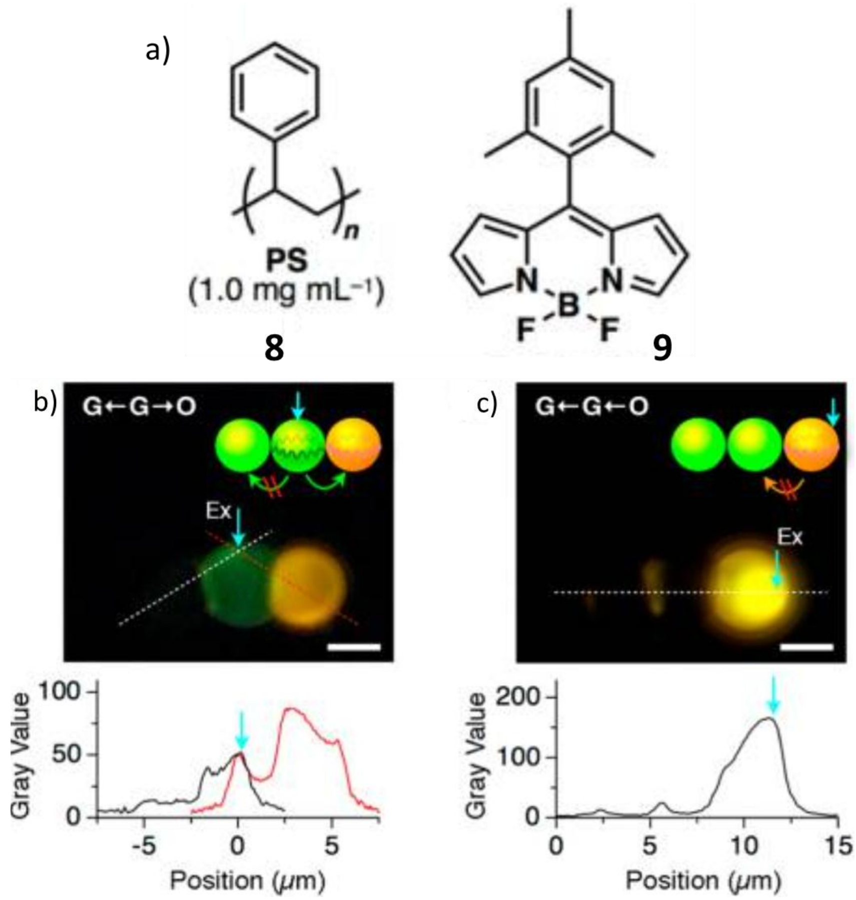

Figure 3.4. a) Molecular structures b, c) FM images of coupled three spheres of G−G−O upon focused laser excitation (λ_{ex} = 470 nm) at the central G (b) and O (c). The bottom graphs show cross section profiles of the PL intensities.

Molecule **9** doped polystyrene exhibited PL colors with green to red depending on the concentration (0.001 (green), 0.1 (yellow), 0.5 and 1 mg mL^{-1} (orange and red, respectively)) of the molecule. Microspheres are prepared by interface precipitation method in which THF solution of a mixture of polystyrene solution (c = 1 mg/mL) and molecule **9** (0.002-1.0 mg mL^{-1}) is carefully added onto a nonsolvent layer of water/EtOH (6/1, v/v) mixture. Diffusion of solvents and the slow evaporation of the THF resulted in the precipitation after 6 h aging. The authors have adopted micromanipulation technique with an electrically controlled stepping stage and a thin microneedle for connecting microspheres. When the spheres are linearly connected in an order of G (G stands for green), G and O (G-G-O), the selective excitation at the middle (G) lead to the PL transfer towards orange (O) (**Figure 3.4b, c**). On the other hand when excited at orange sphere, no PL transfer observed. This confirms the propagation of light wave which occurs selectively in energy transferrable direction.

So far, numerous self-assembly methods have been adopted to prepare 1D/2D organic waveguides and photonic structures.[21-27] Also, polymer based self-aggregated waveguides have been already reported for its potential applications.[28-29] However, there is no report from simple π-conjugated organic molecule which can be used for making extended layered photonic structures as well as waveguides of 2D planar geometric structures based on varying processing conditions. Also, in contrast to inorganic nanomaterial, organic nanomaterials show relatively large binding energy, greater oscillator strength, high exciton splitting energy and stability.[3,7,11,23] Hence, it would be quite fascinating to connect all the photonic properties associated with an organic molecule by merely varying the processing conditions. Herein we report the stimuli responsive fluorescent and layered photonic properties of annealed Bodipy derivative which exhibit waveguiding properties in the polymer gel matrix as well as in the crystalline non-annealed state.

3.3. Results and Discussion

3.3.1. Synthesis of Bodipy-3

Bodipy-3 is synthesized by the Sonogashira coupling between 3,4,5-tributoxy-*N*-(4-ethynylphenyl)benzamide (**15**) and (4-iodophenyl)-1,3,5,7-tetramethyl-4,4-difluoro-4-bora-3a,4a-diaza-*s*-indacene (**16**) in presence of bis(triphenylphosphine)palladium (II) dichloride (10 mol%), and copper (I) iodide (10 mol%) using degassed triethylamine and THF as solvents as per **Scheme 3.2**.[30] Pure product was obtained after purification with 35% yield. The product was characterised by ^{1}H NMR, ^{13}C NMR, HRMS and FT-IR spectroscopic techniques.

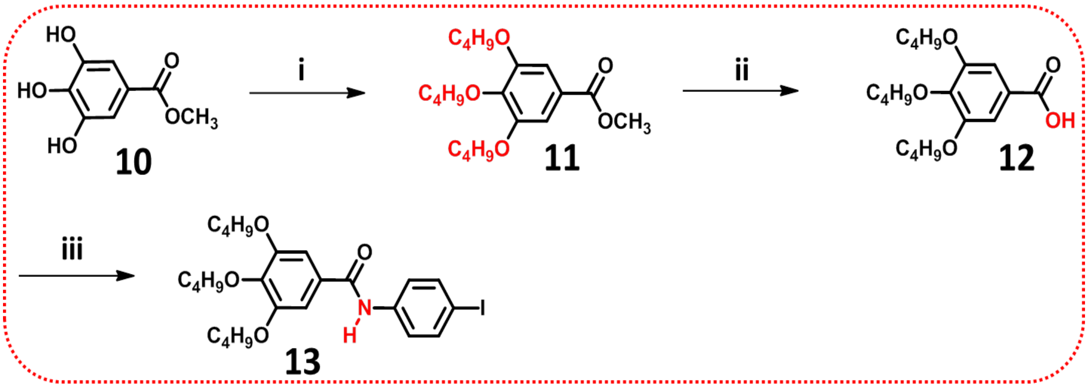

Scheme 3.1. Reagents and conditions: **i**) 1-Bromobutane, K_2CO_3, DMF, 100 °C, 24 h, 78%; **ii**) KOH, ethanol, reflux, 12 h, 80%; **iii**) a) $SOCl_2$, dry dichloromethane, rt., 5 h; b) 4-Iodoaniline, dry toluene, rt., 12 h, 50%.[31]

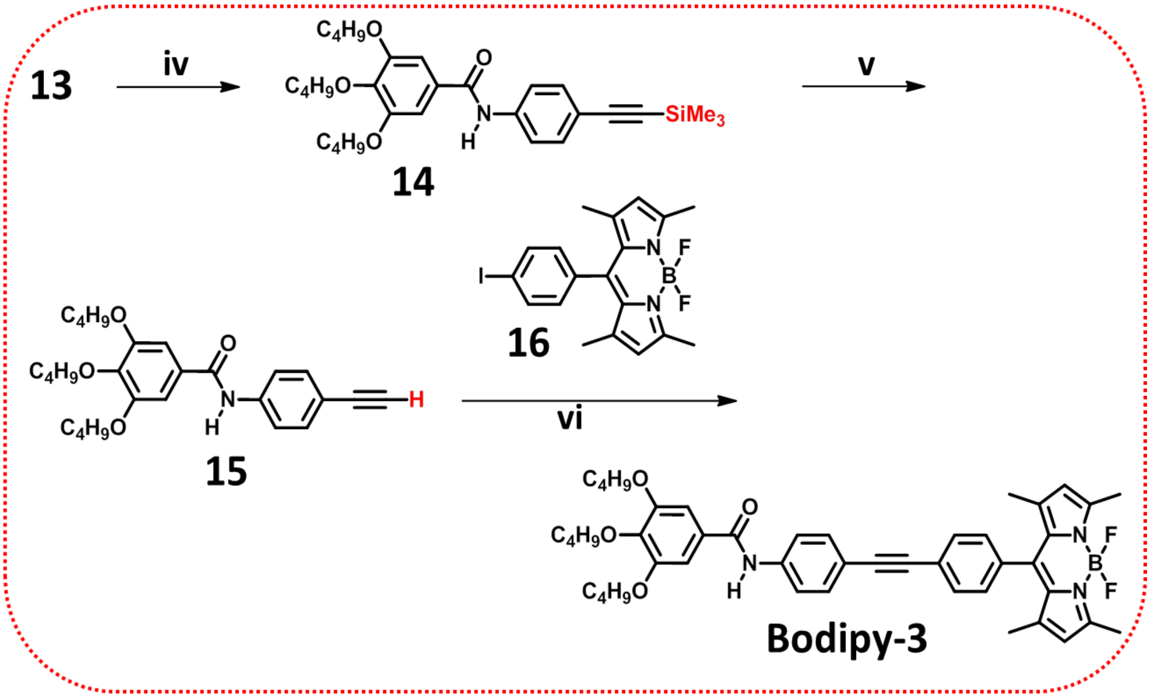

Scheme 3.2. Reagents and conditions: **iv**) Trimethylsilyl acetylene, CuI, $PdCl_2(PPh_3)_2$, dry Et_3N, dry THF (oxygen free), rt., 12 h, 80%; **v**) KF, dichloromethane/methanol (1:5), rt, 12 h, 76% **vi**) CuI, $PdCl_2(PPh_3)_2$, dry Et_3N, dry THF (oxygen free), 60 °C, 24 h, 35%.

3.3.2. Photophysical Properties

3.3.2.1. Absorption, Emission and Reflectance Spectral Properties

In chloroform, toluene and DMSO (1×10^{-4} M), **Bodipy-3** exists in the monomeric state with sharp absorption maxima at 315 and 504 nm with a shoulder band at 474 nm (**Figure 3.5a**). The absorption maximum at 315 nm corresponds to the phenyleneethynylene part, whereas the narrow absorption maximum at 504 nm corresponds to the strong S_0-S_1 electronic transition of the Bodipy chromophore. The broad absorption features observed around 320 and 500 nm indicates the presence of **Bodipy-3** aggregates in both cyclohexane and decane at a concentration of 1 x 10^{-4} M.

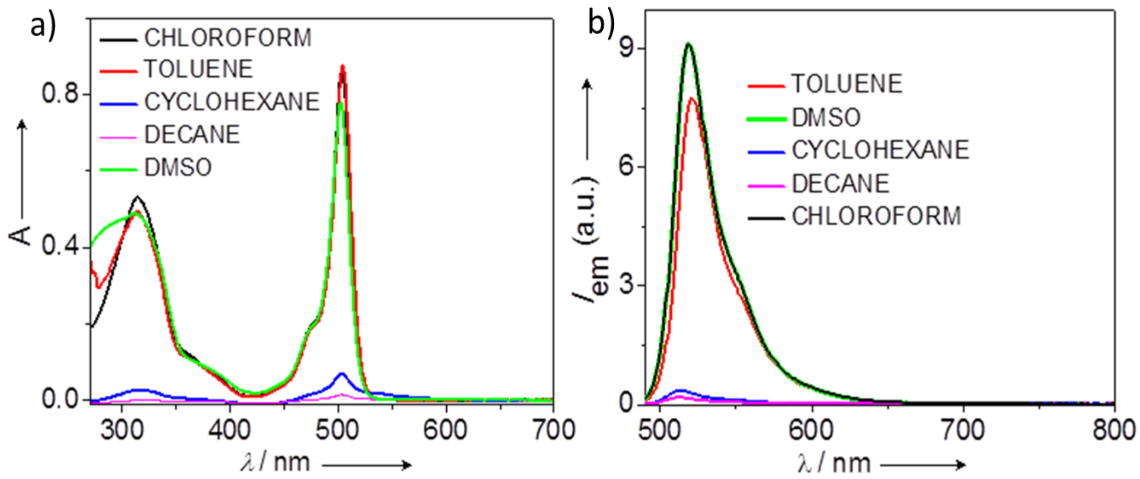

Figure 3.5. a) Absorption, b) emission (λ_{ex} = 475 nm) spectra in different solvents (c = 1 x 10^{-4} M).

The emission spectra in the solution state also indicate **Bodipy-3** aggregates in both decane and cyclohexane as evidenced by weak and broadened emission profiles (**Figure 3.5b)**. The weak luminescence of the aggregate solution is an indication of H-type aggregates. Intense monomeric emission at 520 nm is observed in toluene, chloroform and DMSO solution at a concentration of 1 x 10^{-4} M.

The molecule **Bodipy-3** (**Scheme 3.2**), when annealed in a heating pan above its melting point at 280 °C, melts and undergoes phase transformation and exhibited a metallic green lusture from the orange red initial state (**Figure 3.6a**). Similar way, film prepared from toluene solution (c = 1 x 10^{-2} M) appeared as yellowish-orange under daylight (**Figure 3.6c**) and when annealed, turned into a dual visibly colored film which appeared as dark green in the reflected light (under black background) and orange red in the transmitted (white background) light (**Figure 3.6h-j**). Also, this dual colored film when viewed orthogonally appeared as green under visible light, but as it is tilted slightly through different angle and viewed, orange red color is appeared along with the decrease of green color (**Figure 3.6e-g**). The reflectance spectral comparison of the annealed film with respect to normal angle and at a tilt angle confirms the dual color appearance of the film (**Figure 3.7c**). Also, the reflectance spectral comparison for the annealed and non-annealed film indicates that the former appears highly reflecting at 530 nm (**Figure 3.7a**). Thus, when the annealed film is view through different angle of incident light, exhibited angle-dependent color changes, characteristic of a photonic material (**video 1**). The observed thermochromic changes in reflection are attributed to the optical path length changes associated with layered periodic structures.[15] Thermal annealing resulted in a change in refractive index between alternate layers and thereby manipulation of light occurs in the visible wavelength region. The fluorescence spectra of the non-annealed film has shown emission maxima both at 600 and 720 nm and appeared as yellowish orange emissive. However, the annealed film which displayed red emission has shown only one emission maximum at 650 nm and it extended up to 850 nm region as weak band (**Figure 3.7b**). The annealing process is accompanied by an irreversible luminescence shift from yellow to red (**Figure 3.6b** and **d**). The modulation in fluorescence upon annealing was monitored through variable temperature fluorescence spectral analyses of the powder sample. The emission maximum at 577 nm for the initial powder undergoes slight red-shift with gradual quenching of the emission intensity with respect to increase in temperature (**Figure 3.8a**). No emission is observed in the molten state at 290 °C. On gradual cooling from the isotropic/molten state, the emission maximum at 650 nm is enhanced and reaches maximum intensity at room temperature (**Figure 3.8c**).

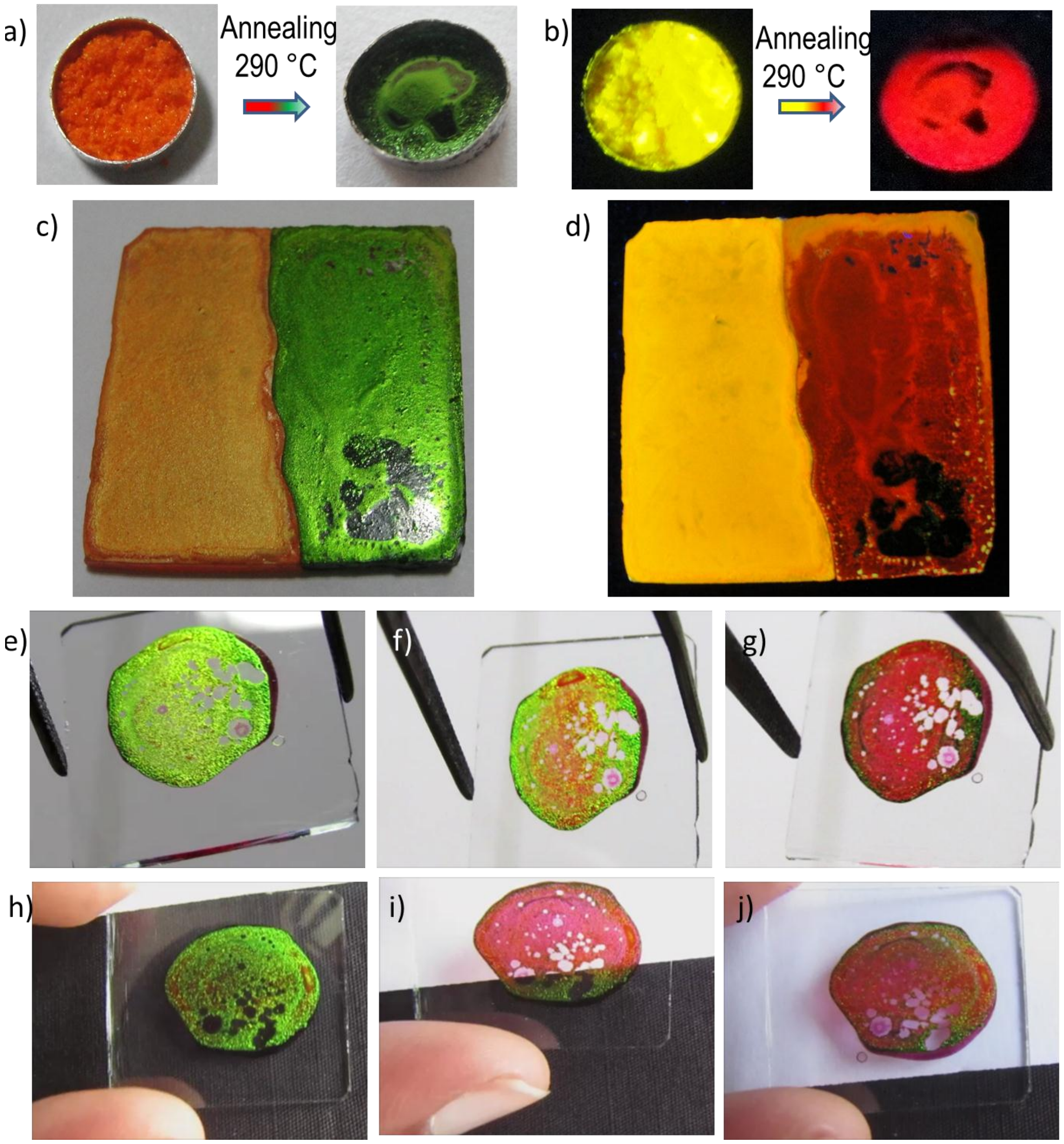

Figure 3.6. Photographs showing powder before and after annealing a) under daylight and b) uv light. c, d) Photographs correspond to film (toluene, $c = 1 \times 10^{-2}$ M) under daylight and uv light, respectively for the annealed (right) and non-annealed (left) parts. e-g) Annealed photonic film exhibiting dual color upon tilting and h-j) dual color appearance under black (reflected light) and white (transmitted light) backgrounds.

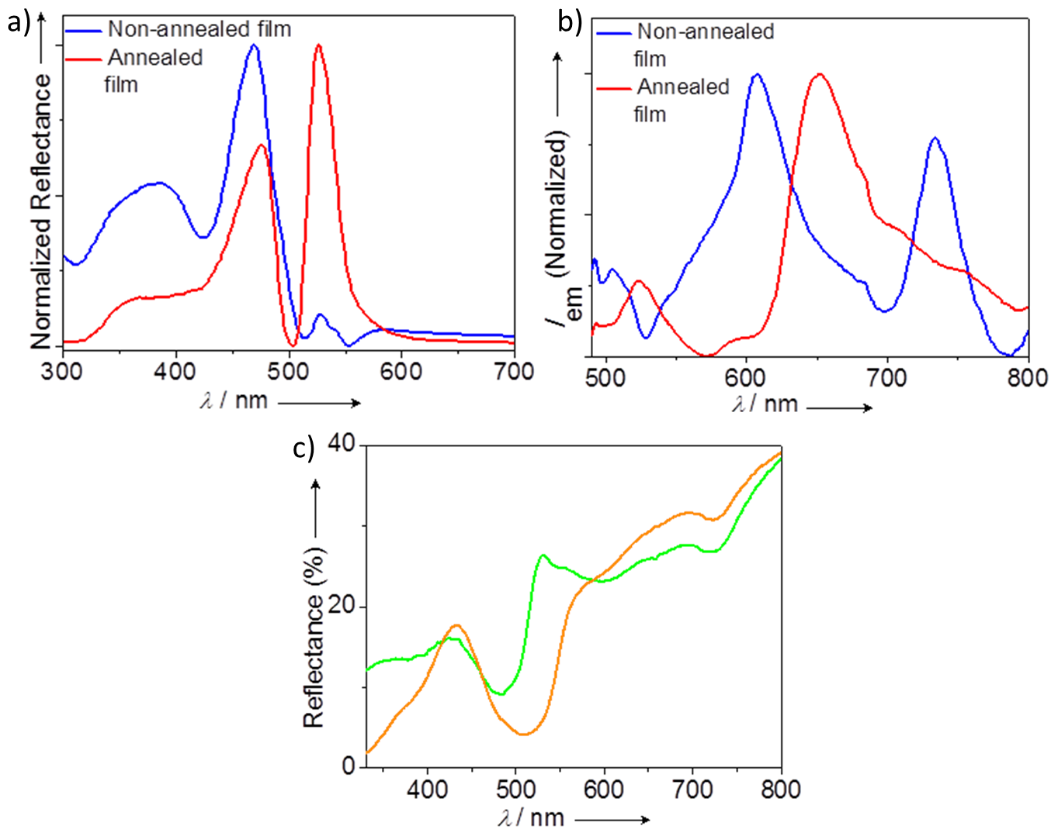

Figure 3.7. a) Normalized reflectance and b) fluorescence spectra of the annealed and non-annealed films. c) Reflectance spectra of annealed film taken at normal angle (green) and at angle 45° (orange red).

Further heating of the annealed film (re-annealing) did not show any change in the emission profile (**Figure 3.8f**). During the heating process, a gradual decrease in the emission intensity at 577 nm is observed and upon cooling back from the molten state, a gradual increase in emission intensity at 650 nm is observed (**Figure 3.8b** and **d**).

Interestingly, the absorption spectrum of the annealed film showed a broad absorption particularly in the region of 350 - 600 nm which extends towards the NIR region with a weak band at 730 nm. On the other hand, the non-annealed film did not show any prominent absorption bands in the NIR region. This observation indicates that annealing resulted the formation of more hierarchically ordered aggregates which can absorb in the NIR region (**Figure 3.8e**).

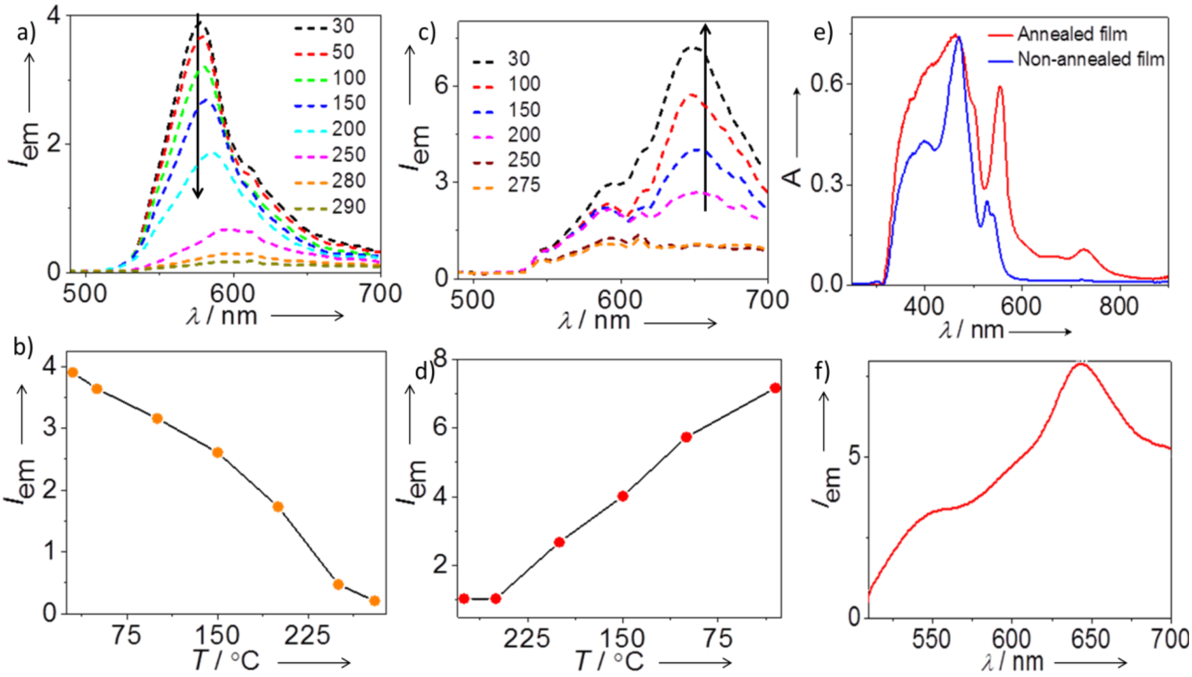

Figure 3.8. a, c) Fluorescence spectral changes during heating and cooling of Bodipy-3 (powder state), respectively. b, d) Emission intensity variation during heating (monitored at 575 nm) and cooling (monitored at 650) processes, respectively. e) Absorption spectra of the annealed and non-annealed film and f) Emission spectrum of the re-annealed film.

In order to understand the nature of the luminescent aggregates, excitation-emission matrix scan experiment has been carried out. From the results, the contour plot reveals the formation of different aggregates upon annealing the film (**Figure 3.9b**). The non-annealed film has got absorption at 350-450 nm corresponding to aggregates and the emission around at 600 nm. Also an absorption in the region of 420-440 nm can be seen with an emission in the NIR region at 730 nm for the non-annealed film (**Figure 3.9a**). Upon annealing, the dimer aggregates is no longer seen in the contour plot, instead new aggregates which absorbs in the region of 340-410 nm with minor contribution above 450 nm, and emitting exclusively at 650 nm can be visualized (**Figure 3.9b**).

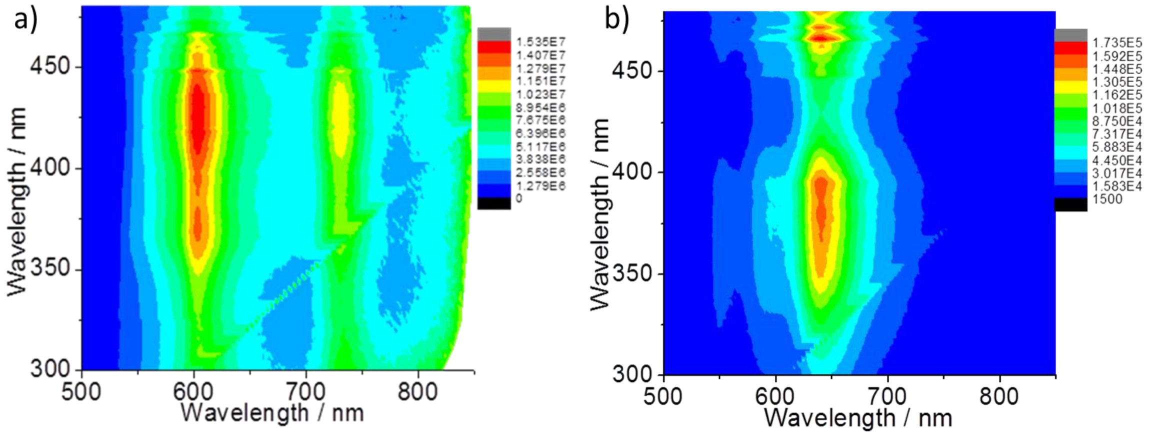

Figure 3.9. Excitation-emission contour plot for a) non-annealed and b) annealed film.

The broadened emission profile of the annealed film (**Figure 1e**) when compared with the non-annealed film indicates the possibility of excimer formation which is also supported by the higher lifetime value observed for the annealed film. More orderly packed structures with greater chromophore interaction might be the reason for the red-shifted emission of the annealed film.

3.3.2.2. Lifetime and Quantum Yield Measurements

The non-annealed film which exhibited yellow emission has an absolute fluorescence quantum yield (φ_f) of 0.09 (± 0.009). The quantum yield value was estimated based on the de Mello method.[32] The annealing process is accompanied by an irreversible luminescence shift (from yellow to red) and a slight change in the quantum yield value from 0.09 to 0.1 (± 0.01).

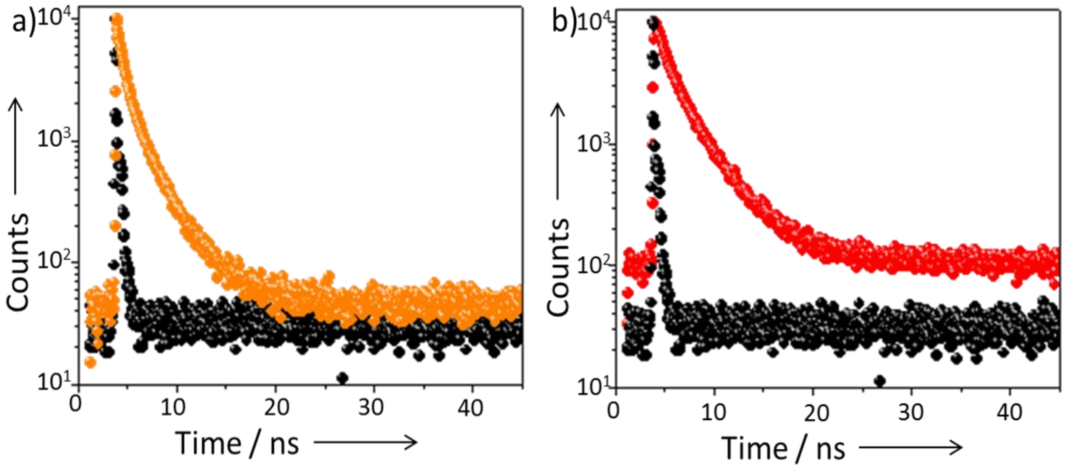

Figure 3.10. Fluorescence lifetime decay profiles of a) non-annealed (λ_{em} = 606 nm) and b) annealed (λ_{em} = 650 nm) films. λ_{ex} = 375 nm.

Lifetime decay profiles (**Figure 3.10**) were monitored exciting with 375 nm LED source. The non-annealed film exhibited a triexponential decay (λ_{em} = 606 nm) with lifetimes of 2.9 (44.9%), 0.66 (26.03%) and 0.02 ns (29.07%). Annealing of the film resulted in the increase in lifetime value. The annealed film also shown a triexponential decay (λ_{em} = 650 nm) with lifetimes of 3.45 (57.1%), 6.22 (11.77%) and 1.31 ns (31.13%).

3.3.3. FT-IR Spectral Studies

The typical broad hydrogen bonded amide NH-stretching band which appeared around 3332 cm^{-1} along with the free NH band at 3417 cm^{-1} for the non-annealed powder (**Figure 3.11c**). Annealing resulted in the breaking of hydrogen bonds; the former broad band gradually disappeared followed by the predominance of free NH-stretching band.

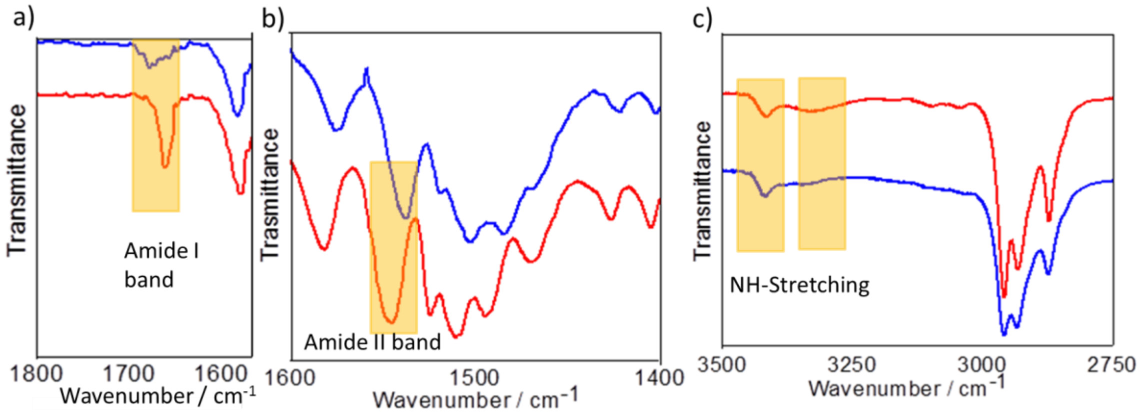

Figure 3.11. FT-IR spectral regions correspond to a) amide I, b) amide II and c) NH-stretching, for the annealed (blue) and non-annealed (red) **Bodipy-3** powder states.

Also the characteristic amide I band which appeared as a hydrogen bonded broad band at 1661 cm^{-1}, got shifted to a narrow band at 1678 cm^{-1} indicating the breakage of hydrogen bonds in the assembly up on annealing (**Figure 3.11a**). This is again confirmed by the observed shift of the amide II band to 1538 cm^{-1} which initially appeared for the non-annealed powder at 1546 cm^{-1} (**Figure 3.11b**).

3.3.4. Basic Characterization of Annealed Powder

In order to rule out any sort of decomposition during the annealing process, we have carried out the TGA analysis which did not show any weight loss even up to 300 °C (**Figure 3.12c**). Also, the annealed powder was characterised with ^{1}H NMR, ESI-MS and UV-vis spectroscopic methods and compared with the respective analysis on non-annealed powder (**Figure 3.13, 3.12a, b** and **d**). The ESI-MS analyses of both the annealed and non-annealed powder in chloroform-methanol solvent mixture have shown same pattern of fragments including molecular ion peak at 760.41. Both the annealed and non-annealed powder were individually characterised by absorption spectroscopy by dissolving in chloroform and rule out any molecular decomposition for the annealed powder.

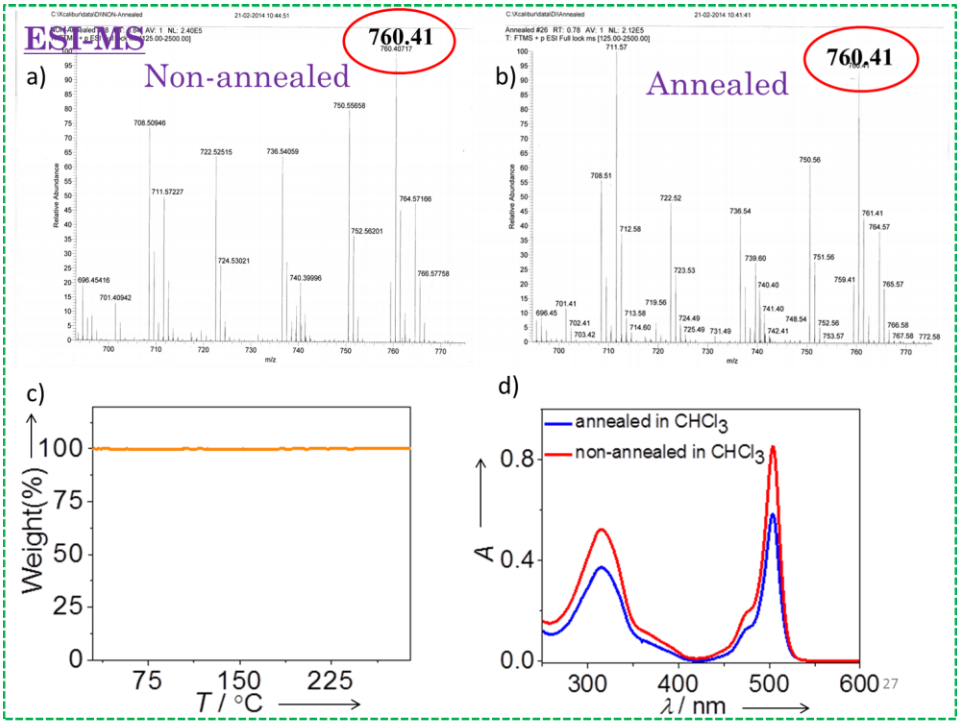

Figure 3.12. ESI-MS of a) non-annealed and b) annealed powder, c) TGA of annealed powder and d) absorption spectral comparison of the annealed and non-annealed powder dissolved in chloroform ($c = 1 \times 10^{-4}$ M).

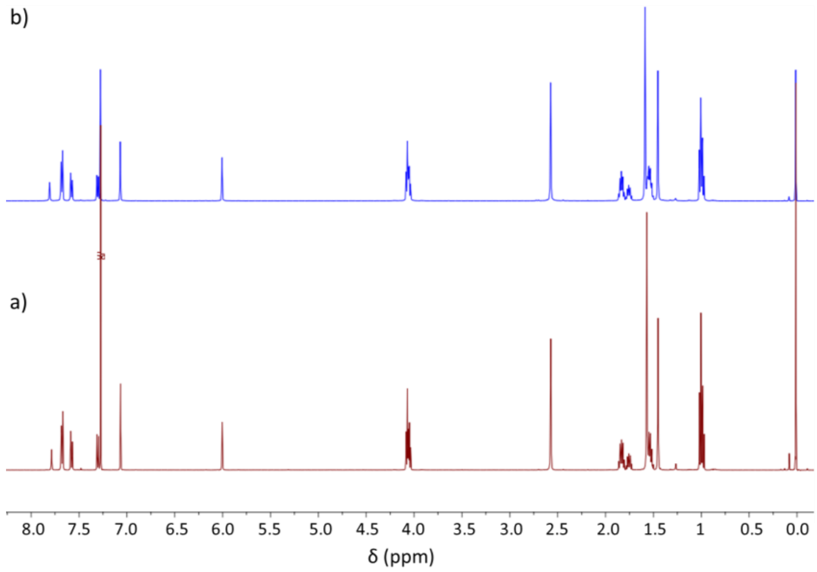

Figure 3.13. ^{1}H NMR spectral comparison of the annealed (blue) and non-annealed (red) powder in $CDCl_3$.

3.3.5. DSC and X-ray Diffraction Analyses

The thermal behavior of the molecule was studied by differential scanning calorimetry (DSC) with a constant heating and cooling rates of 5 °C min^{-1}. In the first heating process of the non-annealed powder, a clear endothermic transition ($\Delta H = 13.63$ J/g) was observed at 215 °C which then lead to an isotropic state at 272 °C ($\Delta H = 49.3$ J/g) (**Figure 3.14a**). This means a clear phase change at a temperature of 215 °C which in turn is supported by variable temperature small angle X-ray diffraction studies (SAXS). Cooling does not lead to the sharp crystallization at 246 °C ($\Delta H = -13.9$ J/g) indicating the slower rate requirement for the reorganization of the molecular packing. Reheating of the annealed sample (**Figure 3.14b**) has shown a broad melting transition at 258 °C ($\Delta H = 26.7$ J/g) which demonstrates a different phase formation after the first annealing process. The absence of crystallization peak in the DSC trace of the annealed powder on cooling may be because of the need for a much slower cooling rate for the crystallization.

In order to understand the cubic to lamellar phase transitions, variable temperature small angle X-ray scattering (SAXS) analysis of the non-annealed powder has been carried out (**Figure 3.14c**). The initial non-annealed powder has shown reflections at *d*-spacing values of 21.6 and 16 Å at room temperature matching with the *d*-spacing ratio of 1: $1/\sqrt{2}$ (cubic phase).[33] At 220 °C, the *d*-spacing values changes dramatically to 35.5 and 18.3 Å matching with the ordered lamellar packing ratio of 1: ½.[34] The, WAXS analysis also supports the less crystalline nature of the annealed powder when compared to the non-annealed powder (**Figure 3.14d**). In the case of WAXS analysis of the annealed powder, the new intense peak at 2θ value 17.37° corresponds to a *d*-spacing value of 5.1 Å which is closely related to the distance observed between the methyl group in Bodipy with acetylenic part due the CH···π interaction (5.25 Å) in the crystal structure. The above particular peak is absent in the WAXS pattern of the non-annealed powder, indicating the fact that annealed powder has more CH···π interaction than the non-annealed one. Moreover, a prominent peak correspond to the 2θ value 23.56° for the non-annealed powder is a measure of the extent π-π stacking, existing in the non-annealed powder. The *d*-spacing value corresponding

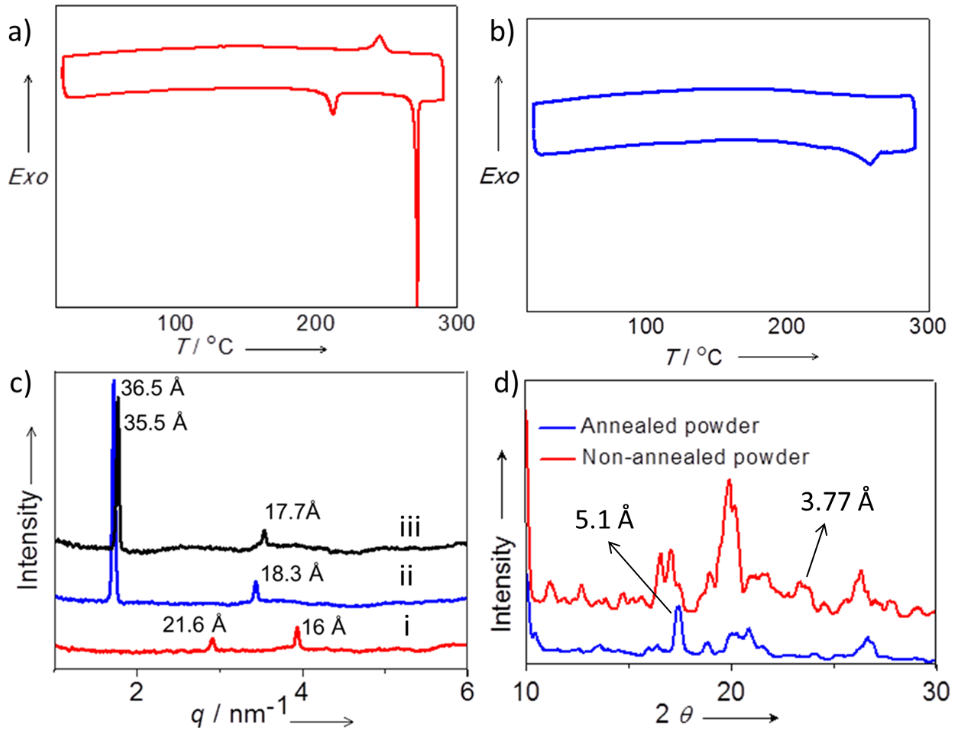

Figure 3.14. DSC of a) non-annealed and b) annealed powder, c) variable temperature SAXS analysis of non-annealed powder, i) at 25 °C, ii) at 220 °C and iii) cooled back to 25 °C. d) WAXS analysis of annealed and non-annealed powder.

to the above peak is found to be 3.77 Å, which is matching with the observed π-π stacking distance of 3.66 Å in the single crystal analysis. The absence of the above mentioned prominent peak in the WAXS profile of annealed powder indicates the probability of less π- π stacking in the annealed powder.

Single crystal analysis of **Bodipy-3** crystal (red colored from toluene) revealed as monoclinic C 2/c space group with a = 41.831(3) Å, b = 12.1742(7) Å, c = 31.758(2) Å, α = 90°, β = 91.874(4)°, γ = 90°. The analysis was conducted at low temperature (150 K) to reduce the vibrations caused by alkyl chains in determining the structure. The unit cell consists of 16 molecules which are arranged in a parallel fashion through NH-CO hydrogen bonding. In the parallel arrangement, the two adjacent molecules are arranged in a tilted fashion such that the angle between the two bodipy chromophores are 87° with a separation distance of 6.5 Å. Correspondingly, the orthogonal *meso* phenyl group also makes an angle of 68° with its counterpart. This makes the strong interaction between chromophores where the possible twisted direction of their transition dipolemoment ensures a J-type packing (θ <= 54.7°) in the extended crystal structure (**Figure 3.15**). Additionally, two molecules are also arranged in an anti-parallel manner where N-H···F-B hydrogen bonding interaction is possible along with strong CH-π interaction between the Bodipy methyl group and acetylenic parts (5.25 Å). Apart from this, another CH···π interaction is possible between the two phenyl groups in the phenyleneethynylene part. The distance between the centroids of pyrrole ring of the Bodipy and the phenyl group of the phenylene acetylene part is found to be 3.64 Å which correspond to that of the π-π stacking interaction. In the crystal packing where the molecule is packed in anti-parallel manner, the distance between chromophores in the same plane along the same

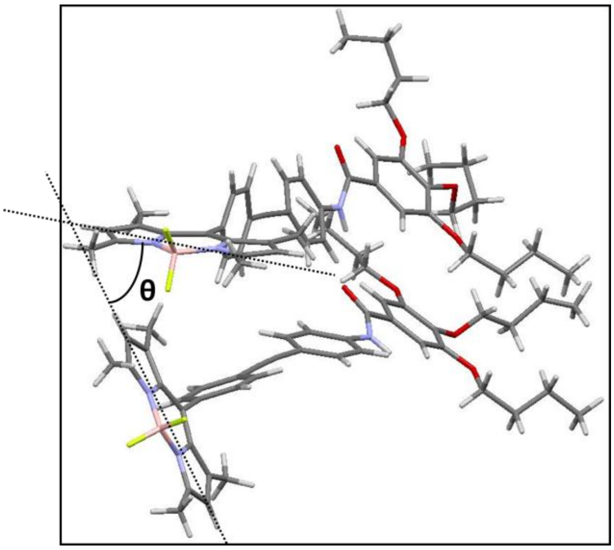

Figure 3.15. Angle between transition dipolemoments of two parallel **Bodipy-3** molecules.

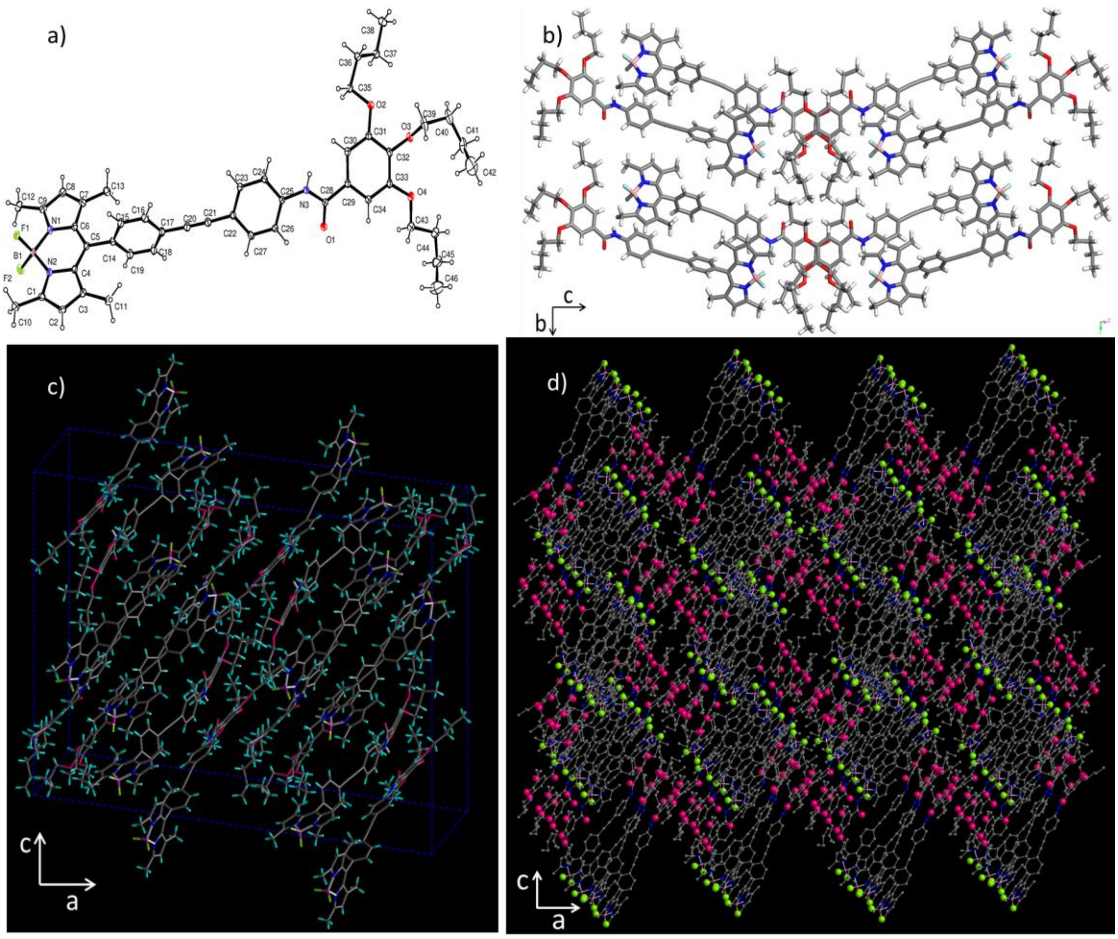

Figure 3.16. a) ORTEP view of **Bodipy-3**, b-d) molecular packing viewed from different axes.

direction is found to be 12.2 Å. On the other hand, distance between chromophores which are lying in the same plane but in opposite direction is 16 Å. Overall, **Bodipy-3** is packed in an anti-parallel manner with predominant CH···π stacking (4.8 Å).The combined effect of all the available interactions in the crystal structure is crucial in determining the supramolecular ordering and the ultimate formation of 2D planar crystals with a thickness of 56 nm (**Figure 3.20c**). The packing growth is along the diagonal *ac* plane (viewed through a [010] plane) as shown in the **Figure 3.16c, d.**

The fluorescent property of annealed photonic material has been utilized to make reversible thermochromic ink by using PEG as binder (10%) and EtOH (90%) as dispersant where PEG acts as a flexible medium to switch between two different aggregates. Letters written with this ink over a filter paper, appeared as red under UV light. However, upon gradual heating to 80 °C over a hot plate, the luminescence shifts to yellowish green which indicates the formation of aggregates similar to that of the initial non-annealed state. Heating leads to evaporation of ethanol and as a result de-swelling of the layered photonic structure may takes place in presence of PEG, which alters the molecular packing. When the substrate is again exposed to ethanol vapor, swelling of PEG takes place and thereby attains the initial extended layered photonic structure with red luminescence (**Figure 3.17** and **video 2**).[35] The process can be repeated many times. The same process can also be applied over alumina substrate. The fluorescence of the annealed powder cannot be reversed by solvent alone.

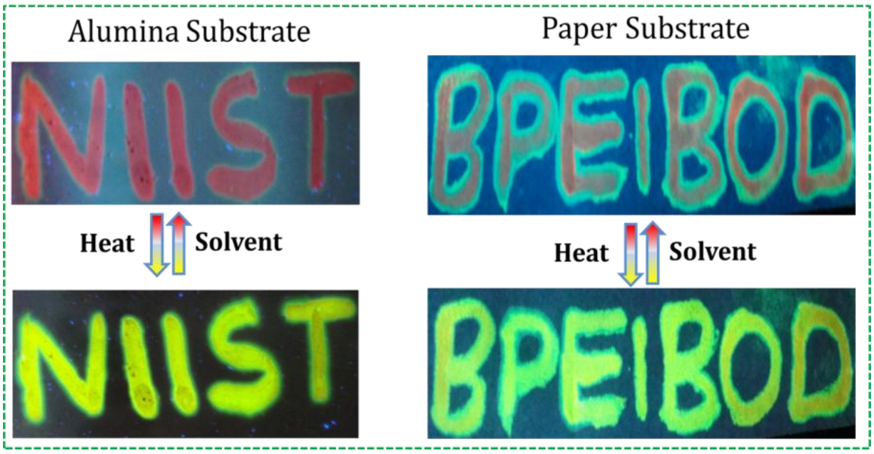

Figure 3.17. Application of annealed powder as stimuli responsive fluorescent ink.

3.3.6. Morphological Analysis

Bodipy-3 forms good film in toluene solution and under fluorescent microscope the film appeared as yellowish orange blocks (**Figure 3.18a**). The fluorescent

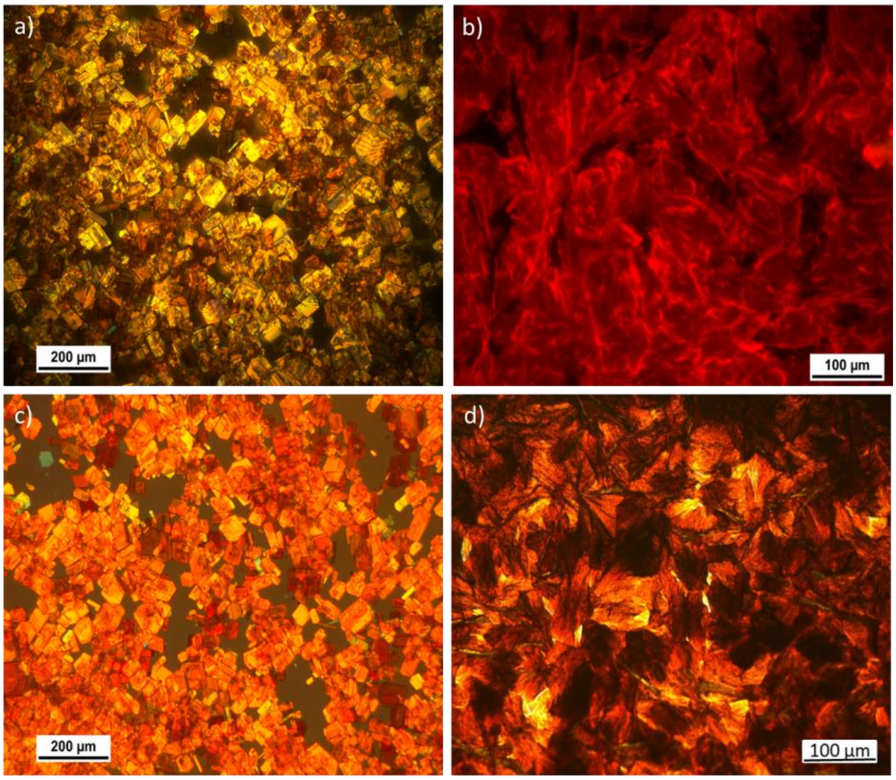

Figure 3.18. Fluorescent microscopic images of a) non-annealed and b) annealed films. c and d) Corresponding images under polarized light, respectively.

microscopic image of the annealed film exhibited layered structure with intense red emission (**Figure 3.18b**). The red emission is particularly confined towards the edges of the layered structures indicating the light propagating nature of the photonic material. The emission confinement can be particularly seen in the annealed film than that of the non-annealed film (**Figure 3.18a, b**).

Also, the polarizing optical microscopic (POM) image of the annealed film surface has shown birefringence with varying light intensities (**Figure 3.18d**) which may be an indication of the anisotropic light propagation property of **Bodipy-3**.[36-37] The non-annealed film has also shown birefringence under polarized optical microscope (**Figure 3.18c**).

SEM analysis of the annealed powder has shown highly ordered two dimensional blocks from the disordered clumsy looking aggregates (**Figure 3.19**). This means that the thermal annealing resulted in the more hierarchically ordered molecular aggregates (Supported by SAXS with intense reflection in the lower angle, **Figure 3.14C**).

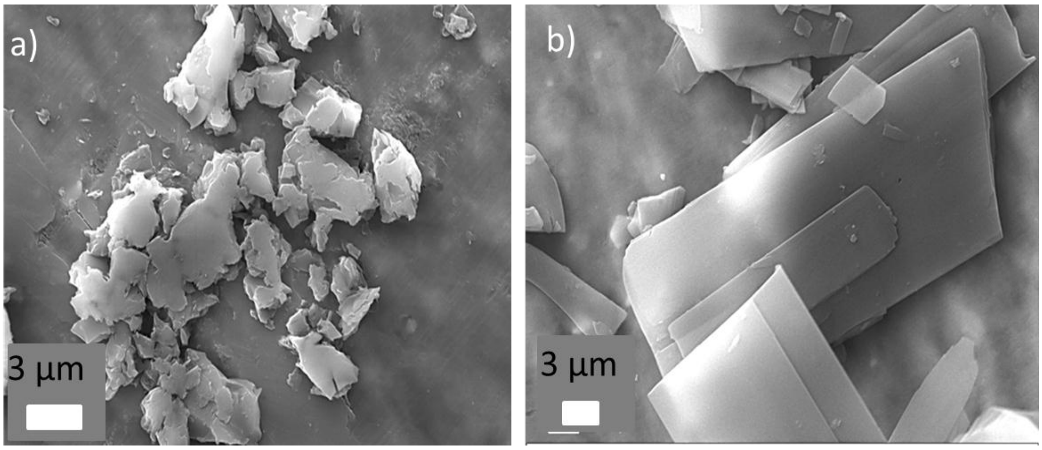

Figure 3.19. SEM images of a) non-annealed and b) annealed powder.

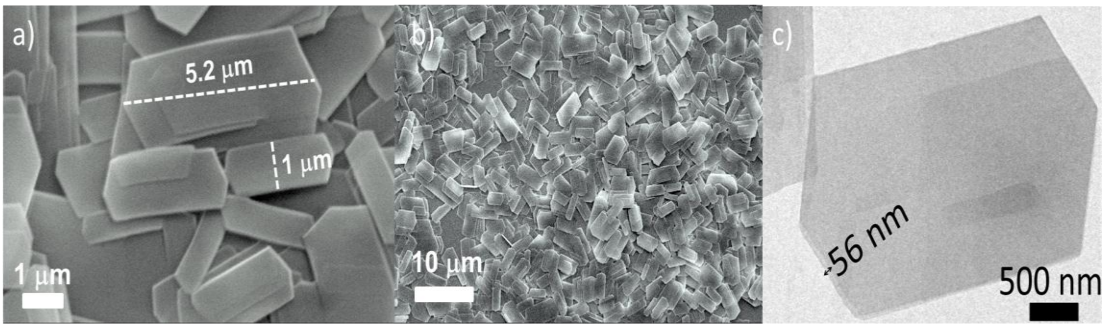

Figure 3.20. a, b) SEM and c) TEM images of aggregates of **Bodipy-3** self-assembled in cyclohexane.

In order to understand the periodicity of the layered structure, we have carried out both SEM and AFM analyses of the annealed film. The AFM cross-sectional area has shown periodic structures both in the micro and in the nano-domains (**Figure 3.21b, d**).

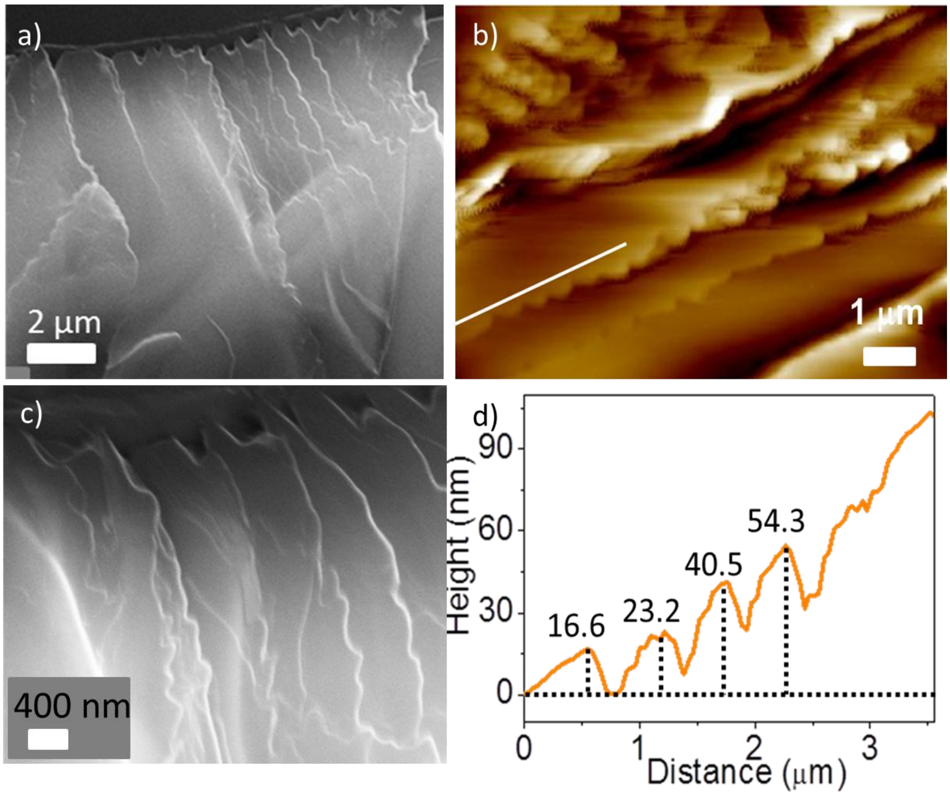

Figure 3.21. a, c) SEM images of the annealed films. b, d) AFM cross-sectional analysis of annealed film and height profile for the marked region.

Horizontal line has an average periodicity of the order of 300-400 nm range. This periodicity order comes in the visible region which is attributed to the photonic nature of the annealed film.[15] Infact, this observation is further supported by the SEM analysis (SEM taken at a tilted angle) of the annealed film where the periodic ordering in the micro and nano-domain is fairly visible (**Figure 3.21a, c**). As a result of layered structures with periodicities, angle dependent visible color changes were observed for the annealed film due to multiple reflection of light from different layers. Also based on the thickness of the film, it may be possible to modulate the photonic band gap of this material in the visible range.

Since the molecule exhibits reflection dependent optical changes, we investigated the optical transport properties in the gel state. Polymer gels are better materials for photonic application because of the rapid response towards the changes in the local environment.[38] Also it is known that dyes embedded in polymer matrix exhibit better optical properties.[29,39,40] For this purpose, the annealed powder is doped into polymerized styrene gel matrix by dissolving in styrene where the molecule exists as monomer in millimolar concentration. **Bodipy-3** dissolved in styrene is in-situ photo-polymerised using 2,2-dimethoxyphenylacetophenone as the initiator (0.1 wt%) by exposing to uv light (365 nm) for 40 h so as to form the polystyrene gel (**Figure 3.22c**).[41] The SEM analysis of a film prepared from the diluted gel in chloroform exhibited inverse opal like pattern or honeycomb like structure (**Figure 3.22a, b**).[42] Fluorescence microscopic images have also shown the pattern clearly (**Figure 3.23a**). Interestingly, when analyzed through confocal microscope (inset), periodic light

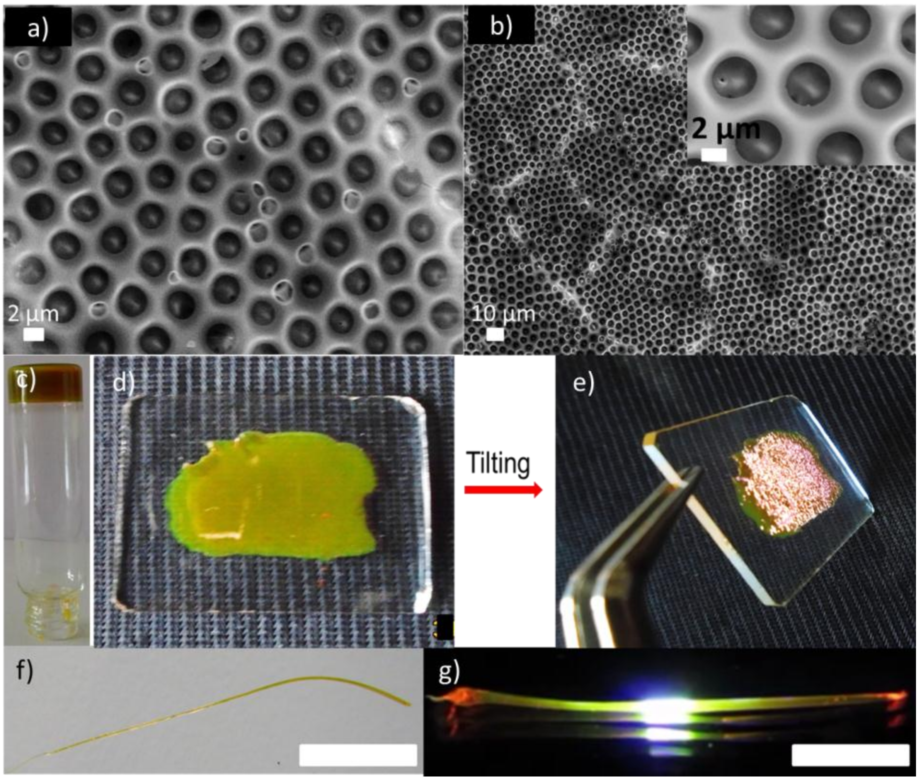

Figure 3.22. a, b) SEM images of the polystyrene gel of annealed powder (**Bodipy-3**) when drop-cast in chloroform solvent, c) **Bodipy-3** annealed powder polystyrene gel. d and e) Polystyrene gel film when drop-cast in chloroform solvent upon tilting shows different color with hidden scratches exposed out. Photographs of macro fibre prepared from viscous chloroform solution of polystyrene gel under f) daylight and exhibiting waveguiding properties under g) UV light, when irradiated at the middle of the fibre. Scale 1 cm for ‘f’ and ‘g’.

intensity variation is observed where some parts appeared as bright and other as dark along the rim (**Figure 3.23a, b**). This may be because of the anisotropic light propagation nature of the photonic material. As expected, this photonic gel film also exhibited day light dual color. An orthogonal view of the film over the glass substrate under day light appeared as green, but a tilted view resulted in a pink tint. It was demonstrated through a scratches made in the surface of film which was barely visible when viewed orthogonally and clearly appeared as reflection of pink light upon tilting (**Figure 3.22d, e**). The photonic property of the material can be modified for security applications as a secret code in determining the authenticity of the document. Thin centimeter long fibers were (**Figure 3.22f**) extruded from the chloroform diluted viscous polystyrene gel. The fibre, when excited at a point with UV light, observed through naked eye that the light intensity is concentrated at its both ends with a red-shift in its wavelength maximum (**Figure 3.22g**). The excited point appeared as yellowish-green emissive while both ends appeared as orange-red. The same fibre is observed through microscope and excited at the middle of the fibre confirming the propagation of light towards opposite ends (**Figure 3.23c, d**). The corresponding

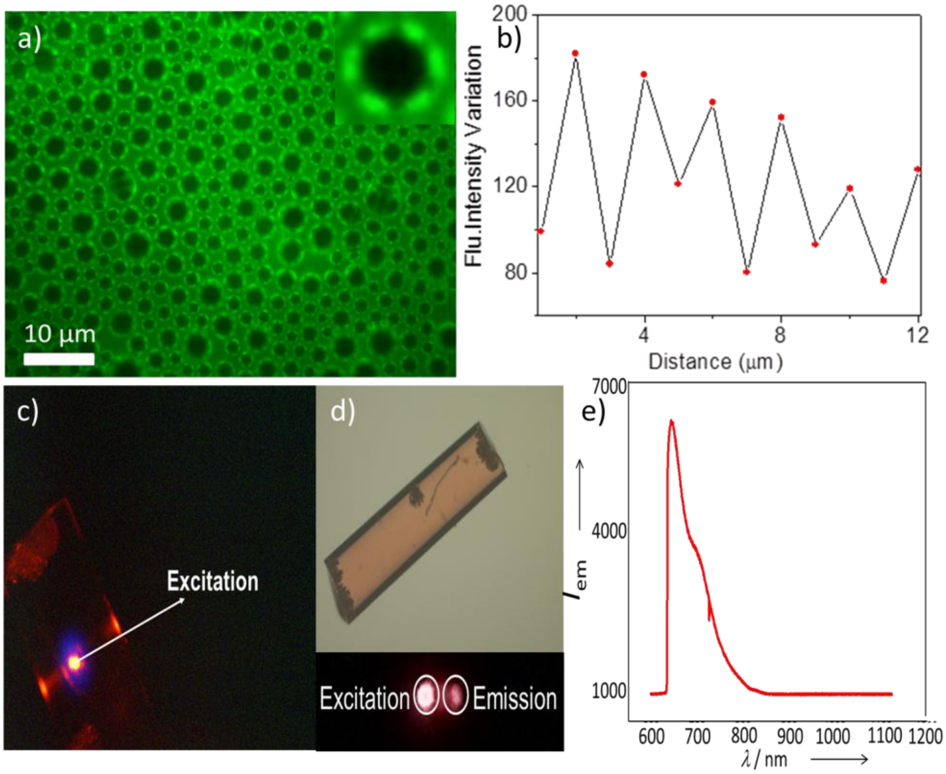

Figure 3.23. a) Confocal microscopic image of the chloroform film of polystyrene gel, b) light intensity variation corresponds to the zoomed circle in **Figure 3.23a**. c) Waveguiding in macro fibre and d) the fibre under ordinary light microscope (mobile phone camera captured image correspond to the excitation and emission position is shown in the downside). e) Output emission profile corresponds to the waveguiding property in fibre.

emission profile recorded for the excitation at the middle of the fibre also confirmed the red-shifted broad emission coming from the fibre (**Figure 3.23e)**. As the excitation source is moved through the fibre along one direction, a progressive blue-shift in the emission maximum is observed at a particular end where the excitation source was heading on (**video 3**). The moment when the excitation source slips out of the fibre, there is no concentration of light intensity at both ends, indicating that the light seen at both tips of the fibre is attributed to the propagation of light along the fibre and not through any scattering event (**video 3**).

3.3.7. Optical Waveguiding Studies

The optical waveguiding properties of microcrystals of **Bodipy-3** prepared from toluene is examined using a home-built photoluminescence microscopy system (**Scheme 3.3**).[5] The prepared microstructures were illuminated with two different laser source (532 nm and 633 nm) using high numerical aperture oil immersion objective lens (100x, 1.3NA). The motivation behind choosing two different excitation wavelengths (as per absorption spectra shown in **Figure 3.24j**) was to study both the passive and active waveguiding effect. The absorption spectrum of the microcrystals shows fairly good absorption at 532 nm and weak absorption around 633 nm. The emission profile of the microcrystal is observed as broad ranging from 530 nm to the 800 nm region (**Figure 3.24k**) possibly due to the more extended molecular level packing. If the emission wavelength is same as excitation wavelength then it is designated as passive waveguiding, whereas if the emission wavelength are of higher order than excitation wavelength, then it is termed as active waveguiding process.[5,7,23] To ensure the single wavelength illumination, appropriate line filters (Semrock Max line, LL01-532) were introduced in the excitation path and corresponding edge filter (Semrock Razoredge, LP03-532RU) was engaged in collection path to reject the elastic scattered light while probing active emission waveguiding properties. For passive waveguiding experiment, we illuminated the planar microcrystal with 532 nm laser source. **Figure 3.24a** shows the optical image of the microstructure with 532 nm laser source. The laser beam was focused approximately at the middle of the plane structures (shown as 'Ex.' in **Figure 3.24a**).

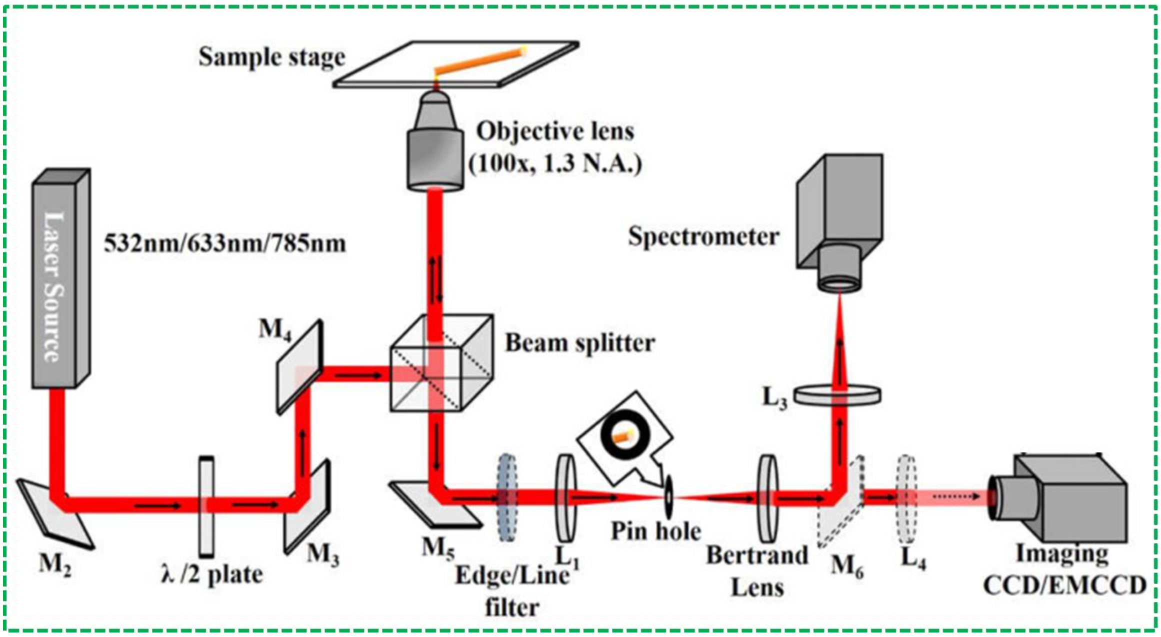

Scheme 3.3. Home built optical microscope set-up used for imaging and measuring waveguiding properties (Adapted from reference 5).

In this particular case there is no propagation of light along the microcrystals observed. Further, even after varying the excitation position along the corners of the planar microstructures (**Figure 3.24b, c** and **d**), no passive propagation of light signal was observed. This observation is confirmed by the absence of spectroscopic signature at the other end of illumination point.

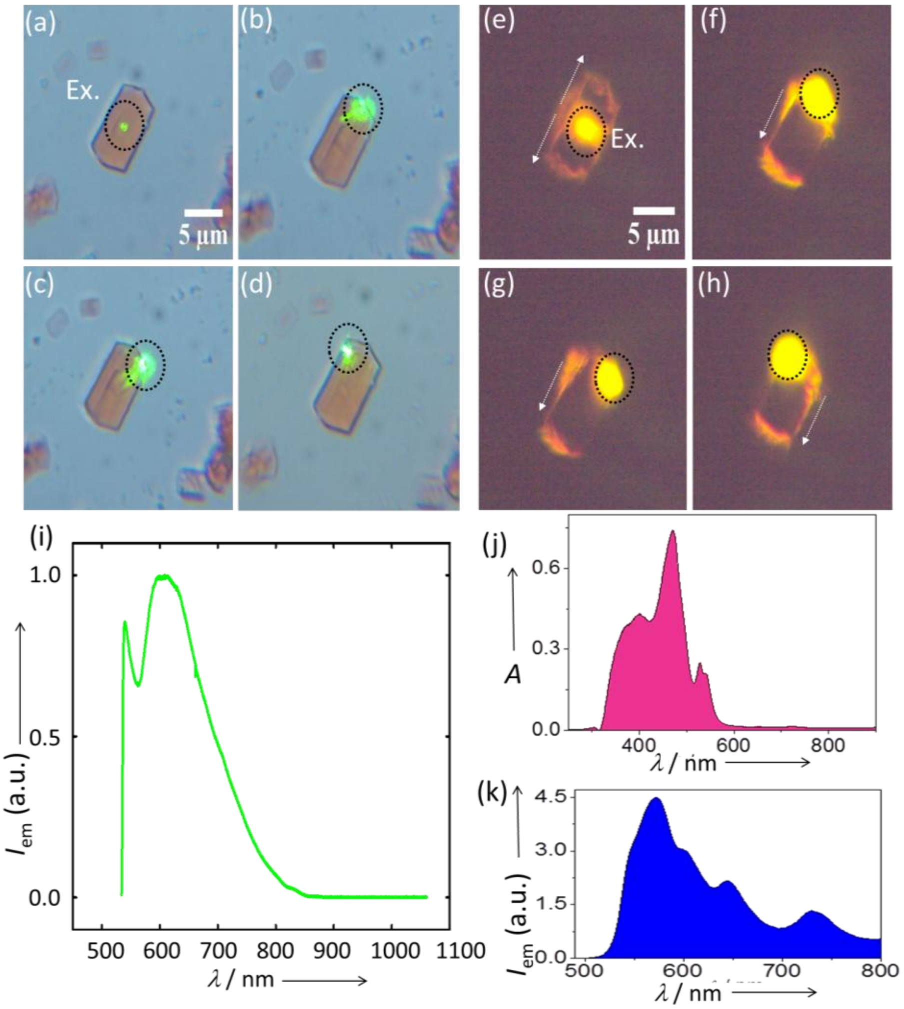

Figure 3.24. Optical images showing excitation at different locations for the planar microcrystal using 532 nm excitation, a-d) passive mode and e-h) active mode. i) Photoluminescence spectra from the emission end. j) Absorption and k) emission spectra of the planar microcrystals.

To probe active waveguiding, the corresponding edge filter was introduced in the collection optics to reject the elastic scattered light. **Figure 3.24e**, represents the captured optical image with laser excitation at the centre of microstructure (denoted as ‘Ex.’). The out-coupled light of higher order wavelength is collected from the edges of the planar crystal. In addition to that, varied the excitation location along the edge of the crystal as in the previous case. Captured the optical images in their respective cases (**Figure 3.24f, g** and **h)** and recorded the spectroscopic signature from the emission end which clearly shows the higher ordered wavelengths at the collection output end (**Figure 3.24i**). It is seen that the out-coupled light can be routed in all the direction by simply varying the excitation location along the planar microstructures, which can have profound implication in nanoscale optical routers, optical modulators, integrated photonic circuits and other optoelectronic applications.[2,3,14,23]

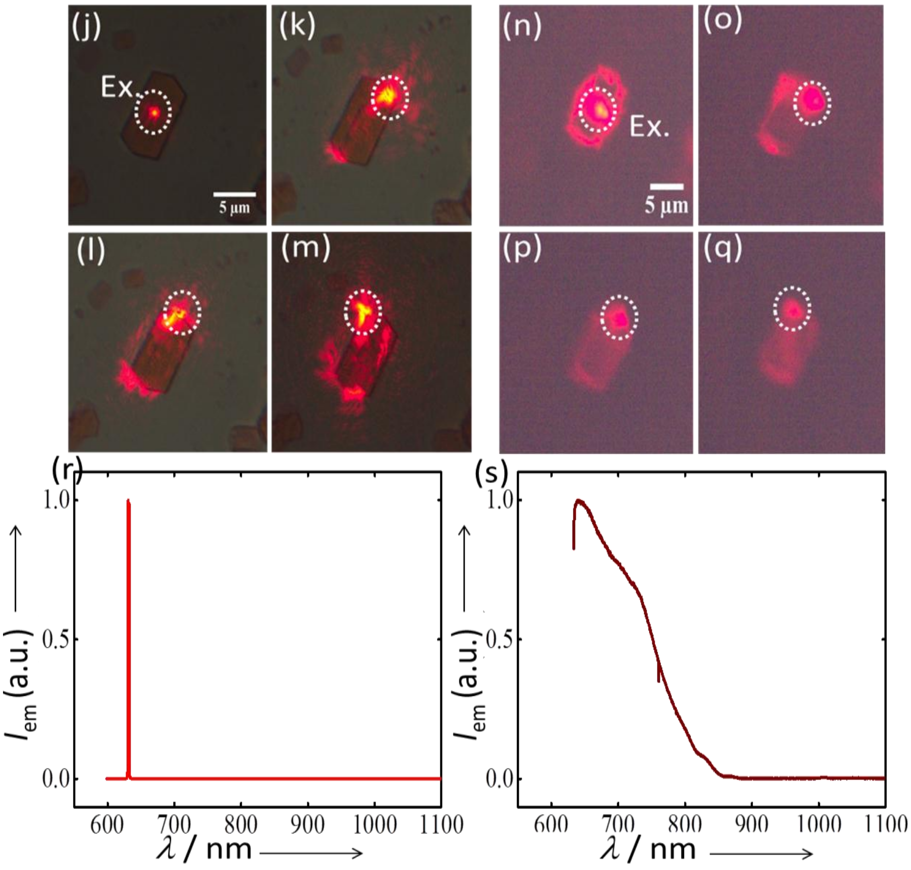

Figure 3.25. Optical images showing excitation at different locations for the planar microcrystal using 633 nm excitation, j-m) passive mode and n-q) active mode. Luminescence output features for r) passive and s) active domains.

The microcrystals were illuminated with 633 nm laser source and repeated the experiment similar to the case of 532 nm excitation. Interestingly, it is observed that planar microcrystal showed duality in light transportation behaviour i.e. light can be manipulated in both passive and active domain. The corresponding optical images are shown in **Figure 3.25j-q** and the respective spectral features were recorded in both domain (shown in **Figure 3.25r** and **s**). The dual nature in its optical waveguiding properties can be attributed to coupling efficiency of incident wavelength and molecular aggregates. Additionally, the crystal-plane dependent light propagation in the microscale planar crystal is observed in the passive domain when excited with 633 nm laser source (**Figure 3.25j-m**). Importantly, such crystal dependent light propagation behaviour can have further implication in realization of optical planar diodes, optical interconnects and photodetectors.[43,44]

With the above data, it is possible to comprehend the optical transport phenomena in planar microcrystals of **Bodipy-3** in the following way. If the illumination wavelength is close to the absorption band, it leads to strong coupling between the incident electromagnetic radiation and the molecular aggregates.[45] Adding to this, organic molecules have large oscillator strength, greater exciton binding energy and exciton splitting energy, size effect and hence leads to formation of long range Frenkel exciton-polaritons.[44] Therefore, active waveguide effect is more dominating when the excitation wavelength are close to absorption band, which is reflecting from the experiments conducted using 532 nm laser excitation. Interestingly, as we move further away from the absorption band, the coupling strength and other associated process show drastic decline, which leads to dualism in waveguiding nature associated with organic molecular aggregates, which is evident in the case of 633 nm excitation. Following this trend, we can anticipate that the planar microcavity would be working as a microscale passive light transporter for specific excitation wavelength far away from absorption. Such a typical way of excitation dependent waveguiding phenomena pave a way to exploit these layered microstructures along with prevailing inorganic layered materials for designing flexible devices, nanoscale optical sensors, routers, antenna and for various photovoltaics applications.[9,11,14,21]

3.4. Conclusion

The **Bodipy-3** based gelator described here exhibited both photonic crystal and waveguiding properties in the gel as well as in the crystalline states. The annealed film of the self-assembled **Bodipy-3** showed angle dependent color change and photoluminescence shifts. The AFM cross-sectional and SEM analyses of the annealed film showed the nano and micro-periodicity associated with the photonic structure as the reason for the angle dependent color changes. The fluorescent property of the annealed photonic material has been utilised to prepare a stimuli responsive ink. An in-situ photo-polymerized gel, processed from the annealed material when made into macro fiber and honey-comb pattern, also demonstrated the light propagating nature of the molecule. The planar micro 2D crystals developed from the molecule exhibited distinct optical waveguiding properties with wavelength dependent waveguiding phenomena. Furthermore, these planar microstructures show significant dependence of light propagation as per crystal plane. The crystal dependent light manipulation may have implications in remote excitation of various optical phenomena. Most importantly, these results may motivate scientists to develop optical planar diodes which are useful for the design of flat geometry assisted flexible/wearable optoelectronic devices and planar chip based integrated optical circuits.

3.5. Experimental Section

3.5.1. Synthesis – General Procedures

General procedure of the drying and purification of solvents, and the purification of all synthesized molecules by column chromatography are described in **Chapter 2**.

3.5.1.1. Synthesis of Methyl 3,4,5-tributoxybenzoate (11)

Compound **10** (5 g, 27.2 mmol) and potassium carbonate (18.73 g, 135.8 mmol) were stirred in a 250 mL round bottom flask containing 80 mL dry DMF. The reaction mixture was stirred for 20 minutes under room temperature and added 1-bromobutane (13.02 g, 95.03 mmol) dropwise. It was then heated to 90 °C for 24 h. After cooling to room temperature, the reaction mixture was poured into water and extracted the organic part with chloroform repeatedly. Washed the organic layer with enough water and brine solution and dried over anhydrous sodium sulphate. Removed the solvent under reduced pressure and then subjected to purification by column chromatography (silica gel, 1% ethylacetate-*n*-hexane) to afford compound (**11**) as a colorless solid (Mp, 70 °C). Yield: 78%, ^{1}H NMR (500 MHz, $CDCl_3$): δ = 7.25 (*s*, 2H, Ar-*H*), 4.03-4.00 (*m*, 6H; $-OCH_2-$), 3.89 (s, 3H; $-OCH_3$), 1.84-1.71(*m*, 6H; $-CH_2-$), 1.49-1.26 (*m*, 6H, $-CH_2-$), 0.89-0.88 (*m*, 9H, -

C*H*$_3$) ppm. HRMS (ESI): calculated for $C_{20}H_{32}O_5$ $[M]^+$: m/z = 352.22497, found: 352.22380.

3.5.1.2. Synthesis of 3,4,5-tributoxybenzoic acid (12)

Compound **11** (6 g, 17.03 mmol) was refluxed in ethanol (60 mL) with KOH (3.1 g, 56.2 mmol) in a 250 mL round bottom flask for 12 h. Cooled to normal temperature and acidified the reaction mixture with dilute HCl, again cooled in ice-cold water and the precipitate was filtered, washed with water and dried under vacuum to get the pure product **12 (**Mp, 65 °C). Yield: 80%, ^{1}H NMR (500 MHz, $CDCl_3$): δ = 7.25 (*s*, 2H; Ar-*H*), 4.08-4.03 (*m*, 6H; -OC*H*$_2$-), 1.84-1.71 (*m*, 6H; -C*H*$_2$-), 1.49-1.26 (*m*, 6H; -C*H*$_2$), 0.89-0.88 (*m*, 9H; -C*H*$_3$) ppm. HRMS (ESI): calculated for $C_{19}H_{30}O_5$ $[M]^+$: m/z = 338.20932, found: 338.20850.

3.5.1.3. Synthesis of 3,4,5-tributoxy-*N*-(4-iodophenyl)benz--amide (13)

Compound **12** (3 g, 8.87 mmol) was dissolved in dry dichloroethane (20 mL) and taken in a 250 mL round bottom flask under argon atmosphere. Thionyl chloride (1.93 mL, 26. 61 mmol) was added dropwise to the reaction chamber and continued stirring for 5 h. Excess solvent and thionyl chloride was purged out by argon gas and dried completely in vacuum. It was then re-dissolved in 20 mL dry toluene and added to another reaction chamber containing 4-iodoaniline (2.33 g, 10.64 mmol) dissolved in toluene (20 mL) and 2 mL of dry triethylamine, stirring continued for another 12 h under argon atmosphere. After completion of the reaction, the solvent toluene was evaporated and residue was extracted using chloroform. The organic layer was washed with water and brine solution and dried over anhydrous sodium sulphate. Purified by silica column chromatography and eluted the compound with 1% ethylacetate-*n*-hexane solvent system to get the pure product **13** as a colorless powder (Mp, 108 °C). Yield: 50%, ^{1}H NMR (500 MHz, $CDCl_3$): δ = 7.71 (*s*, 1H; -N*H*), 7.67-7.66 (*m*, 2H, Phenyl-*H*), 7.426-7.409 (*m*, 2H; Phenyl-*H*), 7.02 (*s*, 2H; Ar-*H*), 4.05-4.00 (*m*, 6H; $-OCH_2-$) 1.83-1.71(*m*, 6H; $-CH_2-$), 1.55-1.48 (*m*, 6H; $-CH_2-$), 1.0-0.95 (*m*, 9H; $-CH_3$) ppm. HRMS (ESI): calculated for $C_{25}H_{34}INO_4$ $[M]^+$: m/z = 539.15325, found: 539.15250.

3.5.1.4. Synthesis of 3,4,5-tributoxy-*N*-(4-((trimethylsilyl)-ethynyl)phenyl)benzamide (14)

Compound **13** (1 g, 1.9 mmol), bis(triphenylphosphine)palladium (II) dichloride (130 mg, 10 mol%), and copper (I) iodide (35 mg, 10 mol%) were added to an oven-dried two-neck round bottom flask equipped with a magnetic stirring bar. The round bottom flask was then sealed with a rubber septum, evacuated and backfilled with argon three times. Degassed triethylamine (10 mL) was added followed by degassed THF (20 mL). After stirring for 5 minutes at room temperature, trimethylsilyl acetylene (0.4 mL, 2.8 mmol) was added dropwise into the reaction mixture and continued stirring for 12 h. The reaction mixture was extracted using chloroform and washed with dilute hydrochloric acid. The organic layer was washed with brine and dried over anhydrous sodium sulphate and then evaporated under reduced pressure. The residue thus obtained was purified by silica gel column chromatography using 2% ethylacetate-*n*-hexane as an eluent (Mp, 102 °C). Yield: 75%, ^{1}H NMR (500 MHz, $CDCl_3$): δ = 7.84 (*s*, 1H; -N*H*), 7.59 (*d*, *J* = 8.5 Hz, 2H; Phenyl-*H*), 7.46 (*d*, *J* = 9 Hz, 2H; Phenyl-*H*), 7.01 (*s*, 2H, Phenyl-*H*), 4.01-3.99 (*m*, 6H; $-OCH_2-$), 1.83-1.71 (*m*, 6H; $-CH_2-$), 1.49-1.43 (*m*, 6H; -C*H*$_2$-), 0.88 (*t*, *J* = 7 Hz, 9H; -C*H*$_3$), 0.25 (*s*, 9H; -Si(C*H*$_3$)$_3$) ppm. HRMS (ESI): m/z calculated for $C_{30}H_{43}NO_4Si$ $[M]^+$: 509.29614, found: 509.29454.

3.5.1.5. Synthesis of 3,4,5-tributoxy-*N*-(4-ethynylphenyl)-benzamide (15)

To a solution of compound **14** (1 g, 1.96 mmol) in 10 mL dichloromethane, KF (2.28 g, 39.2 mmol) in 50 mL methanol was gradually added to it and continued stirring at room temperature for 12 h. After completion of the reaction, the reaction mixture was extracted using chloroform, washed with water, brine and then dried over anhydrous sodium sulphate. Evaporated the solvent under reduced pressure. The residue thus obtained was purified by silica gel column chromatography using 5% ethylacetate-*n*-hexane as an eluent and afforded the compound **15** as a colorless solid (Mp, 75 °C). Yield: 65%, ^{1}H NMR (300 MHz, $CDCl_3$): δ = 7.88 (*s*, 1H; -N*H*), 7.61 (*d*, *J* = 8.5 Hz, 2H; Phenyl-*H*), 7.48 (*d*, *J* = 8.5 Hz, 2H; Phenyl-*H*), 7.01 (*s*, 2H; Phenyl-*H*), 4.02-3.98 (*m*, 6H; -OC*H*$_2$-), 3.06 (*s*, 1H; Acetylenic-*H*), 1.82-1.71 (*m*, 6H; -C*H*$_2$-), 1.47-1.42 (*m*, 6H; -C*H*$_2$-), 0.88 (*t*, *J* = 6.5 Hz, 9H; -C*H*$_3$) ppm. HRMS (ESI): m/z calculated for $C_{27}H_{35}NO_4$ $[M]^+$: 437.25661, found: 437.25461.

3.5.1.6. Synthesis of Bodipy-3

Compound **16** (0.32 g, 0.71 mmol), bis(triphenylphosphine)palladium (II) dichloride (50 mg, 10 mol%), and copper (I) iodide (14 mg, 10 mol%) were added to an oven-dried two-neck round bottom flask equipped with a magnetic stirring bar. The round bottom flask was then sealed with a rubber septum, evacuated and backfilled with argon three times. Degassed triethylamine (30 mL) and THF (50 mL) were added and stirred for 5 minutes at room temperature. Compound **15** (0.37 g, 0.85 mmol) dissolved in 10 mL (1:1) mixture of degassed triethylamine and THF was added and the reaction mixture was stirred at 60 °C for 24 h. The reaction mixture was extracted using chloroform and washed with dilute hydrochloric acid. The organic layer was washed with brine and dried over anhydrous sodium sulphate and then evaporated under reduced pressure. The crude product was then purified by column chromatography using silica gel as adsorbent. The pure compound (**Bodipy-3**) was eluted with 40% dichloromethane-*n*-hexane solvent mixture (Mp, 272 °C). Yield: 32%, FT-IR (KBr): ν_{max} = 3408, 3333, 2953, 2930, 2870, 2210, 1661, 1543, 1522, 1506, 1493, 1466, 1400, 1402, 1331, 1308, 1234, 1194, 1155, 1109, 1086, 1069, 1042, 1017, 983, 945, 838, 813, 765, 755, 708 cm^{-1}; ^{1}H NMR (500 MHz, $CDCl_3$): δ = 7.79 (*s*, 1H; -N*H*), 7.68 (*d*, *J* = 8 Hz, 4H; Phenyl-*H*), 7.58 (*d*, *J* = 8.5 Hz, 2H; Phenyl-*H*), 7.3 (*d*, *J* = 8 Hz, 2H; Phenyl-*H*), 7.07 (*s*, 2H; Phenyl-*H*), 6.0 (*s*, 2H; =C*H*-), 4.08-4.04 (*m*, 6H; -OCH_2-), 2.57 (*s*, 6H; pyrrole-CH_3), 1.86-1.73 (*m*, 6H; -CH_2-),1.45 (*s*, 6H; pyrrole-CH_3), 1.36-1.27 (*m*, 48H; -CH_2-) 1.02-0.97 (*m*, *J* = 6.5 Hz, 9H; -CH_3) ppm; ^{13}C NMR (125 MHz, $CDCl_3$): δ = 165.60, 155.75, 153.33, 143.03, 141.76, 140.85, 138.35, 134.86, 132.57, 132.26, 131.23, 129.59, 128.22, 124.17, 121.38, 119.79, 118.52, 105.83, 90.57, 88.45, 73.22, 69.20, 32.31, 31.37, 19.25, 19.15, 14.61, 13.89, 13.84 ppm. HRMS (ESI): m/z calculated for $C_{46}H_{52}BF_2N_3O_4$ $[M+H]^+$: 760.40983, found: 760.40717.

3.5.2. Characterization Techniques

Instrumental techniques such as NMR, FT-IR, HRMS and MALDI-TOF used for the characterization of molecules are described in **Chapter 2**.

3.5.3. Measurements

Various measurements such as UV-Vis, fluorescence, lifetime, SAXS/WAXS, DSC *etc.* and imaging techniques such as SEM, TEM and AFM are described in **Chapter 2**. The experimental details and the experimental set-up used for the waveguiding studies are explained in **Section 3.3.7 Optical Waveguiding Studies**.

3.5.3.1. Crystal Data of Bodipy-3

The single crystal analysis of the model derivative, **Bodipy-3** was carried out on a Bruker SMART APEX CCD diffractometer with graphite-monochromatized Mo-*K*, λ = 0.71073 Å radiation. The data can be obtained free of charge from the Cambridge crystallographic data centre via www.ccdc.cam.ac.uk/data_request/cif for the **CCDC 1559258.** $C_{46}H_{52}BF_2N_3O_4$, *M* = 759.71, red crystals (plate) with crystal size 0.2 x 0.15 x 0.02 mm, monoclinic, space group C 2/c, a = 41.831(3), b = 12.1742(7), c = 31.758(2) Å; α = 90°, β = 91.874(4)°, γ = 90°. Volume, V = 16164.2(17) Å^3, Z = 16, T = 150(2) K, Reflections collected 118700, θ range for data collection: 1.948 to 25.00°, Absorption correction Semi-empirical from equivalents, Max. and min. transmission: 0.9983 and 0.9828, Refinement method: Full-matrix least-squares on F^2, Data / restraints / parameters: 14229 / 20 / 1009, Goodness-of-fit on F^2 : 0.893, Final R indices [I >2sigma(I)], R1 = 0.0633, wR2 = 0.1542, R indices (all data) R1 = 0.0633, wR2 = 0.1542, $\rho_{calcd.}$ = 1.249 Mg/m^3.

3.6. References

1. a) C. Fenzl, T. Hirsch, O. S. Wolfbeis, *Angew. Chem. Int. Ed.* **2014**, *53*, 2-21; b) J. Ge, Y. Yin, *Angew. Chem. Int. Ed.* **2011**, *50*, 1492-1522; c) E. P. Chan, J. J. Walish, A. M. Urbas, E. L. Thomas, Adv. Mater. 2013, 25, 3934-3947.
2. a) Y. Yan, Y. S. Zhao, *Chem. Soc. Rev.* **2014**, *43*, 4325-4340; b) K. Hwang, D. Kwak, C. Kang, D. Kim, Y. Ahn, Y. Kang, *Angew. Chem. Int. Ed.* **2011**, *50*, 6311-6314.
3. a) Y. S. Zhao, *Organic Nanophotonics: Fundamentals and Applications*, Springer, **2014**.
4. Y. S. Zhao, A. Peng, H. Fu, Y. Ma, J. Yao, *Adv. Mater.* **2008**, *20*, 1661-1665.
5. R. P. Tripathi, A. Dasgupta, R. Chikkaraddy, P. P. Patra, A. B. Vasista, G. P. Kumar, *J. Opt.* **2016**, *18*, 065002.
6. L. K. Van Vugt, B. Piccione, R. Agarwal, *Appl. Phys. Lett.* **2010**, *97*, 061115.
7. R. Chandrasekar, *Phys. Chem. Chem. Phys.* **2014**, *16*, 7173-7183.
8. R. Chikkaraddy, A. Dasgupta, S. Dutta Gupta, G. Pavan Kumar, *Appl. Phys. Lett.* **2013**, *103*, 031112.

9. a) S. S. Babu, V. K. Praveen and A. Ajayaghosh, *Chem. Rev.* **2014**, *114*, 1973–2129; b) Y. S. Zhao, H. Fu, A. Peng, Y. Ma, Q. Liao, J. Yao, *Acc. Chem. Res.* **2009**, *43*, 409-418.

10. H. Liu, J. Kameoka, D. A. Czaplewski, H. Craighead, *Nano Lett.* **2004**, *4*, 671-675.

11. Y. S. Zhao, J. Wu, J. Huang, *J. Am. Chem. Soc.* **2009**, *131*, 3158-3159.

12. D. Singh, D. K. Sharma, S. K. Chaubey, G. P. Kumar, *Opt. Commun.* **2017**, *398*, 112-121.

13. R. P. Tripathi, R. Chikkaraddy, A. Dasgupta, G. Pavan Kumar, *Appl. Phys. Lett.* **2016**, *108*, 031102.

14. J. Clark, G. Lanzani, *Nat. Photonics* 2010, 4, 438-446.

15. A. Seeboth, D. Lotzsch, R. Ruhmann, O. Muehling, *Chem. Rev.* **2014**, *114*, 3037-3068.

16. a) D. C. MacLaren, M. A. White, *J. Mater. Chem.* **2003**, *13*, 1695-1700; b) J. Luthern, A. Peredes, *J. Mater. Sci. Lett.* **2000**, *19*, 185-188; c) I. Fletcher, R. Zink, *In Chemistry and Applications of Leuco dyes*; R. Muthyala Ed.; Springer: New York, **2002**.

17. a) A. Seeboth, C. Yin, J. Kriwanek, D. Lotzsch, R. Schaper, *J. Appl. Polym. Sci.* **2005**, *96*, 1789-1792; b) M. A. Chowdhury, B. S. Butola, M. Joshi, *Color. Technol.* **2013**, *129*, 232-237.

18. S. Valkama, H. Kosonen, J. Ruokolainen, T. Haatainen, M. Torkkeli, R. Serimaa, G. T. Brinke, O. Ikkala, *Nat. Mater.* **2004**, *3*, 872-876.

19. G. M. Miyake, V. A. Piunova, R. A. Weitekamp, R. H. Grubs, *Angew. Chem. Int. Ed.* **2012**, *51*, 11246-11248.

20. a) I. Suárez, E. J. J.-Pérez, J. Bisquert, I. M.-Seró, J. P. M.-Pastor, *Adv. Mater.* **2015**, *27*, 6157-6162; b) N. Chandrasekhar, M. A. Mohiddon, R. Chandrasekhar, *Adv. Optical Mater.* **2013**, *1*, 305-311.

21. P. Hui, R. Chandrasekhar, *Adv. Mater.* **2013**, *25*, 2963-2967.

22. Q. H. Cui, Y. S. Zhao, J. Yao, *Adv. Mater.* **2014**, *26*, 6852-6870.

23. S. Basak, R. Chandrasekhar, *J. Mater. Chem. C* **2014**, *2*, 1404-1408.

24. N. Chandrasekhar, R. Chandrasekhar, *Angew. Chem. Int. Ed.* **2012**, *51*, 3556-3561.

25. D. Okada, T. Nakamura, D. Braam, T. D. Dao, S. Ishii, T. Nagao, A. Lorke, T. Nabeshima, Y. Yamamoto, *ACS Nano* 2016, **10**, 7058–7063.

26. W. Yao, Y. Yan, L. Xue, C. Zhang, G. Li, Q. Zheng, Y. S. Zhao, H. Jiang, J. Yao, *Angew. Chem. Int. Ed.* **2013**, *52*, 8713-8717.

27. a) K. Takazawa, Y. Kitahama, Y. Kimura, G. Kido, *Nano Lett.* **2005**, *5*, 1293-1296; b) J. F. G.-López, M. Ibisate, R. Sapienza, L. S. F.-Pérez, A. Blanco, C. López, *Adv. Mater.* **2011**, *23*, 30-69.

28. S. Yun, S. Park, B. Park, Y. Kim, S. K. Park, S. Nam, K.-U. Kyung, *Adv. Mater* **2014**, *26*, 4474-4480.

29. a) M. Choi, M. Humar, S. Kim, S.-H. Yun, *Adv. Mater.* **2015**, *27*, 4081-4086; b) M. Choi, J. W. Choi, S. Kim, S. Nizamoglu, S. K. Hahn, S. H. Yun, *Nat. Photonics* **2013**, *7*, 987-994.

30. R. Thirumalai, R. D. Mukhopadhyay, V. K. Praveen, A. Ajayaghosh, *Sci. Rep.* **2015**, *5*, 09842-09852.

31. a) R. Thirumalai, R. D. Mukhopadhyay, V. K. Praveen, A. Ajayaghosh, *Sci. Rep.* 2015, **5**, 09842; b) A. Rödle, B. Ritschel, C. Mück-Lichtenfeld, V. Stepanenko and G. Fernández, *Chem. Eur. J.* **2016**, *22*, 15772-15777.

32. J. C. de Mello, H. F. Wittmann, R. T. Friend, *Adv. Mater.* **1997**, **9**, 230-232.

33. M. Lehmann, M. Jahr, *Chem. Mater.* **2008**, *20*, 5453-5456.

34. S. Yagai, T. Kinoshita, Y. Kikkawa, T. Karatsu, A. Kitamura, Y. Honsho, S. Seki, *Chem. Eur. J.* **2009**, *15*, 9320-9324.

35. H. Fudouzi, Y. Xia, *Adv. Mater.* **2003**, *15*, 892-896.

36. B. Q. Bao, B. M. Goh, B. Yan, T. Yu, Z. Shen, K. P. Loh, *Adv. Mater.* **2010**, *22*, 3661-3666.

37. D. O' Carrol, G. Redmond, *Chem. Mater.* **2008**, *20*, 6501-6508.

38. E. P. Chan, J. J. Walish, A. M. Urbas, E. L. Thomas, *Adv. Mater.* **2013**, *25*, 3934-3947.

39. P. Hanczyc, L. Sznitko, C. Zhong, A. J. Heeger, *ACS Photonics* **2015**, *2*, 1755-1762.

40. J. Guo, X. Liu, N. Jiang, A. K. Yetisen, H. yuk, C. Xang, A. Khademhosseini, X. Zhao, S.-H. Yun, *Adv. Mater* **2016**, *28*, 10244-10249.

41. S. Srinivasan, P. A. Babu, S. Mahesh, A. Ajayaghosh, *J. Am. Chem. Soc.* **2009**, *131*, 15122-15123.

42. a) H. Li, L. Chang, J. Wang, L. Yang, Y. Song, *J. Mater. Chem.* **2008**, *18*, 5098-5103; b) H. Ma, J. Hao, *Chem. Soc. Rev.* **2011**, *40*, 5457-5471; c) M. Pelton, *Nat. Photonics* **2015**, *9*, 427-235.

43. M.-K. Wei, C.-W. Lin, C.-C. Yang, Y.-W. Kiang, J.-H. Lee, H.-Y. Lin, *Int. J. Mol. Sci.* **2010**, *11*, 1527-1545.

44. D. J. Xue, J. J. Wang, Y. Q. Wang, S. Xin, Y. G. Guo, L. J. Wan, *Adv. Mater.* **2011**, *23*, 3704-3707.

45. D. G. Lidzey, D. D. Bradley, A. Armitage, S. Walker, M. S. Skolnick, *Science* **2000**, *288*, 1620-1623.

Chapter 4

A Bodipy Derived Liquid Crystalline π-Gelator that Forms Micron Sized Toroidal Structures

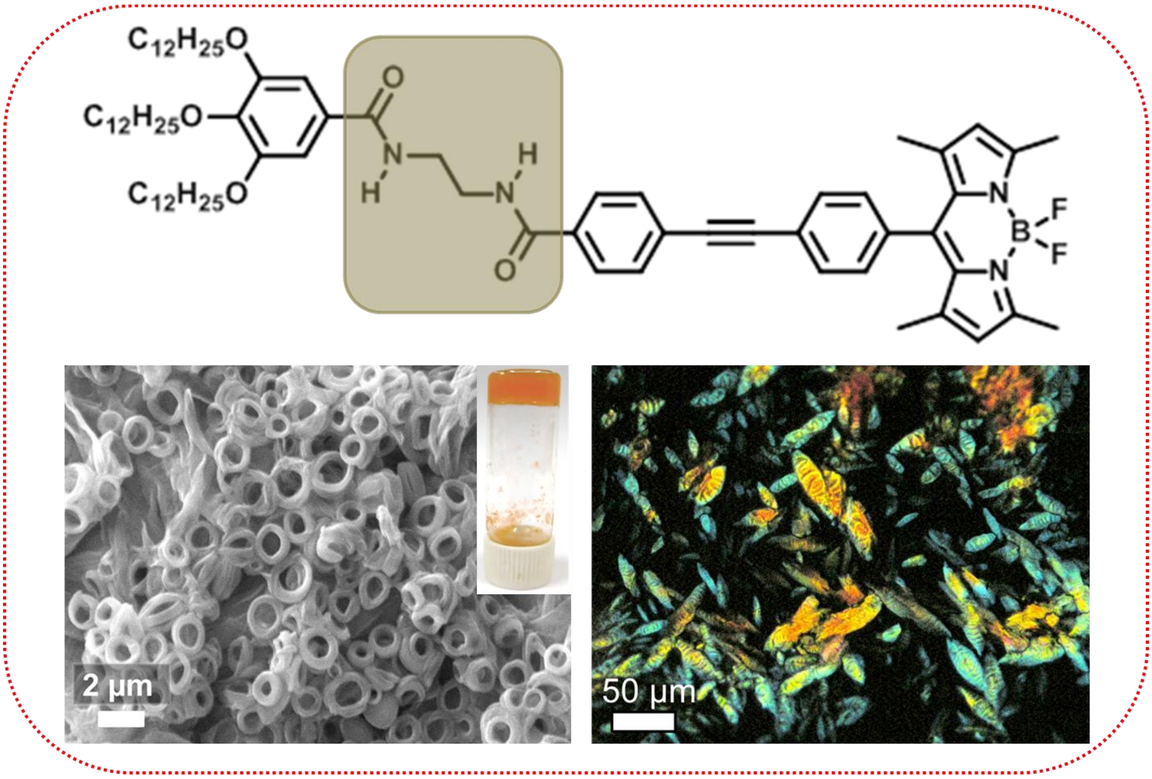

4.1. Abstract

Chemists have shown several strategies for the formation of complex architectures such as toroids and vesicles. While there are several reports on the formation of nanotoroids, micrometer sized toroids of synthetic molecules are not common. Here we report a simple method to specifically design toroids in larger size and numbers through a gelation process. A meso π-extended ***Bodipy-4*** *forms*

a reversible gel in DMSO at a concentration of 1 x 10^{-2} *M comprising of macroscopic luminescent toroids. Detailed studies revealed that at a concentration 1 x* 10^{-4} *M in DMSO, aggregates of **Bodipy-4** forms disc like particles. These structures coalesce to form ribbon or tape like structures, which ultimately curled up and coiled leading to the formation of micron sized toroids. Additionally, aggregates of **Bodipy-4** in DMSO exhibits smectic liquid crystalline phase when observed through a polarising optical microscope while cooling from molten state.*

4.2. Introduction

π- Gelators are considered as special class of molecules because of their intriguing self-assembling properties which lead to the development of multi-luminescent supramolecular architectures and are recognized by their ubiquitous tendency to form entangled 3D fibrous network structures.[1] Often these structures are influenced by the cooperative effect of various supramolecular noncovalent interactions associated with the system.[2-3] Among the self-assembled structures known, toroids find a special place on account of the structural similarity with many of the biological functional molecules and specific functions in nature.[4-5] In one of such examples, the nature has shown an unusual ability to manage light energy in photosynthetic light harvesting bacteria where the membrane proteins are organised in a specific circular fashion.[6-7] Not only the generation of toroids places enormous challenge to synthetic organic chemists but also their stability and mechanical robustness added woes to their efforts. Chemists have come up with several strategies such as the complementary hydrogen bonding interaction, coassembly of amphiphilic systems in proper solvents *etc*. to make toroidal assemblies.[8] It has been challenging for the chemists to organize the chromophores precisely in a way what the nature does. One obvious solution for the above problem is the bottom up self-assembly approach.[9-11] Often, all these methods for the generation of toroids end up in low yield where strict conditions and complex molecular systems are unavoidable.

With the bottom-up self-assembly approach; by exploiting the complementary hydrogen bonding interactions, it is possible to organize the molecules in linear as well as circular fashion depending on the ratio of molecular synthons used.[12] Whitesides and coworkers have extensively studied the coassembly of melamine and cyanurate (**Scheme 4.1**) which form hexameric macrocyclic structures called rosettes when mixed in 1:1 ratio in nonpolar solvents.[13-15] More hierarchically ordered structures are obtained by the stacking of rosette assemblies through π–π interaction. Ajayaghosh and coworkers have reported the formation of toroids from linear π-conjugated systems by exploiting the complementary hydrogen bonding interaction between melamine and cyanurate moieties.[16] The initially formed hydrogen bonded rosette assemblies by the melamine attached oligo(*p*-phenyleneethynylene) (OPE) and cyanurate in aliphatic solvent led to the formation of nanotoroids.

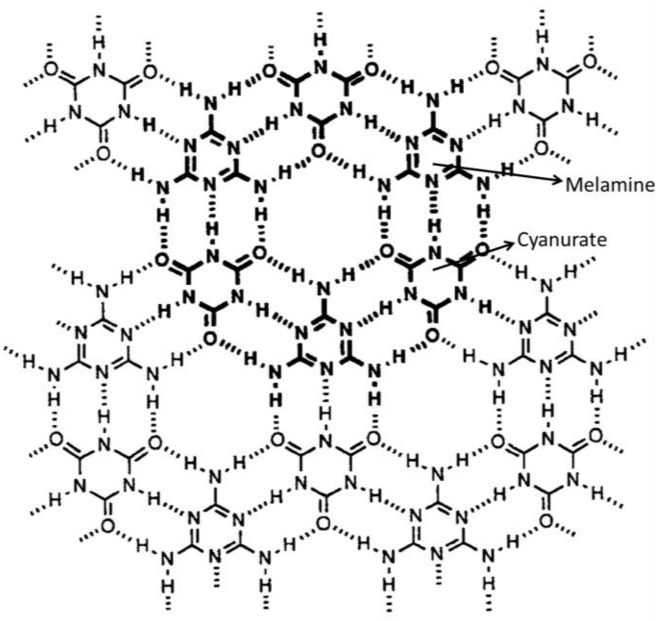

Scheme 4.1. Self-assembly of melamine-cyanurate (M_3. CA_3).

Coassembly of molecules **1** and **2** leads to the formation of discrete rosettes ($\mathbf{1}_3.\mathbf{2}_3$). Initially, the OPE chromophores adopt H-type packing when fixed with the complementary part in nonpolar cyclohexane which is clearly distinguished by the blue shift observed in the absorption band at 334 nm, when compared to the monomeric band in chloroform at 338 nm. Toroids are formed by the stacking of the individual rosettes. AFM cross-sectional analysis has shown the circumference of toroids as 67 nm. Yagai and coworkers have extensively used hydrogen bonding synthons such as barbiturate, cyanurate and melamine, which are linked with chromophores for the formation of rosettes, rings and toroidal structures.[17] Authors also studied reversible transformation between nanorings and open ended fibers under varying self-assembly conditions.[18]

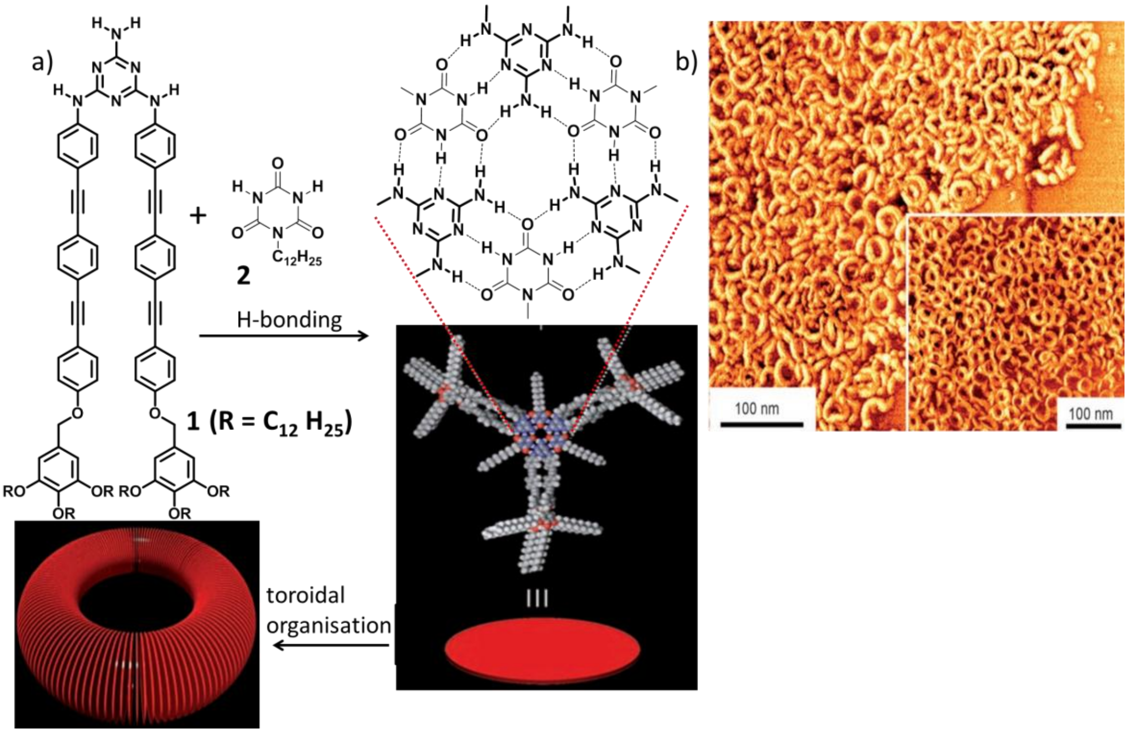

Figure 4.1. a) Structures and the self-assembly of melamine linked OPE (**1**), cyanurate (**2**) and the representation of toroid formation. b) AFM phase image showing toroids from equimolar mixture of **1** and **2** in decane (*c* = 5 x 10^{-5} M).

Amphiphilic building blocks are reported to form toroidal architectures. Lee *et al.* have reported the design of bis(ethylene glycol) chain and a longer tris(ethylene glycol) chain (for molecules **3** and **4**, respectively) as a flexible hydrophilic segment, with a hydrophobic segment (hepta-*p*-phenyl group) for achieving toroidal structures by coassembly with a molecule **5**.[19] In aqueous solution, molecules **3** and **4** individually self-assemble to form planar sheets and ribbon like nanostructures, respectively. Molecule **5** with a bulky hydrophilic dendron, introduces a curvature at the interface of the amphiphile for forming toroids. The toroid has internal and external pore diameter of 1.5-2 nm and ~ 10 nm, respectively, indicating that they are composed of single layer of molecules where hepta-*p*-phenyl rod segments are oriented perpendicular to the plane of the rings.

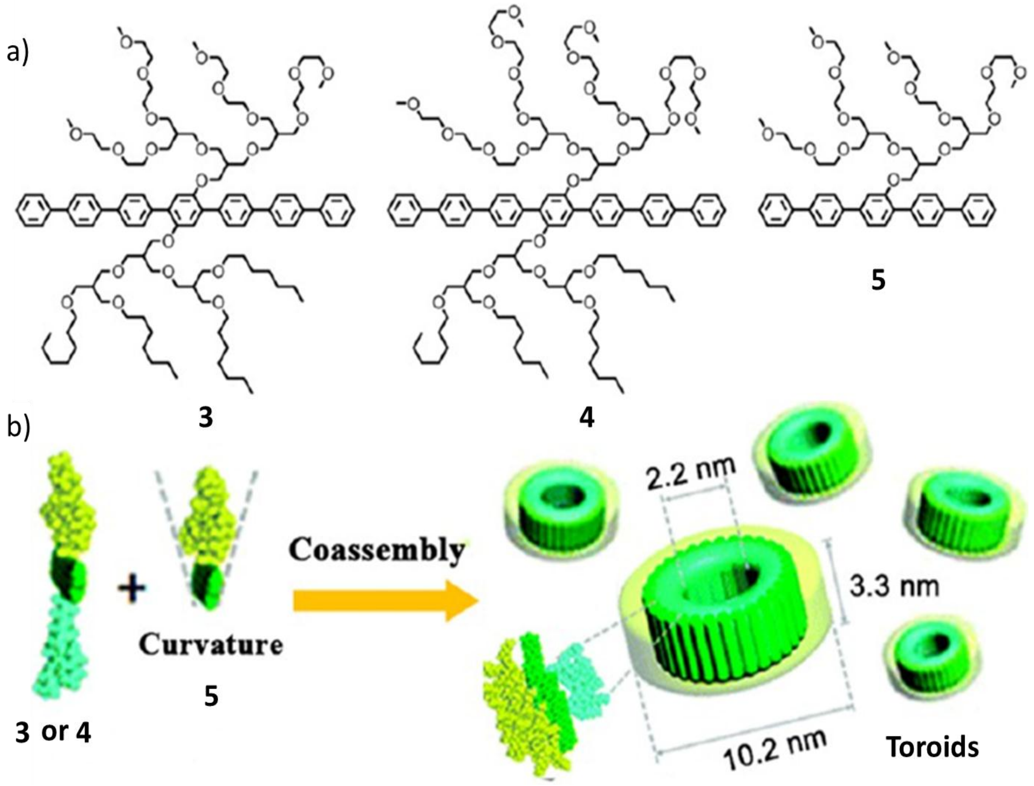

Figure 4.2. a) Chemical structures of **3**, **4**, **5** and b) graphical representation of toroid formation by coassembly of **3** or **4** with **5**.

In a different strategy, toroids are constructed through stacking of macrocycles which in turn is formed from bent-shaped aromatic segments.[20] For instance, amphiphiles **6** and **7** having oligoether dendron side group and *meta*-substituted aromatic segment form toroidal nanostructures by the self-assembly of hexameric macrocycles with internal and external diameters of 3 and 8 nm, respectively. Molecule **7** has a similar structure like **6**, however has a pyridine group at the centre in addition to the aldehydic groups at the ends. These design concept consisting of weak dipolar interaction of the aldehyde group and the steric repulsion of water cluster made way for the slipped stacking between adjacent aromatic segments thereby J-type stacked hexameric macrocycles are formed which is confirmed from the red-shifted absorption and emission spectra.

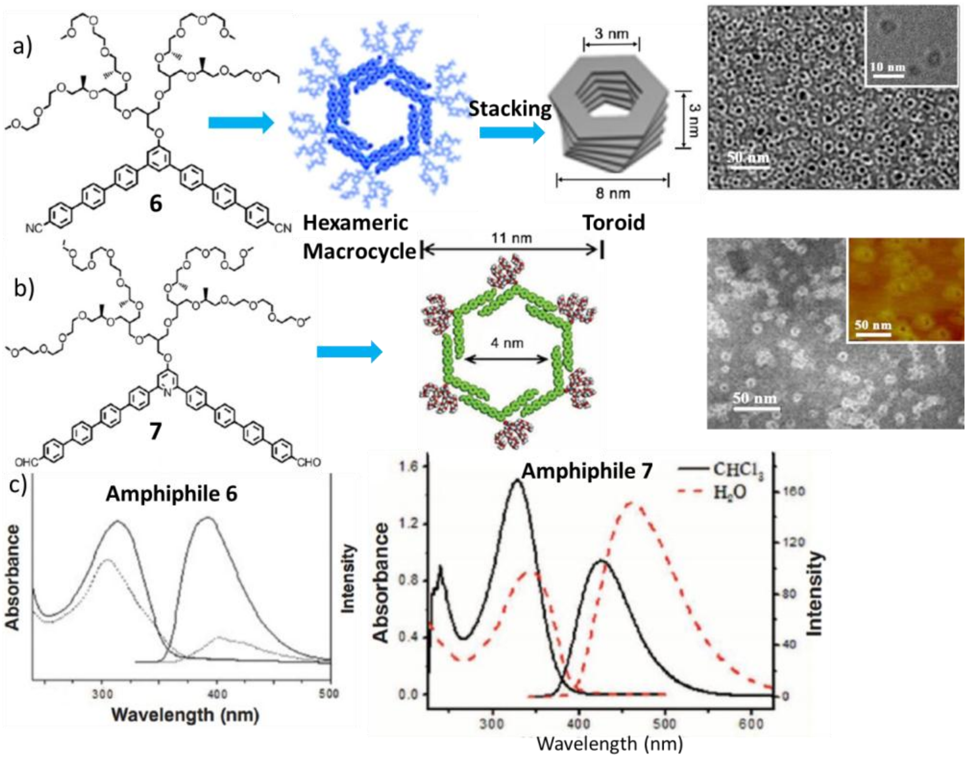

Figure 4.3. a) Molecular structure of **6** and the schematic representation of formation of toroids. The corresponding negatively stained TEM image showing toroids on the right side (inset is a cryo TEM image). b) Molecular structure of **7** and the schematic representation of macrocycle formation. The corresponding TEM (negatively stained) and AFM images (inset) are shown on the right side, *c* = 0.002 wt% aqueous solution. c) Absorption and emission spectra of molecules **6** and **7** in chloroform (solid line) and in aqueous solution (dashed line).

Synthetic peptide building blocks are known to form toroids by self-assembly.[21] For example, the molecule **8** is a block copolypeptide comprising of rigid hydrophobic segment that forms *β*-sheet and sugar attached poly(L-arginine) as hydrophilic segment. The *β*-sheet forming peptide blocks consist of alternative units of tryphtophan, positively charged lysine units and negatively charged glutamic acid. This rationally designed molecule self-assembles into toroidal architectures in aqueous solution.

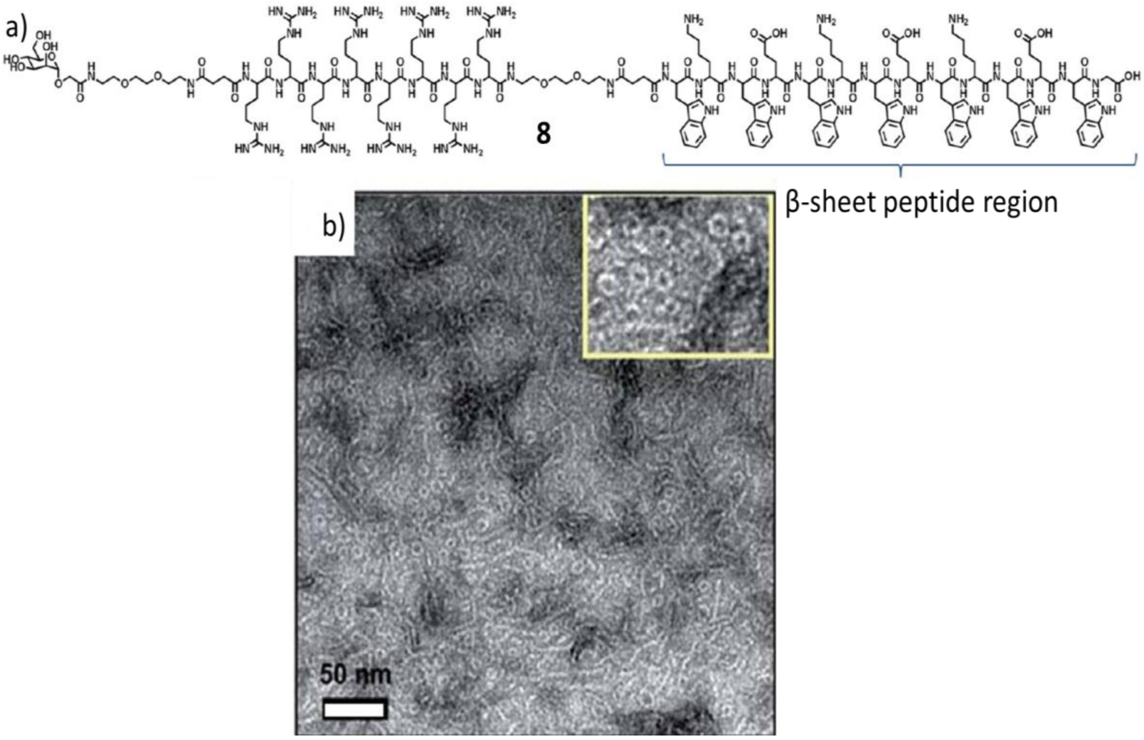

Figure 4.4. a) Chemical structure of block peptide **8** containing *β*-sheet peptide and poly(L-arginine), b) negatively stained TEM image of **8** in PBS and inset is showing magnified image.

Coordination directed self-assembly of oligo(phenyleneethynylene) dicarboxylic acid (OPEA) with $Zn(OAc)_2$ under controlled synthetic conditions has been reported to form toroidal structures.[22] The 1D coordination polymer chains in this case are stacked through π-π interaction which is evident from the *d*-spacing value of 4 Å. In addition, these π-stacked planes are connected by interdigitated alkyl chains as evident by the peak at 7.73° with a corresponding *d*-spacing value of 1.2 nm. FE-SEM and TEM revealed disc-like particles which upon varying the reaction condition up to 36 h resulted in the formation of vesicular, bowl and toroidal shaped nanostructures.

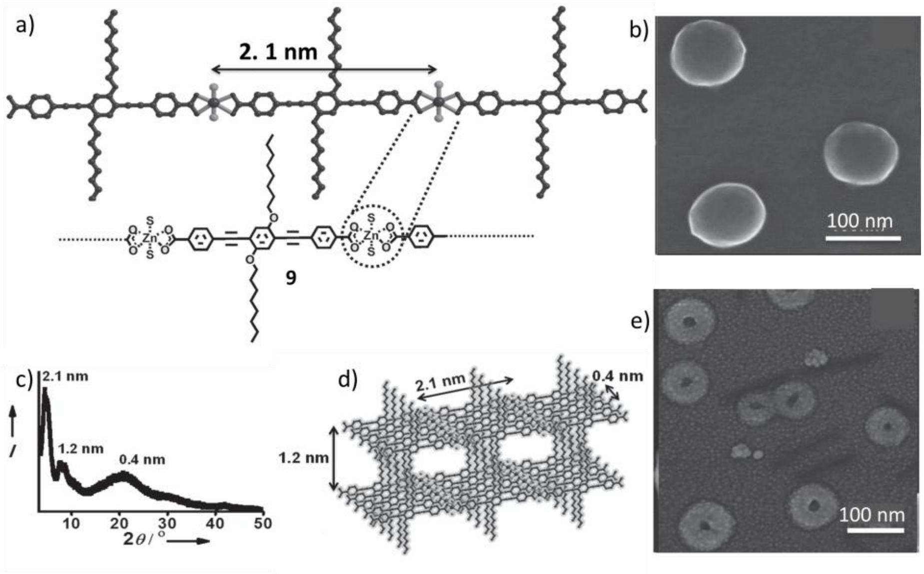

Figure 4.5. a) 1D coordination chain of Zn(OPE).$(H_2O)_2$. b, e) FESEM images. c) PXRD pattern of the assembly. d) Schematic representation of the molecular packing.

Recently, Yang *et al.* reported uniform toroid formation through the supramolecular cyclisation of rodlike micelles constructed from poly(γ-benzyl-L-glutamate)-graft-poly(ethylene glycol) graft copolymers by two step self-assembly. Uniform rodlike micelles are prepared by dialyzing the polymer dissolved in THF/DMF against water. Addition of THF in the second step leads to cyclisation of rodlike micelles to toroids.[23]

Based on the above reports, it is understood that toroidal structures can be constructed by bottom up self-assembly approach. However, in most of the cases, the molecular systems used are complex or involved coassembly of two molecules. In addition, the yield and the stability of the toroids are found to be poor. Supramolecular gels are well known for the formation of entangled 3D fibrous network structures, but a stable and robust nano-micro sized toroidal formation from a gel matrix over large area is a challenge. In this chapter, the unusual behavior of a Bodipy derivative connected to a trialkoxy benzene moiety through two flexible amide bonds is described. This molecule exhibited smectic liquid crystalline behavior. Interestingly, this molecule could specifically gelate DMSO at a concentration of 12 mg/mL. Morphological analysis of the DMSO xerogel revealed the formation of micrometer sized toroidal assembly which is not common among organogelators. Details of these studies are described.

4.3. Results and Discussion

4.3.1. Synthesis of Bodipy-4

Bodipy-4 is synthesized by the Sonogashira coupling between 3,4,5-tris(dodecyloxy)-*N*-(2-(4-ethynylbenzamido)ethyl)benzamide (**16**) and (4-iodophenyl)-1,3,5,7-tetramethyl-4,4-difluoro-4-bora-3a,4a-diaza-*s*-indacene (**17**) in presence of bis(triphenylphosphine)palladium (II) dichloride (10 mol%), and copper (I) iodide (10 mol%) using degassed triethylamine and THF as solvents in 30% yield (**Scheme 4.3**).[24] The compound **16** was synthesized starting from compound **10** in 76% yield as shown in **Scheme 4.2**. All intermediate compounds were characterised by ^{1}H-NMR and HRMS analyses and the final molecule **Bodipy-4** was characterised by ^{1}H-NMR, ^{13}C-NMR, HRMS and FT-IR spectroscopic techniques.

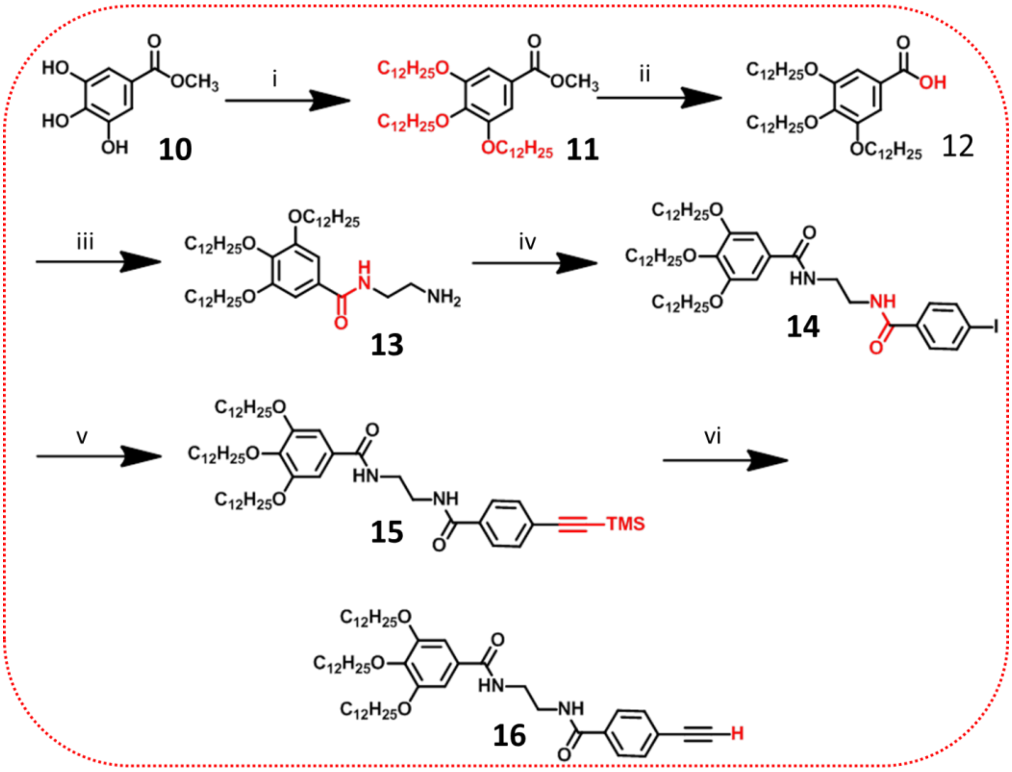

Scheme 4.2. Reagents and conditions:i) 1-Bromododecane, K_2CO_3, DMF, 100 °C, 24 h, 78%; ii) KOH, ethanol, reflux, 12 h, 80%; iii) EDA, BOP, DCM, rt, 3 h, 85%; iv) 4-Iodo benzoic acid, BOP, TEA, DCM, rt, 16 h, 70%; v) Trimethylsilyl acetylene, CuI, $PdCl_2(PPh_3)_2$, dry Et_3N, dry THF (oxygen free), rt., 12 h, 80%; vi) KF, dichloromethane/methanol (1:5), rt, 12 h, 76%.

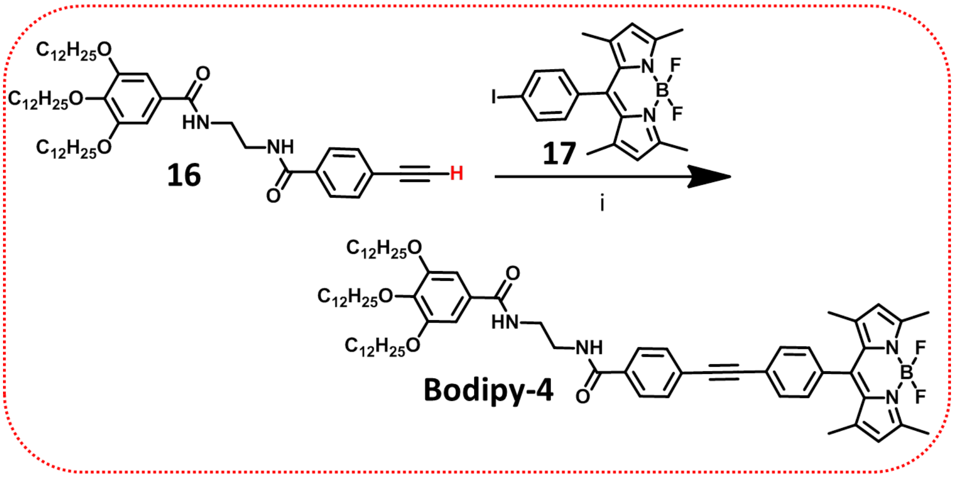

Scheme 4.3. Reagents and conditions:i) CuI, $PdCl_2(PPh_3)_2$, dry Et_3N, dry THF (oxygen free), 60 °C, 24 h, 33%.

4.3.2. Photophysical Study

4.3.2.1. Absorption and Emission Spectral Properties

Absorption spectrum of **Bodipy-4** reveals that the molecule exists in the monomeric state in chloroform (1 x 10^{-4} M) with an absorption band at 300 nm, corresponding to the phenlyeneethynylene part along with a shoulder at 475 nm (S_0-S_1, 0→1) and a sharp band at 505 nm (S_0-S_1, 0→0), which are the characteristic of the bodipy moiety.[25] In DMSO at 1 x 10^{-3} M concentration, the sharp absorption band was broadened and red-shifted indicating the aggregation of the molecule (**Figure 4.6a**). The variable temperature absorption spectral changes of **Bodipy-4** at a concentration of 1 x 10^{-3} M in DMSO is shown in **Figure 4.6d**. Upon increasing the temperature from 10 - 50 °C, a gradual increase in the absorption peaks at 300 and 505 nm is observed indicating the breakage of the aggregates to the monomer. Breakage of the distinct shoulder band at 550 nm to monomeric band upon increasing the temperature from 15 - 75 °C in DMSO at high concentration (c = 1 x 10^{-2} M, **Figure 4.7b**) also confirms the reversibility of aggregates with respect to temperature.

By analyzing the structure of the molecule as well as considering the previous reports of diamide systems, it is proposed that **Bodipy-4** can possibly exist in intramolecularly hydrogen bonded state at lower concentrations.[26, 27] However, at higher concentrations, intermolecular hydrogen bonding may prevail. In order to understand the nature of the self-assembly process with respect to concentration, we have carried out a cooling experiment (c = 1 x 10^{-4} and 1 x 10^{-3} M DMSO) by monitoring the variation of the monomeric absorbance at a specific wavelength of

504 nm upon varying the temperature from 80 - 15 °C. A gradual self-assembly process is observed on ploting the fraction of aggregates (α_{Agg}) *vs* temperature at

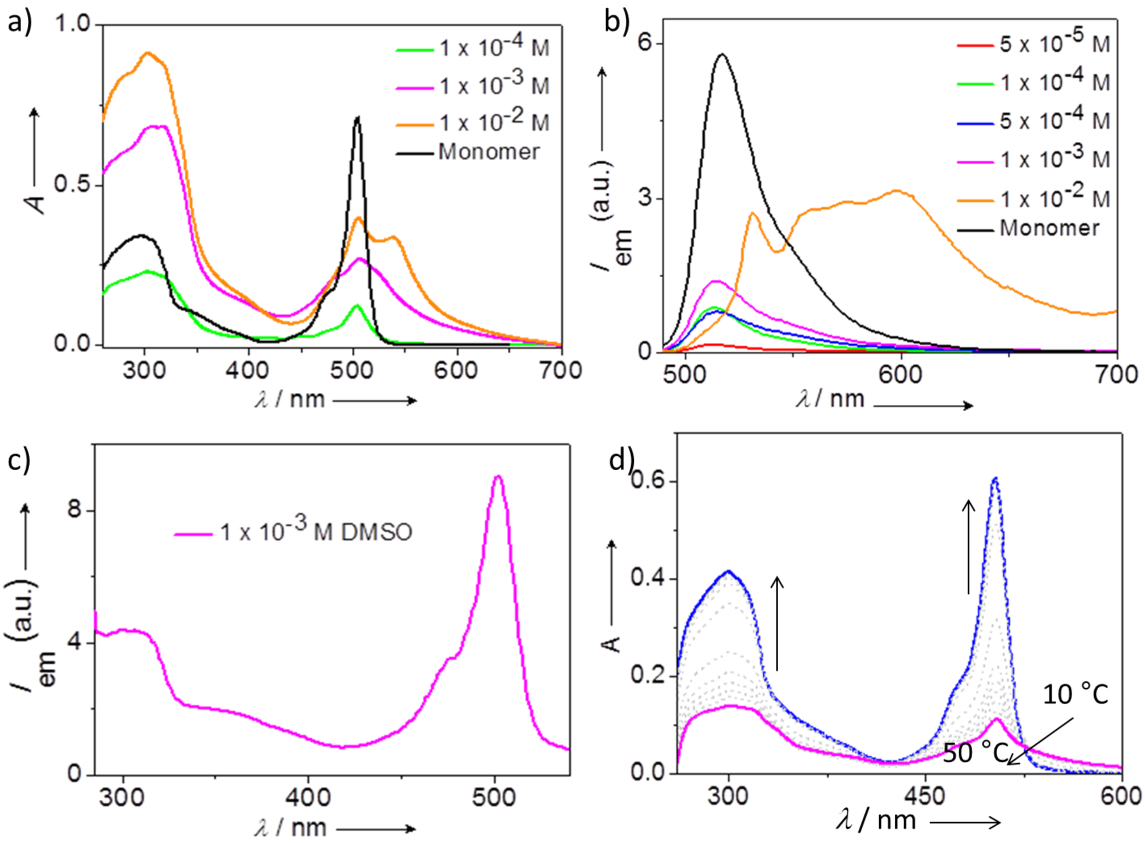

Figure 4.6. a) Absorption spectra in monomer ($CHCl_3$, 1 x 10^{-4} M) and DMSO aggregates (1 x 10^{-4}, 1 x 10^{-3}, 1 x 10^{-2} M). b) Emission profiles (λ_{ex} = 475 nm) of monomer (black, $CHCl_3$ 1 x 10^{-4} M) and different concentrations of aggregated solutions in DMSO. c) Excitation spectrum of DMSO aggregated solution (λ_{em} = 560 nm) and d) Variable temperature absorption spectra of 1 x 10^{-3} M DMSO solution.

a concentration of 1 x 10^{-3} M for a cooling rate of 1 K min^{-1}. The plot indicated that the nucleation process which is not sharp, happens even at high temperature (74 °C) followed by the gradual elongation process resembling an isodesmic pathway mechanism (**Figure 4.7a**).[28] This observation implies that at higher concentration, intermolecular interaction will be strong which drives the nucleation process to happen even at higher temperature, leading to extended supramolecular polymers. When the aggregated solution of **Bodipy-4** in DMSO at a concentration 1 x 10^{-3} M is heated to the monomeric state (where all inter- and intramolecular hydrogen bonding breaks) and gradually cooled, intermolecular hydrogen bonded dimer may form and further aggregation is driven by open dimer structure (**Figure 4.8e, f**). On the other hand, the fraction of aggregates (α_{Agg}) *vs* temperature for 1 x 10^{-4} M has indicated that the self-assembly pathway is highly cooperative, probably driven by intramolecular hydrogen bonding to form closed dimers thereby sharp nucleation happens at lower temperature (27 °C). Thus, the large difference observed in the aggregation pathways may be due to the different kinds of dimeric and extended structures existing at lower (1 x 10^{-4} M) and higher (1 x 10^{-3} M) concentrations respectively (**Figure 4.8**). The spontaneous nucleation at high concentration is due to the presence of open dimer structure (**Figure 4.8e, f**).

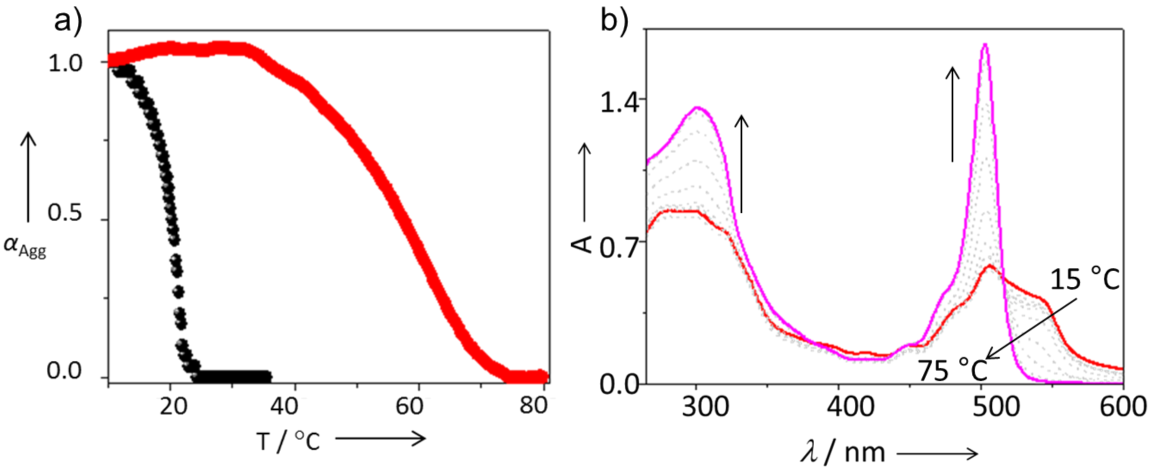

Figure 4.7. a) Fraction of aggregates (α_{Agg}) *vs* temperature plot for 1 x 10^{-4} (black) and 1 x 10^{-3} M (red). b) Variable temperature absorption spectra of 1 x 10^{-2} M DMSO solution.

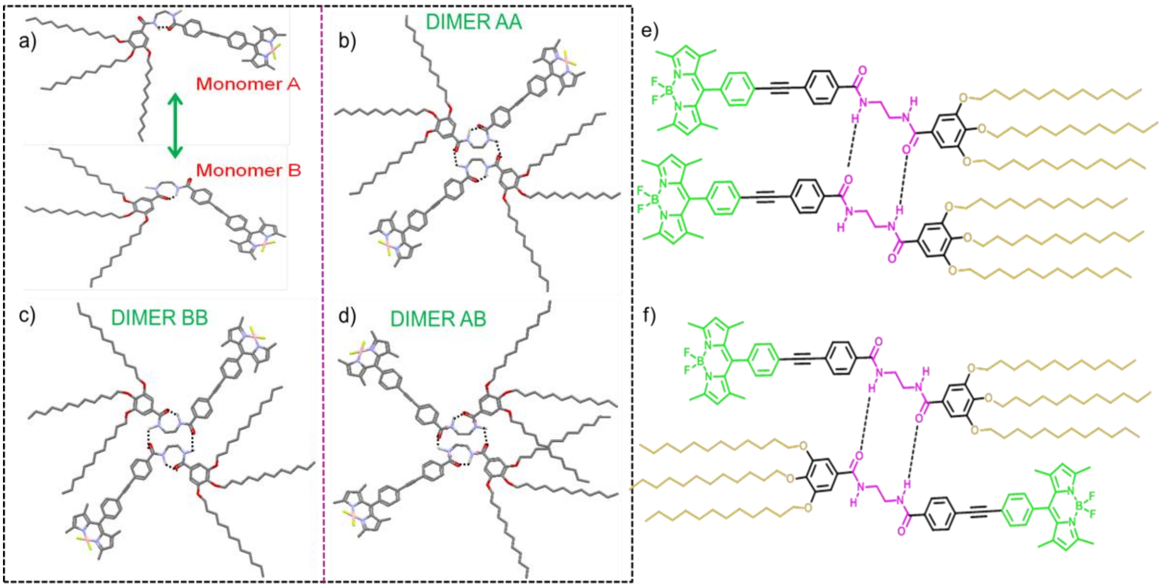

Figure 4.8. Proposed intramolecularly hydrogen bonded a) monomeric and b-d) dimeric structures at low concentration (c = 1 x 10^{-4} M). e, f) Proposed intermolecularly hydrogen bonded dimeric structures at high concentration (c = 1 x 10^{-3} M).

Monomer emission appeared as an intense band at 515 nm in chloroform (c = 1 x 10^{-3} M, DMSO) when excited with a wavelength of 475 nm. However, in DMSO solution (c = 1 x 10^{-3} M), the emission was significantly quenched indicating that the aggregates are weakly emissive. When the concentration is increased to 1 x 10^{-2} M, a new broad emission profile is observed with an emission maximum at 600 nm indicating the formation of extended aggregates (**Figure 4.6b**).[29]

4.3.2.2. Lifetime and Quantum Yield Measurements

The fluorescence lifetime decay profile of **Bodipy-4** in DMSO (c = 1 x 10^{-2} M) exhibited a bi-exponential decay with lifetime values of 2.6 (37.18%) and 0.87 (62.82%) ns when monitored at 560 nm. However, in $CHCl_3$ (c = 1 x 10^{-4} M) a mono exponential decay is observed with a lifetime of 2.66 ns when the emission is monitored at 520 nm.

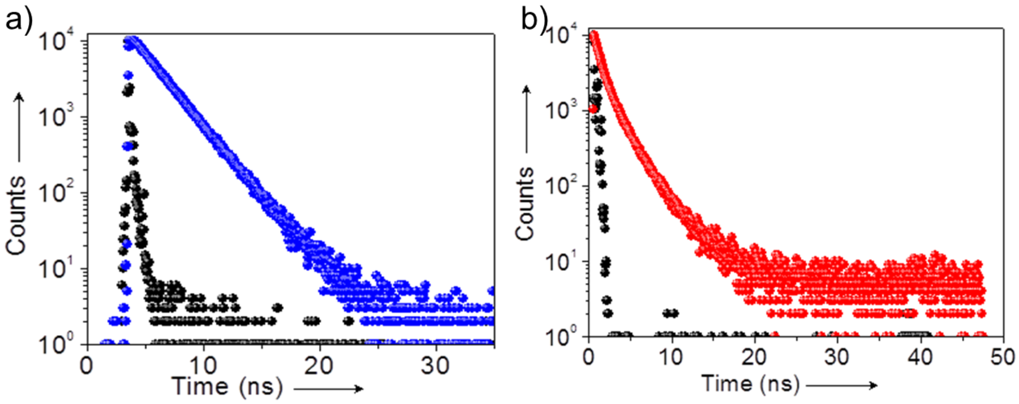

Figure 4.9. Fluorescence decay profiles of a) monomer (CHCl$_3$, 1 x 10^{-4} M, λ_{em} = 520 nm), b) DMSO (1 x 10^{-2} M, λ_{em} = 560 nm). All cases, excitation source used, λ_{ex} = 375 nm.

In CHCl$_3$ (c = 1 x 10^{-4} M), **Bodipy-4** showed a relative quantum yield of 0.51 (fluorescein in 0.1 N NaOH as standard, φ_f = 0.81, λ_{ex} = 475 nm). In DMSO (c = 1 x 10^{-2} M) the relative quantum yield of the molecule was 0.08.

4.3.3. NMR Experiments

We have carried out ROESY-NMR experiment to understand the dimer structure of **Bodipy-4** in a solvent mixture of DMSO-d6/CDCl$_3$ (85:15) at a concentration of 1 x 10^{-2} M.[30, 31] CDCl$_3$ has been added to reduce the effect of viscosity and increase the solubility. The coupling between protons '**i**' and '**g**', '**a**' and '**c**' can be explained based on the intramolecular spatial coupling, while the coupling interaction between the protons '**g**' and '**b**' can only be explained through intermolecular spatial coupling where the molecules form dimeric structure as shown in **Figure 4.10**.

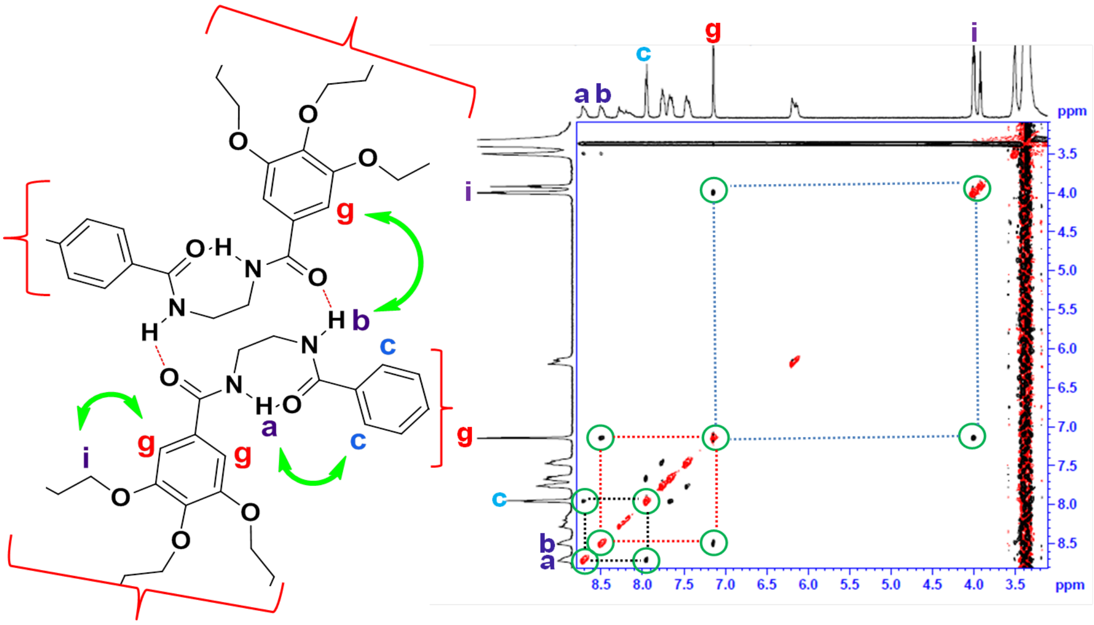

Figure 4.10. Dimer structure and the ROESY NMR in DMSO-d6 + $CDCl_3$ (85:15%) for *c* = 1 x 10^{-2} M. The green double headed arrows indicate the observed proton coupling. Green circles indicate the protons which are involved in coupling.

In order to understand the through bond coupling, we have carried out COSY experiments for the above solution. It is observed that the protons '**k**, **k′**' couples with '**f**' and '**m**', respectively. Similarly, the protons '**e**' and '**d**', '**b**' and '**a**' also exhibit through bond coupling (**Figure 4.11**). The existence of inter and intramolecular hydrogen bonding is confirmed by the observed equal change in the chemical shift values (δ = 0.25 ppm) with respect to different temperature (298-343 K) for the aggregates of **Bodipy-4** in DMSO-d6 + $CDCl_3$ (80:20%).

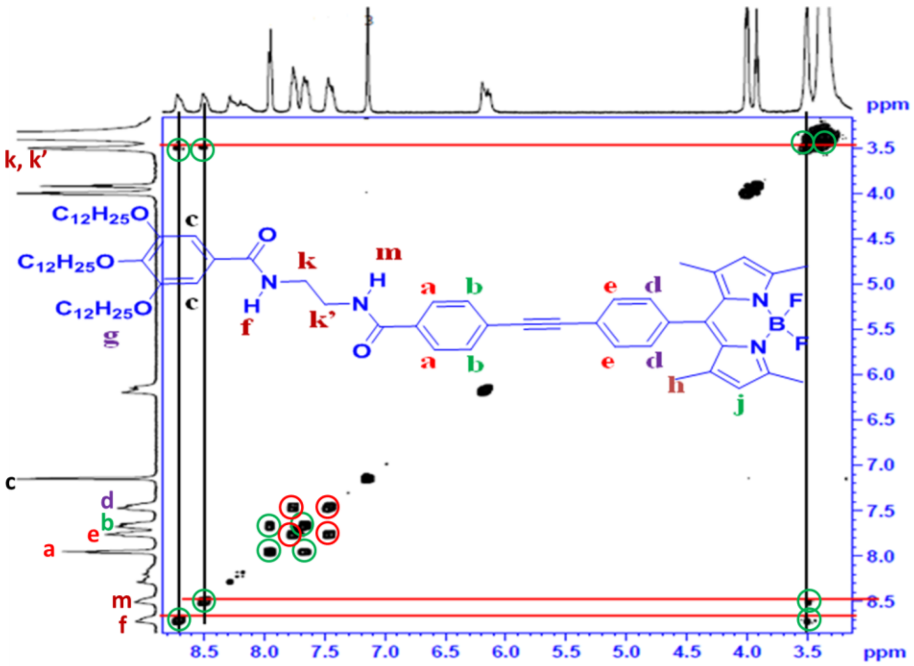

Figure 4.11. COSY NMR in DMSO-d6 + $CDCl_3$ (85:15%). The green and red circles indicate the observed proton coupling.

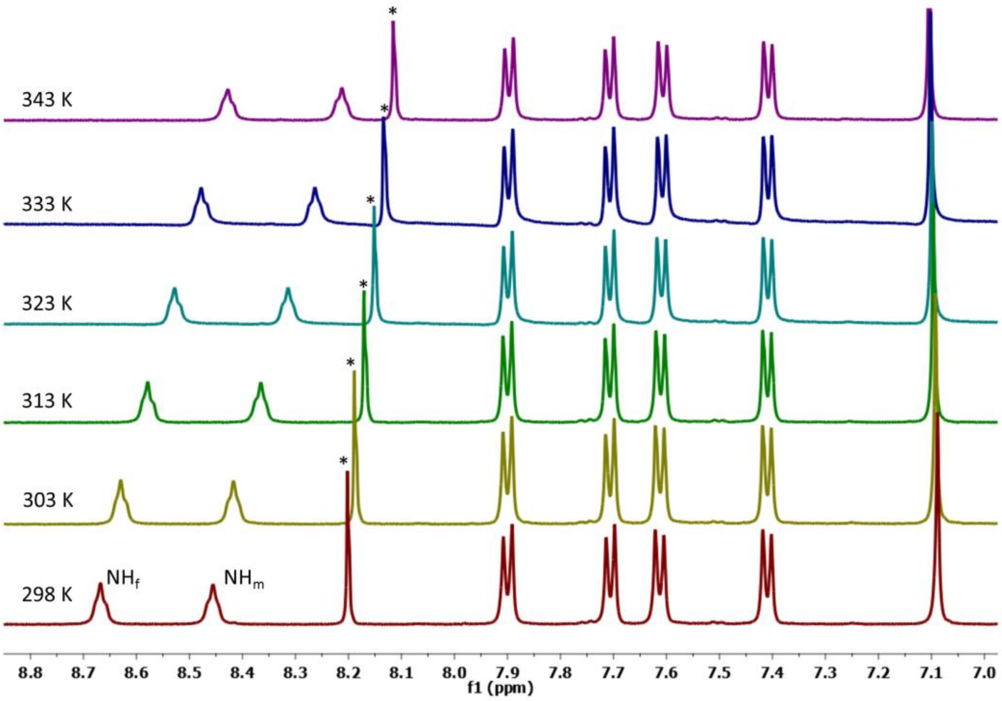

Figure 4.12. ^{1}H-NMR profiles showing changes in chemical shift values of **Bodipy-4** in DMSO-d6 + $CDCl_3$ (80:20%) ($c = 5 \times 10^{-3}$ M) for different temperatures**.** * Protons from $CDCl_3$.

The variable temperature ^{1}H NMR spectral analysis of **Bodipy-4** in DMSO-d6 + $CDCl_3$ (80:20) is shown in **Figure 4.12**. The chemical shift value correspond to that of NH- proton 'f' has undergone a decrease from 8.67 to 8.43 ppm for a temperature of 298 and 348 K, respectively. In the similar way, NH-proton '**m**' has also undergone a decrease in chemical shift values from 8.46 to 8.21 for the respective temperatures as mentioned previously. These changes in the chemical shift values are the indication of the hydrogen bonding and the self-assembly of the molecules.

4.3.4. FT-IR Spectral Studies

The FT-IR spectroscopic studies conducted at different concentrations (1×10^{-3} and 1×10^{-4} M) for the DMSO solution of **Bodipy-4** confirms the presence of intramolecular hydrogen bond, existing in the dimeric structures.[32,33] The persistence of IR C=O stretching band at 1656 cm^{-1} even at dilute conditions (DMSO 1×10^{-4} M) is a clear indication of the presence of intramolecular hydrogen

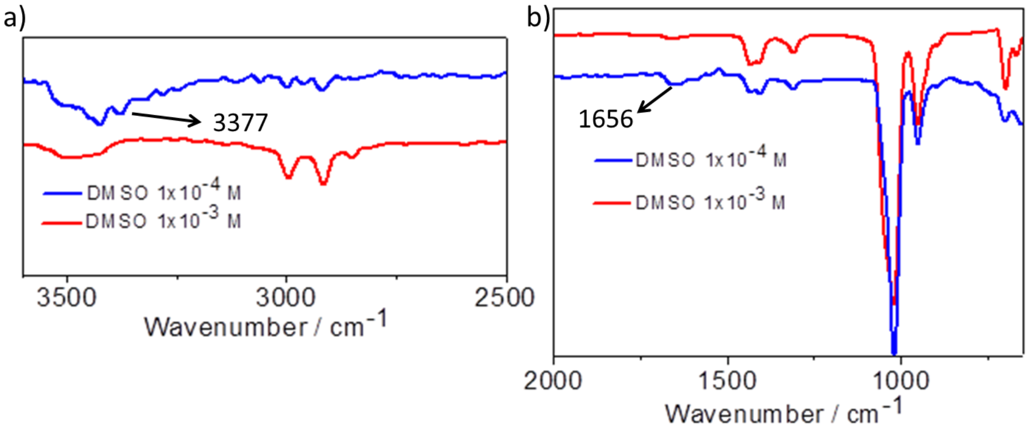

Figure 4.13. FT-IR studies of **Bodipy-4** in 1×10^{-3} and 1×10^{-4} M DMSO solution.

bonding in the molecule. Similarly, band at 3377 cm^{-1} which corresponds to that of intramolecularly hydrogen bonded NH-stretching can be seen even at lower concentration.

4.3.5. Gelation Studies

Gelation studies of **Bodipy-4** has been carried out in a series of solvents. Except DMSO, none of the other solvents tested show gelation. Heating and the sudden cooling of the 1 x 10^{-2} M solution in DMSO resulted in the formation of an yellow luminescent (575, 600 nm) reversible gel (**Figure 4.14a**). The critical gelation concentration (CGC) and stability of gels were measured by the 'inversion tube method'. Gel melting temperature (T_{gel}) was determined by the 'dropping ball method' and the critical gelation concentration is found to be 1 x 10^{-2} M and the gel melting temperature was found to be 52 °C (**Figure 4.14b**).

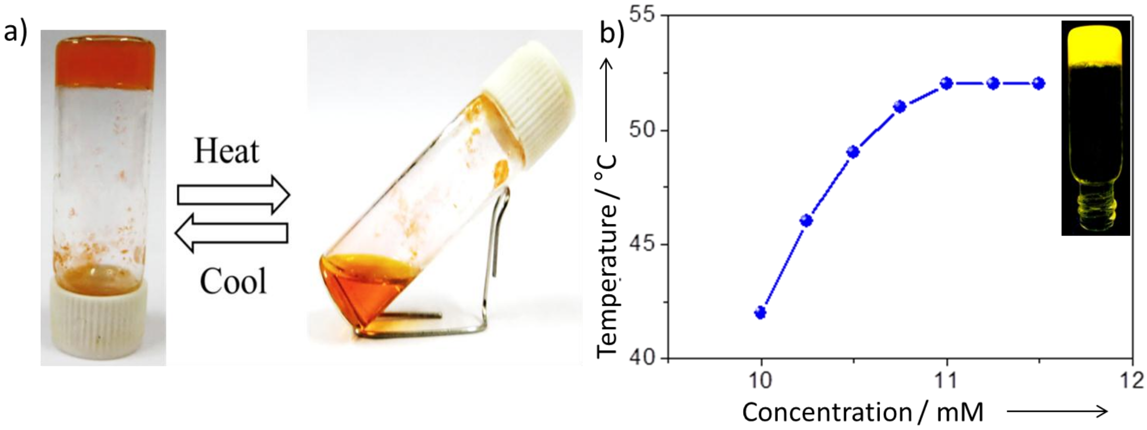

Figure 4.14. a) Daylight photograph of the **Bodipy-4** reversible DMSO gel and b) T_{gel} plot (inset, photograph of fluorescent gel).

4.3.6. Morphological Analysis

Scanning electron microscopic (SEM) images of a DMSO xerogel of **Bodipy-4** reveal the presence of toroidal structures (**Figure 4.15**). This observation is against the usual formation of 3D entangled network structures normally observed in organogelators.[1] The coexistence of flexible tape like structures along with toroidal structures as seen in SEM indicates the possible formation of toroids through the curling and multiple coiling of 2D tapes. These toroids have an average outer diameter of 1 μm and an inner diameter of 600 nm (**Figure 4.15a**). Even though there are several reports on the formation of nanotoroids, the formation of micrometer sized toroids as seen in the case of **Bodipy-4** is a rare observation.

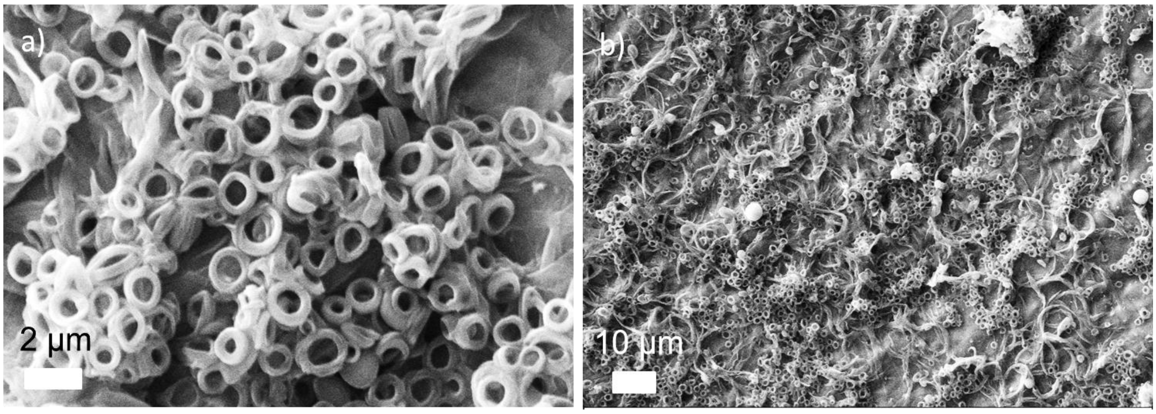

Figure 4.15. a, b) SEM images of the **Bodipy-4** gel (*c* = 1 x 10^{-2} M) showing microtoroids over larger area and good yield.

Addition of small amount of water into the DMSO gel resulted in the decoiling of the toroids as seen in the SEM images (**Figure 4.16a, b**). For example, SEM images of the xerogel prepared from DMSO (90%) and water (10%) is shown in **Figure 4.16a, b**. These images reveal the presence of more 2D tapes which are coiled at several places to form toroids. Additonally, 2D tapes are clearly observed in SEM images (**Figure 4.16c, d**) of **Bodipy-4** aggregated solution in DMSO (*c* = 1 x 10^{-3} M).

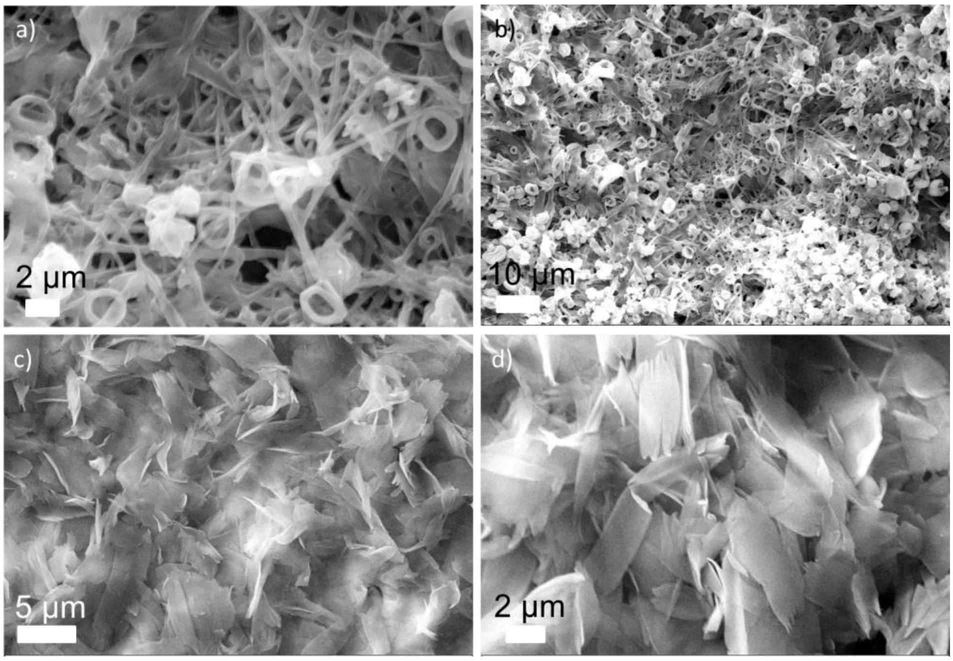

Figure 4.16. a, b) SEM images for a xerogel (c = 1 x 10^{-2} M) formed from (DMSO (90%) / H_2O (10%)). c, d) SEM images of 2D tapes formed from **Bodipy-4** DMSO aggregated solution (c = 1 x 10^{-3} M).

Transmission electron microscopy (TEM) images of a 100 times diluted gel solution showed the presence of individual toroids and tapes. From the TEM

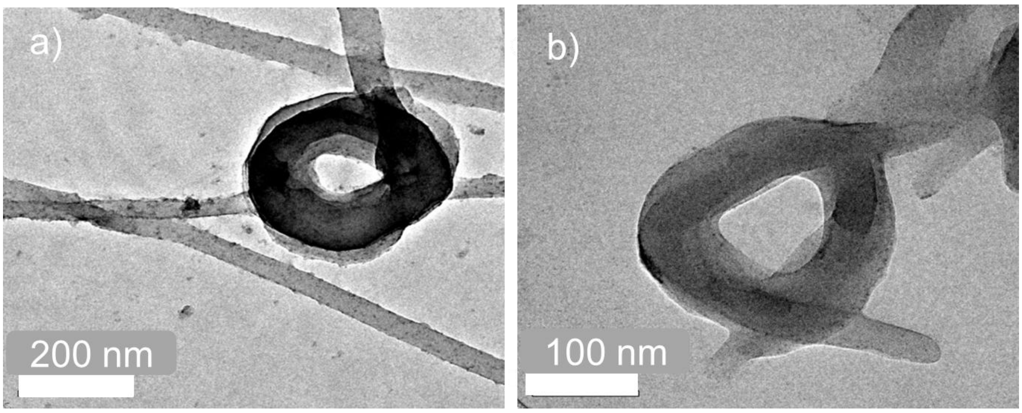

Figure 4.17. a, b) TEM images of nanotoroids obtained after diluting the DMSO gel (c = 1 x 10^{-4} M). Toroids flanked by thin fibres are also seen.

image, it is clear that the toroids are formed by the coiling of the tapes (**Figure 4.17a-d**). These nanotoroids have an approximate internal and external diameter of 80-100 nm.

Atomic force microscopy (AFM) images of a DMSO solution of **Bodipy-4** (1 x 10^{-4} M, diluted from DMSO gel) drop cast on a freshly cleaved mica sheet, showed the formation of 2D tapes which are coiled to form toroids (**Figure 4.18a, c** and **d**). The height of the tapes is found to be 1.7 nm. The width of the tape is approximately 20 nm and the average diameter of the toroids is ~ 180 nm.

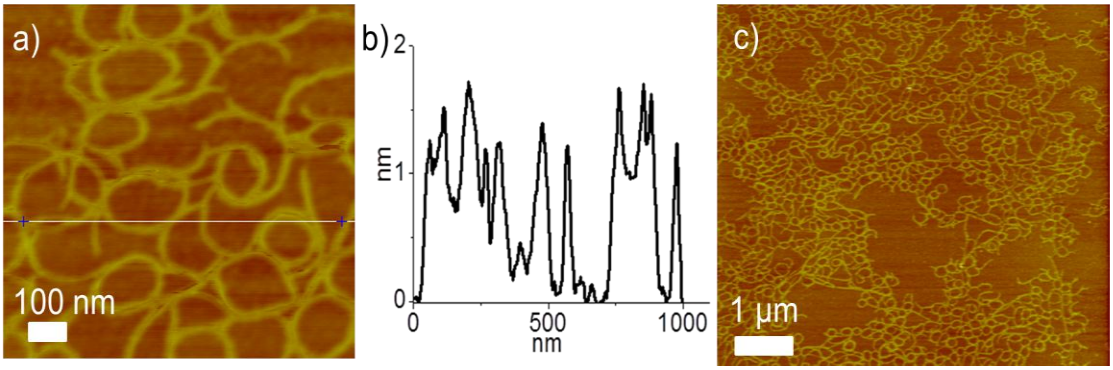

Figure 4.18. a, c) Thin coiled entangled tapes on dilution (1 x 10^{-4} M) of **Bodipy-4** DMSO gel. b) Height profile of the curved thin tapes as marked in **Figure 4.18a**.

It has been found that the rate of cooling from the high temperature monomeric state, has significant influence on the self-assembly pathway and the resultant morphology. For 1 x 10^{-4} M, fast cooling led to short fibres and slow cooling led to form particles (**Figure 4.19a and b)**. However, in the case of 1 x 10^{-3} M DMSO solution, slow cooling with a rate of 1 K min^{-1} led to linear fibres whereas fast cooling led to curled fibres as seen in the AFM analysis (**Figure 4.19e and f**). This may indicate the presence of two different competitive self-assembly mechanism operating for a particular concentration (1 x 10^{-4} M) because of the possible formation of different dimer structures (**Figure 4.8b-d and e, f**) for fast and slow cooling processes. For the fast cooling of 1 x 10^{-3} M DMSO solution, curling of fibres takes place as a result of the formation of intermolecularly hydrogen bonded dimer structure. Conversely, slow cooling lead to linear tapes which exhibited a higher elongation temperature (T_e = 74 °C).

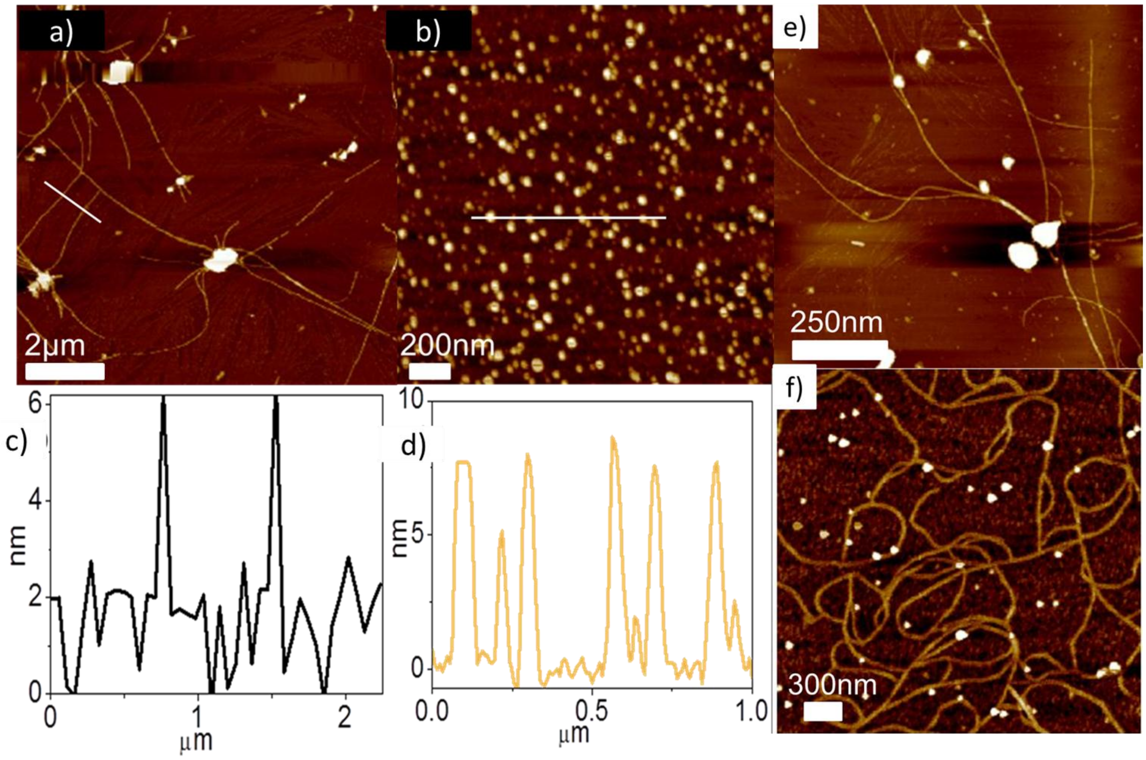

Figure 4.19. Effect of concentration and cooling rate on self-assembled structures. a, b) For fast and slow cooling (1 K min^{-1}) rate 1 x 10^{-4} DMSO aggregated solution, respectively and c, d) their respective height profiles. e, f) Slow (1 K min^{-1}) and fast cooling of 1 x 10^{-3} M DMSO aggregated solutions, respectively.

To understand the mechanism of toroid formation, TEM experiments were performed with DMSO solutions of different concentration. At a concentration of 1 x 10^{-4} M, TEM images showed the formation of disc-like nanoparticles (**Figure 4.20**). When concentration is increased to 1 x 10^{-3} M, it is found that the discs coalesces to form 1D assembly. It is known that the linear coalescence of vesicles leads to the formation of linear tapes due to intermolecular interaction.[34-38] At a higher concentration (1 x 10^{-2} M, gel) due to greater intermolecular interaction, the twisted flexible tapes experiences more strain to undergo curling process to reach the ultimate toroidal structures.

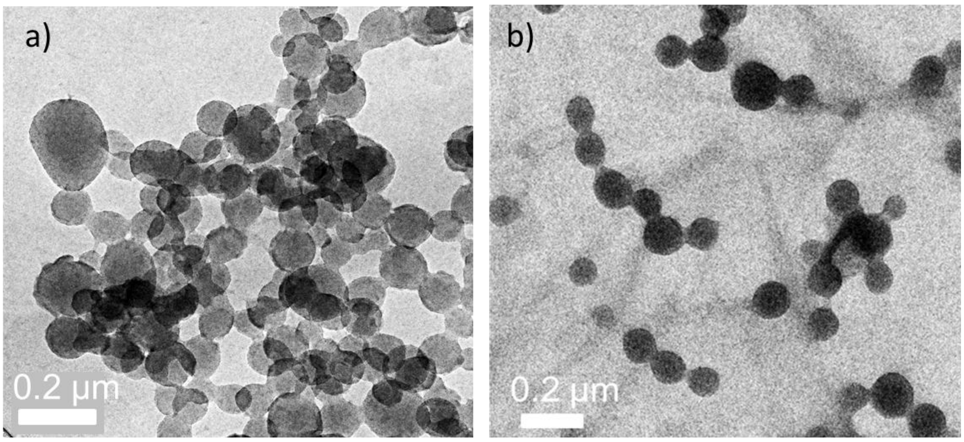

Figure 4.20. TEM images of **Bodipy-4** showing a) disc-like particles (c = 1 x 10^{-4} M, DMSO), b) coalescing of disc-like particles to form 1D assembly (c = 1 x 10^{-3} M, DMSO).

At lower concentration, since the intermolecular hydrogen bonding is less favoured, the assembly is mainly driven by the intramolecular hydrogen bonded dimer structure. These dimers may further assemble through π-stacking leading to the disc-like structures. As the concentration is increased, intermolecular hydrogen bonding will be favoured leading to 1D supramolecular polymeric

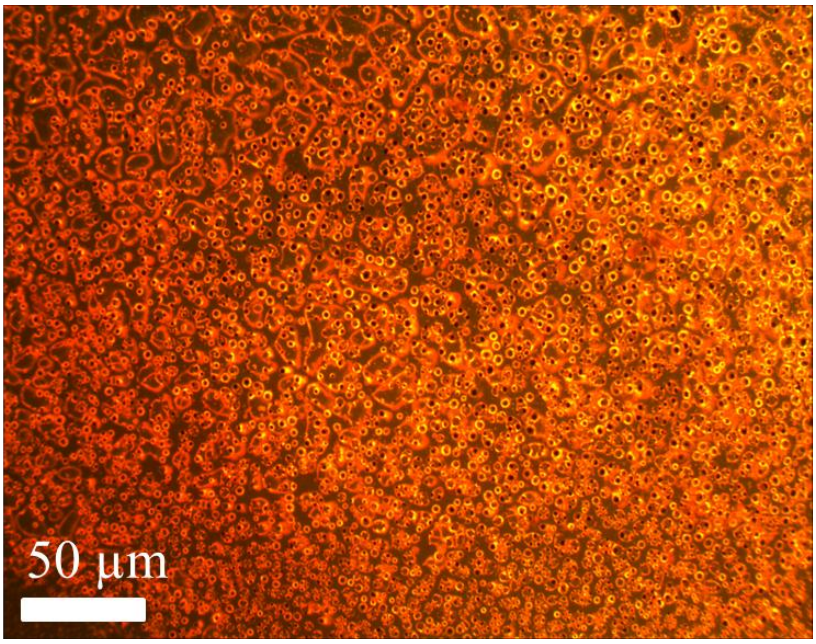

Figure 4.21. Confocal fluorescent microscopic images of toroid, gel state (1 x 10^{-2} M).

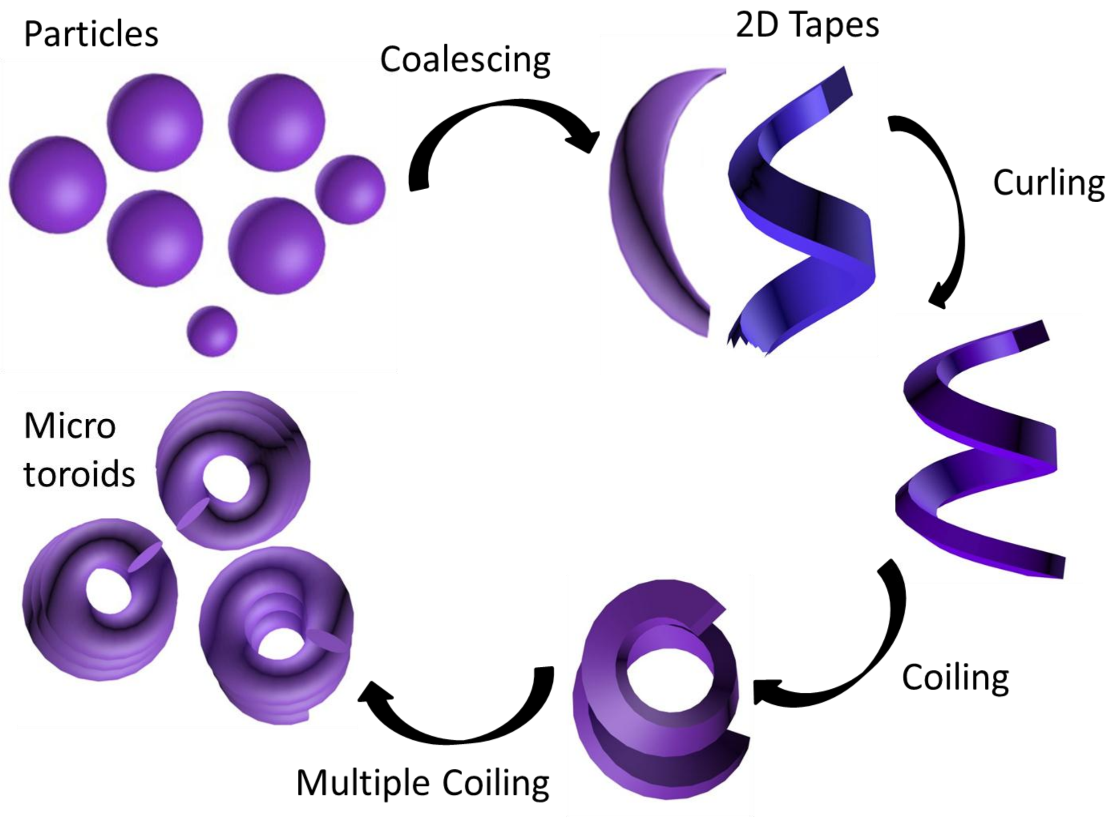

Figure 4.22. Schematic representation of the formation of microtoroids from disc-like particles.

tapes. During the xerogel formation upon evaporation of the solvent on substrates, curling of the tapes occurs. These curled tapes subsequently coil to form a few layers one over other leading to the formation of toroids as seen in the SEM and TEM images. The driving force for the curling and coiling of tapes probably orginate from the sudden cooling of the assembly at high concentration (1 x 10^{-2} M). These fluorescent toroidal structures could also be visualized through confocal fluorescent microscope (**Figure 4.21**).

4.3.7. Liquid Crystalline Properties

A DMSO solution of **Bodipy-4** when viewed through a polarizing optical microscope (POM) after drop casting on a glass slide exhibited birefringent texture characteristic of a smectic phase (**Figure 4.23a**).[39] However, upon cooling the DMSO aggregates from the isotropic state to 153 °C, smectic batonnets were observed (**Figure 4.23b**).[40-42] On the other hand, when the **Bodipy-4** powder was cooled from the isotropic state to 120 °C, focal conic fan shaped texture characteristic of smectic A phase was observed and it was stable up to the crystallisation temperature 83 °C (**Figure 4.23c**).[43] The LC phase to the crystallisation transition can be seen (appeared as green) clearly through POM at 100 °C (**Figure 4.23d**).

To gain more insight on the liquid crystalline phase change, we have carried out the differential scanning calorimetry (DSC) experiment with a heating/cooling rate 5 °C/min and calculated the energetics involved in the phase change. The DSC thermogram analysis for the first heating cycle has shown a phase change at

35 ºC from smectic phase to crystalline state with an enthalpy change of 4.34 J/g before the sharp crystalline melting transition at 175 ºC (**Figure 4.23e**). Not so

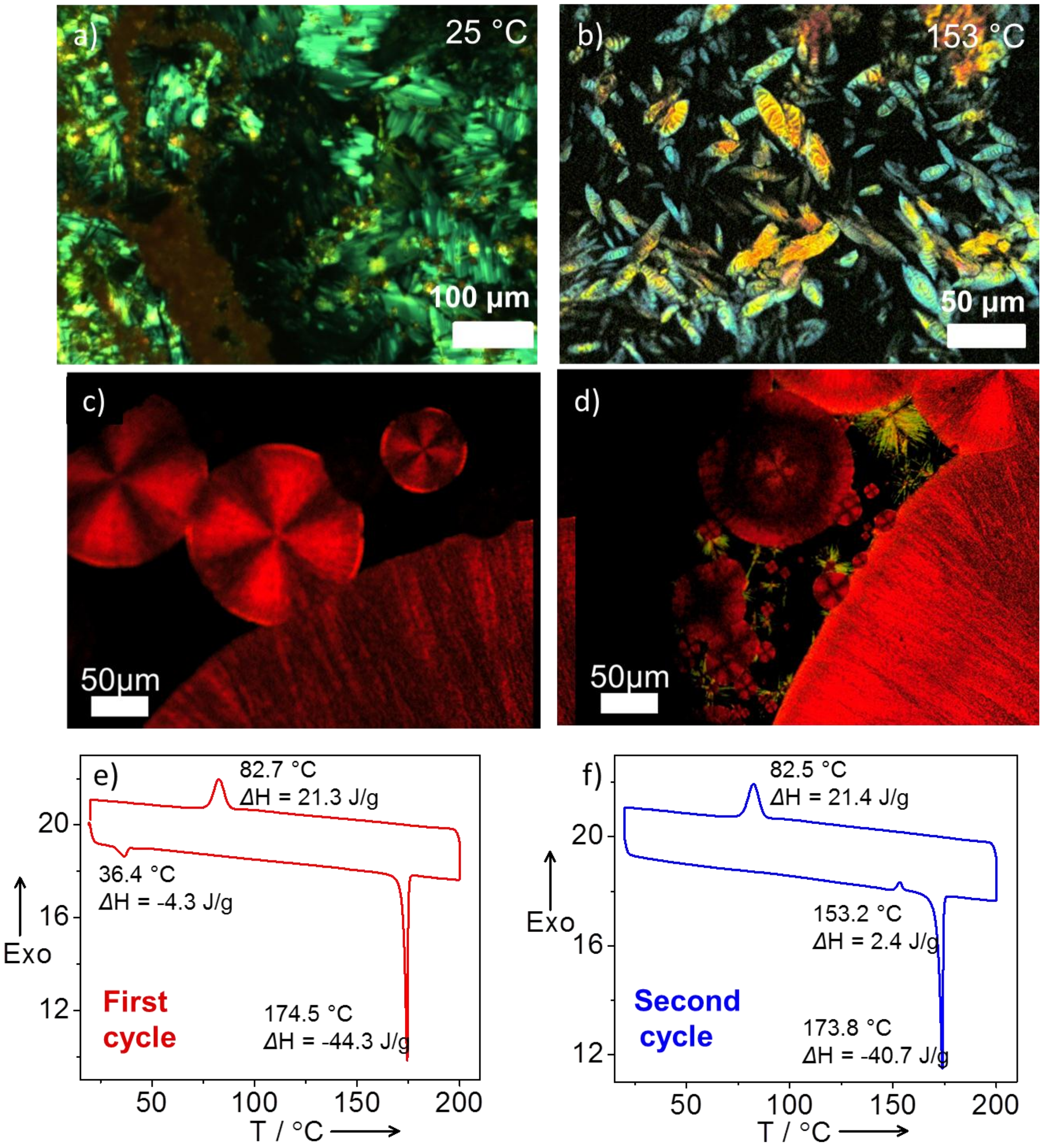

Figure 4.23. a, b) POM images of xerogel at 25 and 153 °C, respectively. c, d) Focal conic textures at 120 and 100 °C. e, f) DSC profiles of the xerogel for first and second heating/cooling cycles, respectively.

sharp crystallisation peak is observed at 84 °C on cooling the isotropic melt with a rate of 5 ºC/min. Between this wide range of temperatures of melting and crystallization, smectic texture was observed while cooling the solid material from its isotropic state (**Figure 4.23c**). The second heating cycle of DSC thermogram has shown (**Figure 4.23f**) an exothermic transition at 153 ºC before the melting transition with an enthalpy change of 2.46 J/g. At the above transition temperature of 153 °C only the texture corresponding to smectic batonnets were observed. The liquid crystalline textures are observed upon slow cooling (1 K min^{-1}) from the isotropic state.

4.3.8. SAXS and WAXS Analyses

The observation in DSC and POM is well supported by the diffraction pattern changes observed in the variable temperature SAXS and WAXS experiments performed on powder samples (**Figure 4.24**). The sharp reflection in the SAXS pattern at 25 ºC for a scattering vector of 1.1186 nm^{-1} corresponds to that of an interlayer *d*-spacing of 56.14 Å. The above distance is pretty much above than that of the length of the molecule (42 Å) in an optimized condition, indicating the possibility of an extended inter-digitated smectic (lamellar) ordering. The layer *d*-spacing undergoes some progressive increase with respect to temperature because of the tilting normally observed in smectic liquid crystalline phases. An average tilt angle (39°) was calculated based on the equation, $d_{001} = L \cos \theta$ (where L = length of the fully extended alkyl chain interdigitated dimer structure (74 Å) and d_{001} is the layer spacing (57.2 Å).[44, 45] The WAXS analysis of the powder sample clearly supports the phase change observed in the DSC thermogram at 35 ºC. The changes are more prominent in the wide angle region of the spectrum. For instance, in the wide angle region of $2\theta = 20$, a diffused reflection and a dramatic

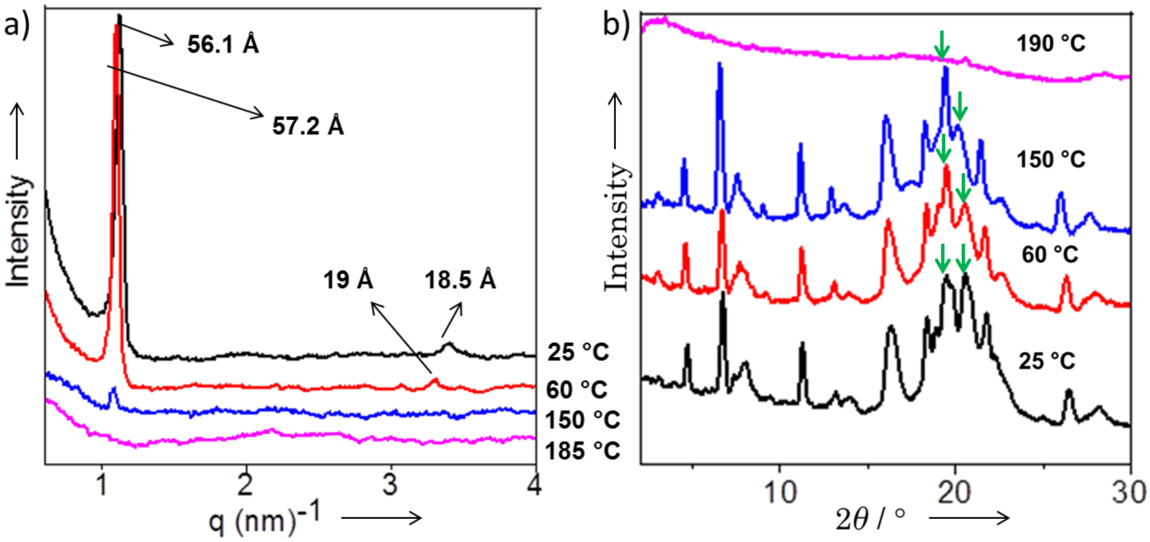

Figure 4.24. a, b) Variable temperature SAXS & WAXS analyses of **Bodipy-4** powder.

Change in the splitting pattern constituting the structural modifications due to alkyl chain packing are observed. At 25 °C, the broad peak at the wide angle 2θ value of 28.2 corresponding to a *d*-spacing value of 3.16 Å, undergoes a very slight change to 3.22 Å ($2\theta = 27.69$), when it was heated to 150 °C. The ratio of the peak intensities of the two peaks at 2θ values 19.49 and 20.56 undergo a change from 1:1 ratio to 1:4 (**Figure 4.24b**) nearly at 150 °C, supporting the formation of a highly ordered smectic phase formation due to greater π-stacking of molecular assemblies. More peaks at the wide angle region indicate the regular packing of mesogens. The intense peak at a *d*-spacing value of 56.8 Å is assigned to the fully interdigitated structure of the molecule.

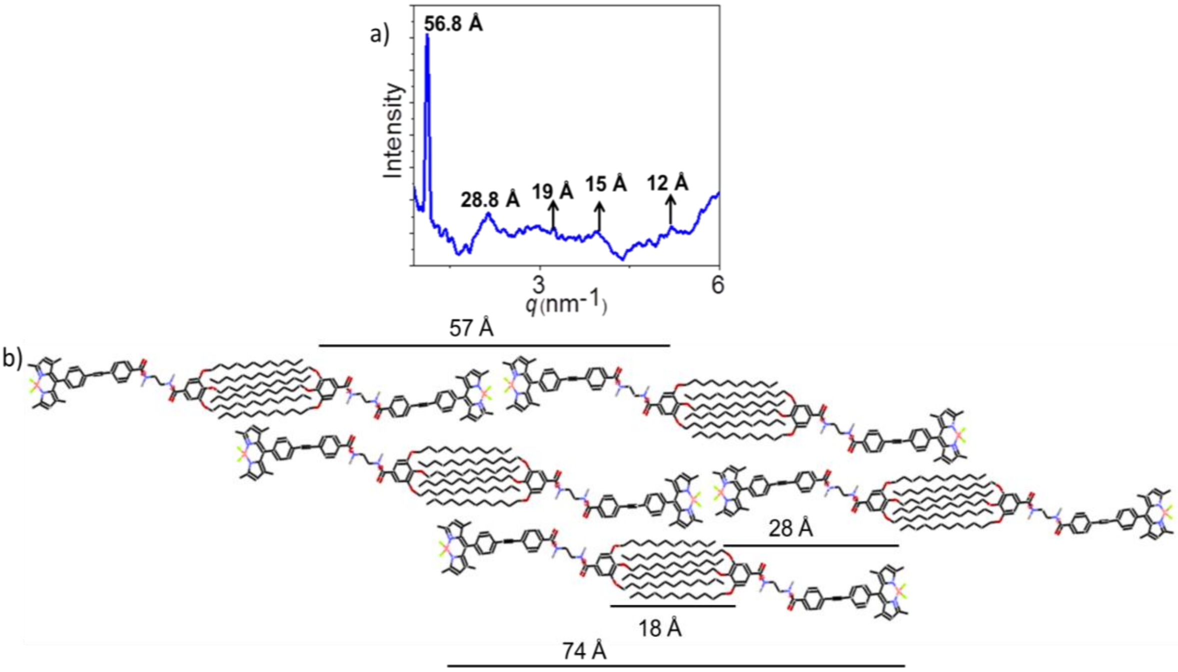

Figure 4.25. a) SAXS analysis of the xerogel. b) Probable molecular organisation in the xerogel state.

In the xerogel state, **Bodipy-4** packs in a slipped J-type fashion to form extended lamellar assembly as evident from SAXS (**Figure 4.25**). The slipped J-type packing is driven by intermolecular hydrogen bonding, which is clear from the variable temperature NMR and IR data. In the SAXS analysis, where the peak corresponding to *d*-spacing value of 18 Å is due to the interdigitated alkyl chains between two **Bodipy-4** units. The non-alkyl part of the **Bodipy-4** found a distance of 28 Å, which appeared as a broad peak. The prominent peak in the SAXS which appeared at 56.8 Å will be the repeating unit in molecular packing when the two interdigitated dimers with their chromophores units are closely packed. Additionally, the *d*-spacing values in the lower angle region possess a ratio of 1: ½: 1/3, which correspond to extended lamellar structure.[46-48]

4.4. Conclusion

Bodipy-4 shows concentration dependent self-assembly (discs to toroids) and luminescent properties. At lower concentration, intramolecularly H-bonded monomers are formed which are converted to intermolecularly hydrogen bonded dimers. These dimers undergo π-stacking to form disc-like particles. As the concentration increases, extended intermolecular hydrogen bonding will be more predominant, forming 1D supramolecular polymers, which further π-stacks to form 2D tapes. Finally, during the evaporation of solvents from the DMSO gel, these tapes undergo curling and multiple coiling one over other to form micro toroids. The self-assembly process is also temperature dependent where fast cooling at high concentration leads to coiled fibrous structures. Additionally, the **Bodipy-4** aggregates in DMSO exhibit birefringence at room temperature and form smectic batonnets when cooled from the isotropic state. The results indicate that **Bodipy-4** is a unique self-assembly module, that form gel specifically in DMSO leading to exotic micro toroids.

4.5. Experimental Section

4.5.1. Synthesis – General Procedures

General procedures for the drying and the purification of solvents, and the procedure for column chromatography are described in previous chapters.

Syntheses of compounds **11, 12** and **17** have already explained in **Chapter 2**.

4.5.1.1. Synthesis of *N*-(2-aminoethyl)-3,4,5-tris(dodecyloxy) benzamide (13)

Compound **12** (1 g, 1.48 mmol) was dissolved in dry dichloromethane (50 mL). BOP ((Benzotriazol-1-yloxy)tris(dimethylamino)phosphonium hexafluoro-phosphate) reagent (0.72 g, 1.63 mmol) and ethylenediamine (0.49 mL, 7.4 mmol) were added and the reaction mixture was stirred for 3 h at room temperature under inert atmosphere. Thereafter, the reaction mixture was washed with excess water and extracted the organic part using dichloromethane. The solvent was evaporated to get the crude product which was purified by column chromatography using silica gel and 97% chloroform-methanol solvent mixture to get a white solid (Mp, 105 °C). Yield: 85%, ^{1}H NMR (500 MHz, $CDCl_3$): δ = 7.01 (*s*, 2H; Ar-*H*), 6.85 (*s*, 1H; -N*H*-), 3.98 (*t*, *J* = 5.75 Hz, 6H; -OCH_2-), 3.48 (*t*, *J* = 5.5 Hz, 2H; -CH_2-), 2.94 (*t*, *J* = 5.5 Hz, 2H; -CH_2-), 2.1-1.95 (*m*, 4H; -CH_2-), 1.81- 1.71(*m*, 6H; -CH_2-), 1.46-1.26 (*m*, 50H; -CH_2-), 0.88-0.89 (*t*, *J* = 6.75 Hz, 9H; -CH_3). ^{13}C NMR (125 MHz, $CDCl_3$): δ = 167.81, 153.04, 141.05, 129.30, 105.67, 73.49, 69.30, 42.18, 41.23, 31.93, 29.65, 26.09, 22.69, 14.11, ppm. HRMS: calculated for $C_{45}H_{84}N_2O_4$ $[M+H]^+$: *m/z* = 717.65, found: 717.72.

4.5.1.2. Synthesis of 3,4,5-tris(dodecyloxy)-*N*-(2-(4-iodo -benzamido)ethyl benzamide (14)

Compound **13** (0.5 g, 0.7 mmol) was dissolved in dry dichloromethane (60 mL) in an oven-dried two-neck round bottom flask equipped with a magnetic stirring bar. (Benzotriazol-1-yloxy)tris(dimethylamino)phosphonium hexafluorophosph-

-ate (0.37 g, 0.84 mmol) and 4-iodo benzoic acid (0.21 g, 0.84 mmol) were added followed by triethylamine (0.12 mL, 0.84 mmol). The reaction mixture was stirred for 16 h at room temperature under inert atmosphere. Subsequently, the content was washed with excess water and extracted the organic part using dichloromethane. After evaporation of the solvent, the crude product was purified in a silica gel column using 97% chloroform-methanol solvent mixture (Mp, 110 °C). Yield: 70%, ^{1}H NMR (500 MHz, $CDCl_3$): δ = 7.76 (*d*, *J* = 8 Hz, 2H; Ar-*H*), 7.54 (*d*, *J* = 8.5 Hz, 2H; Ar-*H*), 7.45 (*s*, 1H; -N*H*-), 7.12 (*s*, 1H; -N*H*-), 6.98 (*s*, 2H; Ar-*H*), 3.98 (*t*, *J* = 6.5 Hz, 6H; $-OCH_2-$), 3.66 (*s*, 4H; $-CH_2-$), 1.82-1.72 (*m*, 6H; $-CH_2-$), 1.46-1.44 (*m*, 6H; $-CH_2-$), 1.33-1.30 (*m*, 48H; $-CH_2-$), 0.88 (*t*, *J* = 7 Hz, 9H; $-CH_3$). ^{13}C NMR (125 MHz, $CDCl_3$): δ = 168.99, 167.86, 153.08, 141.13, 137.76, 133.20, 128.70, 128.61, 105.52, 98.71, 73.53, 69.21, 41.12, 40.76, 31.94, 30.32, 29.73, 29.70, 29.59, 29.43, 29.38, 29.36, 26.12, 26.08, 22.70, 14.12, ppm. MALDI TOF-MS (matrix: α-cyano-4-hydroxycinnamic acid): calculated for $C_{52}H_{87}IN_2O_5$ $[M+H]^+$: *m/z* = 947.57, found: 947.91.

4.5.1.3. Synthesis of 3,4,5-tris(dodecyloxy)-*N*-(2-(4-((trimethylsilyl)ethynyl)benzamido)ethyl)benzamide (15)

Compound **14** (2.6 g, 2.7 mmol), bis(triphenylphosphine)palladium (II) dichloride (0.189 g, 10 mol%), and copper (I) iodide (52 mg, 10 mol%) were stirred in oxygen free tetrahydrofuran (20 mL) and triethylamine (10 mL) solvent system at room temperature for 15 minutes in argon atmosphere. Trimethylsilyl acetylene (0.58 mL, 4.1 mmol) was added drop wise into the reaction chamber and continued stirring for another 12 h. The reaction mixture was treated with dilute hydrochloric acid and extracted the organic part with chloroform, washed with water and brine. Purified the product by silica gel column chromatography and eluted with 97% chloroform-methanol solvent mixture. The product **15** was obtained (Mp, 102 °C). Yield: 80%, ^{1}H NMR (500 MHz, $CDCl_3$): δ = 7.77 (*d*, *J* = 8.5 Hz, 2H; Ar-*H*), 7.50 (*d*, *J* = 8.5 Hz, 2H; Ar-*H*), 7.48 (*s*, 1H; -N*H*-), 7.36 (*s*, 1H; -N*H*-), 7.01 (*s*, 2H; Ar-*H*), 3.98 (*t*, *J* = 6 Hz, 6H; $-OCH_2-$), 3.66 (*s*, 4H; $-CH_2-$), 1.82-1.72 (*m*, 6H; $-CH_2-$), 1.48-1.44 (*m*, 6H; $-CH_2-$), 1.31-1.27 (*m*, 48H; $-CH_2-$), 0.89 (*t*, *J* = 6.75 Hz, 9H; $-CH_3$), 0.27 (*s*, 9H; $-Si-(CH_3)_3$). ^{13}C NMR (125 MHz, $CDCl_3$): δ = 168.99, 167.86, 153.08, 141.13, 137.76, 133.20, 128.70, 128.61, 105.52, 98.9, 98.71, 73.53, 69.21, 53.5, 41.12, 40.76, 31.94, 30.32, 29.73, 29.70, 29.59, 29.43, 29.38, 29.36, 26.12, 26.08, 22.70, 14.12, 3.4 ppm. HRMS: calculated for $C_{57}H_{96}N_2O_5Si$ $[M+H]^+$: *m/z* = 917.72, found: 917.92.

4.5.1.4. Synthesis of 3,4,5-tris(dodecyloxy)-*N*-(-2-(4-ethynyl benzamido) ethyl)benzamide (16)

The silyl derivative **15** (1.9 g, 2.25 mmol) was dissolved in 10 mL of dichloromethane and stirred for 10 minutes. Potassium fluoride was slowly added (2.41 g, 41.5 mmol) in 50 mL methanol to the reaction chamber and stirred for 8 h at room temperature. The reaction mixture was extracted with chloroform and washed with water, brine and dried the organic part over anhydrous sodium sulphate. Purification was performed by column chromatography using silica gel and eluted with 97% chloroform-methanol solvent mixture. The product was obtained as a white solid (Mp, 97 °C). Yield: 76%, ^{1}H NMR (500 MHz, $CDCl_3$): δ = 7.79 (*d*, *J* = 8 Hz, 2H; Ar-*H*), 7.54 (*d*, J = 8.5 Hz, 2H; Ar-*H*), 7.38 (*s*, 1H; -N*H*-

), 7.12 (*s*, 1H; -N*H*-), 7.00 (*s*, 2H; Ar-*H*), 4.01-3.98 (*m*, 6H; -OCH_2-), 3.70 (*s*, 4H; -CH_2-), 3.20 (*s*, 1H; Acetylenic-*H*), 1.83-1.71 (*m*, 6H; -CH_2-), 1.47-1.44 (*m*, 6H; -CH_2-), 1.31-1.27(*m*, 48H; -CH_2-), 0.89 (*t*, *J* = 6.75 Hz, 9H; -CH_3). ^{13}C NMR (125 MHz, $CDCl_3$): δ = 168.86, 167.98, 153.06, 141.06, 133.27, 132.06, 128.66, 126.96, 126.61, 105.51, 103.98, 97.14, 73.50, 69.18, 40.95, 40.90, 31.93, 30.32, 29.71, 29.69, 29.59, 29.42, 29.37, 26.11, 26.07, 22.69 ppm. HRMS: calculated for $C_{54}H_{88}N_2O_5$ $[M]^+$: *m/z* = 844.67, found: 844.22.

4.5.1.5. Synthesis of Bodipy-4

Compound **17** (0.15 g, 34.2 mmol), bis(triphenylphosphine)palladium (II) dichloride (24 mg, 10 mol%), and copper (I) iodide (6.4 mg, 10 mol%) were added to an oven-dried two-neck round bottom flask equipped with a magnetic stirring bar. The round bottom flask was then sealed with a rubber septum, evacuated and backfilled with argon three times. Degassed triethylamine (30 mL) and THF (60 mL) were added. After stirring for 5 minutes at room temperature, the compound **16** (0.35 g, 41 mmol) dissolved in 30 mL (1:1) mixture of degassed triethylamine and THF was added and the reaction mixture was stirred at 60 °C for 24 h. The reaction mixture was extracted using chloroform and washed with dilute hydrochloric acid. The organic layer was washed with brine and dried over anhydrous sodium sulphate and then evaporated under reduced pressure. The crude product was then purified by column chromatography using silica gel as adsorbent. The pure compound (**Bodipy-4**) was eluted with 97% chloroform-methanol solvent mixture as orange red solid (Mp, 175 °C). Yield: 33%, FT-IR (KBr): ν_{max} = 3242, 3043, 2923, 2852, 2733, 2683, 2300, 2222, 1730, 1633, 1578, 1547, 1504, 1467, 1452, 1345, 1306, 1261, 1234, 1193, 1155, 1114, 1088, 1020, 982, 854, 832, 804, 765, 705; ^{1}H NMR (500 MHz, $CDCl_3$): δ = 7.83 (*d*, *J* = 8.5 Hz, 2H; Ar-*H*), 7.68 (*d*, *J* = 8 Hz, 2H; Ar-*H*), 7.61 (*d*, *J* = 8.5 Hz, 2H; Ar-*H*), 7.33 (*d*, *J* = 8.5 Hz, 2H; Ar-*H*), 7.31 (s, 1H; -N*H*-), 7.03 (*s*, 1H; -N*H*-), 6.99 (*s*, 2H; Ar-*H*), 6.00 (*s*, 2H; =C*H*-), 4.04-3.98 (*m*, 6H; $-OCH_2-$), 3.72 (*s*, 4H; $-CH_2-$), 2.56 (*s*, 6H; pyrrole-CH_3), 1.84-1.71 (*m*, 6H; $-CH_2-$), 1.48-1.44 (*m*, 6H; $-CH_2-$), 1.43 (*s*, 6H; pyrrole-CH_3), 1.33-1.26 (*m*, 48H; $-CH_2-$), 0.88 (*t*, *J* = 6.75 Hz, 9H; $-CH_3$) ppm; ^{13}C NMR (125 MHz, $CDCl_3$): δ = 168.96, 167.82, 155.85, 153.11, 142.96, 141.15, 140.61, 135.43, 133.48, 132.42, 131.80, 131.17, 128.68, 128.32, 127.17, 126.28, 123.61, 121.41, 105.49, 90.98, 89.86, 73.52, 69.23, 41.27, 40.93, 31.93, 30.31, 29.72, 29.66, 29.59, 29.42, 29.37, 26.11, 26.08, 22.70, 14.60, 14.13 ppm. MALDI TOF-MS (matrix: α-cyano-4-hydroxycinnamic acid): calculated for $C_{73}H_{105}BF_2N_4O_5$ $[M+H]^+$: *m/z* = 1168.45, found: 1168.50.

4.5.2. Characterization Techniques

NMR spectra were measured on a 300 or 500 MHz Bruker Avance DPX spectrometer. Chemical shifts are reported in parts per million (ppm) using tetramethylsilane (TMS) (δ H = 0 ppm) as an internal reference. The resonance multiplicity is described as *s* (singlet), *d* (doublet), *t* (triplet) and *m* (multiplet). FT-IR spectra were recorded on a Shimadzu IR Prestige-21 Fourier Transform Infrared Spectrophotometer (FT-IR) using KBr pellet method. Electrospray ionization (ESI) high-resolution mass spectra were recorded on using Thermo Scientific Exactive mass spectrometer. Matrix-assisted laser desorption ionization time-of-flight (MALDI-TOF) mass spectra were obtained on a Shimadzu

AXIMA-CFR PLUS spectrometer using α-cyano-4-hydroxycinnamic acid as the matrix.

4.5.3. Measurements

The electronic absorption spectra were recorded on a Shimadzu spectrophotometer UV-2100. The fluorescence spectra were recorded on a SPEX-Fluorolog-3 FL3-221 spectrofluorimeter. Optical studies in solution-state were carried out in 1 cm and 1 mm quartz cuvettes. Quantum yield measurements were carried out using fluorescein in 0.1 N NaOH as the standard which has a reported quantum yield of $\Phi_f = 0.91$.

Lifetime measurements were carried out using IBH (model 5000 DPS) time-correlated single photon counting (TCSPC) system. Experiments were carried out with 375 nm LED excitation source (pulse width < 100 ps, repetition rate 1 MHz). FT-IR spectra was recorded on a Shimadzu IR Prestige-21 FT-IR spectrophotometer. SEM images were taken on a Zeiss EVO 18 cryo SEM Special Edn with variable pressure detector working at 20-30 kV after sputtering with gold. Samples were prepared by drop casting of **Bodipy-4** in DMSO over a smooth aluminium foil. The drop cast samples were allowed to dry under normal condition for one day and subsequently subjected to drying under vacuum for 12 h. TEM analysis is carried out on a FEI Tecnai G2 30 EDAX microscope with an accelerating voltage of 100 kV. Samples prepared by drop-casting the aggregated solution over carbon coated copper grid and the images are obtained without staining. AFM analyses were carried out both in Multimode SPM (Veeco Nanoscope V) and in Multimode SPM (Bruker Nanoscope V). Samples were prepared by drop casting 2 µL solution of the sample on a freshly cleaved mica surface and dried under air. Imaging was done under ambient conditions in tapping mode. Fluorescence microscopy images were taken by using Leica DFC 290 microscope and confocal microscope (Pathway 855, BD Biosciences, USA). The WAXS analysis was carried out using XEUSS SAXS/WAXS system by Xenocs operated at 50 kV and 0.6 mA which is attached with a heating set-up (Linkam THMS 600 hot stage) for variable temperature measurements. The data were collected in the transmission mode geometry using Cu-K_α radiation of wavelength 1.54 Å. DSC measurements were carried out using Perkin Elmer Pyris 6 DSC where sample is heated to 175 °C at a heating and cooling rate of 5 °C min^{-1}. DLS analysis was carried out with a Zetasizer Nano S from Malvern Instruments at 25 °C. Solution used to detect hydrodynamic diameter (HDD) by DLS was passed through Millipore filters with a pore size of 0.22 µm to remove dust.

The gel melting temperature was determined by the dropping ball method.[49] In the dropping ball method, a steel ball (~100 mg) was placed on the top of a 1 mL volume of the gel in a sealed glass vial. The gel is slowly heated, while the position of the ball on the top of the gel was continuously observed, until the gel no longer bears the ball. The temperature at which the ball reaches the bottom of the vial was taken as the sol-gel phase transition temperature (T_{gel}).

Fluorescein in 0.1M NaOH (φ_f = 0.81) used as the standard for the relative quantum yield determination of **Bodipy-4** in chloroform and in the aggregated

DMSO solution (λ_{ex} = 470 nm). The experiments were done using optically matching solutions at the excitation wavelengths.

The relative quantum yield (Φ_f) is calculated by the following equation,

$\Phi_u = (\Phi_s.\ A_s.\ F_u.\ n^2_u) / (A_u.\ F_s.\ n^2_s)$

Φ_u = Quantum yield of the unknown sample, Φ_s = Quantum yield of the standard sample, A_s = Absorbance of the standard solution, A_u = Absorbance of the unknown solution, F_u = Fluorescent area of unknown sample F_s = Fluorescent area of standard sample, n_u = Refractive Index of unknown solution n_s = Refractive Index of standard solution.

Fraction of aggregates (α_{Agg}) is calculated by using the following equation,

$\alpha_{Agg} = (A_T - A_{mono}) / (A_{agg} - A_{mono})$ where α_{Agg} = Fraction of aggregates,

A_T = Absorbance at a particular temperature, A_{agg} = Absorbance at aggregated state and A_{mono} = Absorbance at monomeric state.

4.6. References

1. a) S. S. Babu, V. K. Praveen, A. Ajayaghosh, *Chem. Rev.* **2014**, *114,* 1973-2129; b) A. Ajayaghosh, V. K. Praveen, *Acc. Chem. Res.* **2007**, *40,* 644-656; c) P. Terech, R. G. Weiss, *Chem. Rev.* **1997**, *97*, 3133-3160; d) J. W. Steed, *Chem. Soc. Rev.* **2010**, *39*, 3686-3699.
2. a) L. Maggini, D. Bonifazi, *Chem. Soc. Rev.* **2012**, *41*, 211-241; b) F. J. M. Hoeben, P. Jonkheijm, E. W. Meijer, A. P. H. J. Schenning, *Chem. Rev.* **2005**, *105*, 1491-1546.

3. a) J.-M. Lehn, *Supramolecular Chemistry*; VCH: Winheim, Germany, **1995**; b) H.-J. Schneider, A. Yatsimirsky, *Principles and Methods in Supramolecular Chemistry*; Wiley: Chichester, **2000**.
4. V. A. Bloomfield, *Biopolymers* **1997**, *44*, 269-282.
5. D. Luo, W. M. Saltzman, *Nat. Biotechnol.* 2000, *18*, 893-895.
6. T. Renger, *Proc. Chem.* **2011**, *3(1)*, 236-247.
7. L. Cleary, H. Chan, C. Chuang, R. J. Silbey, J. Cao, *PNAS* **2013**, *110*, 8537-8542.
8. Y. Kim, W. Li, S. Shin, M. Lee, *Acc. Chem. Res.* **2013**, *46*, 2888-2897.
9. a) G. M Whitesides, *Science* **2002**, *295*, 2418-2421; b) D. N. Reinhoudt, M. Crego- Calama, *Science* **2002**, 295, 2418-2421.
10. T. Aida, E.W. Meijer, S. I. Stupp, *Science* **2012**, *335*, 813-817.
11. a) S. J. George, A. Ajayaghosh, P. Jonkheijm, A. P.H. J. Schenning, E. W. Meijer, *Angew. Chem. Int. Ed.* **2004**, *43*, 3422-3425; b) V. K. Praveen, S. J. George, R. Varghese, C. Vijayakumar, A. Ajayaghosh, *J. Am. Chem. Soc.* **2006**, *128*, 7542-7550.
12. D. C. Sherrington, K. A. Taskinen, *Chem. Soc. Rev.* **2001**, *30*, 83-93.
13. C. T. Seto, G. M. Whitesides, *J. Am. Chem. Soc.* **1990**, *112*, 6409-6411.
14. J. P. Mathias, E. E. Simanek, J. A. Zerkowski, C. T. Seto, G. M. Whitesides *J. Am. Chem. Soc.* **1994**, *116*, 4316-4325.
15. G. M. Whitesides, E. E. Simanek, J. P. Mathias, C. T. Seto, D. N. Chin, M. Mammen and D. M. Gordon, *Acc. Chem. Res.* **1995**, *28*, 37-44.

16. S. Yagai, S. Mahesh, Y. Kikkawa, K. Unoike, T. Karatsu, A. Kitamura, A. Ajayaghosh, *Angew. Chem. Int. Ed.* **2008**, *47*, 4691-4694.

17. a) S. Yagai, Y. Goto, T. Karatsu, A. Kitamura,Y. Kikkawa, *Chem. Eur. J.* **2011**, *17*, 13657-13660; b) S. Yagai, H. Aonuma, Y. Kikkawa, S. Kubota, T. Karatsu, A. Kitamura, S. Mahesh, A. Ajayaghosh, *Chem. Eur. J.* **2010**, *16,* 8652-8661.

18. S. Yagai, S. Kubota, H. Saito, K. Unoike, T. Karatsu, A. Kitamura, A. Ajayaghosh, M. Kanesato, Y. Kikkawa, *J. Am. Chem. Soc.* **2009**, *131*, 5408-5410.

19. E. Lee, J. K. Kim, M. Lee, *J. Am. Chem. Soc.* **2009**, *131*, 18242-18243.

20. a) H.-J. Kim, S.-K. Kang, Y.-K. Lee, C. Seok, J.-K. Lee, W.-C. Zin, M. Lee, *Angew. Chem. Int. Ed.* **2010**, *49,* 8471-8475; b) Z. Huang, S.-K. Kang, M. Banno, T. Yamaguchi, D. Lee, C. Seok, E. Yashima, M. Lee, *Science* **2012**, *337,* 1521-1526.

21. Y. Lim, E. Lee, M. Lee, *Macromol. Rapid Commun.* **2011**, *32*, 191-196.

22. V. M. Suresh, S. J. George, T. K. Maji, *Adv. Funct. Mater.* **2013**, *23,* 5585-5590.

23. C. Yang, L. Gao, J. Lin, L. Wang, C. Cai, Y. Wei, Z. Li, *Angew. Chem. Int. Ed.* **2017**, *56,* 5546-5550.

24. S. Cherumukkil, S. Ghosh, V. K. Praveen, A. Ajayaghosh, *Chem. Sci.* **2017**, DOI: 10.1039/C7SC01696D.

25. W. Qin, M. Baruah, M. V. D. Auweraer, F. C. D. Schryver, N. Boens, *J. Phys. Chem. A* **2005**, *109*, 7371-7384.

26. S. Ogi, V. Stepanenko, J. Thein, F. Wurthner, *J. Am. Chem. Soc.* **2016**, *138*, 670-678.

27. a) S. Ogi, V. Stepanenko, K. Sugiyasu, M. Takeuchi, F. Wurthner, *J. Am. Chem. Soc.* **2015**, *137*, 3300-3307; b) S. Ogi, K. Sugiyasu, S. Manna, S. Samitsu, M. Takeuchi, *Nat. Chem.* **2014**, *6*, 188-195; c) E. Mattia, S. Otto, *Nat. Nanotechnol.* **2015**, *10*, 111-119.

28. Z. Chen, A. Lohr, C. R. S.-Möller, F. Würthner, *Chem. Soc. Rev.* **2009**, *38*, 564-584.

29. F. Camerel, L. Bonardi, M. Schmutz, R. Ziessel, *J. Am. Chem. Soc.* **2006**, *128*, 4548-4549.

30. A. Florian, M. J. Mayoral, V. Stepanenko, G. Fernandez, *Chem. Eur. J.* **2012**, *18*, 14957-14961.

31. N. K. Allampally, A. Florian, M. J. Mayoral, C. Rest, V. Stepanenko, G. Fernández, *Chem. Eur. J.* **2014**, *20*, 10669-10678.

32. W. H. James, C. W. Müller, E. V. Buchanan, M. G. D. Nix, L. Guo, L. Roskop, M. S. Gordon, L. V. Slipchenko, S. H. Gellman, T. S. Zwier, *J. Am. Chem. Soc.* **2009**, *131*, 14243-14245.

33. W.-D. Jang, T. Aida, *Macromolecules* **2004**, *37*, 7325-7330.

34. V. S. Balachandran, S. R. Jadhav, P. Pradhan, S. D. Carlo, G. John, *Angew. Chem. Int. Ed.* **2010**, *49*, 9509-9512.

35. D. Ke, C. Zhan, A. D. Q. Li, J. Yao, *Angew. Chem. Int. Ed.* **2011**, *50*, 3715-3719.

36. E. Betthausen, C. Hanske, M. Müller, A. Fery, F. H. Schacher, A. H. E. Müller, D. J. Pochan, *Macromolecules* **2014**, *47*, 1672-1683.

37. N. S. S. Kumar, S. Varghese, G. Narayan, S. Das, *Angew. Chem. Int. Ed.* **2006**, *45*, 6317-6321.

38. M. R. Molla, S. Ghosh, *Chem. Eur. J.* **2012**, *18*, 9860-9869.

39. S. Yagai, T. Kinoshita, M. Higashi, K. Kishikawa, T. Nakanishi, T. Karatsu, A. Kitamura, *J. Am. Chem. Soc.* **2007**, *129*, 13277-13287.

40. E. R. Soule, N. M. Abukhdeir, A. D. Rey, *Macromolecules* **2009**, *42*, 9486-9497.

41. G. Shanker, C. V. Yelamaggad, *J. Phys. Chem. B* **2011**, *115*, 10849-10859.

42. C. G. Nardele, S. K. Asha, *J. Phys. Chem. B* **2014**, *118*, 1670-1684.

43. F. Mathevet, P. Masson, J.-F. Nicoud, A. Skoulios, *J. Am. Chem. Soc.* **2005**, *127*, 9053-9061.

44. E. Vergara, E. Arias, Ivana Moggio, C. G.-Vega, R. F. Ziolo, R. M. Jimenez-Barrera, D. Navarro, O. Rodríguez, S. Fernandez, Manuel Herrera, *Langmuir* **2015**, *31*, 6909-6916.

45. L.-Y. Wang, H.-Y. Tsai, H.-C. Lin, *Macromolecules* **2010**, *43*, 1277-1288.

46. S. Yagai, S. Okamura, Y. Nakano, M. Yamauchi, K. Kishikawa, T. Karatsu, A. Kitamura, A. Ueno, D. Kuzuhara, H. Yamada, T. Seki, H. Ito, *Nat. Commun.* **2014**, *5*, 4013.

47. J. M. Malicka, A. Sandeep, F. Monti, E. Bandini, M. Gazzano, C. Ranjith, V. K. Praveen, A. Ajayaghosh, N. Armaroli, *Chem. Eur. J.* **2013**, *19*, 12991-13001.

48. R. Thirumalai, R. D. Mukhopadhyay, V. K. Praveen and A. Ajayaghosh, *Sci. Rep.* **2015**, *5*, 09842.

49. K. Murata, M. Aoki, T. Suzuki, T. Harada, H. Kawabata, T. Komori, F. Ohseto, K. Ueda, S. Shinkai, *J. Am. Chem. Soc.* **1994**, *116*, 6664-6676.

Papers Presented at Conferences (Posters/Oral)

1. Bodipy based mechanochromic liquid crystalline self-assembly. **S. Cherumukkil,** A. Ajayaghosh.

   A poster presented in the CRSI conference at IITB, 2013, February 7-10.

List of Publications from the Thesis Work

1. An Unprecedented Amplification of Near-Infrared Emission in a Bodipy Derived π-System by Stress or Gelation. **S**. **Cherumukkil**, S. Ghosh, V. K. Praveen and A. Ajayaghosh

   Chem. Sci. **2017**, *8*, 5644-5649.
2. A Bodipy Derived Photonic Material for Security and Waveguiding Applications. **S. Cherumukkil**, R. P. N. Tripathi, S. Ghosh, G. V. Pavan Kumar and A. Ajayaghosh (Manuscript under preparation).
3. A Bodipy Derived Liquid Crystalline π-Gelator that Forms Micron Sized Toroidal Structures. **S. Cherumukkil** and A. Ajayaghosh (Manuscript under preparation).

List of Publications from Other Related Works

1. Pyridyl-Amides as a Multimode Self-Assembly Driver for the Design of a Stimuli Responsive π-Gelator. K. K. Kartha, V. K. Praveen, S. S. Babu, **S. Cherumukkil** and A. Ajayaghosh.

   Chem. Asian J. **2015**, 10, 2250-2256.

2. Color-Tunable Cyano-Substituted Divinylene Arene Luminogens as Fluorescent π-Gelators. F. Aparicio, **S. Cherumukkil**, A. Ajayaghosh and L. Sanchez.

   Langmuir **2016**, *32*, 284-289.